

PH.D. THESIS

CAVITY-ENHANCED OPTICAL CLOCKS



This thesis has been submitted to the PhD School of
The Faculty of Science, University of Copenhagen

BY
STEFAN ALARIC SCHÄFFER

Cavity-enhanced optical clocks

Author Stefan Alaric Schäffer
Advisor Jan Westenkær Thomsen



*As partial fulfillment of the requirements for the degree of
Doctor of Philosophy*

Group for Precision Measurements with Ultracold Atoms,
The Niels Bohr Institute

July 21st, 2019

ABSTRACT

Atomic clocks have revolutionized the world of metrology since their first demonstration in 1955. These frequency measurement devices have led to the possibility of fast communications and computation technologies, navigation systems such as the GPS, and a wealth of fundamental applications that continue to push forward physics. The enormous potential allowed by using atomic clocks continues to motivate their further development and improvement. Atomic clocks have moved from room-temperature samples of atoms to laser-cooled atoms, and are now moving from microwave to optical transitions in the state-of-the-art systems. The further improvement of optical atomic clocks rests on incorporating new techniques, often borrowed from the world of quantum optics. Here we investigate two approaches to optical atomic clocks inspired by spectroscopy and cavity quantum electrodynamics (CQED). These approaches both promise the possibility of continuous clock operation, and seeks to resolve some of the current limitations of atomic clocks.

The first approach relies on cavity-enhanced spectroscopy of cold strontium atoms using the Noise-Immune Cavity-Enhanced Optical Heterodyne Molecular spectroscopy (NICE-OHMS) method. This method is a passive interrogation of the atoms as in current optical atomic clocks, but with a significantly altered measurement method. We investigate the dynamics of the system and quantify the perturbation by the optical cavity. The method uses atomic phase-shift-measurements, and exploits this signal directly as an error-signal in order to stabilize the frequency of the probing laser. The optical cavity is seen to distort the dispersion feature when the atom number increases above a certain threshold, and the consequences for a frequency lock are analyzed. Theoretical predictions of the obtainable laser linewidth in the mHz range is shown and a preliminary frequency lock is realized.

The second approach relies on the same physical system, but is operated in a fundamentally different way. Rather than using the atoms as a passive reference here we seek to have the atoms emit lasing light directly on a narrow atomic transition. This is done within the cavity mode analogously to a traditional laser, and constitutes an active approach to the optical atomic clock. The system is operated on the limit of the so-called bad-cavity regime. In this regime superradiant lasing becomes possible, where atomic dipoles synchronize through the cavity mediated coupling, and can emit coherently into the cavity mode. Characterization of the resonant exchange of excitations in the atom-cavity system is performed, and the experiments are shown to exhibit excellent agreement with our theoretical model and simulations. The spectral behavior of the emitted light is analyzed, and an evaluation of the frequency stability is performed. This shows the road for the

future development of active optical clocks in the form of superradiant lasers – a road that is already being pursued in order to realize a continuously lasing system.

We also present recent developments on two state-of-the-art optical lattice clocks at the U.S. National Institute of Standards and Technology NIST, based on ytterbium atoms. The Yb optical lattice clocks show excellent performance in the three main figures of merit for atomic clocks: accuracy, stability and reproducibility. Record-breaking performances in all aspects are reported, and the resulting consequences for a future change of the SI definition of the second is briefly discussed. The clocks show accuracy that permits determination of the gravitational potential to an accuracy better than the current possibilities with GPS systems. This marks the era where atomic clocks are becoming one of the most precise way to measure absolute gravitational potential.

RESUMÉ

Siden atomure blev opfundet i 1955 har de revolutioneret den moderne metrologi-verden. De har muliggjort udviklingen af hurtig telekommunikation, navigationssystemer såsom GPS, samt et væld af fundamentale undersøgelser der stadig driver fysikken fremad. Det store potentiale som brugen af atomure medfører, betyder også at interessen i deres fortsatte udvikling er stor. Atomure er gået fra at bruge varme atomer til laser-kølede atomer, og fra at være baseret på mikrobølgesignaler til at bruge optiske signaler i de bedste nutidige ure. Den videre udvikling af atomure kræver nye teknikker, som ofte lånes fra kvanteoptik. I denne afhandling undersøger vi to tilgange til optiske atomure som er baseret på spektroskopi og kavitetskvanteelektrodynamik (CQED). Disse tilgange lover både muligheden for kontinuære målinger af uret frekvens, og sigter samtidig mod at løse nogle af de begrænsninger som moderne atomure møder.

Den første tilgang er baseret på kavitetsforstærket spektroskopi af kolde strontiumatomer og bruger en metode kaldet støjimmun, kavitetsforstærket, optisk, heterodyn molekylær spektroskopi (NICE-OHMS). Ligesom nuværende optiske atomure er det en teknik der benytter atomerne som passive elementer, men måler på en væsentligt anderledes måde. Vi undersøger dynamikken i systemet og redegør for den korrektion af dets opførsel som den optiske kavitet resulterer i. Metoden bruger fasemålinger af atomerne og bruger dette signal direkte til at låse frekvensen af en målelaser. Vi finder at kaviteten forvrænger det målte dispersionssignal når atomtallet overstiger en vis terskel, og analyserer konsekvenserne for en frekvenslås. Vi viser teoretiske forudsigelser om en potentiel laserliniebredde i mHz-regimet, og realiserer en præliminær frekvenslås.

Den anden tilgang baserer sig på det samme eksperimentelle fysiske system, men fungerer på en fundamentalt anderledes måde. Frem for at bruge atomerne som en passiv reference, forsøger vi at få dem til at udsende laser lys direkte på en smal atomar overgang. Laserlyset udsendes i kavitetsfeltet som i en klassisk laser, og det resulterer altså i en version af atomuret, hvor atomerne aktivt genererer det lys der bruges. Vi benytter systemet på grænsen af bad-cavity regimet, hvor superradiant lasing bliver muligt. Denne form for lasing baserer sig på synkroniserede dipoler som interagerer gennem kavitetsfeltet, og sidenhen kan udsende lys kohærent in i kaviteten. Vi karakteriserer den resonante ombytning af energi mellem atom og kavitet og viser at eksperimentet og vores teoretiske simulation stemmer overordentligt godt overens. Vi karakteriserer spektret af den udsendte lys, og måler frekvensstabiliteten. Denne del viser vejen for den videre udvikling af aktive atomure baseret på superradiante lasere – en retning vi allerede følger for at

realisere et kontinuært lasende system.

Vi præsenterer også nylig udvikling af to af verdens bedste optisk-gitter atomure med ytterbium atomer på U.S. National Institute of Standards and Technology (NIST). Urene viser fremragende opførsel i de tre centrale karakteristika for atomure: Nøjagtighed, stabilitet og reproducerbarhed. Rekordtal i alle parametre vises, og konsekvenserne for en fremtidig omdefinition af SI-sekundet diskuteres kort. Atomurene tillader måling af jordens tyngdepotentiale med nøjagtighed som er bedre end det er muligt med GPS-systemer. Dette markerer tidspunktet hvor atomure er blevet et af de mest præcise metoder til at måle gravitationsfeltet.

CONTENTS

Preface and publications	viii
1 Frequency references and atomic clocks	1
1.1 Stability and accuracy	2
1.2 Optical frequency references	6
1.3 Superradiant optical clocks	8
2 Introduction to cold atoms in cavities	11
2.1 Transitions of strontium	12
2.2 Atoms and cavities	13
2.3 Cold atoms	19
3 Experimental systems	23
3.1 Atom cloud machine	23
3.2 Reference lasers	32
4 NICE-OHMS	39
4.1 Saturated spectroscopy in a cavity	40
4.2 NICE-OHMS detection scheme	43
4.3 Classical theory of cavity interaction	45
4.4 Atom-field interaction	48
4.5 Beyond the linear regime	50
4.6 Frequency stability	56
5 A pulsed laser in the crossover regime to superradiance	59
5.1 Gain in an unconfined cold ensemble	60
5.2 Atom-cavity interaction	66
5.3 Lasing pulses	70
5.4 Lasing threshold	71
5.5 Time-evolution of the lasing pulses	73
5.6 Seeded lasing	77
5.7 Spectral properties	80
5.8 Frequency stability	84
6 Ytterbium optical lattice clocks at NIST	87
6.1 Electronic sideband locking to a multi-color cavity	90
6.2 Lattice laser	91

6.3	BBR shift from localized heating in a window	93
6.4	DC Stark shift measurement and cancellation	95
6.5	Frequency evaluations	97
7	Conclusions and outlook	103
7.1	Prospects for a NICE-OHMS clock	103
7.2	Prospects for a superradiant clock	104
A	Design details for a continuous cold-atom machine at NBI	107
A.1	Oven design	108
A.2	MOT coils	108
A.3	Interference filter laser	110
A.4	Some cavity designs	113
B	Environmental noise	119
B.1	Vibration measurements	119
B.2	Acoustic measurements	121
C	Included papers	123
	Dynamics of bad-cavity-enhanced interaction with cold Sr atoms for laser stabilization [99]	123
	Towards passive and active laser stabilization using cavity-enhanced atomic interaction [98]	134
	Lasing on a narrow transition in a cold thermal strontium ensemble [100]	141
	Acknowledgments	151
	List of Figures	153
	List of Tables	155
	Bibliography	157

PREFACE AND PUBLICATIONS

This thesis presents some of the work performed while I was a PhD Fellow at the Niels Bohr Institute, University of Copenhagen. Most of my work has been focused on experiments with cold strontium atoms. The atoms are trapped in an optical cavity, with the purpose of allowing novel approaches to highly stable frequency references and atomic clocks. I have had the pleasure of supervising and co-supervising four master students, as well as a number of bachelor students and smaller student projects. The experimental work in the laboratory was complemented with acting as a teaching assistant in the bachelor courses optics and atomic physics during 2015 and 2016. I have had the pleasure of attending one or two conferences every year both as a speaker and to present posters. Public outreach has included general talks on the possibilities of atomic clocks, participation in a podcast series¹.

Initial work in my PhD centered on the NICE-OHMS approach to dispersive measurements on a cold sample of strontium atoms. This work is a continuation of the investigations made during my masters thesis [18], [19], [97]. We give a theoretical description of the experimentally observed highly nonlinear dispersion signals, and present prospects and limitations for a laser stabilization scheme based on this approach in [99]. This work is presented in chapter 4. Later my focus changed towards the possibility of using our thermal ensemble of atoms to generate superradiant lasing directly on a forbidden transition in strontium. This was realized and presented in [100] along a numerical model and simulations of the system that allows significant insights into the velocity-dynamics of the atoms. A subsequent publication on the spectral properties of this system is currently under preparation. Work on superradiance in the system is presented in chapter 5.

I have had the opportunity to take part in the application process for several EU grants, of which we are currently participating in four. Like my own work these research projects follow the idea of using our system as a passive reference, and subsequently to produce superradiant lasing. In the EURAMET project USOQS² and the QuantERA project Q-Clocks³ we collaborate with metrological institutes in Europe, and aim to realize a continuous version of our passive cold-atom frequency stabilization and investigate the possibilities of superradiance. The work on superradiant lasing has resulted in a cross-European collaboration with the

¹Henrik Prætorius, "Tid er relativ: Din overlæbe er ældre end din underlæbe.", Den Nysgerrige Jordbo, January 18, 2019. URL: <http://henrikpraetorius.dk/check-min-podcast-den-nysgerrige-jordbo>

²Ultra-Stable optical Oscillators from Quantum coherent and entangled Systems

³Cavity-Enhanced Quantum Optical Clocks

iqClock⁴ consortium <https://www.iqclock.eu/> as part of the EU quantum flagship. Through this consortium we are now collaborating on both experiments and theoretical investigations with several other European universities. Recently a supporting International Training Network (ITN) proposal to the iqClock consortium was accepted – the MoSaiQC⁵ collaboration. This will allow the initial steps taken in this thesis to lead on to improved understanding and performance of such systems.

During my PhD I spent 5 months as a guest researcher at the U. S. National Institute of Standards and Technology (NIST) in Boulder, CO in USA with the group of Andrew D. Ludlow. I had the opportunity to work on the two Yb optical lattice clocks there, and be part of the day-to-day research. I was quickly allowed to be part of a number of investigations on the clocks. I have attempted to give a cursory overview of this work in chapter 6, but have left the main focus of this thesis to be on the work conducted in Copenhagen. During my time at NIST I was involved in the publication of [4], [70], [71], [123], [124].

My PhD work has resulted in the following papers:

Publications

1. **S. A. Schäffer**, B. T. R. Christensen, M. R. Henriksen, and J. W. Thomsen: *Dynamics of bad-cavity enhanced interaction with cold Sr atoms for laser stabilization*, Physical Review A, 96, 013847, (2017).

[99] — We investigate the dispersive response of cold strontium atoms coupled to an optical cavity mode. The full dispersive lineshape is seen to be heavily modified by the cavity, in a highly nonlinear way that is then explained theoretically. The potential of the system for laser frequency stabilization is investigated and the locking bandwidth limitations imposed by the distortion of the dispersion signal are discussed.

I performed the experiments, analyzed the data and was the main author of the document.

2. **S. A. Schäffer**, B. T. R. Christensen, S. M. Rathmann, M. H. Appel, M. R. Henriksen, and J. W. Thomsen: *Towards passive and active laser stabilization using cavity-enhanced atomic interaction*, J. Phys.: Conf. Ser. 810, 012002, (2017).

[98] — We present the prospects of using a simple cold strontium atom system for novel atomic clocks in either passive, dispersive measurements or active lasing configurations.

The paper is based on an invited talk about my ongoing research at the time. I was the main author of the manuscript.

3. J. Yao, J. Sherman, T. Fortier, J. Yao, T. Parker, J. Levine, J. Savory, S. Romisch, W. McGrew, X. Zhang, D. Nicolodi, R. Fasano, **S. Schäffer**, K. Beloy, and A. Ludlow: *Progress on optical-clock-based time scale at NIST: Simulations and preliminary real-data analysis*, Navigation, 1-8, (2018).

[124] — Minor contributions — Simulations of the effect of incorporating an intermittently running optical atomic lattice clock into a real time scale,

⁴integrated quantum Clock

⁵Modular Systems for Advanced Integrated Quantum Clocks

as well as analysis of the NIST Yb optical lattice clock performance in such a setting.

I worked on and operated the atomic clock for the time-scale.

4. K. Beloy, X. Zhang, W. F. McGrew, N. Hinkley, T. H. Yoon, D. Nicolodi, R. J. Fasano, **S. A. Schäffer**, R. C. Brown, and A. D. Ludlow *A Faraday-shielded, DC Stark-free optical lattice clock*, Physical Review Letters, *120*, 183201 (2018).
Journal cover photo.

[4] — A presentation of methods to map out and compensate DC stark shifts on the frequency of an atomic clock transition. We show the effectiveness of a Faraday-shield in reducing the fractional frequency shift and its uncertainty to below 10^{-19} .

I worked on the experimental setup, recorded data, and was part of the experimental discussions. I took part in the manuscript iteration process.

5. M. Tang and **S. A. Schäffer**: *Det aktive atomur – en laser i sin reneste form*, KVANT, *4* (2018)

[109] — A presentation of the concept of an active atomic clock, its working principle and our approach to realizing it.

I performed the experiments, discussed the data analysis and wrote the paper alongside MT.

6. W. F. McGrew, X. Zhang, , R. J. Fasano, **S. A. Schäffer**, K. Beloy, D. Nicolodi, R. C. Brown, N. Hinkley, G. Milani, M. Shioppo, T. H. Yoon, and A. D. Ludlow *Atomic clock performance enabling geodesy below the centimetre level*, Nature, *564*, 87–90 (2018)

[70] — We show excellent performance of an Yb optical lattice clock in terms of frequency stability, accuracy, and repeatability. The uncertainty budgets for the optical Yb lattice clocks at NIST, Boulder are presented, and we discuss their sensitivity to gravitational redshift. This sensitivity renders the clocks more precise than canonical approaches to measuring the height relative to the Geode.

I worked on the experimental setup, performed measurements, and contributed to the evaluation of the frequency uncertainty. I took part in the manuscript iteration process.

7. W. F. McGrew, X. Zhang, , R. J. Fasano, D. Nicolodi, K. Beloy, H. Leopardi, J. Yao, J. A. Sherman, **S. A. Schäffer**, J. Savory, S. Römisch, C. W. Oates, T. M. Fortier, T. E. Parker, and A. D. Ludlow *Towards the optical second: verifying optical clocks at the SI limit*, Optica, *6*, 4, 448-454 (2019)

[71] — An absolute frequency measurement of the optical Yb lattice clocks at NIST, Boulder is presented. The most accurate measurement to date. Through previous frequency ratio measurements this work allows consistency checks on a number of frequency measurement "loops". We also set limits on the drift and coupling to gravity of the electron-proton mass ratio.

I worked on the experimental setup and performed measurements.

Under review

In addition the following publications have been submitted, but are not published at the time of writing:

1. **S. A. Schäffer**, M. Tang, M. R. Henriksen, A. A. Jørgensen, B. T. R. Christensen and J. W. Thomsen: *Lasing on a narrow transition in a cold thermal Sr ensemble*, Under review with Physical Review A (2019).

[100] — Experimental realization of a superradiant lasing pulse in the crossover regime between the good and bad cavity limit. Numerical simulations of the system are presented and seen to agree very well with the experiment. The theoretical description also permits an investigation of the velocity-dynamics of the thermal ensemble of atoms during lasing. I designed the experimental approach, recorded and analyzed data. I was the main author of the manuscript.

2. J. Yao, J. Sherman, T. Fortier, H. Leopardi, T. Parker, W. McGrew, X. Zhang, D. Nicolodi, R. Fasano, **S. Schäffer**, K. Beloy, J. Savory, S. Romisch, C. Oates, S. Diddams, A. Ludlow and J. Levine: *Optical-Clock-Based Time Scale*, Arxiv:1902.06858, Submitted to Nature Photonics (2019).

[124] — An experimental and numerical investigation of using Yb optical atomic clocks in a real time scale at NIST, Boulder. Current optical atomic clocks cannot run continuously, and often run only for a fraction of a day. Using an ensemble of masers we show the effect of reduced operating time of a reference optical atomic clock.

I worked on and operated the atomic clock for the time-scale.

FREQUENCY REFERENCES AND ATOMIC CLOCKS

Contents

1.1	Stability and accuracy	2
1.2	Optical frequency references	6
1.3	Superradiant optical clocks	8

Much of modern technology relies upon the precise timing of processes and signals. To do this, accurate and stable frequency references are necessary. There has been a wealth of innovations and improvements in this area over the last 70 years, leading to miniature crystal oscillators almost completely replacing mechanical pendula in most compact time-keeping devices. Fundamental research has also pushed intensively on this development, and atomic clocks based on well-defined electronic transitions in atoms were first demonstrated 64 years ago [29]. They have now replaced the use of mechanical objects and astronomical phenomena as the international standard for time¹. The SI unit of a second has thus been defined with respect to a hyperfine transition in cesium-133, between the $F = 3, m_f = 0$ and $F = 4, m_f = 0$ ground states which has been chosen as exactly 9.192631770 GHz [5]. See figure 1.1.

As a consequence of this definition the second is today the unit that can be determined with the absolute highest degree of accuracy. State-of-the-art atomic clocks based on other atoms have been shown to perform at fractional accuracy and stability levels below 10^{-18} [14], [70], [83]. For the best cesium atomic fountain clocks that are the current basis for our timescale, the fractional frequency accuracy

¹Curiously, Denmark has retained a law from 1893 defining the danish time with respect to the position of the sun in the sky. This is, however, ignored in practice, and the international standard is used.

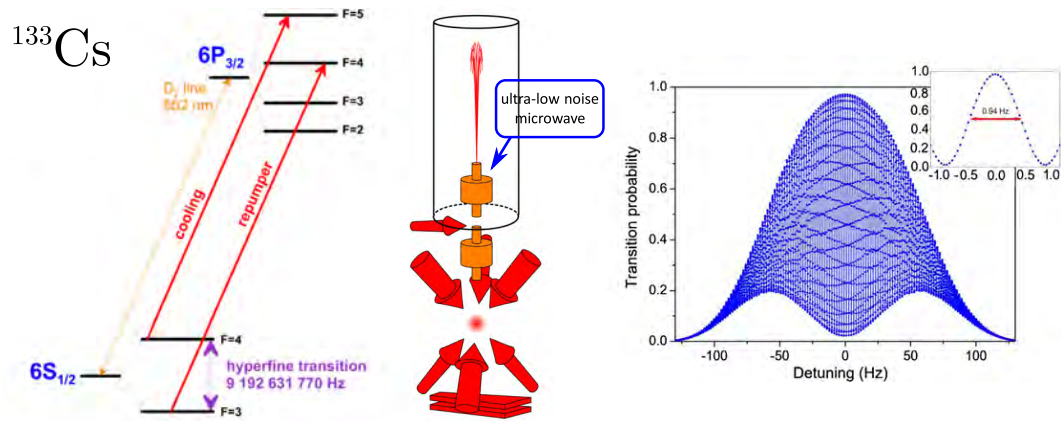


Figure 1.1: Cs atomic clock concept from [7]. **Left:** energy levels of the Cs atom. **Center:** conceptual overview of the Cs fountain atomic clock currently used as the state-of-the-art cs atomic clock. This system relies on laser cooling of the atoms and a ballistic atomic trajectory relying on the gravitational pull of earth. **Right:** Ramsey spectroscopy signal used for stabilization of the microwave frequency.

is at the $2 \cdot 10^{-16}$ level [121], and enables a wealth of applications beyond mere timekeeping. While timekeeping itself can be characterized as the act of tracking the time-dependency of events, having an accurate way of doing this allows high precision measurements of such diverse things as chronological ordering of financial transactions, positioning by use of, e.g., the Global Navigation Satellite System (GNSS) or mapping out of the gravitational field on earth [40], [70], [72]. It is also interesting for fundamental physics such as tracking the time-dependency of fundamental constants [2], [27], [28], [32], [33], [71], [86], [93], measuring gravitational waves [53] or looking for signatures of dark matter candidates [118].

There are however limits to the performance of atomic clocks. Some of these limitations come from the fact that the best atomic clocks are not field deployable². This means that many of the possible applications cannot be taken advantage of, as several people and entire laboratory environments are necessary for proper operation. Other limitations are more fundamental, and have to do with the design of current atomic clocks. These limitations of performance drive a development of new approaches for atomic clocks, that could allow them to transgress the current limitations as well as a will to develop more compact, transportable systems with high performance. In this thesis we will investigate some of the approaches that have been suggested as novel optical clocks based on cavity-enhanced performance.

1.1 Stability and accuracy

Any reference of measurement can be characterized by how well its value is known. When reproducing such an instrument the ability to reproduce its exact intended value, is what we denote as accuracy. The quality of the reference determines how well-defined that value is. If it is not constant in time, this is due to instability. The ideal reference must have a very high degree of both accuracy and stability.

²Though, there are several works towards this end. See, e.g., [54], [115]

Atomic and molecular frequency standards perform quite well in these regards, as they are based on the fundamental interaction of Atomic nuclei and electrons or of multiple atoms. On the other hand, when constructing a mechanical oscillator such as a pendulum, or a crystal oscillator, the dimensions, density and rigidity of the material are of very high importance. Two such oscillators can have identical size and mass, but behave quite differently if their mass distribution or elasticity is different. The simplest behaviors are the most predictable, and if the behavior is predictable, reproducing it will be much easier. Sadly it is often the fate of physical systems to be either simple to construct or simple to model - rarely do you get both. This becomes evident if you want to perfectly replicate a mechanical system. While you can approximate a system quite easily, the highest level of accuracy would demand a system that is constructed from the exact same atomic configurations. This is exceedingly hard with a solid consisting of more than 10^{23} atoms, closely packed in one or multiple crystalline structures. If you restrict yourself to the properties of single atom or molecules, however, reproducing the system under investigation just requires that you can bring about another sample of that atom.

This feature of atomic clocks takes advantage of the universality of atoms. An atom of a given isotope will always display the same properties when exposed to identical conditions. It relies on the indistinguishability of fundamental particles such as electrons, neutrons and protons. Creating an atomic clock, then, starts by choosing the isotope and energy levels that one wants to use. In the case of the current SI definition of the second mentioned above the $F = 3, m_f = 0$ to $F = 4, m_f = 0$ cesium-133 (Cs) isotope was chosen, and it is further specified that this definition refers to an environment of 0 K [5]. This refers back to the fact that identical systems behave identically only when exposed to the exact same environment. So even controlling the exact atomic configuration of two mechanical oscillators is only useful if you can ensure identical environments for them as well. While this is hard for any system, reducing the interaction with the environment is the most straightforward approach to realizing it. In atomic references this is typically approached by using a gas of atoms in a vacuum system. This removes any direct mechanical coupling with a vibrating or thermal environment. Figure 1.2 illustrate some of the remaining perturbations to be considered.

Because the environment influences the behavior of a frequency reference, this is typically one of the limiting factors in the ultimate stability of a system. A high accuracy frequency reference is then contingent on knowing all perturbations on your system, to ensure you can correct any offset from the ideal value. A high frequency stability is dependent on your ability to control the environment as a function of time. In an atomic clock, an atomic transition is used as a reference, and the well-defined frequency of an electromagnetic field with the correct photon energy to excite the transition is used to measure it. In effect, what is used as the time-keeper is thus not the atoms themselves, but a field whose frequency is constantly compared to the transition of interest and corrected in order to remain on resonance.

The primary interaction with the Cs atoms is done via a microwave field. This is convenient because RF frequencies around 9 GHz can be used in and measured by appropriate electronics. To interrogate the atoms, a highly coherent source of

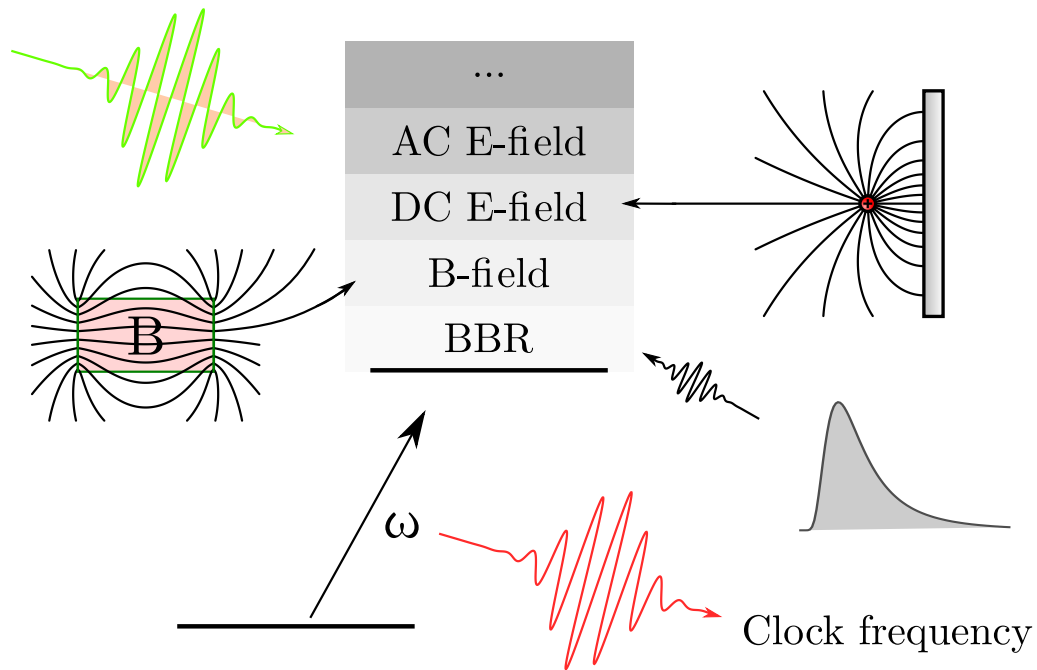


Figure 1.2: The frequency ω of an atomic transition is perturbed by a number of electric and magnetic fields in the environment. Here we show the black body radiation field (BBR) due to final temperature of the environment, the background magnetic field (B-field), any charges causing static electric fields (DC E-field) as well as radiation causing oscillating electromagnetic fields (AC E-fields). Additional shifts from, e.g., interacting particles are possible and the full environment needs to be considered.

microwaves is used, e.g, synthesized using a hydrogen maser. A maser is the predecessor of the laser, and uses hydrogen as a gain medium. This is an excellent frequency reference in itself [22] whose accuracy, however, is in general much lower. By combining the high stability of a hydrogen maser with the accuracy of a cold Cs ensemble, an excellent result can be achieved [121].

The accuracy and stability of a clock is typically measured relative to its oscillating frequency. While two different types of clocks might both have an uncertainty of ± 1 oscillation per second (± 1 Hz), it makes a huge difference if the absolute frequency at which the clock operates is at 2 Hz – an uncertainty of $\pm 50\%$ – or at 1000 Hz – an uncertainty of only $\pm 0.1\%$. As a result the fractional frequency stability or accuracy is typically the figure of merit for such systems. The best commercially available hydrogen masers have fractional frequency stabilities of $8 \cdot 10^{-14}$ at 1 s [22]. With an absolute frequency of about 1.4 GHz this corresponds to an absolute frequency stability of about 0.1 mHz.

Because noise can occur at many different characteristic frequencies, the precision of a frequency reference is only meaningful when the relevant averaging time is provided. High-frequency noise will limit the stability at short times while technical noise and drift of experimental parameters can limit the system performance for long averaging times. An excellent introduction to noise analysis of time-series and frequency standards is given in [91].

An essential tool to characterize these behaviors is the Allan deviation which we

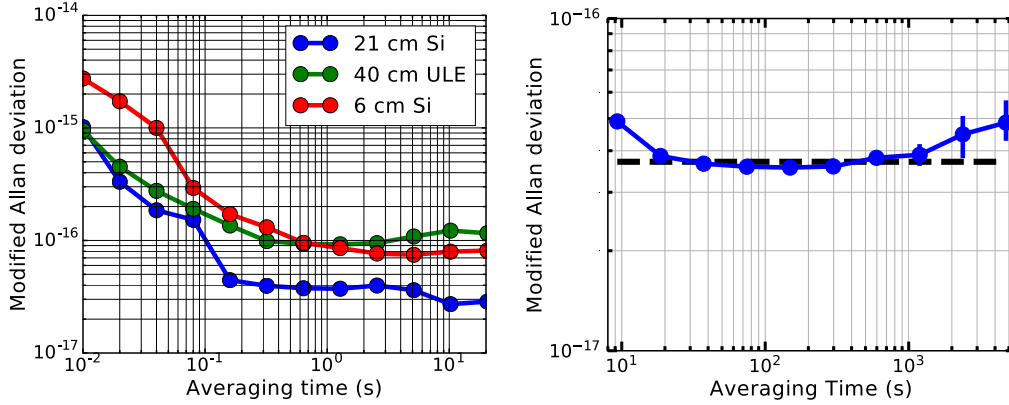


Figure 1.3: Modified Allan deviation from [83] showcasing the fractional frequency stability of **left**: three distinct ultra stable reference lasers at JILA, CO, USA recorded by the three-cornered hat method. Two cavities are based on monocrystalline Si spacers while the last is based on the more traditionally used ULE glass the length of the spacer is indicated and influences the stability greatly. **right**: The typical instability increases only on the timescale of hours.

will use repeatedly in this thesis. The Allan deviation provides a time-dependent number for the noise in the system analogous to many values for standard deviations from a single dataset treated by multiple binning ranges. In its simplest form, the Allan deviation can be given as [91]:

$$\sigma_y^2(\tau) = \frac{1}{2(M-1)} \sum_{i=1}^{M-1} [\bar{y}_{i+1} - \bar{y}_i]^2, \quad (1.1)$$

where τ is the averaging or sampling period used. \bar{y}_i is the i -th of M averages over data values during τ . From this expression we see one of the great merits of the Allan deviation. For a number of data points following a normal distribution about some mean value, σ_y will decrease as τ increases. As the samples (τ) become larger, the mean values y_i will approach one another. This showcases the fact that the mean value of the distribution is known to a higher degree, when the averaging time is longer. If the mean value drifts, the standard deviation is no longer well defined, but highly dependent on sample length. An Allan deviation, however, can in a simple manner convey the typical behaviors at different time-scales. More advanced variations on the Allan deviation exist, with the most noteworthy being the overlapping, total and modified Allan deviations, here we will use all three, depending on the context.

Figure 1.3 shows an example of a modified Allan deviation from some of the most stable reference lasers in the world. Notice that the trend of all three systems is initially decreasing, but then flattens out around 1 s. This is a typical behavior for mechanical references whose frequency starts to drift around this timescale.

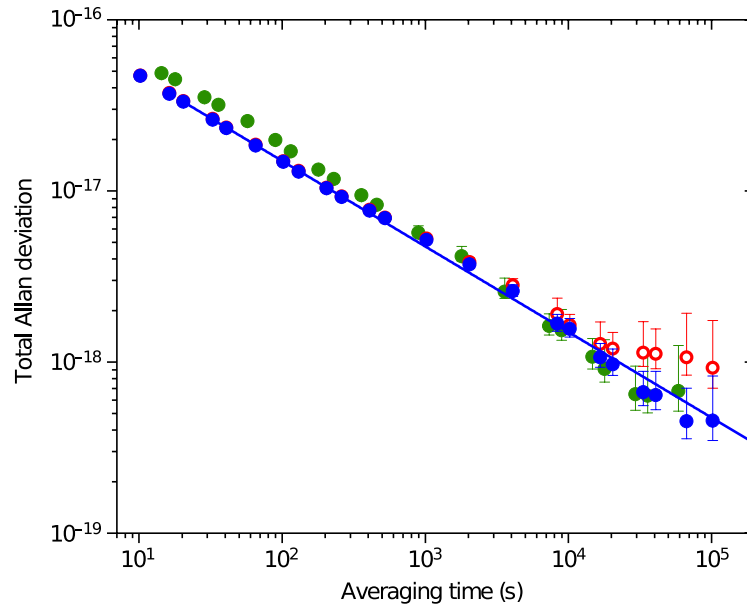


Figure 1.4: Total Allan deviation from [70]. Green and Blue datasets correspond to different modes of operating the atomic clock, while red points showcase the drift caused by not correcting for drift in temperature variations of the vacuum chamber. See chapter 6.

1.2 Optical frequency references

Since the primary figure of merit for frequency references is the fractional frequency stability and accuracy, moving to higher absolute frequencies is an excellent way to improve your standard. While the Cs standard operates in the microwave regime of order 10^9 Hz, atomic transitions in the optical regime readily provides absolute frequencies in the 10^{14} Hz range. If you are able to retain the low absolute uncertainty, the performance thus increases by around five orders of magnitude. This is a huge progress that is being taken advantage of in the current development of optical atomic clocks. The Allan deviation shown in figure 1.3 is an example of the improvements possible by using optical frequencies. It shows systems reaching fractional instabilities below 10^{-16} in 1 s. The drift and technical noise that limits these systems can be avoided by using atomic references as discussed above. Optical atomic clocks based on ions or optical lattices are currently at the forefront of the development, showcasing fractional frequency uncertainties in the low 10^{-18} [70] to high 10^{-19} [14], and fractional frequency instability of down to mid 10^{-19} [70]. The typical operating principle of such clocks relies on both an ultra stable laser such as the ones shown in 1.3, and subsequent interrogation of and stabilization to the atomic reference. Figure 1.4 shows the performance of the ytterbium clock I worked on while at NIST, see chapter 6. At the time of writing this is one of the best performing optical atomic clocks, with a fractional frequency uncertainty of $1.4 \cdot 10^{-18}$. Notice that this Allan deviation is only shown for times higher than 10 s. For shorter times, the performance of the system is characterized by the prestabilized laser, and not the stabilization to the atomic reference.

An atomic clock is stabilized by interrogating the atomic transition, and the

stability is dictated by the quality of this interrogation. As such, an expression for the ultimate stability of an optical clock can be given as [90]

$$\sigma_y(\tau) = \frac{1}{K} \frac{1}{Q} \frac{1}{SNR} \sqrt{\frac{T_c}{\tau}}. \quad (1.2)$$

Here K is a factor of order 1 given by the signal lineshape and $Q = \nu/\Delta\nu$ is the associated quality factor given by the absolute frequency ν and the linewidth $\Delta\nu$. The signal-to-noise ratio is given by SNR , and the interrogation time by τ for operation with a cycle time T_c . Ignoring the lineshape factor K we see that three fundamental limitations are given. The signal-to-noise ratio, signal Q-value, and fractional interrogation time.

The Q-value of the signal is set in part by choosing an energy range for the resonance. In the case of optical atomic clocks, the transitions are well-defined, and often only a single relevant clock transition – if any – can be found for a given isotope³. Choosing the atomic species, thus determines the Q-value of the atomic transition. The signal will be a convolution of the atomic and interrogation laser lineshapes, and the Q-value of the interrogation laser thus becomes equally important. This has resulted in the development of highly stable reference lasers [68], [92], [127] such as the ones shown in figure 1.3. The sensitivity of the reference cavities used for these lasers, is so high that they are now limited by the length variations caused by thermal fluctuations in the mirror coating and cavity spacer itself [21], [82]. The linewidth of these lasers is moving ever closer to the linewidth of the atomic transition, but remain a limiting factor in many systems.

In section 3.2 we will look at the comparison of two classical reference cavities in our laboratory. In chapter 5 we will investigate bad-cavity systems that rely on cavities, but are able to suppress the noise originating from them.

A low signal-to-noise ratio (SNR) of the measurement limits the performance of the system by writing noise on the correction signal. This is often a technical challenge where optimization engineering of the detector and electronics become important. Alternatively one must ensure that the size of the signal is as large as possible, and this is often dependent on the detection method. Optical atomic clocks almost exclusively rely on the method of electron shelving. The atoms are excited on the narrow clock transition and a secondary, bright transition is used to detect the excitation efficiency, by scattering photons off the ground state atoms. This approach amplifies the signal significantly compared to the case of direct absorption spectroscopy. In Chapter 4 we will investigate an interrogation technique that relies on cavity-enhanced dispersive measurements of the transition rather than electron shelving or absorption spectroscopy. This method was first proposed in the context of molecular spectroscopy [126], but we show its use in interrogating narrow transitions of cold strontium atoms. It provides an approach to significantly improving the SNR of an atomic clock system. A hybrid of the electron shelving and dispersive approach has recently been proposed for use in Sr optical lattice clocks [114].

³A notable example of an atom with more than one clock transition is ytterbium-171 (or 173), where the use of two separate clock transitions has been suggested as a highly sensitive method for testing fundamental physics [94]

The final factor of relevance is the fractional interrogation time. Atomic clocks typically rely on a preparation period, where atoms are cooled and trapped, and a subsequent interrogation period, where the measurement itself takes place. If the preparation of the atoms is demanding in time, the spacing between consecutive measurements becomes long. This makes the clock vulnerable to the noise of the interrogation laser. The long cycle times can be reduced by attempting a simplified cooling scheme at the expense of control over the atoms. This is an approach taken in Chapter 4. Other groups are investigating the possibility of non-destructive detection of the atomic state [114]. Long interrogation times are needed to resolve the atomic transition without its spectrum being Fourier limited. The cold-atom-based laser presented in Chapter 5 is a step along this path, as it lays the foundation for the development of a fully continuous laser based on narrow clock transitions.

There is also a need to increase the accessibility of high-accuracy atomic clock systems for use in real-world applications. This puts a high stress on reducing the footprint and complexity. The current record-holding optical atomic clocks take up tens of square meters of laboratory workspace, and requires the constant attention of multiple PhD students or researchers during operation. An optical atomic clock that can be employed for industry or even be sent into space, has to run independently and have a footprint on the order of one square meter or less. There are already some initiatives towards the realization of a compact and automated optical atomic clock based on the canonical design⁴ [54], [103]. Our proof-of-concept approaches in chapters 4 and 5 are technically simple compared to a full blown optical lattice clock, as they rely on fewer cooling stages and control lasers. This reduces the engineering complexity of the systems, as well as the total footprint.

1.3 Superradiant optical clocks

In recent years the concept of a superradiant optical atomic clock has been proposed [17] and pursued by several groups [10], [57], [80], [84], [122]. This is a system that is fundamentally different from classical atomic clocks, in that the clock frequency is directly generated by the atomic ensemble. In this sense the clock frequency is actively generated by the atoms, rather than being synthesized by interrogation of a passive ensemble. Such an atomic clock promises the conceptual simplification of a laser whose frequency is spectrally narrow and stable as well as accurate by design.

A traditional laser relies on a broadband amplification medium within a very frequency-selective resonance cavity. Photons emitted by the atoms cause stimulated emission from other atoms, leading to phase-coherent behavior. Since only a narrow range of frequencies can be emitted into the cavity mode, this determines the final laser frequency. In a superradiant laser, however, the medium is spectrally narrow and rests within a comparatively broadband enhancement cavity. The concept of a superradiant laser relies on the idea first formulated by Dicke [25] that atoms may emit by virtue of collective spontaneous emission. The cavity thus

⁴See, e.g., <https://www.iqclock.eu/> for a European project aiming to implement a state-of-the-art optical atomic lattice clock in a telecommunications center.

acts to modify the atomic coupling to the surrounding field, but largely does not influence the emitted spectrum. This is also known as the bad-cavity regime.

In fact the first proposals for superradiant lasing did not necessitate an enhancement cavity at all. Instead the atomic density was assumed to be high enough that the phase of emitted photons from individual atoms was indistinguishable. This is relatively easily realized with microwave fields but becomes extremely demanding at optical frequencies. The standing-wave field of an optical cavity ensures that the phase of the emitted photon is not completely random. In the superradiant laser the atomic ensemble is considered as a single system rather than individual component atoms, and this system can be said to emit spontaneously with a rate much faster than the spontaneous decay rate of a single atom – thus giving it the name superradiance. Dicke later refers to this type of laser as a coherence-brightened laser [26] since it is the atomic coherence build-up rather than the broadband power amplification that permits the lasing process.

With a continuous source of excited atoms it is possible to sustain superradiant emission and obtain a continuous signal. By using spectrally narrow atomic transitions for such a laser it has been proposed that mHz laser linewidths are feasible [73]. This goes beyond the current capabilities of ultra-stable lasers and would be a great asset as either a replacement of or an improvement to state-of-the-art clocks.

Superradiance experiments have been investigated extensively since the 1970s [1], [39], [56], [69], [102], but after the fast evolution of cold atom systems in the last decade, interest for its use in frequency references has emerged. Since the coherence of the system is stored in the atoms rather than the photon field, noise in the enhancement cavity will be suppressed when compared to a traditional laser. In [84] a suppression of the superradiant laser cavity noise by a factor of 70 was shown for heated Cs atoms, while [80] realized a suppression of a factor of $5 \cdot 10^5$ with ultra-cold strontium atoms in an optical lattice.

In this thesis (chapter 5 we investigate a half-way-regime with cold atoms that are not confined in any optical lattice. We use an easily accessible transition in strontium which is spectrally wider than the narrow clock transition typically used in optical lattice clocks and in [80]. This results in faster dynamics of the system, but also a severely reduced experimental complexity. The experiments presented here are all based on pulsed lasing, but light the way towards a continuous system. At the time of writing our group has entered a collaboration with several other universities on the construction of the first truly continuous superradiant laser based on cold atoms.⁵

⁵The iqClock project between University of Copenhagen in Denmark, University of Amsterdam in the Netherlands, University Nicolaus Copernicus in Poland, Technische Universität Wien and Innsbruck Universität in Austria as well as University of Birmingham in the U.K. <https://www.iqclock.eu/>

INTRODUCTION TO COLD ATOMS IN CAVITIES

Contents

2.1	Transitions of strontium	12
2.2	Atoms and cavities	13
2.2.1	Atom-field interaction	13
	Spectral characteristics	16
	Coherent evolution	16
2.2.2	Atom-cavity interaction	16
	Atom-cavity coupling rate	17
	Collective coupling	18
2.3	Cold atoms	19
2.3.1	Decoherence from cooling beams	21

In this chapter we will present some background for the physical system that is used in chapters 4 and 5. It is based on strontium atoms cooled, trapped, and coupled to the mode of an optical cavity. The details of trapping and cooling the atoms will not be elaborated here, but can be found in a basic text on the subject [74]. The detailed parameters and design of the laser cooling in the cold strontium atom experiment used here can be found in [20], [44], [97].

First we will look at the atomic level structure of strontium. This will allow us to give an overview of the experimental approach. We will consider the interaction between atoms and optical fields, and set up a framework for this interaction. Atomic coupling to modes of an optical cavity is then presented as a basis for subsequent discussions.

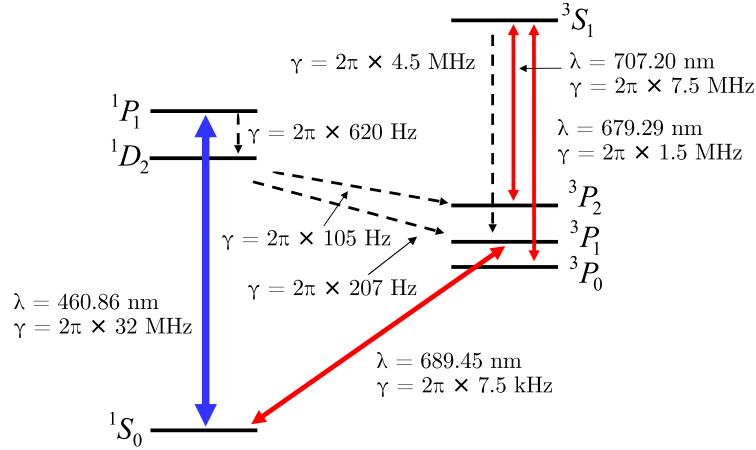


Figure 2.1: Energy levels and transitions in ^{88}Sr . The transition used for laser cooling here is shown in blue. Red lines show the repumping and probing transitions of relevance here. Additional decay channels are indicated by dashed lines.

2.1 Transitions of strontium

Strontium is an alkaline earth metal, convenient for cold atoms experiments because of its electronic energy level structure that is well suited for laser cooling. Strontium has four stable isotopes; one fermionic, ^{87}Sr , and three bosonic, ^{84}Sr , ^{86}Sr and ^{88}Sr . All of our experiments are performed on the bosonic ^{88}Sr , since it has far the highest natural abundance at 82.58%. Figure 2.1 shows the relevant energy levels of ^{88}Sr . Since the isotope has zero nuclear spin ($F = 0$) there is no hyperfine structure. For now we assume zero magnetic field, and can thus ignore the Zeeman splitting. In the ground state Sr is in the 1S_0 singlet state. From this state a broad transition to 1P_1 state exists. The natural decay rate of $\gamma/2\pi = 32 \text{ MHz}$ allows efficient cooling and trapping of atoms on this line. The decay rate also limits the attainable temperature to a few mK. For optical lattice clocks further cooling is necessary, but in our case we are satisfied with a typical value of $T = 5 \text{ mK}$.

When cooling the atoms, a large number of absorption-emission cycles takes place, where atoms absorb photons in a preferential way that can control their momentum. Ideally then, the cooling transition should be completely closed in order to avoid populating dark states during the cooling cycle. In the case of 1P_1 there exists a secondary, and much weaker, decay channel with a rate of $\gamma = 2\pi \cdot 621 \text{ Hz}$ to the 1D_2 state, and on to the 3P manifold. This causes a reduced cooling efficiency, as atoms decaying to this level will no longer be cooled. Adding repumping lasers that cycles the atoms from 3P_2 and 3P_0 to the 3S_1 state allows decay back to the ground state, where atoms will reenter the cooling cycle.

From the ground state, the triplet state 3P_1 is forbidden by the dipole selection rules, but becomes allowed due to an admixture of the 1P_1 state. This results in a transition linewidth of $\gamma/2\pi = 7.5 \text{ kHz}$. The other states of the triplet are additionally forbidden by the total momentum J selection rule. Due to the nuclear spin of ^{87}Sr the $^1S_0 \rightarrow ^3P_0$ transition has a linewidth on the order of 1 mHz, but in ^{88}Sr it can only be opened by applying an external magnetic field. This transition is

used as the clock transition in state-of-the-art lattice clocks based on both isotopes [38], [41], [62], [63], [83], [106]. Because the transition is far simpler to interrogate, we use the kHz-width $^1S_0 \rightarrow ^3P_1$ transition in all of our experiments presented in chapters 4 and 5.

Since our research concerns primarily atoms coupled to an optical cavity, we will look at some fundamental theoretical descriptions of such a system in the subsequent section. The interaction between an optical field and an atomic system will first be investigated. The behavior of a cavity, and its modification of the electromagnetic field will then be presented before we look at the experimental system itself in chapter 3.

2.2 Atoms and cavities

Optical cavities are a common tool in Atomic, Molecular and Optical (AMO) physics, as they are self-overlapping interferometers. This means that they can enhance specific behaviors of an optical system. Because the field is overlapped with itself in a cavity, interference between field components traveling in opposing directions place stringent demands on mode size and wavelength of the field. Since field interference takes place within the cavity mode, however, this also complicates the description of interaction by introducing position-dependency.

When we consider the wavefront of the electromagnetic field, or interpret the field as photons rather than waves, an additional feature of a cavity system turns up. As the photons bounce back and forth between the mirrors of a cavity, they pass through the same region multiple times. This results in a power buildup, when the electromagnetic field is on resonance with the cavity, and allows a local amplification the field. For the case of an atomic or molecular sample placed inside the cavity, there is an effective increase of the sample size. Here we introduce some basic concepts of interaction between atoms and an electromagnetic field and then consider the influence of the cavity on such systems. Excellent textbooks are written on these subjects [23], [75], [76] and this is not the right place to introduce the concepts methodologically. Instead we will attempt to give necessary definitions for the forthcoming chapters.

2.2.1 Atom-field interaction

In the interaction between atoms and electromagnetic field, we are interested in describing both the macroscopic properties of the atomic ensemble, and the microscopic properties of a single atom interacting with the field. Both provide valuable information in the description of the phenomena we are trying to understand. Initially we will look at the interaction with a macroscopic system. A dilute gas of N atoms per volume.

The gas will have some polarization induced by the electric field \vec{E} .

$$\vec{P} = \epsilon_0 \chi(\omega) \vec{E} \quad (2.1)$$

Here $\chi(\omega)$ is the frequency-dependent susceptibility of the gas and ϵ_0 is the vacuum permittivity. Initially we assume that the system behaves linearly and ignore higher-

order susceptibilities that will scale with the square, cube, etc. of the electric field. We make the electric dipole approximation which amounts to postulating that the field is constant over the size of the atom. In atomic physics this leads to a number of selection rules for the possible transitions between electronic energy levels. This causes the large variation in transition linewidths we saw in section 2.1 where higher order couplings will enable a weak coupling between some levels. In later chapters nonlinear behavior of the atom-field interaction becomes relevant, but this will be dealt with through a full quantum mechanical or semi-classical treatment of the systems from first principles.

Following [23], [77] we can deduce the expression for the classical susceptibility by considering an alternate expression for the polarization as the total dipole moment induced in the atoms per unit volume.

$$\vec{P} = \sum_N qd(\omega) = Nqd(\omega), \quad (2.2)$$

where q is the electron charge. The dipole moment of a single atom can be approximated by considering the electron as a harmonic oscillator driven by an external field \vec{E} :

$$d(\omega) = \frac{q\vec{E}}{m_e(\omega_0^2 - \omega^2 + i\gamma\omega)} \quad (2.3)$$

where the electron mass is given by m_e . The resonance FWHM linewidth is given by γ and its angular frequency as ω_0 . We can combine equations (2.1), (2.2) and (2.3) to give an expression for the complex susceptibility

$$\begin{aligned} \chi &= \chi' + i\chi'' \\ &= \frac{Nq^2}{m_e\epsilon_0} \frac{1}{\omega_0^2 - \omega^2 + i\gamma\omega}. \end{aligned} \quad (2.4)$$

The two components of the susceptibility gives the dispersion and attenuation of the gas respectively. We can see how this affects a propagating wave by introducing a complex refractive index $n = n' + in'' = kc/\omega$. Using this to describe a wave propagating along the z -axis, we obtain the expression:

$$\begin{aligned} \vec{E}(\vec{r}, t) &= \vec{E}_0(x, y)\text{Re}\{e^{i(kz - \omega t)}\} \\ &= \vec{E}_0(x, y)e^{-n''\omega z/c}\text{Re}\{e^{i(n'\omega z/c - \omega t)}\} \end{aligned} \quad (2.5)$$

which shows attenuation of the electric field proportionally to n'' , and a phase-shift proportional to n' . In the weak-field limit we can obtain the classical Lambert-Beer law for absorption (A) of intensity $I \propto I_0 e^{-A}$. The complex refractive index obeys the relation $n = \sqrt{1 + \chi(\omega)}$, and for dilute media where $|\chi(\omega)| \ll 1$, we can approximate it as $n \sim 1 + \chi(\omega)/2$. When the refractive index is much larger than one, the system is no longer as well-behaved. This can happen for a high atomic density or, as we will see in chapter 4, for a dilute gas embedded in an optical cavity.

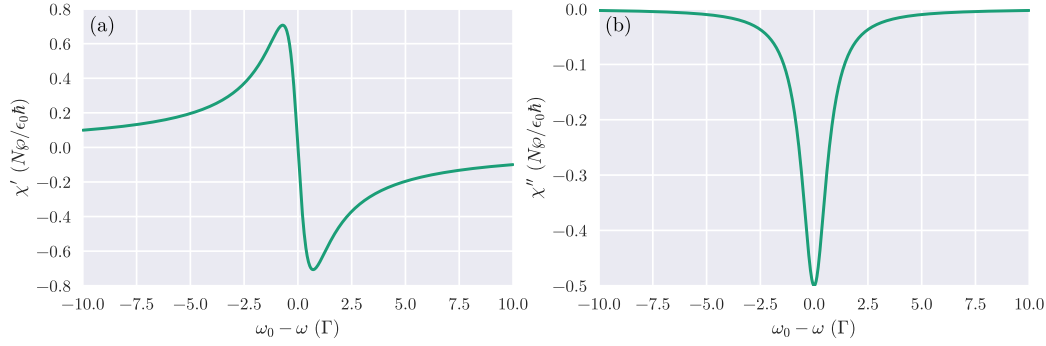


Figure 2.2: Plots of the real (a) and imaginary (b) part of χ . The real part corresponds to the dispersion of an E-field around resonance whereas the imaginary part corresponds to the attenuation due to scattering or absorption.

Close to resonance where $\omega_0 \sim \omega$ we can assume $(\omega_0^2 - \omega^2)^2 \approx 2\omega_0(\omega_0 - \omega)^2$ which allows us to further reduce the susceptibility as

$$\chi = \frac{Nq^2}{m_e \epsilon_0 2\omega_0} \frac{(\omega_0 - \omega) - i\frac{\gamma}{2}}{(\omega_0 - \omega)^2 + \left(\frac{\gamma}{2}\right)^2}. \quad (2.6)$$

Jumping ahead to a quantum mechanical picture we replace the classical electron description by a more general one related to the dipole moment of the given transition $q^2/2m_e\omega_0 \rightarrow \wp/\hbar$. Due to the discrete energy levels of atoms a power broadening factor appears in the denominator [75].

$$\chi' = \frac{N\wp}{\epsilon_0 \hbar} \frac{(\omega_0 - \omega)}{(\omega_0 - \omega)^2 + \left(\frac{\gamma}{2}\right)^2 (1 + I/I_s)} \quad (2.7)$$

$$\chi'' = \frac{N\wp}{\epsilon_0 \hbar} \frac{-\frac{\gamma}{2}}{(\omega_0 - \omega)^2 + \left(\frac{\gamma}{2}\right)^2 (1 + I/I_s)}, \quad (2.8)$$

where $I_s = \pi \hbar c \gamma / 3 \lambda^3$ is the saturation intensity of the transition at resonance. We plot the real and imaginary parts of the susceptibility in figure 2.2, where we can see that the absorptive features, (b), are represented by χ'' and the dispersive features, (a), by χ' as expected from equation (2.5).

The two components χ' and χ'' fulfill the Kramers-Kronig relations

$$\chi'(\omega) = \frac{2}{\pi} \mathcal{P} \int_0^{\infty} \frac{\omega' \chi''(\omega')}{\omega'^2 - \omega^2} d\omega' \quad \text{and} \quad \chi''(\omega) = -\frac{2\omega}{\pi} \mathcal{P} \int_0^{\infty} \frac{\chi'(\omega')}{\omega'^2 - \omega^2} d\omega'. \quad (2.9)$$

Here \mathcal{P} refers to the principal part of the integral due to the existence of singularities - as a minimum the one at $\omega' = \omega$. This relation tells us that it is always possible to derive one part of the susceptibility from the other by Hilbert transformation. As such, it is in principle possible to fully characterize the interaction with the system by looking only at the phase- or absorptive response. In practice however, this would require full knowledge of the system response for all frequencies, and it is typically useful to directly measure both responses.

Spectral characteristics

The above considerations explain how the induced dipole moment in an atom results in absorption of energy and dispersion of a classical continuous field. An ensemble of atoms will decay with a decay rate given by the Einstein A coefficient, which can itself be derived from the dipole interactions considered above. This decay rate corresponds to the spectral width of the unperturbed transition, and can also be derived from a Wigner-Weisskopf treatment of an atom interacting with free space [75].

$$\gamma = \frac{\omega^3 \wp^2}{3\pi\epsilon_0 \hbar c^3}. \quad (2.10)$$

From this expression we see that a higher energy of the transition typically results in an increased decay rate, and that the fractional transition linewidth $\frac{1}{Q} = \frac{\gamma}{\omega}$ scales as the square of the transition frequency. In general then, this would indicate that a low energy transition is desirable for clocks where we want a large Q . However, due to the existence of dipole and higher-order forbidden transitions with small but finite effective dipole moments \wp , some optical transitions have abnormally small decay rates. Taking the $\gamma = 2\pi \cdot 32$ MHz dipole allowed $^1S_0 \rightarrow ^1P_1$ cooling transition in strontium as an example, one could expect a mHz spectral linewidth only by moving to a transition frequency of about 200 GHz. Instead the clock transition in ^{87}Sr is around 430 THz, permitting the high Q -factor we are after in equation (1.2).

Coherent evolution

Atomic absorption and driven emission can result in a coherent evolution of the atomic state. By illuminating a ground-state atom with CW (constant wave) monochromatic light it can thus undergo Rabi flopping. In this process a finite amount of energy causes the atom to be placed in a well-defined superposition of the ground and excited state. The probability of being in the excited state $|e\rangle$ can then be given as

$$|c_e(t)|^2 = \frac{|\mathcal{R}_0|^2}{\mathcal{R}^2} \sin^2\left(\frac{\mathcal{R}t}{2}\right), \quad (2.11)$$

where $|\mathcal{R}_0| = \left|\frac{\wp E_0}{\hbar}\right|$ is the Rabi flopping frequency and $\mathcal{R} = \sqrt{\delta^2 + |\mathcal{R}_0|^2}$ is the generalized Rabi frequency. Dependent on the detuning between field and atomic transition, δ , the electric field amplitude, E_0 , and the interaction time, t , a well-defined excitation is then obtained. In chapter 5 we take advantage of this in order to excite the atoms with a so-called pi-pulse, where the condition $\mathcal{R}t = \pi$ is met, ensuring maximal excitation.

2.2.2 Atom-cavity interaction

When atoms are placed in a cavity the field is modified, just like its interaction with the atoms. Compared to the case of free space, the density of field modes is significantly decreased for the solid angle of emission into the cavity, which changes the lifetimes of the atomic states. The interference within the cavity of the traveling

wave with itself results in a standing wave, causing a position dependent coupling. The potentially high number of reflections and long lifetime of a photon within the cavity means that a single photon can interact multiple times with an atom resulting in an accumulated dispersion and attenuation according to the derivation in section 2.2.1. The bidirectionality of the field can be used for saturation spectroscopy as described in chapter 4. To quantify the modified interaction we will define the coupling factor between a single atom and the cavity mode, as well as the strong-coupling condition for normal-mode splitting – sometimes referred to as (vacuum) Rabi splitting. We move to a picture where the atom and cavity are considered as one system. The interaction of the environment or external fields with this system, will then produce an array of new behaviors.

Atom-cavity coupling rate

The coupling between the cavity field and the atom is determined by the effective dipole interaction. We model the coupling factor $g = g_0 \zeta_{LM} \zeta_{TM}$ as a maximal coupling g_0 with spatial dependency given by the axial (longitudinal mode) dependencies in the cavity, ζ_{LM} , and the transverse mode dependency ζ_{TM} . The maximal coupling is given by

$$g_0 = \frac{\wp}{\hbar} \sqrt{\frac{\hbar \omega_c}{2\epsilon_0 V_{\text{eff}}}} \quad (2.12)$$

where $V_{\text{eff}} = \iint_0^{\infty, L} \exp(-2r^2/w^2) \sin^2(kz) \cdot 2\pi \cdot r \cdot dr dz \approx \pi w_0^2 L/4$ is the effective mode volume of the Gaussian standing-wave cavity mode, given by the length of the cavity, L , and the cavity waist radius, $w \approx w_0$, which is assumed constant. This will in general be a good approximation for our interaction cavities. We can write the coupling rate components as

$$g_0 = \sqrt{\frac{6c^3 \gamma \omega_c}{w_0^2 L \omega_0^3}}, \quad \zeta_{LM}^j = \sin\left(\frac{\omega_c z_j}{c} - \delta_j t\right), \quad \zeta_{TM}^j = \exp\left(-\frac{r_j^2}{w_0^2}\right). \quad (2.13)$$

Here ω_c is the cavity resonance frequency. The longitudinal mode scaling $\zeta_{LM}^j(z^j)$ depends on the axial position of the j -th atom relative to the standing wave of the cavity mode and the transverse mode scaling $\zeta_{TM}^j(r_j)$ on its radial position. $\delta_j = \frac{\omega_l}{c} v_j$ is the Doppler shift in terms of the atomic velocity v_j .

We consider the atom and cavity as the system of interest, and any coupling to the environment is a loss of energy. This happens as a function of the spontaneous decay rate of the atom and the cavity field decay rate into the environment: γ and κ . The atom-cavity coupling rate g_0 on the other hand describes a conserved energy, and a build-up of coherence in the system. These rates make out the cooperativity factor of the system

$$C_0 = \frac{(2g_0)^2}{\gamma \kappa}. \quad (2.14)$$

The cooperativity is a measure of the coupling strength of the system, where the strong-coupling regime $C_0 \gg 1$ entails that the coherence in the system is more often

retained than not. This inhibits the natural decay of the system coherence. One of the consequences is that the system is no longer well-described by the individual energy levels of the atom and the cavity. Instead the dressed state picture is a better representation, resulting in what is known from classical physics as the normal mode splitting.

In the dressed state picture the degeneracy of the bare atomic states and the cavity energy levels is lifted, and a splitting between the energy levels arises, proportional to the generalized Rabi frequency \mathcal{R} . This is known as the Rabi, or normal mode splitting (NMS). At atom-cavity resonance, $\omega_c = \omega_e$, the splitting becomes $2g_0 \sqrt{n+1}$ where n is the number of photons in the cavity field.

Collective coupling

In the case of an N -atom system coupled to a cavity, the effective atom-field interaction is enhanced by the square root of the atom number and the effective Rabi frequency becomes

$$\begin{aligned}\mathcal{R}_N &= \mathcal{R}_0 \sqrt{N} \\ &= 2g_0 \sqrt{N(n+1)}\end{aligned}\quad (2.15)$$

The enhanced coupling rate increases the NMS equivalently. The condition for resolving the NMS with vacuum in the cavity is then

$$2g_0 \sqrt{N} > \kappa \quad \text{or} \quad C_N \gamma > \kappa \quad (2.16)$$

where $C_N = NC_0$ is the collective cooperativity. For a collective cooperativity larger than unity the system is said to be in the *collective* strong-coupling regime. For N identical atoms, this indicates that the collective coherence build-up exceeds that of the decay rates. C_N turns out to be a figure of merit for the emission strength of a lasing pulse, or the signal size of a spectroscopic system. The linewidth of both spectroscopic and lasing systems (Chapter 4 and 5) are proportional to the cooperative decay rate $C_0\gamma$ [67], [73]. The cooperativity can also be derived either from consideration of the system absorption properties [13]

$$C_N = \frac{2}{\pi} \alpha l \mathcal{F}, \quad (2.17)$$

where α is the small-signal absorption for a resonant atom-cavity system, \mathcal{F} is the finesse of the optical cavity, and l is the cavity length. This expression allows us to understand how the collective cooperativity is directly related to the optical density of the hybrid atom-cavity system. Or equivalently the single-atom cooperativity can be given directly from almost purely geometrical considerations as [110]

$$C_0 = \frac{6}{\pi^3} \mathcal{F} \frac{\lambda^2}{w_0^2} \quad (2.18)$$

where λ is the transition wavelength. We can recognize the ratio between the diffraction limited length resolution, $d = \lambda^2/2w_0$, and the cavity waist, w_0 , indicating

whether the position of two atoms within the cavity waist can be resolved. The larger this ratio is, the better *mode-matching* we have between the optical mode and the light emitted from the atom. This formulation originates from the consideration that the cooperativity of an atom in a cavity is the free-space cooperativity of a Gaussian mode of waist w_0 modified by the cavity conditions. The free-space cooperativity can be expressed in terms of the ratio of the resonant scattering cross section, $\sigma_0 = 6\pi/k_0^2$, to the effective area of the Gaussian beam, $A = \pi w_0^2/2$, as [110]

$$C_{fs} = \frac{3}{2} \left(\frac{\lambda}{\pi w_0} \right)^2 = \frac{3}{\pi^2} \frac{d}{w_0} \approx \frac{\sigma_0}{2A} \quad (2.19)$$

The cavity conditions introduce a factor of \mathcal{F}/π accounting for the average number of photon round trips and a factor of 2^2 from the standing wave enhancement of optical intensity compared to a running wave.

For our systems the assumption of identical atoms is not generally applicable, however, and we will have to introduce an effective linewidth or coupling rate g_{eff} in order to appreciate the cooperativity of our systems according to equations (2.14), (2.18) and (2.19). In the next section we will take a closer look at how the atoms behave when they are cooled and trapped, and also why they cannot be assumed to be identical.

2.3 Cold atoms

The atomic gas of strontium atoms we will be considering is cooled and trapped using laser cooling. This is done in order to localize the atoms, to increase the density ρ , and in order to reduce their average velocity. As most laser cooling relies on absorption and scattering of photons by atoms, it is inherently a random process where the specific cooling method and transition parameters of relevance can limit the achievable temperature and confinement. An excellent introduction to the trapping and confinement of atoms can be found in [74].

In a ballistic interpretation of the atomic ensemble, kinetic energy of an individual atom is translated into an effective temperature. For the ensemble as a whole then, the temperature describes the expected velocity distribution. In three dimensions the probability density function of the velocities v of atoms in a thermal equilibrium at temperature T follows a Maxwell-Boltzmann distribution

$$f(\vec{v})d^3v = \left(\frac{m}{2\pi k_B T} \right)^{3/2} e^{-\frac{m|\vec{v}|^2}{2k_B T}} d^3v, \quad (2.20)$$

where m is the atomic weight and k_B is the Boltzmann constant. Integrating over two of the dimensions yield the one-dimensional Gaussian distribution

$$f(\vec{v}_x)dv_x = \left(\frac{m}{2\pi k_B T} \right)^{1/2} e^{-\frac{mv_x^2}{2k_B T}} dv_x. \quad (2.21)$$

When probing the atoms with a laser their velocity along a single dimension is probed, leading to a Doppler shift $\delta_D = \vec{k} \cdot \vec{v}_x$ of their resonance frequency. The standard deviation of the atomic velocity within an ensemble of temperature T can

then be found along one dimension. From it we derive the expected inhomogeneous Doppler broadening of the ensemble:

$$v_\sigma = \sqrt{\frac{k_B T}{m}} \quad \text{so} \quad \Gamma_D = |\vec{k}| \sqrt{\frac{k_B T}{m}}. \quad (2.22)$$

Here Γ_D is the Full Width at Half Maximum (FWHM) of the Gaussian Doppler profile, and $k = |\vec{k}|$ is the wave number. The coupling of the motional state of an atom to the external field must obey conservation of momentum. In the most simple case then, the full momentum of a photon $p = \hbar k$ is transferred to the atom upon absorption. A unidirectional beam of light thus causes a force along its direction of propagation

$$\vec{F} = \frac{d\vec{p}}{dt} = \hbar \vec{k} \Gamma_{sc} \quad (2.23)$$

where Γ_{sc} is the atomic scattering rate. This results in a well-defined control, where a velocity component can in principle be exactly canceled by the appropriate momentum transfer from photons. For an ^{88}Sr atom at room temperature, the most probable momentum is $p_{mp} = 3.5 \cdot 10^{-23}$ which means that the number of absorbed photons necessary to slow it to a halt is of order $n = 2.5 \cdot 10^4$. Since a large number of absorbed photons is typically necessary to considerably reduce the velocity of an atom, an efficient cooling scheme must have the atoms return to the ground state efficiently in order to allow further absorption. If the decay to the atomic ground state happens through spontaneous emission, it is equally likely to happen in any spatial direction. The momentum given to the atom due to spontaneous emission will thus approximately average to zero over a large number of cycles.

The cooling efficiency is maximal when the light is on resonance with the transition. Since the change in velocity during cooling can be quite large, an atom can shift out of resonance with the cooling beam, as its velocity is reduced. A given ensemble of atoms can additionally have a Doppler distributed spectrum much wider than the bare cooling transition. A typical configuration for cooling atoms along a given axis is thus to have bidirectional laser beams detuned by some frequency from the bare atomic transition frequency. This results in a scheme where atoms at rest experience the same force in both directions, whereas moving atoms experience a net force opposite to their direction of propagation. A large detuning facilitates a large capture range of atomic velocities. A detuning approaching $\Delta = -\gamma/2$ results in the most efficient cooling, due to a steep slope of the cooling force with respect to position [74].

These kinds of cooling methods are known as Doppler cooling schemes, where broad atomic transitions with a large decay rates result in efficient cooling. However, there is a well-defined limit to the cooling efficiency, which strikes at the heart of the random spontaneous emission process. The finite decay rate γ also implies a spread in the distribution of momentum lost as the atom relaxes to its ground state. With the assumption of a monochromatic excitation beam, the spread in energy of the emitted photons result in a random momentum walk of the atom. This limits

the achievable temperature to

$$T_D = \frac{\hbar\gamma}{2k_B}, \quad (2.24)$$

known as the Doppler temperature or Doppler cooling limit. Since large cooling efficiency requires a large atomic spontaneous decay rate, then, a compromise between cooling efficiency and achievable temperature is made when choosing the cooling transition. It is possible to artificially broaden the chosen cooling transition by, e.g., spectrally broadening the cooling laser.

For the case of cooling on the $\lambda_{MOT} = 461$ nm line in ^{88}Sr the transition linewidth results in a Doppler limit of $T_D = 0.8$ mK. With our current system we use a 3D MOT which induces spatial as well as velocity-dependent frequency dependence. the 6-beam configuration uses $P_{MOT} = 2$ mW in each cooling arm and beams with Gaussian waists of $w_0 = 0.9$ mm. With a detuning of $\Delta = -1.3\gamma = -41$ MHz we routinely achieve temperatures of $T \approx 5$ mK. The total number of trapped atoms reaches about $N = 10^8$ with a distribution radius of $\sigma = 0.8$ mm. If we assume a Gaussian distribution of atoms this corresponds to a peak density of $\rho_{max} \approx 1.2 \cdot 10^{10}$ atoms/cm³.

2.3.1 Decoherence from cooling beams

Our experimental system generates the cold atomic sample inside the interrogation cavity. This means that the atoms will be driven on the broad cooling transition, which causes significant decoherence on more narrow transitions, like the $\lambda = 689$ nm probing transition, coupled to their common ground state. In order to avoid this decoherence the experiment is always run in a cyclic fashion, where atoms are first loaded into the trap, and the trap is subsequently released leading to the atomic ensemble expanding and disappearing. A time-window on the order of 1 ms is then available for measurements before the atoms are lost.

To justify the need for a cyclic experimental procedure, we can set up the optical Bloch equations for the atoms as a 3-level system. We use a V-type configuration in order to simulate the 1P_1 , 1S_0 , and 3P_1 states of figure 2.1, as $|1\rangle$, $|2\rangle$, and $|3\rangle$ respectively. The ground state population evolution $\dot{\rho}_{22}$ will be coupled to both the ρ_{12} and the ρ_{23} coherences with a rate proportional to the transition Rabi frequencies of the respective laser fields. These dynamics reach a steady state within a few tens of μs , allowing an effective decoherence rate of the of the ground state (1S_0) to be determined. This turns out to be given by the scattering rate of 461 nm light:

$$\gamma_{sc} = \frac{\gamma_{12}}{2} \frac{s_0}{1 + s_0 + \left(\frac{2(\omega - \omega_0)}{\gamma_{12}}\right)^2}, \quad (2.25)$$

where $s_0 = 0.221$ is the resonant saturation parameter for the transition, and $\gamma_{12}/2\pi = 32$ MHz is the natural decay rate of 1P_1 to 1S_0 . The laser detuning is $\omega - \omega_0 = -2\pi \cdot 41$ MHz. For our 3D MOT parameters we find a scattering rate of $\gamma_{sc} = 2.9 \cdot 10^6$ photons/s. This is sufficient to destroy most of the coherent response of the atom field interaction we investigate in the following.

EXPERIMENTAL SYSTEMS

Contents

3.1	Atom cloud machine	23
3.1.1	Laser systems	24
	Cooling light	26
	Repumping light	29
	Probe light	29
	Pumping light	31
3.1.2	Physics cavity	32
3.2	Reference lasers	32
3.2.1	The clock laser system	32
3.2.2	The reference laser system	33
3.2.3	Frequency characterization	35

3.1 Atom cloud machine

In this chapter we present some of the experimental details of the Sr I machine, where the results from the following chapters 4 and 5 are obtained. This machine consists of a vacuum enclosure and an array of lasers and optical components. The strontium atoms are heated in an oven inside the vacuum chamber, slowed using a Zeeman slower, and finally cooled and trapped in a 3D MOT. The atoms are trapped in the science chamber, where they overlap with the mode of an optical cavity. Here we will not go through the detailed workings of the cooling scheme, as this information can be found in a number of references elsewhere. The interested reader is referred to the general introduction in [74] and the experiment-specific overview in [97].

In this section we will go through some of the components of the machinery in detail, in order to present both possibilities and limitations of the current subsystem configurations. In any cold-atoms experiment where lasers are used to control and manipulate the atoms, there is a great deal of beam-shaping and polarization control which we will largely ignore here. Instead we focus on the conceptual construction of the systems with particular emphasis on active optoelectronic components.

3.1.1 Laser systems

The Sr I machine uses a range of lasers in order to access the different levels of interest, and all lasers in the system rely on laser diodes that are incorporated in home-built External-Cavity Diode Laser-ensembles (ECDLs). The lasers are all built in one of three configurations shown in figure 3.1: Littman-Metcalf, Littrow, or Cateye.

Compared to a bare laser diode, an ECDL adds additional spectral filtering, which both improves the frequency control, and the spectral linewidth of the light. Frequency tuning of a laser diode happens through the supplied current and the temperature of the diode. The diode current primarily affects the charge carrier density of the material, whereas the temperature changes mechanical properties of the diode, which can both shift the gain curve, and change the length of the diode itself. Ideally these two parameters would be independent, but in reality they are slightly correlated, since an increase in temperature can affect the charge carrier density, which in turn can result in an increased temperature through the emitted power.

The effect of temperature on the length of the laser diode is important since the facets of the diode will create a small cavity, which sets conditions on the possible standing-wave frequencies. The diode can be AR coated in order to heavily suppress this effect, but due to availability of diodes this has not been the case for most of our lasers. In an ECDL the diode-cavity is always coupled to an "external" cavity, which in all cases discussed here uses the backside of the diode as one cavity mirror, and can use either a grating or a mirror as the other. The mode-overlap between the internal and external cavities create a repeating pattern of resonances, within which the emission spectrum of the laser diode is amplified rather than suppressed. Finally the spectral filtering capabilities of the grating or interference filter acts to narrow the range of possible lasing modes. Ideally the filtering is sufficiently narrow that a single lasing mode can be significantly stronger than any other. This is the case if the condition

$$FSR_{EC+DLC} > BW_{\text{filter}} \quad (3.1)$$

where FSR_{EC+DLC} is the free spectral range between resonances of the combined external-cavity and diode-laser-cavity and the grating or interference filter optical bandwidth is given by BW_{filter} .

There can be advantages and disadvantages to the different ECDL configurations, which has shaped the design choice. The Littrow configuration is by far the simplest. The configuration uses the -1st order of a grating as the cavity feedback and the zeroth order as the output. These systems typically have high efficiencies

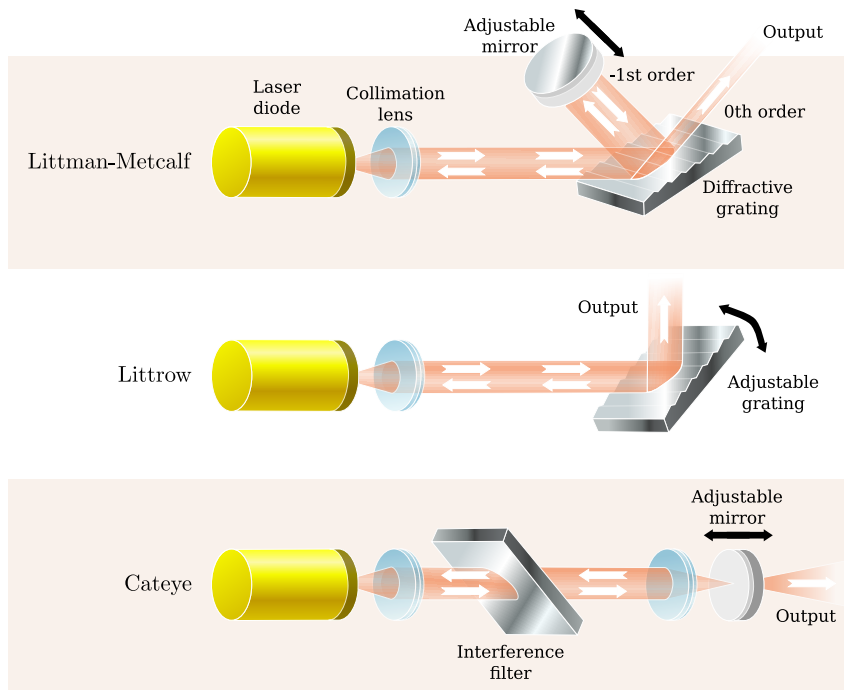


Figure 3.1: Three types of ECDL configurations which are all used at various places in the experimental system. Laser diodes (LD) are shown in yellow, and gratings and interference filters are shown in silver. All configurations rely on collimation of the LD field. The Littman-Metcalf and Littrow configurations both rely on gratings to form the external cavity, whereas the cateye configuration uses a transmission interference filter. The Littman-Metcalf and the cateye configurations rely on a translating mirror to adjust the external cavity resonance, whereas the Littrow configurations uses tilt of the grating angle. Figure adapted from [97]

which allows for high output power. A drawback is that the output beam will change angle when the frequency is tuned, due to the changing grating angle.

In the Littman-Metcalf configuration the grating is used at grazing incidence, and the -1st order is reflected off a mirror rather than being sent directly back to the laser diode. This configuration is typically more flexible to align because of the mirror, and allows for a stationary output beam upon tuning the mirror position. A disadvantage is the lower grating efficiency at grazing incidence, which can reduce the output power. The cateye configuration does not use a reflective grating, but rather a transmission interference filter. This results in a linear cavity which can significantly lower astigmatism. The cateye configuration reduces the sensitivity to mirror imperfections and shaking, because of the small spot-size. The interference filter must be angled to select the correct frequency, which can translate the axis of the intracavity laser beam. Fine-tuning the frequency can be done by adjusting the end mirror just as in the Littman-Metcalf configuration.

In table 3.1 we note all lasers used in the experiment. With the exception of the 689 nm reference laser (see section 3.2.2) all systems have been constructed in the lab. Below we will go through the individual laser paths in the experimental system.

Table 3.1: Laser systems in Sr I with typical power levels, wavelengths and construction schemes. LD indicates injection locking of a simple laser diode, and TA is a tapered amplifier.

λ (nm)	Use	Scheme	P_{out} (mW)	
461	Cooling	Cateye	30	Under preparation
679	Repumping	Littman-Metcalf	3	
689	Probing	Littrow	12	Clock laser
689	Reference	Cateye	30	Reference laser
707	Repumping	Littman-Metcalf	14	
922	Doubling	Littrow	17	seed for TA
461	Cooling	Doubling cavity	70	
689	Pumping	Injection, LD	30	seed for TA
689	Pumping	Injection, TA	300	
689	Probing	Injection, LD	10	
922	Doubling	Injection, TA	950	seed for doubling cavity

Cooling light

The cooling scheme relies on laser cooling at around 461 nm. The light is generated by using a frequency doubling cavity with a PPKTP crystal. This crystal allows frequency doubling of infrared light at 922 nm to 461 nm with an efficiency that scales as P_{922}^2 . In figure 3.2 this part of the laser path is shown in a red box. The infrared light is initially generated in a Littrow configuration and sent through a tapered amplifier to boost the power from the 17 mW level to around 950 mW. After each laser an optical isolator ensures that back-reflections which could cause noise in the laser power, is significantly suppressed. The doubling cavity is a bow-tie type cavity, with a PPKTP (Periodically poled KTiOPO₄) crystal inside. The length of the cavity is controlled with a ring-piezo on one of the cavity mirrors. The cavity resonance is locked to the incident 922 nm laser via the reflected signal. Because the doubling crystal in the cavity is highly polarization sensitive, a Hänsch-Couillaud type lock can be used. The error signal for the HC lock is generated by mixing polarizations on a balanced photodetector (BPD), and it is fed back to the piezo voltage via a servo system.

The doubling cavity generates about 70 mW of blue light. A small fraction of this ($\sim 650 \mu\text{W}$) is used for the reference oven. The light is sent through AOM-Ref, see figure 3.2, where it is shifted by $\Delta_{AOM-Ref} = +368$ MHz in order to keep the main laser away from resonance with the atoms. The resonant light is used for fluorescence spectroscopy on the atoms in our reference oven. We obtain an error signal for the laser frequency control by adding a $\delta = 9.5$ kHz dither to the AOM frequency, and using a lock-in amplifier. The error signal is fed back to the current of the 922 nm ECDL.

The reference oven has a jet of uniform atoms with a transverse Doppler broadening of about $\sigma_D \approx 10$ MHz. It consists of a simple enclosure with solid strontium, that is heated to about 520 °C with a 1 mm center-hole. Atoms ejected from the hole have a large transverse spread which is reduced by three skimmers placed at distances of 60, 180 and 300 mm from the oven. The skimmers have 2 mm center holes as well as large open side-panels in order to facilitate vacuum pumping. It is

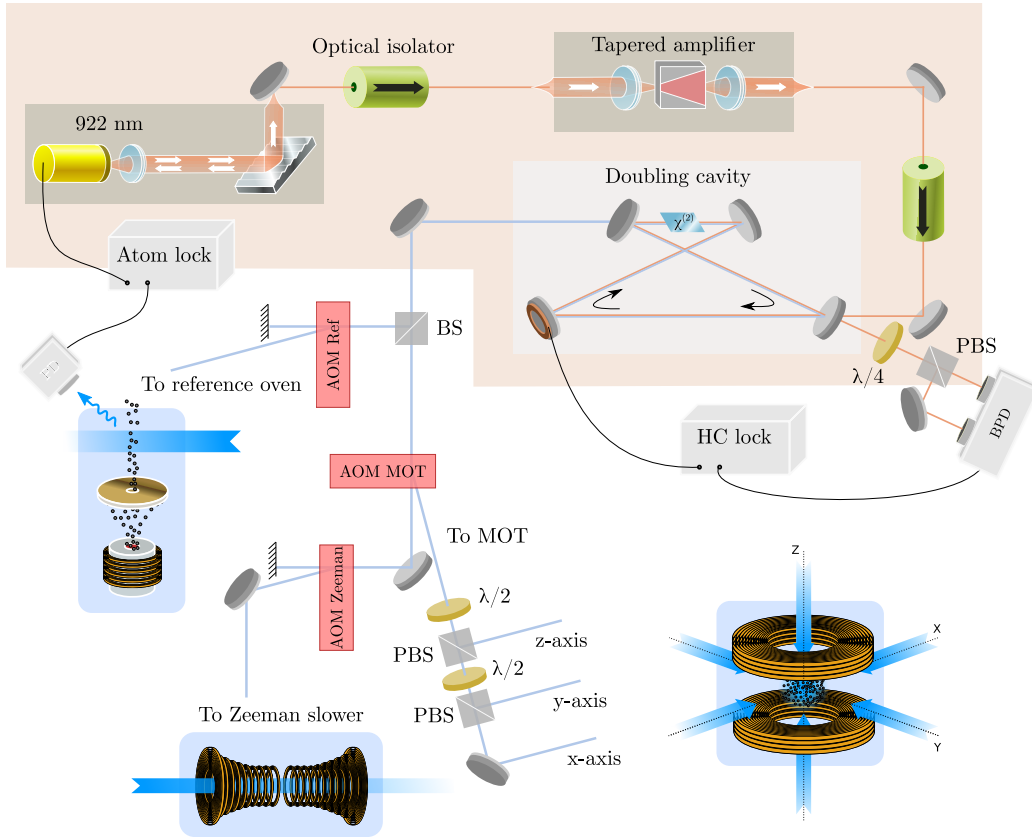


Figure 3.2: An overview of the cooling laser path. The laser light is generated on the marked, red section. Here 922 nm light is initially generated in a Littrow ECDL configuration. After the light is amplified it is coupled into a butterfly cavity, where frequency doubling takes place through nonlinear interaction with a PPKTP crystal. The cavity length is locked to resonance with the 922 nm laser, using a HC-type lock. The error signal is generated by rotating the polarization of the cavity reflected light using a $\lambda/4$ -plate, and detecting it on a balanced photodetector (BPD). The doubling cavity generated blue light at 461 nm is distributed between a reference oven, the Zeeman slower, and the three axes of a MOT. Distribution of the optical power is controlled via the RF amplitude supplied to the AOMs and a number of $\lambda/2$ -plates. The 922 nm laser is locked to ensure resonance with the atoms via a fluorescence detection photodiode (PD) at the reference oven, and a subsequent lock-in amplifier.

possible to use multiple ports along the vacuum chamber for atom spectroscopy.

Once this frequency locking loop is closed, two subsequent AOMs act to bring the light to the correct detunings for the 3D MOT light and Zeeman slower respectively. The MOT is operated at a detuning of $\Delta = -41$ MHz from the bare atomic transition, which is achieved by setting AOM-MOT to $\Delta_{\text{AOM-MOT}} = +327$ MHz, before dividing the beams into the vertical z-branch, and then the horizontal x- and y-branches. The Zeeman arm uses the zeroth order from AOM-MOT to generate a beam at a total detuning of $\Delta = -439$ MHz with AOM-Zeeman, $\Delta_{\text{AOM-Zeeman}} = -112$ MHz.

All AOMs in the 461 nm laser path are single-pass free-space AOMs. This means that the system is very inflexible to frequency detuning, as this will inevitably result

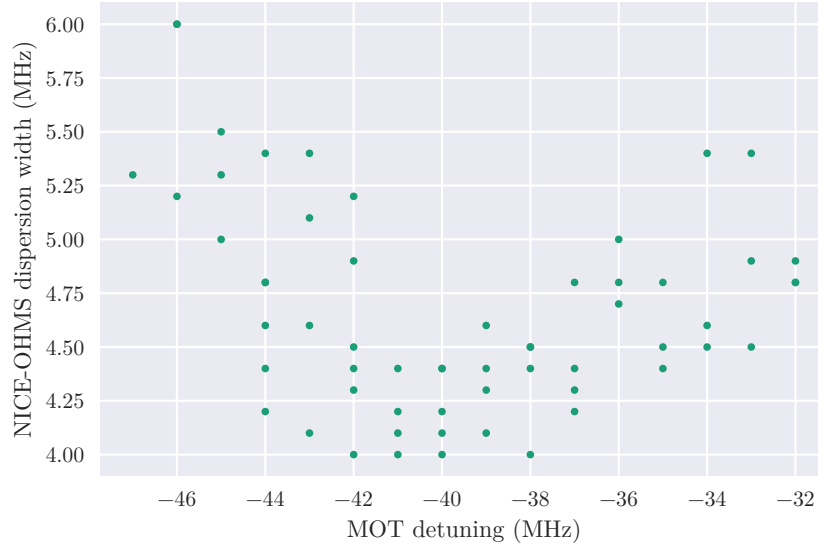


Figure 3.3: Measurement of the Doppler dispersion width of the blue MOT transition in our ^{88}Sr system. The reference oven AOM was used to change the detuning of the MOT beams. We plot the dispersion widths as a function of the detuning of the MOT beams with respect to the bare atomic transition. A minimal signal width is found for $\Delta_{\text{MOT}} \approx -41$ MHz.

in misalignment of the beams. Since there are no fibers in the path, the wavefronts also have a tendency to become somewhat distorted. The robustness of the MOT would gain significantly from adding fiber couplings to the three MOT arms. An alternative AOM scheme with the implementation of one or more double-pass AOMs would additionally allow for a more robust optimization of the MOT and Zeeman frequencies.

The minimal distortion from AOM detuning is achieved by detuning the frequency of AOM-Ref. We use this in order to optimize the frequency detuning of the MOT light with respect to atomic density and temperature. By adjusting the AOM frequency and measuring the width of the dispersion signal from the cold atoms, we achieve the frequency dependency shown in figure 3.3. Here we use the NICE-OHMS method detailed in chapter 4 in order to measure the atom-cavity dispersive response. The peak-peak width of the Doppler dispersion curve is then found for each AOM detuning. In the fully linear regime, the peak-peak width of the dispersion signal corresponds closely to the FWHM of the Doppler broadened absorption linewidth. While this is no longer the case in the non-linear regime that our system is in, there is still a proportionality between the dispersion width and the ensemble temperature.

Without giving a value for the ensemble temperature we thus find that the dispersion feature is most narrow for AOM-Ref values of $\Delta_{\text{AOM-ref}} = 368$ MHz. This corresponds to a MOT laser detuning of $\Delta_{\text{MOT}} \approx -41$ MHz with respect to bare atomic resonance. Since we are detuning AOM-Ref we will also effectively be detuning the Zeeman beam frequency, potentially reducing the number of atoms. However, we neglect the effect of detuned Zeeman light, since we expect the MOT

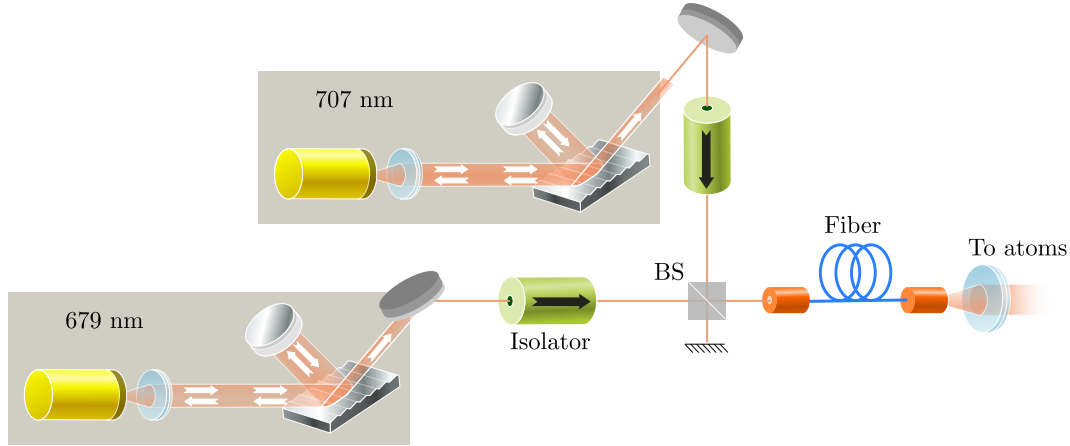


Figure 3.4: An overview of the repumping laser path. Two Littman-Metcalf configuration ECDLs generate light at 679 nm and 707 nm respectively. The light is combined on a simple beamsplitter (BS), and sent through a fiber, whose output is expanded and sent to the atomic sample.

beams to be more sensitive to this detuning.

Repumping light

We use two lasers in a repumping configuration during the cooling scheme. The fast cooling transition at 461 nm is not perfectly closed, and as such there is a finite leaking rate from the excited 1P_1 state to the meta-stable 3P_2 state. In figure 2.1 the energy levels are shown with the repumping lasers at 679 nm and 707 nm respectively.

Figure 3.4 shows the laser path of the repumping lasers. Both are based on the Littman-Metcalf ECDL configuration. Their beams are overlapped, and coupled to an optical fiber. This ensures optimal mode overlap of the beams as they impinge on the atoms. Due to the diodes used the output power of the 679 nm laser is limited to about $P_{679} = 3$ mW, whereas the 707 nm laser typically operates somewhat higher in power at about $P_{707} = 14$ mW. For both lasers this is sufficient to drive the atomic repumping with approximate scattering rates of

$$\gamma_{sc}^{707} = 1.9(7) \cdot 10^7 \text{s}^{-1} \quad \text{and} \quad \gamma_{sc}^{679} = 3.4(11) \cdot 10^6 \text{s}^{-1}. \quad (3.2)$$

Here we use equation (2.25) and assume that the atoms are at rest.

Probe light

We refer to the light resonant with the physics cavity, $\lambda = 689$ nm, as the probe light. This light can be resonant with the narrow $^1S_0 \leftrightarrow ^3P_1$ transition, and is used for probing the atoms in order to estimate the ensemble overlap with the cavity mode. In addition this is the probing light responsible for the saturation spectroscopy that we will discuss in chapter 4. The clock laser setup, see section 3.2.1, is used as a master laser for the probing light. It's spectral properties are important to the detection techniques we use in our different schemes. Here we go through the laser path at the Sr I table as shown schematically in figure 3.5. About 2 mW of power is emitted through a 10 m optical fiber from the clock laser table. The light is

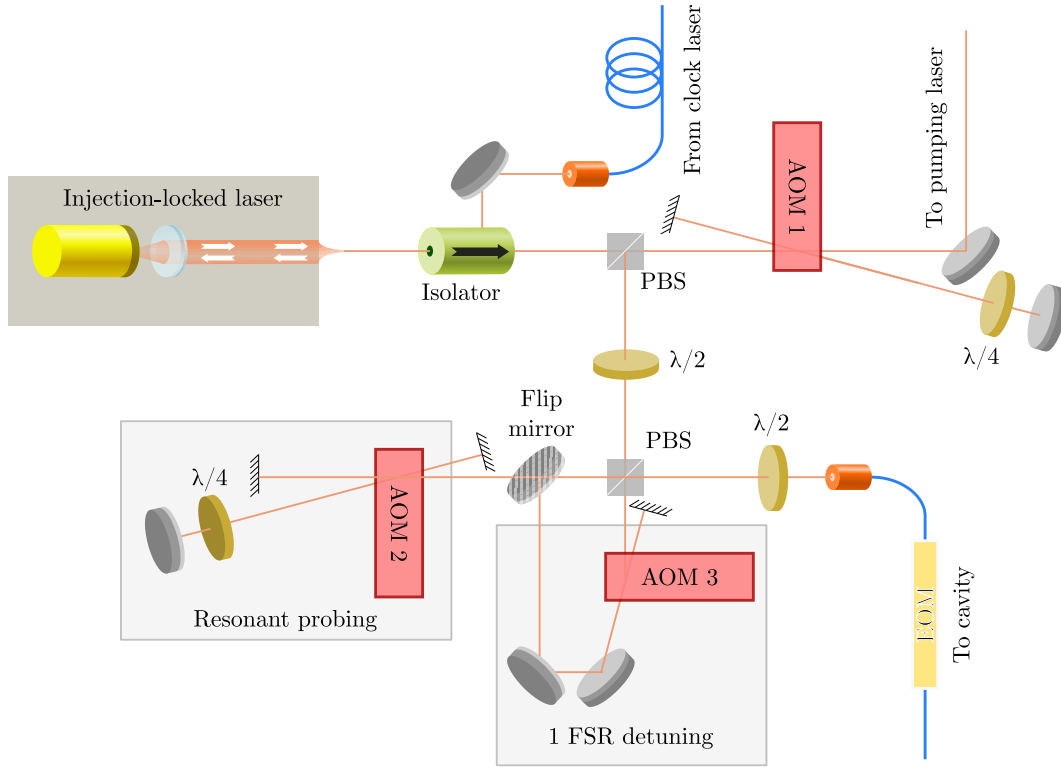


Figure 3.5: An overview of the probe laser path on the experiment table. Light generated at the clock laser table is sent through an optical fiber and used to injection lock a laser diode. This results in a 10 mW output power which is frequency shifted through two AOMs. The first AOM (1) is double pass, allowing for easy frequency control. The first unused zero order is picked off to feed a secondary laser path for optical pumping. The second AOM can be either a double or single pass, depending on whether we want the carrier frequency to be at atom resonance (AOM 2) or detuned by 1 FSR of the interrogation cavity (AOM 3). The light is then sent through a fiber-coupled EOM where PDH and NICE-OHMS sidebands can be generated.

directly used to seed an injection-locked laser through the exhaust port of an optical isolator. The injection locked laser acts as an amplifier producing about 10 mW of light whose frequency is controlled through a number of AOMs. Because we need to be able to tune the laser frequency, we use double-pass AOM configurations. These rely on using the first order diffraction of the AOM, and retro-reflecting it through the AOM. This results in a second first order diffraction that will overlap with the incoming light. A polarization beamsplitter (PBS) is then used in conjunction with a $\lambda/4$ waveplate in order to separate the out-coming beam from the incoming beam. Notice in figure 3.5 that the zeroth order of the first pass is sent to the pumping laser.

AOM 1 is stationary in frequency and set to $\Delta_{AOM-1} = -345$ MHz. The beam can be sent to the AOM 2 or AOM 3 setup depending on whether we are interested in a resonant probe (AOM 2) or a detuned probe field (AOM 3). Sending the beam to AOM 2 gives a shift of about $\Delta_{AOM-2} = +325$ MHz for each pass, resulting in a total detuning of $\Delta = -40$ MHz from the bare clock laser. This brings the laser to resonance with the atoms, except for the steady drift in frequency with the drift and

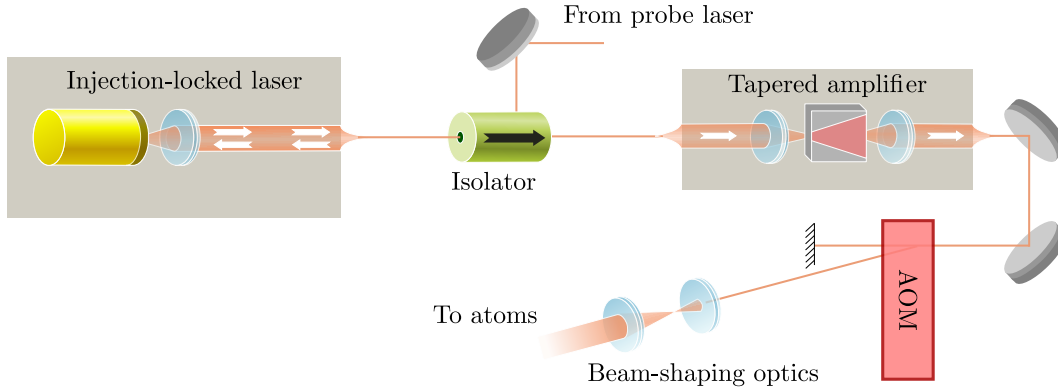


Figure 3.6: An overview of the pumping laser path. A branch of light from the probing laser is picked off to seed an injection locked laser diode. The light is further amplified from 30 mW to about 300 mW in a tapered amplifier (TA), and the frequency is shifted by about 38 MHz in an AOM. The AOM is used to rapidly turn on and off the pumping light sent to the atoms. A π -pulse is about 190 ns with an incident power of $P_{\text{pump}} \approx 100$ mW.

aging of the clock laser setup. By using a flip mirror and changing some waveplate orientations, the light can be directed towards AOM 3 allowing for a smaller shift of $\Delta_{\text{AOM-3}} = -130$ MHz. This produces a beam detuned one FSR of the physics cavity FSR = 781.14 MHz away from the atomic resonance. In contrast to AOM 1 and AOM 2, AOM 3 is a single-pass AOM.

After passing through the AOMs the light is coupled to a fiber-coupled electro-optic modulator (EOM). This EOM allows for a large modulation depth for modest RF powers compared to the free-space version, and is used both for sidebands at the physics cavity FSR (if needed), and to generate the PDH sidebands at $\Omega = 10$ MHz.

Pumping light

Light from AOM 1 in the probe path is sent to a second injection-locked laser diode, see figure 3.6, which generates light for the pumping beam used in chapter 5. The injected power is about 2 mW and the diode acts to amplify this to about 30 mW. Since this is still insufficient for inversion-pumping on the $^1\text{S}_0 \leftrightarrow ^3\text{P}_0$ transition the light is further amplified in a tapered amplifier (TA). The tapered amplifier efficiency has a square-dependency, so the primary amplification is necessary in order to obtain the required power levels. Out of the TA the power is about 300 mW, which is sent through a single-pass AOM at $\Delta_{\text{AOM-pump}} = -40$ MHz. Beam-shaping is necessary to make the intensity distribution across the atomic sample approximately homogeneous, and the final power level sent through the physics chamber is $P_{\text{pump}} \approx 100$ mW. The beam is incident at an angle of 45° with respect to the cavity axis, and shaped to have waist sizes of $w_0^x = 2.7$ mm and $w_0^y = 1.5$ mm along the greater and minor axis of an elliptic Gaussian. The greater axis is rotated 35° with respect to the plane spanned by the pumping beam itself and the cavity axis.

3.1.2 Physics cavity

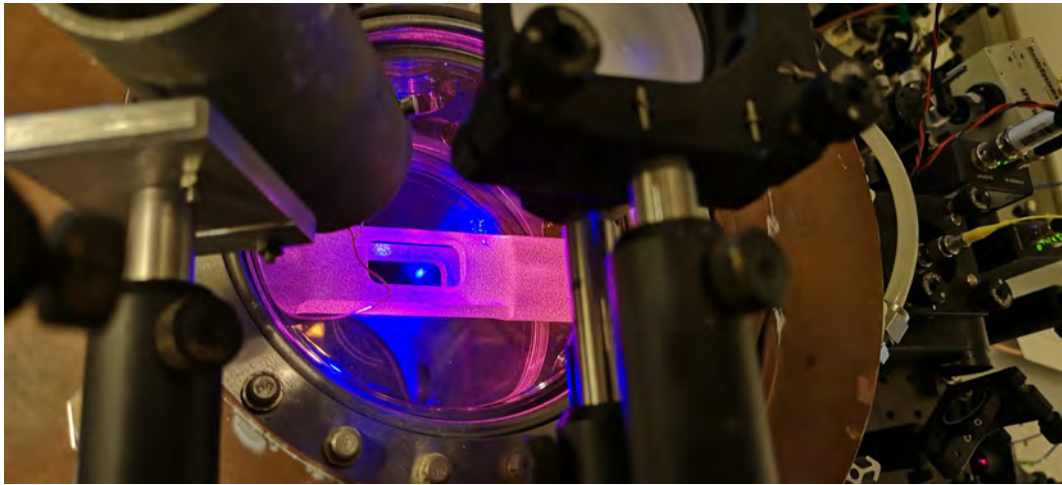


Figure 3.7: *Picture of the physics cavity with red light scattered from the matte Zerodur spacer, and a cloud of cold strontium atoms fluorescing in bright blue at the center. Cutouts in the cavity spacer allow for cooling and trapping of the atoms directly inside the physics cavity.*

Inside the vacuum chamber the atoms are placed within a physics cavity. In the context of the NICE-OHMS technique of chapter 4 it is referred to as the interrogation cavity, and in the context of laser generation in chapter 5 it is referred to as the lasing cavity. The cavity is a cylindrical Zerodur rod with mirrors glued to the ends, and cutouts to allow the laser cooling beams to pass through. Figure 3.7 shows a photo of the cavity, with red light scattering off the glass, and a blue cloud of atoms fluorescing in the center. The cavity mirrors are 1 inch in diameter, with a radius of curvature (ROC) of 9 m. The cavity length is approximately $L = 19.2$ cm resulting in a waist radius of $w_0 = 450$ μm . One mirror is mounted on a ring-piezo in order to allow for tuning of the cavity resonance. The mirror power reflectances are approximately $R = 99.8\%$. The measured linewidth is 620 kHz, and the free spectral range (FSR) is 781.14 MHz, resulting in a finesse of $\mathcal{F} = 1260$.

3.2 Reference lasers

In this section we will look at the two reference lasers used for interrogation and as frequency references for the experiments done in chapters 4 and 5. Both lasers are 689 nm lasers based on ECDL systems and referenced to stable reference cavities. The clock laser is used for locking the length of the physics cavity as well as for interrogation and stabilization in the NICE-OHMS system of chapter 4. In chapter 5 we will also see it used for some of the beating measurements with lasing pulses. The reference laser is used only in chapter 5 to measure spectra and frequency stability of the lasing pulses.

3.2.1 The clock laser system

The clock laser is based on a home built ECDL in the Littrow configuration, stabilized to an optical cavity with a finesse of about $F = 8000$ and a free spectral range of

$FSR = 1.5$ GHz. The current laser diode is an AR coated Eagleyard¹ diode installed in September 2018. The laser frequency is locked by using the PDH-technique on the cavity, and feeding back fast on the laser diode current and slowly on the voltage over a piezo-electric element mounted on the ECDL grating.

Figure 3.8 shows an image of the setup with the laser output branched out to a cavity-arm and an experiment-arm respectively. The cavity arm has a double-pass AOM at 358 MHz, which brings the laser onto resonance with the cavity mode, and an EOM for generating Pound-Drever-Hall (PDH) sidebands at 10 MHz. The light is led onto the cavity breadboard via free space optics, and the cavity rests inside a vacuum chamber which is rigidly mounted on the optical table. In the experiment-arm the light is coupled directly into a polarization maintaining (PM) optical fiber, and directed to the slave diode on the Sr-I table.

The clock laser table is a 10 cm thick honeycomb breadboard floating on air-filled pillows ensuring rigidity and high suppression of vibrations through the floor. The vibration isolation of the laboratory floor is already of very high quality (see appendix B.1), but regular road works, large vehicles and helicopters in the surrounding areas pose a challenge. In order to minimize air-currents a simple PMMA enclosure was designed. Additional foam panels inside of this enclosure partially dampens air-borne acoustic vibrations.

The temperature of the cavity spacer is stabilized by two independent peltier-elements mounted externally on the vacuum chamber front and back. The reference temperature is set to 24 °C without knowledge of the thermal-expansion coefficient zero-crossing temperature of the ultra-low expansion (ULE) glass used for the spacer. The clock system is thus relatively simple in its servo-electronics, with only two characteristics locked. The fiber noise added between the clock laser table and the experiment (10 m PM fiber in a lab environment) is uncompensated.

Figure 3.9 shows the spectrum of the PDH error signal recorded with a resolution bandwidth of 1 kHz. Noise is at the -40 dBm to -60 dBm level, with relatively wide and flat servo bumps peaked around 617 kHz.

3.2.2 The reference laser system

The reference laser system was built, used, and disassembled again within only a few months. This reference laser is based on stabilization of a commercial laser² to an ultra-stable cavity that was kindly on loan from Observatoire de Paris, SYRTE [104]. Since the infrastructure that we have built at the Niels Bohr Institute will serve as the basis for the construction of our own reference cavity, it was possible to incorporate the cavity into a well-equipped environment. We thus installed the setup in a low-noise environment (see appendix B.2) with an acoustic insulating enclosure³, and a vibration isolating platform⁴. The inside of the acoustic enclosure can be seen in figure 3.10. Since the enclosure is based on MDF wood panels, a 2 inch thick 600 mm × 900 mm honeycomb breadboard is used as a common platform

¹Part number: EYP-RWE-0690-00703-1000-SOT02-0000

²MOGlabs CEL

³Accurion AE-1200 custom

⁴Accurion i4

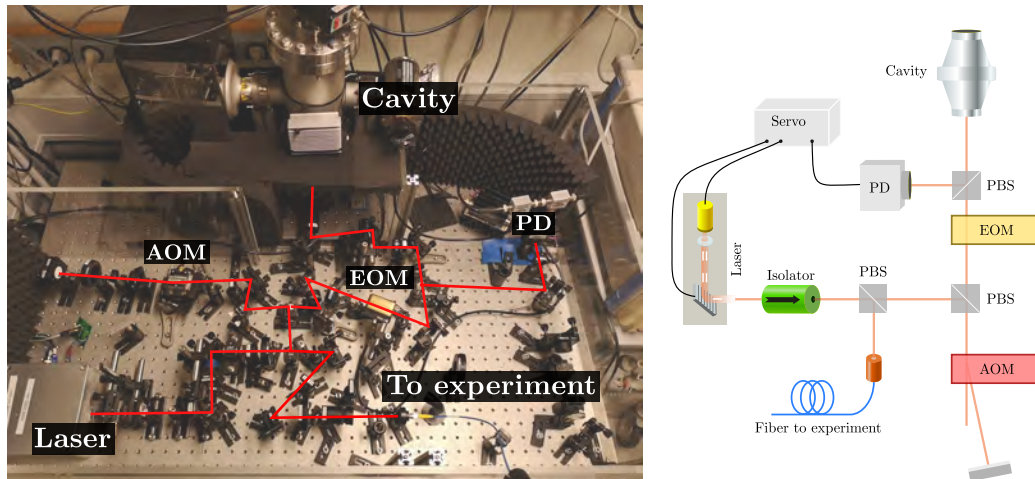


Figure 3.8: The setup of the clock laser. The whole system is mounted on a 10 cm honeycomb breadboard which floats on air-pressurized pillows. In the back a vacuum chamber with the ULE cavity spacer mounted vertically is seen. A home-built Littrow-configuration ECDL laser is used as the source (located in a gray aluminum box in the bottom left of the picture). The laser system is encased in a PMMA structure to minimize air currents. In combination with foam panels this enclosure also provides some level of acoustic isolation. The cavity ensemble is rigidly mounted on the breadboard, and the laser light is free-space coupled into the cavity. Light is distributed to the experiment via an optical fiber. Also shown is a schematic of the system. The active elements are a double-pass AOM and an EOM. A reference cavity and a photodiode (PD) is used to discriminate and detect the error signal that is fed back to the laser current and piezo via servo electronics. The polarization is manipulated to ensure correct propagation through three polarizing beamsplitters (PBS).

to provide rigidity and mass. The reference cavity rests on an active vibration isolation platform, and the laser on an additional honeycomb breadboard mounted on sorbothane spacers. This provides mechanical isolation between the two parts when working on the system while locking the laser frequency.

In figure 3.11 a simplified schematic of the reference laser system is shown. It consists of a laser breadboard (red) with a cavity arm and an experiment arm. Both arms are sent through optical fibers. In order to reduce phase-noise from these fibers, an interferometer is set up before the fiber in each arm. Sidebands for the PDH signal on the cavity are generated by an EOM in the cavity arm on the laser breadboard. At the end of each fiber a reference surface is set up for fiber noise cancellation (FNC), visible on the cavity part (yellow) of figure 3.11. In addition to the ultra-stable cavity two photodetectors (PD) are also placed on the cavity breadboard. The PD in reflection is used for the PDH stabilization and the PD in transmission is used for power stabilization of the cavity input light.

The laser is an interference-filter based ECDL (cat-eye configuration), whose frequency can be controlled by adjusting the laser diode current, or its cavity length by means of a piezo voltage. The light is sent through an optical isolator before being split between the two arms on a polarizing beamsplitter (PBS). The interferometers for FNC consist of 30:70 and 90:10 beamsplitters (BS) respectively for the cavity arm and experiment arm. The AOM frequencies are set at $\nu_{AOM}^{cav} = 240$ MHz and

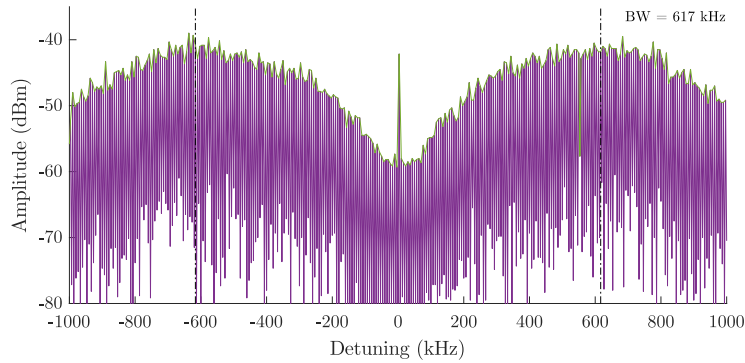


Figure 3.9: The PDH error signal spectrum of the clock laser, with slow feedback to the ECDL piezo and fast feedback to the laser diode current. Full measurement in purple, with the green curve showing only points above -60 dBm. The measurement was made with a resolution bandwidth of 100 Hz. We have manually added 20 dB to the signal amplitude to account for the signal reduction when measuring through a coupler. The servo bandwidth ($BW = 617$ kHz) is found as the frequency range below servo resonances.

$\nu_{AOM}^{exp} = 310$ MHz. The interferometer is a Michelson-Morley type, with a BS and two end-mirrors. One arm is local, whereas the other is through the optical fiber. Photodetectors in these interferometers then allow stabilization of the phase of the light, by feeding back to the RF frequency on the respective AOMs. Because the AOM is within one of the interferometer arms, the error signal will be at a frequency of $2 \cdot \nu_{AOM}$. By beating this against a stable frequency⁵ and actuating on the VCO frequency the phase noise is thus suppressed. An EOM in the cavity-arm allows 20 MHz phase modulation of the light in order to generate the PDH sidebands.

The cavity breadboard (yellow) contains the stable reference cavity. Light is coupled onto the breadboard from an optical fiber. A beamsplitter (BS) with a reference mirror acts as the fiber noise cancellation (FNC) reference surface. Light is coupled into the cavity and both the reflected and transmitted signals are detected in order to allow frequency stabilization on the laser, and power stabilization on Cav-AOM respectively. Typical power levels before power locking is $P = 350$ μ W at the fiber output, and $P = 30$ μ W in cavity transmission. After power locking the transmission signal is servoed to $P = 10$ μ W.

The spectrum of the PDH error signal when all parts of the system feedback loops are locked is shown in figure 3.12 with a carrier frequency at 20 MHz and servo resonances appearing at ± 440 kHz. The noise level is significantly lower than in the clock laser shown in figure 3.9, but the locking BW reduced. We use a MOGLabs FSC as the servo.

3.2.3 Frequency characterization

We beat the clock and reference lasers against each other in order to estimate the frequency noise. This is done at the Sr I experiment table following the 45 m phase-

⁵We typically use HP/Agilent/Keysight 8648A/B/C/D 1E5 for such references. These have a fractional frequency instability of $< 10^{-9}$ per day, and a phase noise of < -90 dBc/Hz for $\nu > 5$ Hz.

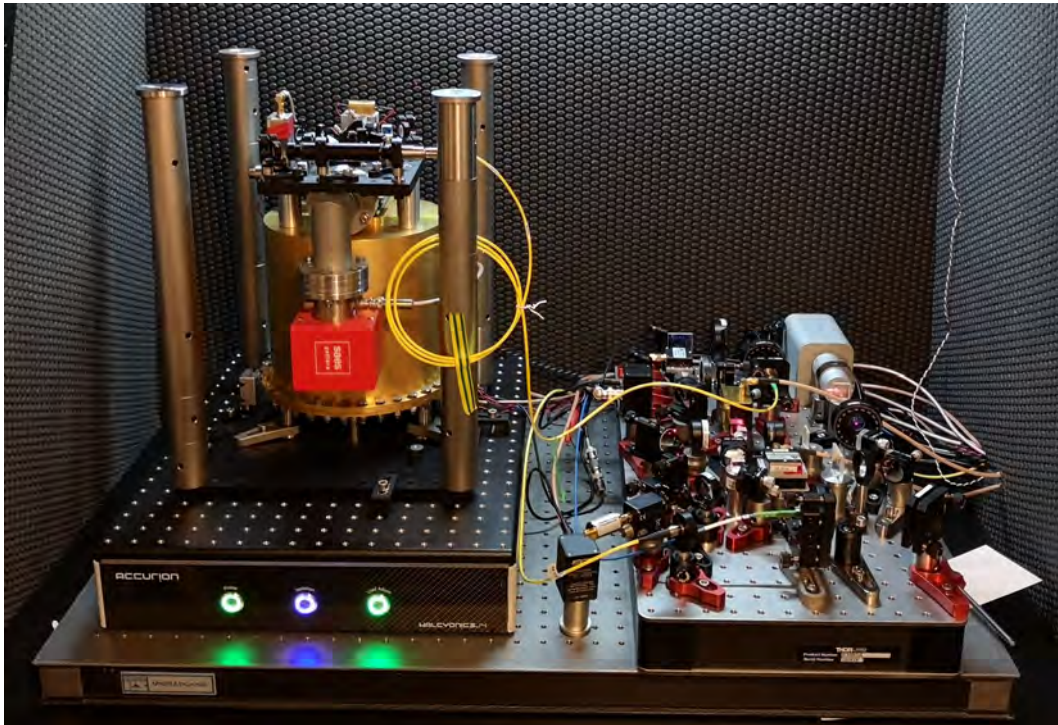


Figure 3.10: Inside the acoustic enclosure of the reference laser. The reference cavity with its golden vacuum chamber and protection pillars was kindly lend to us by Rodolphe Le Targe at Observatoire de Paris, SYRTE. It rests on a vibration isolation platform from Accurion. Next to it is the breadboard for the laser with its two branches connected to the cavity setup and the experiment respectively via optical fiber. All of this rests on a 600 mm \times 900 mm honeycomb breadboard to ensure rigidity.

stabilized fiber from the reference laser, and a 10 m uncompensated optical fiber from the clock laser. The clock laser does not employ power stabilization or ensure minimal thermal sensitivity of the length of the ULE cavity, so we expect this setup to be the limiting factor in terms of drift of the beat frequency.

We performed a number of beats at 118 MHz and measured the frequency using a commercial counter⁶. The counter has a deadtime of about 1 μ s per measurement, which we ignore here and limit ourselves to measurements times of $\tau > 1$ ms. In figure 3.13 we show the overlapping Allan deviation of the comparison for four different cases.

We steadily improved the locking of the reference laser to the stable cavity from SYRTE, while our own clock laser was left unchanged. The blue curve is a low-bandwidth lock of 200 kHz with an uncompensated 45 m fiber from the reference cavity to the interference point. The yellow and orange plots are measured with an improved bandwidth of 440 kHz on the reference laser lock. When adding fiber noise cancellation (yellow), the long-term drift is reduced significantly. By adding power stabilization to the reference cavity error signal, and further improving the locking bandwidth to about 550 kHz, the purple points are obtained with a minimum deviation of below 40 Hz or $9 \cdot 10^{-14}$ at 1 s. At shorter times the noise

⁶Pendulum CNT-90 Counter/Timer/Analyzer OPT. 30/90

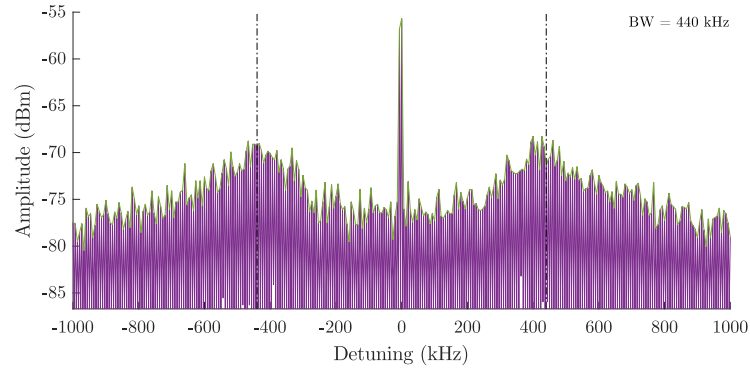


Figure 3.12: The PDH error signal spectrum of the reference laser, with slow feedback to the ECDL piezo, fast feedback to the laser diode current, and power stabilization of the cavity transmission. The measurement was made with a resolution bandwidth of 1 kHz. Full measurement in purple, with the green curve showing all points that are not at the lower detection limit of the spectrum analyzer (-100 dBm). We have manually added 20 dB to the signal amplitude to account for the signal reduction when measuring through a coupler. The servo bandwidth ($BW = 440$ kHz) is found as the frequency range below servo resonances.

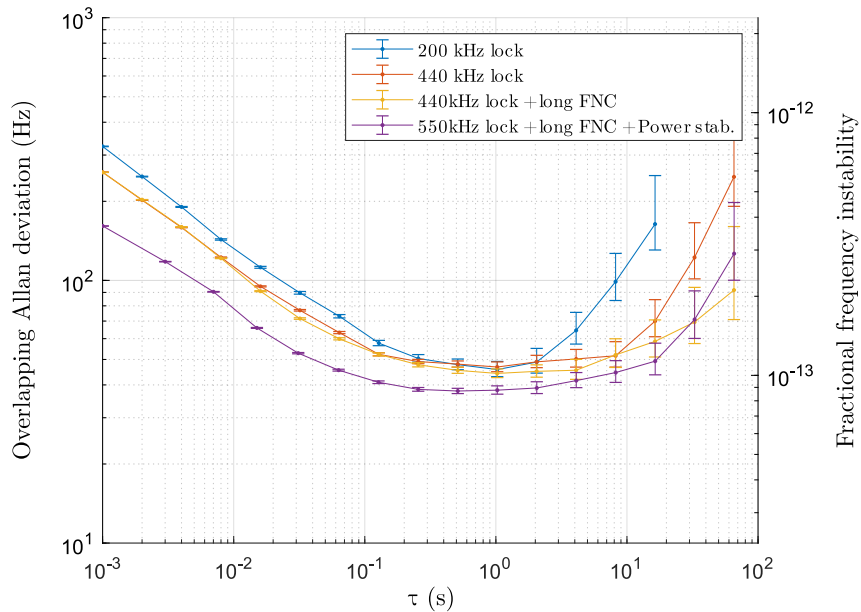


Figure 3.13: Comparison between the Clock laser and the reference laser. The beat between our own clock laser and the reference laser based on a stable cavity from Observatoire de Paris, SYRTE. We steadily improved the locking of the reference laser to the stable cavity from SYRTE, while our own clock laser was left unchanged. Here we show four different curves, exemplifying the improvements that were made. The blue curve is a low-bandwidth lock of 200 kHz with an uncompensated 45 m fiber from the reference cavity to the interference point. The yellow and orange plots are measured with an improved bandwidth of 440 kHz on the reference laser lock. When adding fiber noise cancellation (yellow), the long-term drift is reduced significantly. By adding power stabilization to the cavity error signal, and further improving the locking bandwidth to ≈ 550 kHz, the purple points are obtained with a minimum deviation of below 40 Hz or $9 \cdot 10^{-14}$ at 1 s. If both lasers behave similarly the single laser frequency deviation is about 28 Hz or $6 \cdot 10^{-14}$ at 1 s.

NICE-OHMS

Contents

4.1	Saturated spectroscopy in a cavity	40
4.2	NICE-OHMS detection scheme	43
4.3	Classical theory of cavity interaction	45
4.3.1	Cavity transfer function	47
4.4	Atom-field interaction	48
4.5	Beyond the linear regime	50
4.5.1	Projected frequency stability	51
4.5.2	Dynamical locking range limitations	52
4.5.3	Cavity lock effects	53
4.6	Frequency stability	56

In this chapter we present investigations of a phase-response approach to atomic or molecular spectroscopy inside of an optical cavity. Noise-Immune Cavity-Enhanced Optical Heterodyne Molecular Spectroscopy (NICE-OHMS) uses non-resonant side bands to act as reference fields in a heterodyne beat measurement. This can be used to measure the dispersion feature of an atomic or molecular resonance. The method was devised [126] by one of the namesakes of the PDH method, Jan Hall, as well as Long Sheng Ma and Jun Ye, who currently has the best strontium optical lattice clock in the world [83]. As the name of the technique suggests it aims to bring the advantage of cavity-enhanced systems and heterodyne measurements together.

Optical atomic lattice clocks operate in the Lamb-Dicke regime, where the confinement within an optical lattice means that allowed motional energies are separated in energy by a value greater than the transition linewidth. This suppresses Doppler broadening of the resonance to first order, severely reducing inhomogeneous broadening effects. The NICE-OHMS technique relies on resonant spec-

troscopy inside of an optical cavity, which makes it a saturation spectroscopy technique. This means that the inhomogeneous Doppler broadening of the atomic ensemble can be neglected to first order. This comes at the cost of ignoring all finite-velocity atoms, effectively reducing the atom number of your sample. The finite velocity of the atoms turns out to affect the system in other subtle ways, e.g., through doppleron resonances.

After a short introduction to saturated spectroscopy and a theoretical model for our system, we will look at typical spectroscopic signals from our system. In order to correctly interpret the full dispersion lineshape we find that we need to modify the quantum mechanical model derived in [112]. We present some theoretical predictions for the attainable spectral linewidth of a laser locked to such a feature, as well preliminary steps towards a frequency reference based on this technique. This chapter is based partially on the results presented in [99] and [98]. The work is a continuation of previous research performed by the author as presented in [18], [19], [45], [97].

4.1 Saturated spectroscopy in a cavity

Our ensemble of cold atoms can be treated as simple two-level systems consisting of an excited state, $|e\rangle$, and a ground state, $|g\rangle$. In strontium the transition that we are probing is a closed transition, and if we neglect collisions the only decay of the system is thus from $|e\rangle$ to $|g\rangle$ at a rate of γ_{eg} . The transition lineshape is Lorentzian, but homogeneous broadening effects can increase the linewidth beyond γ_{eg} and inhomogeneous broadening effects can misshape the effective linewidth of the full ensemble.

We start out by looking at the inhomogeneous broadening. In our case the most important inhomogeneous broadening is caused by the Doppler broadening due to the spread in atomic velocities. Their thermal distribution is given by a Maxwell-Boltzmann distribution. Since we only probe the atoms along a single axis, we are interested solely in the distribution along that axis. This distribution is Gaussian with a width of $\sigma_v = \sqrt{\frac{k_B T}{M}}$, which for a finite temperature of $T = 5$ mK on the $^1S_0 \leftrightarrow ^3P_1$ transition in ^{88}Sr corresponds to a Doppler spectrum with a FWHM of $\Gamma_D = 2\pi \cdot 2.3$ MHz.

The spectral profile of the atomic ensemble will then be a convolution of both the homogeneous and inhomogeneous broadening effects. For our purposes we can initially restrict ourselves to Lorentzian and Gaussian profiles, indicating that the final spectrum will be a Voigt profile. Figure 4.1 illustrates the shapes of Voigt profiles for different ratios between the widths of the Gaussian and Lorentzian lineshape. The Lorentzian width has a lower bound given by the natural transition decay rate $\gamma_{eg}/2\pi = 7.5$ kHz, but is limited by a homogeneous power-broadening of up to $\Gamma_{power}/2\pi \approx 200$ kHz. This places us somewhere between the case of figure 4.1 (b) and (c), where the Voigt profiles closely resemble a Gaussian distribution.

The power broadening of the spectrum originates from the nonlinear response of a two-level system to a driving intensity, when the excitation rate Λ approaches that of the decay rate γ_{eg} . This can be viewed in terms of the fundamental processes

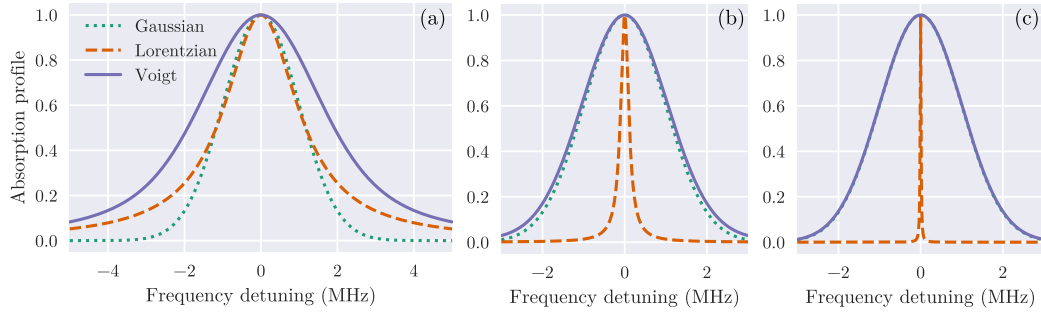


Figure 4.1: Spectral profile of a Voigt originating from Gaussian, Γ_D , and Lorentzian, Γ_{power} , distributions of different relative widths. (a) $\Gamma_D/\Gamma_{power} = 1$. (b) $\Gamma_D/\Gamma_{power} = 10$. (c) $\Gamma_D/\Gamma_{power} = 100$.

such as absorption and stimulated emission and is quantified through, e.g., the rate equations. An expression for the absorption lineshape, as derived in [34], can be given by the atomic density n , and maximal absorption cross section $\sigma_0 = 3\frac{\lambda_0^2}{2\pi}$, where λ_0 is the resonant wavelength.

$$\alpha(\omega, I) = n\sigma_0 \frac{(\gamma_{eg}/2)^2}{(\omega - \omega_0)^2 + \left(\frac{\gamma_{eg}}{2}\right)^2 (1 + I/I_{sat})}, \quad (4.1)$$

where the resonance frequency is given by ω_0 . The saturation intensity at resonance is related to the transition linewidth and energy $I_{sat} = \frac{\pi}{3} \frac{hc\gamma_{eg}}{\lambda_0^3}$. The power broadened absorption lineshape is itself a Lorentzian with a increased width of

$$\Gamma_{power} = \Gamma \left(1 + \frac{I}{I_{sat}}\right)^{1/2}, \quad (4.2)$$

and a reduced amplitude of $\frac{1}{1+I/I_{sat}}$.

Since the Doppler broadening of an ensemble is an incoherent effect, it is possible to address atoms within certain velocity ranges by tuning your light to resonance with them. If a light field resonant with atoms in a certain velocity range is sufficiently strong, these atoms will be saturated, and the absorption of the atomic ensemble will be reduced at the corresponding frequency when measuring with a second probing laser. This is illustrated in figure 4.2 for the case of a saturation beam on resonance with the bare atomic transition ω_0 .

The saturation permits a measurement of a sharp spectroscopic feature, even from an initially Doppler broadened ensemble. If the saturation beam and the beam used to probe the ensemble have equal an opposite detunings with respect to ω_0 , it is the unperturbed atoms (at rest with respect to the laboratory frame of reference) that are saturated. One technically elegant way to realize this is by ensuring that the beams have identical frequencies, but opposing directions of propagation. By scanning the laser frequency in such a scheme, saturation will only be detected for $\omega = \omega_0$.

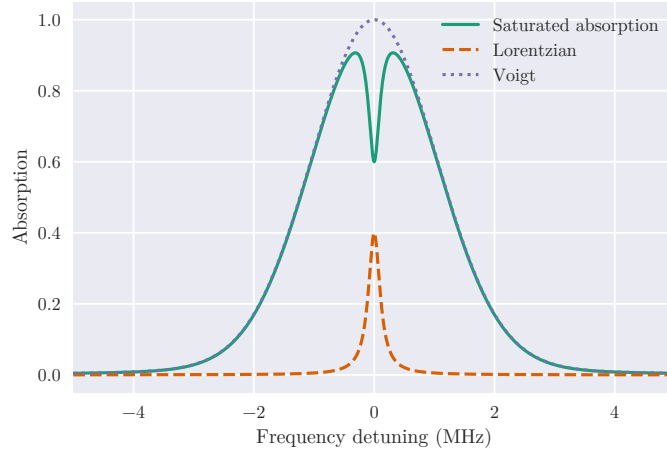


Figure 4.2: Absorption profile of a Doppler-broadened ensemble of atoms with a homogeneous power broadening of order $\Gamma_D/\Gamma_{power} = 10$. Atoms at rest are saturated resulting in a Voigt profile with a Lamb dip appearing as a Lorentzian dip at the center. Constituent Voigt and Lorentzian profiles are shown.

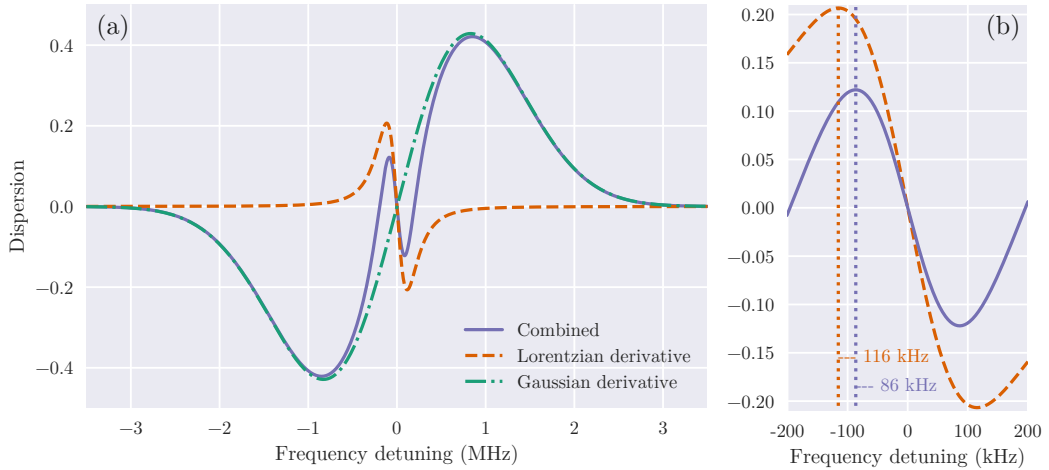


Figure 4.3: Sum (blue) of ideal Gaussian (green) and Lorentzian (orange) dispersion features exhibiting line-narrowing, and slope reduction of the resulting Lorentzian-like dispersion. While the inhomogeneous broadening of an atomic ensemble will in general lead to a Voigt profile and not a Gaussian profile. Here we assume a regime where $\Gamma_D/\Gamma_{power} \gg 1$, making a Gaussian an excellent approximation. (a) shows the full signal and (b) shows the line-narrowing, and slope-reduction of the sum with respect to the bare Lorentzian derivative.

Here it is only appropriate to return to optical cavities. Optical cavities ensure two things. They amplify the power levels of the input field, and they provide a perfectly balanced bi-directional field. This makes cavities a trusty companion of saturated absorption spectroscopy in many different applications. Since we are interested in the narrow spectral feature of a Doppler-free spectroscopic method for laser stabilization, we will focus on the dispersion signal in the following. The absorption profile will be largely ignored.

A wrong, but nevertheless informative, approach to the dispersion signal is to consider the derivative of the absorption signal. In figure 4.3 we look at the sum of a Lorentzian and a Gaussian derivative of opposite signs. The large Gaussian feature from the Doppler-profile incurs a sign-reversal of the slope right at resonance because of the Lorentzian saturation. As is shown in 4.3 (b) the magnitude of the slope of the final signal will be smaller than the pure Lorentzian, just as the width will be reduced because of the Doppler-background. This is unfortunate from the point of view of obtaining a good frequency-discrimination. The slope can, however, be much steeper than that of the Doppler feature, depending on the saturation parameter. While the true dispersion features (figure 2.2) are slightly different from the derivatives shown here, the considerations are the same.

By locking the cavity resonance to the laser frequency, we can map out the actual dispersion signal of the cavity-coupled atoms. Thus far we have not considered how the cavity modifies the signal, but this will be shown in both sections 4.4 and 4.5. In the following section we will look into the detection scheme for the NICE-OHMS signal itself, and how that allows us to measure the phase-response of the system.

4.2 NICE-OHMS detection scheme

In figure 4.4 we show a schematic of the setup. Atoms are probed inside of an optical cavity, and we set up our system to be able to detect both the transmitted power of the cavity and the phase-response. The cavity mode ensures that we always have perfectly balanced powers in the two counter-propagating beams inside the cavity. For sufficiently high powers we will then saturate the atoms with velocity $\vec{v} = 0$ parallel to the cavity axis. The transmitted power shows us a wide Doppler-absorption profile, with saturation in the center. The width of the Doppler-profile is given by the temperature of the ensemble and yields temperatures of approximately $T = 5$ mK. Notice that the signal-to-noise ratio (SNR) of the absorption signal is quite poor, but that of the phase-response is significantly better.

The frequency of the probing laser is controlled through an AOM as detailed in 3.1.1. We phase-modulate the laser in an EOM to add spectral sidebands to the carrier frequency at $\nu_{\text{PDH}} = 10$ MHz and $\nu_{\text{FSR}} = 781$ MHz respectively. On figure 4.5 an overview of the frequency components involved can be seen. The cavity length is then locked to resonance with the probing beam by using the reflected signal in a PDH lock, and feeding back to a ring-piezo on one of the cavity mirrors. The modulation at ν_{FSR} allows sidebands resonant with the cavity to be transmitted without interacting with the atomic ensemble itself.

For the light interacting with the cavity, we can neglect the PDH sidebands, and describe the input laser field as

$$E_{\text{in}} = E_0 \sum_{j=-\infty}^{\infty} J_j(y) e^{i(\omega_l + j2\pi\nu_{\text{FSR}})t}. \quad (4.3)$$

Here E_0 is the amplitude of the electric field, and the phase-modulation of the laser leads to sideband amplitudes that follows the j -th order Bessel function of the first

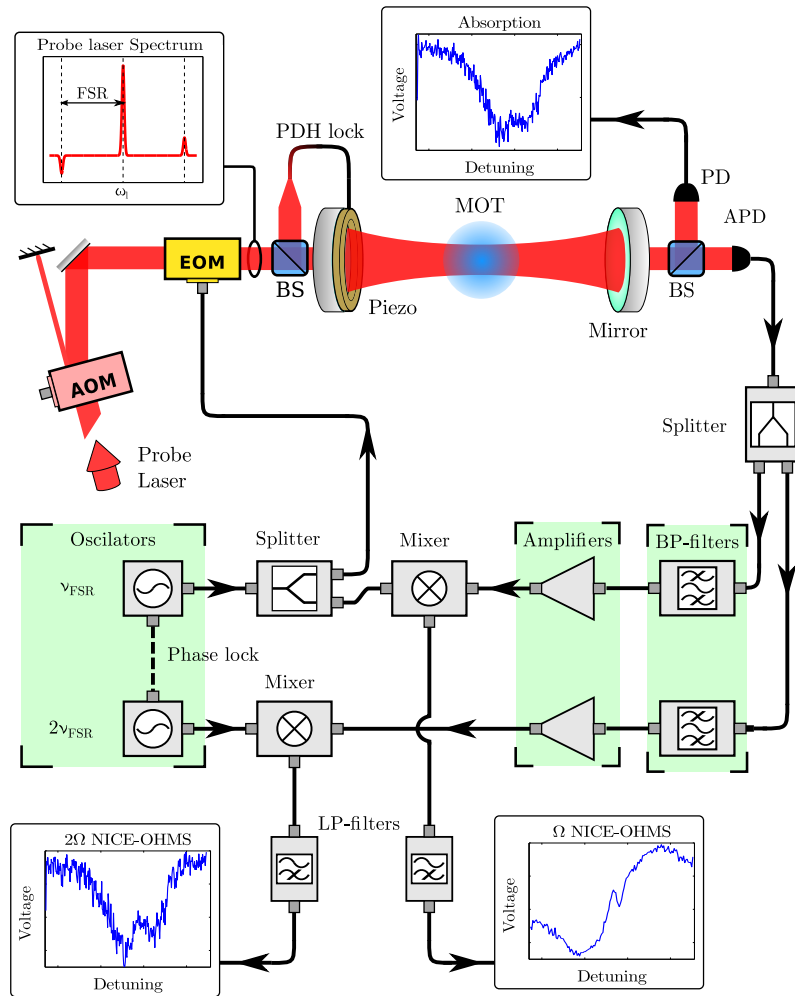


Figure 4.4: Schematic of the NICE-OHMS measurements system and detection electronics. Atoms are trapped in a MOT overlapping with the cavity mode. The interrogation laser is sent through an AOM to control frequency detuning. An EOM adds sidebands to the interrogation laser at the FSR of the cavity. Additional sidebands at 10 MHz are used for a PDH lock which ensures that the cavity is always kept on resonance with the laser. After detection a slow photodiode (PD) and a fast avalanche photodiode (APD) is used to detect the signal and provide a direct absorption signal and a beat signal with the probe laser sidebands respectively. By demodulating the beat signal the phase response and atomic absorption can be retrieved at v_{FSR} and $2v_{FSR}$ respectively. Adapted from [97].

kind, $J_j(y)$. In the transmitted signal we will then have a total power which is detected on a slow (50 MHz) photodiode (PD) as well as beat signals which are detected on a fast (1.5 GHz) Avalanche photodiode (APD). The APD signal is filtered and demodulated at the beat frequency v_{FSR} or $2v_{FSR}$. This allows us to observe the signal in a frame rotating at the oscillation frequency of the light itself, and the detected signal is thus proportional to the field amplitudes and the relative phases.

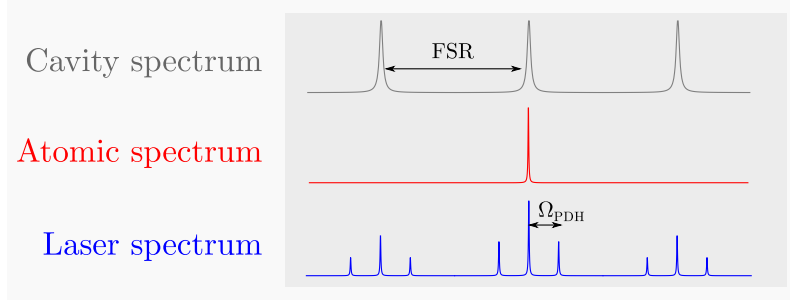


Figure 4.5: The NICE-OHMS scheme in terms of laser frequency components and their relation to cavity and atomic resonances. The carrier frequency is on resonance with the atomic transition, while sidebands at ν_{FSR} are transmitted through the cavity without interaction with the atoms. Additional sidebands at Ω_{PDH} are used to generate the PDH signal. Notice that the cavity lock will be based on the sum of three simultaneous error-signals. When the carrier is mostly absorbed by the atoms, this enables the lock to remain on.

4.3 Classical theory of cavity interaction

With the input field to the cavity described as simply a sum of fields at different frequencies, all resonant with the cavity, we can give a classical description of the interaction between the field and a cavity with some complex-phase medium. We ignore for the moment the exact behavior of this medium, and describe it in a generic way. This will allow us to later reintroduce the atomic phase-shift derived in a semi-classical framework.

We relate the output field to the input via a complex transfer function $\zeta(\theta)$ where $\theta(\omega)$ is the field-dependent complex phase resulting from propagation in the cavity and interaction with the atoms. We assume a linear behavior such that the transfer function fulfills $E_{\text{out}} = \zeta(\theta)E_{\text{in}}$. The real part of the transfer function will then correspond to the relative amplitude of the transmitted field, whereas the imaginary part will correspond to the dispersion. Light passing through a symmetrical Fabry-Perot cavity can be described by a light ray bouncing back and forth between the mirrors of the cavity, with power reflection (transmission) coefficients R (T). Looking at the j -th frequency component of the field only, we get a transfer function [90]

$$\zeta_j = \frac{T e^{i\phi_j}}{1 - R e^{2i\phi_j}}, \quad (4.4)$$

where we have assumed that our cavity mirrors are identical and lossless. Since ϕ_j is a complex phase, absorption within the cavity medium is still allowed. For the sidebands there is no interaction with the atomic ensemble, and the phase-shift is simply given by the single-passage bare cavity phase shift $\phi_j = \phi_{\text{cav}}^j$ for $j \neq 0$. The carrier component interacts with the atomic ensemble, however, and sees a phase shift:

$$\phi_0 = \phi_{\text{cav}}^0 + \phi_D + i\phi_A, \quad (4.5)$$

where ϕ_D is the atomic dispersion and ϕ_A the atomic absorption for a single passage. Since we operate in a steady state with no external pumping, there will be no gain in the system and we always have $\phi_A \leq 1$. The bare cavity induced phase-shift is

given by $\phi_{cav}^j = \phi_\Delta + \pi j$ which is dependent on the number of half-wavelengths in the cavity standing wave of the j -th sideband, and an offset-phase $\phi_\Delta = 0$ for the case of an ideal cavity lock.

Combining the transfer functions for different j , we can write the output field as a superposition of the input field components

$$E_{\text{out}} = E_0 \sum_{j=-\infty}^{\infty} J_j(y) \zeta_j e^{i(\omega_l + j2\pi\nu_{\text{FSR}})t}. \quad (4.6)$$

This field is directly incident on the photodetectors and we obtain the DC signal

$$S_{\text{DC}} \propto 2|E_0|^2 J_0(y)^2 |\zeta_0|^2, \quad (4.7)$$

on the slow detector. The fast detector picks up the beat signal between adjacent sidebands, which we can demodulate with an appropriate choice of phase in order to obtain the first or second overtone signal:

$$\begin{aligned} S_{\text{FSR}} &\propto -2i|E_0|^2 J_0(y) J_1(y) (\zeta_0 \zeta_1^* - \zeta_0^* \zeta_1) \\ S_{2\text{-FSR}} &\propto -2|E_0|^2 J_0(y) J_2(y) (\zeta_0 \zeta_1^* + \zeta_0^* \zeta_1) - 2|E_0|^2 J_1(y)^2 |\zeta_1|^2. \end{aligned} \quad (4.8)$$

Here we have included up to second order in sidebands, as higher order terms only become relevant for a high modulation index $y > 1.5$. We have additionally taken advantage of the simplification $\zeta_j = (-1)^{|j|-1} \zeta_1$ for $j \neq 0$. By looking closer at our phase conditions we can further simplify these expressions.

In steady state, the cavity lock will ensure that the cavity is on resonance with the carrier component, which results in the condition

$$\phi_{\text{cav}}^0 + \phi_D = n\pi, \quad \text{for } n \in \mathbb{Z} \quad (4.9)$$

Using this condition together with equation (4.5) we can rewrite equation (4.4) to obtain a purely real number¹

$$\zeta_0 = \frac{T e^{-\phi_A}}{1 - R e^{-2\phi_A}}, \quad (4.10)$$

which depends only on the atomic absorption. The atomic phase dispersion information is then transferred to the sidebands through the cavity locking condition

$$\begin{aligned} \phi_j &= \phi_{\text{cav}}^j \quad \text{for } j \neq 0 \\ &= \phi_{\text{cav}} + j\pi \\ &= (n + j)\pi - \phi_D. \end{aligned} \quad (4.11)$$

Ignoring again the overall sign from $e^{in\pi}$, we get the sideband transfer function

$$\zeta_j = \frac{T e^{i(j\pi - \phi_D)}}{1 - R e^{2i(j\pi - \phi_D)}} \quad \text{for } j \neq 0. \quad (4.12)$$

¹We ignore an overall sign from $e^{in\pi}$.

We can then recast the expressions for the signals in equations (4.8) as:

$$\begin{aligned} S_{\text{FSR}} &\propto -4|E_0|^2 J_0(y) J_1(y) \zeta_0 \text{Im}(\zeta_1) \\ S_{2\text{-FSR}} &\propto -4|E_0|^2 \left(J_0(y) J_2(y) \zeta_0 \text{Re}(\zeta_1) + \frac{1}{2} J_1(y)^2 |\zeta_1|^2 \right). \end{aligned} \quad (4.13)$$

The first overtone is proportional to the atom-cavity dispersion $\text{Im}(\zeta_1)$ and provides the error-signal we are after for laser stabilization. The DC component of the signal will give the absorption profile, but it turns out that the second overtone signal $S_{2\text{-FSR}}$ is also proportional to the absorption of the system, and allows us to detect the signal at high frequencies with a potentially improved signal-to-noise ratio as a consequence.

4.3.1 Cavity transfer function

Before we look at the atom-field interaction inside the cavity, we will take a closer look at the consequences of the cavity phase relations and how this can eventually distort the phase dispersion at large atomic phase-shifts. Because of energy conservation, the absolute-square of the complex transfer function we defined above cannot exceed unity in a system without gain, $|\zeta|^2 \leq 1$. This implies that there is some maximal allowed value for the phase-response of the system $\text{Im}(\zeta_1)$. To simplify things we initially assume that there is no absorption in the cavity $\text{Re}(\zeta_1) = 0$. This, of course, is unphysical in a situation where we are probing atoms resonantly, but leads us to the trivial case where the magnitude of the phase-shift must fulfill $|\text{Im}(\zeta_1)| \leq 1$.

For dilute media the phase-shift caused by the atoms is small, and we are thus in a regime where the transfer function is linear and $\text{Im}(\zeta_1) \propto \phi$. For larger phase-shifts, however, this is no longer the case. Larger total phase shift is caused either by a material inside the cavity with higher dispersion, or simply by increasing the cavity finesse, and thus the effective interaction length. In figure 4.6 we plot the imaginary part of a transfer function similar to equation (4.4) as a function of mirror transmission, T , and the single-passage phase shift ϕ of some intracavity material. We assume lossless cavity mirrors, $T + R = 1$, and zero absorption, $\phi_A = 0$.

At high mirror transmission, the cavity has no effect, and the transfer function becomes $\zeta \propto e^{-\phi_A} \sin(\phi_D)$. A sinusoidal behavior with a phase-period of 2π . In the figure we see only the behavior for mirror transmissions between $T = 1\%$ and $T = 0.01\%$. Here the periodicity of 2π remains, but only for small $\phi \leq 5$ mrad do we see the dispersive behavior. As the transmission decreases (finesse increases) the cavity dispersion feature grows more and more sharp. The thick black line indicates a mirror reflectivity of $T = 0.2\%$ which corresponds to the mirrors we use in the experiment.

Since the cavity transfer function maps out a dispersive behavior for increased phase-shift inside the cavity, there will be a limit imposed on measurements of the atomic phase-shift. If the atomic phase-shift for a given cavity finesse remains small, we stay within the linear regime close to resonance. When the laser and cavity are detuned together, the single-passage phase shift of the atoms increases. This means that the dispersive behaviors of the atoms and the cavity will be convoluted.

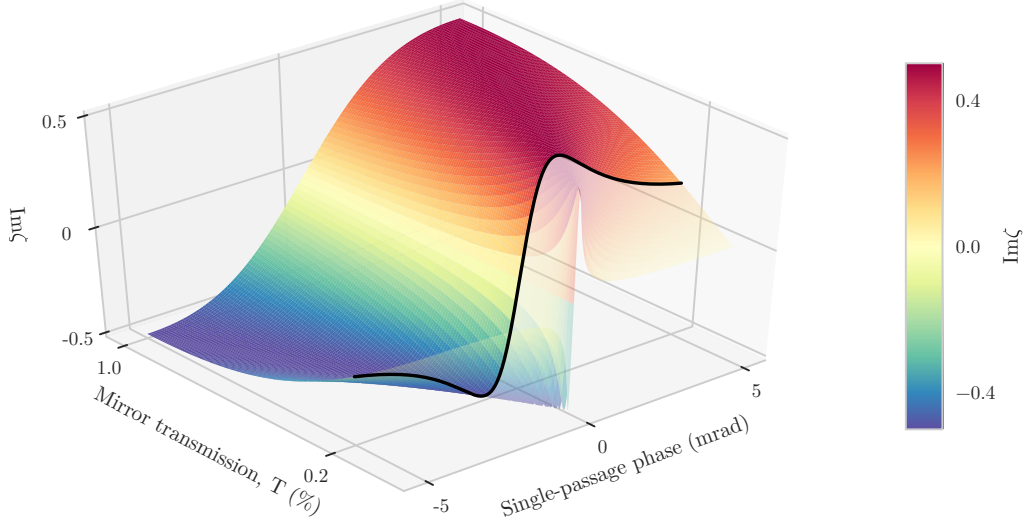


Figure 4.6: Cavity dispersion plotted against cavity mirror transmission and single-pass intracavity phase shift. For small intracavity phase shifts the dispersion as a function of phase shift is linear, but it flattens out and eventually inverts the slope for higher phase shifts. Adapted from [99].

Including this convolution in the theoretical description turns out to be necessary in order to appropriately fit it to the experimental measurements.

The atomic absorption will decrease the maximal value of the total dispersion $\text{Im}(\zeta_1)$. The dispersion feature of the atom-cavity system might approach its maximal value at a given detuning, but the value of that maximum will itself be a function of detuning. This is a result of the fact that both the atomic dispersion ϕ_D and absorption ϕ_A varies as the frequency is changed. The maximal value of the dispersion then, increases as we detune our system away from atomic resonance. We will see examples of this behavior in section 4.5. Before we show the spectroscopic data we will look at the semi-classical theory of interaction between atoms with quantized energies and a classical probing field.

4.4 Atom-field interaction

Here we give a brief overview of the theoretical model used by following [112], [120]. Here a Born-Markov master equation approach is taken, assuming a reservoir unperturbed by the system, and with no memory on the time scale of the cavity coupling rate as well as cavity and atomic decay rates $1/(g_0, \kappa, \gamma)$. The time-evolution of the density operator $\hat{\rho}$ is given as:

$$\frac{d}{dt}\hat{\rho} = \frac{1}{i\hbar} [\hat{H}, \hat{\rho}] + \hat{\mathcal{L}}[\hat{\rho}]. \quad (4.14)$$

The Liouvillian, $\hat{\mathcal{L}}$, describes the incoherent processes of the system, whereas the coherent evolution is given by the interaction-picture Hamiltonian:

$$\hat{H} = \hat{H}_{\text{atom}} + \hat{H}_{\text{drive}} + \hat{H}_{\text{interaction}} \quad (4.15)$$

The ensemble of cold atoms is modeled as two-level emitters who can couple to the TEM₀₀ mode of an optical cavity. The cavity field is modeled as a strong classical field because of the resonant probing laser.

$$\hat{H}_{\text{drive}} = \hbar\eta(\hat{a}^\dagger + \hat{a}), \quad \eta = \sqrt{\frac{\kappa P_{\text{in}}}{\hbar\omega_1}}. \quad (4.16)$$

Here κ is the cavity decay rate, P_{in} is the optical power coupled into the cavity, η is the classical drive amplitude and ω_1 the probe-laser frequency. In the interaction picture, we take the rotating-wave approximation and obtain the Hamiltonian:

$$\hat{H} = \frac{\hbar\Delta_{ac}}{2} \sum_{j=1}^N \hat{\sigma}_j^z + \hbar\eta(\hat{a}^\dagger + \hat{a}) + \hbar \sum_{j=1}^N g_j(t)(\hat{a}^\dagger \hat{\sigma}_j^- + \hat{\sigma}_j^+ \hat{a}). \quad (4.17)$$

Here we have placed ourselves in a coordinate system that rotates at the cavity frequency, ω_c and assume $\omega_c = \omega_1$. The atomic operators for the j -th atom are given by $\hat{\sigma}_j^{z,-,+}$, N denotes the total number of atoms, and $\Delta_{ac} = \omega_a - \omega_c$ is the atom-cavity detuning. The cavity field operators are \hat{a}^\dagger and \hat{a} , and their coupling to an atom is given by equation (2.13).

The Liouvillian describes the contributions from loss of photons through the cavity field, κ , spontaneous decay of the excited atomic state, γ , and the inhomogeneous dephasing rate, Γ_{dec} :

$$\begin{aligned} \hat{\mathcal{L}}[\hat{\rho}] = & -\frac{\kappa}{2} (\hat{a}^\dagger \hat{a} \hat{\rho} + \hat{\rho} \hat{a}^\dagger \hat{a} - 2\hat{a} \hat{\rho} \hat{a}^\dagger) \\ & - \frac{\gamma}{2} \sum_{j=1}^N (\hat{\sigma}_j^+ \hat{\sigma}_j^- \hat{\rho} + \hat{\rho} \hat{\sigma}_j^+ \hat{\sigma}_j^- - 2\hat{\sigma}_j^- \hat{\rho} \hat{\sigma}_j^+) \\ & + \frac{\Gamma_{\text{dec}}}{2} \sum_{j=1}^N (\hat{\sigma}_j^z \hat{\rho} \hat{\sigma}_j^z - \hat{\rho}), \end{aligned} \quad (4.18)$$

Armed with this mapping we can derive a mean-field description of the time-evolution in the system represented by three coupled equations.

$$\begin{aligned} \langle \dot{\hat{a}} \rangle &= -\kappa \langle \hat{a} \rangle + i\eta + i \sum_{j=1}^N g_j(t) \langle \hat{\sigma}^- \rangle_j, \\ \langle \dot{\hat{\sigma}}^- \rangle_j &= -(\Gamma_{\text{dec}} + i\Delta) \langle \hat{\sigma}^- \rangle_j - ig_j(t) \langle \hat{a} \rangle \langle \hat{\sigma}^z \rangle_j, \\ \langle \dot{\hat{\sigma}}^z \rangle_j &= -\gamma (\langle \hat{\sigma}^z \rangle_j + 1) - 2ig_j(t) (\langle \hat{a}^\dagger \rangle \langle \hat{\sigma}^- \rangle_j - \langle \hat{a} \rangle \langle \hat{\sigma}^+ \rangle_j). \end{aligned} \quad (4.19)$$

Because we ignore all cross-correlations between different j as well as between atoms and cavity field, $\langle \hat{a} \hat{\sigma}_j^+ \rangle$ this leaves us with a total of $2N + 1$ equations. In [112], [120] these are used to derive expressions for the steady-state frequency-dependent transmitted power and phase shift relative to the input field.

$$\begin{aligned} \frac{P_{\text{out}}}{P_{\text{in}}} &= \left| \frac{-i\langle \hat{a} \rangle}{\eta/\kappa} \right|^2 \\ \phi &= \arg \left(-i\langle \hat{a} \rangle \frac{\kappa}{\eta} \right), \end{aligned} \quad (4.20)$$

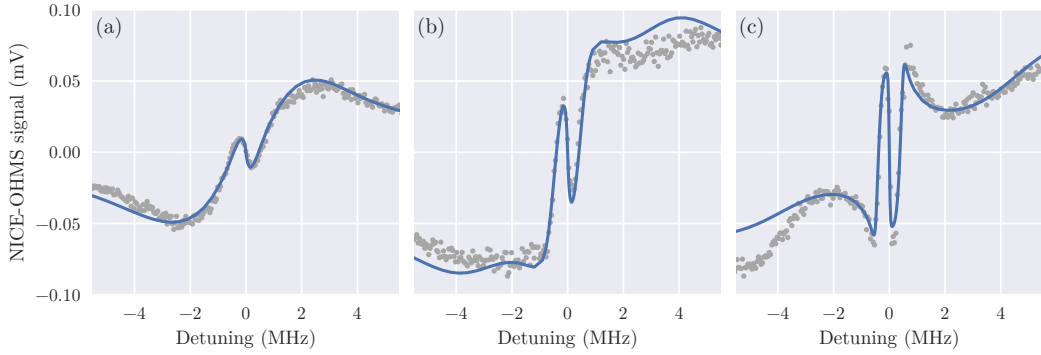


Figure 4.7: Dispersion signals crossing over to the non-linear cavity response region. Gray dots are experimental measurements, whereas full blue lines are theoretical curves. We vary the atom number by reducing the atomic cooling time. (a) For an atom number of $N = 3.8 \cdot 10^6$ and an estimated temperature of $T = 16$ mK, the dispersion signal behaves almost linearly with respect to atomic phase shift. The amplitude of the Doppler dispersion is squashed slightly. (b) For a slightly lower temperature of $T = 13$ mK, and an atom number of $N = 1.4 \cdot 10^7$, the Doppler phase shift reaches the dispersion limit of the cavity. This results in a dispersion shape which is very different from the sum of derivatives shown in figure 4.3. (c) At even higher atom number $N = 4 \cdot 10^7$, and $T = 13$ mK, the dispersion limit has been crossed. This results in an apparent inversion of the Doppler phase peaks. While the peaks of the saturation feature are also starting to flatten out, the effect is less visible here. Adapted from [99].

inserting (4.16) we obtain for the output power:

$$P_{\text{out}}(\omega_l) = \kappa \hbar \omega_l |\langle \hat{a} \rangle|^2. \quad (4.21)$$

The resulting behavior is found using both a numerical approach, and a semi-classical Floquet analysis. Both approaches are seen to agree well with each other. These results pertain only to the part of the field that interact directly with the atoms. The frequency sidebands that are essential to the NICE-OHMS detection method are assumed to have negligible interaction.

4.5 Beyond the linear regime

We can now look at the recorded dispersion signals from the experiments and compare them with our theoretical considerations. In figure 4.7 we show the dispersion feature of the atom-cavity system as the atom number within the cavity mode – and thus the total phase shift – is varied. While the signal is obtained as we describe in section 4.3, the theoretical curves are plotted by fitting the temperature and atom number within the experimental uncertainties.

In these measurements the ensemble temperature is slightly higher than usual, with a fitted value of $T = 13$ mK. We vary the atom number experimentally by decreasing the cooling time, and thus the number of loaded atoms. However, it seems that this results in an increased temperature for very short loading times, and for figure 4.7 (a), the temperature is thus at $T = 16$ mK. The fitted atom numbers are $N = 3.8 \cdot 10^6$, $N = 1.4 \cdot 10^7$ and $N = 4 \cdot 10^7$ respectively, and the

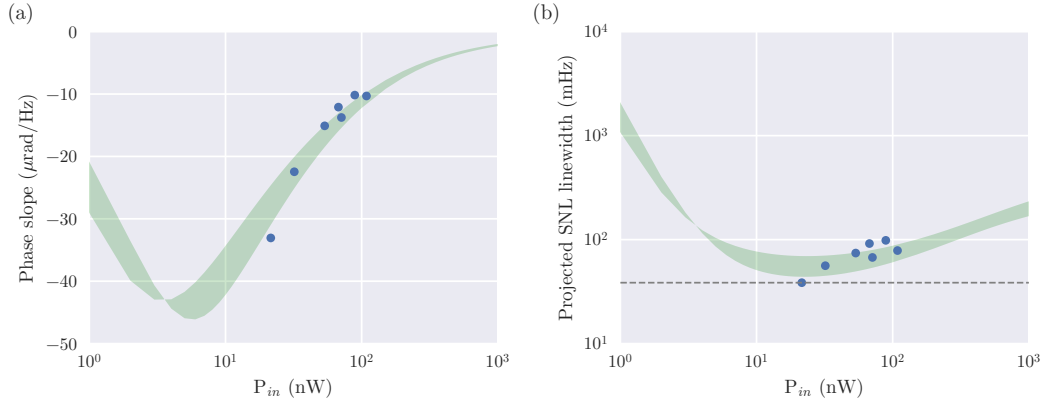


Figure 4.8: **(a)** Phase slope at resonance, with theoretical bounding curves corresponding to $N = 2.7 \cdot 10^7 \pm 5 \cdot 10^5$ and $T = 4 \pm 1$ mK. Blue dots indicate phase slope values of experimental measurements with appropriate probing powers P_{in} . **(b)** Projected shot-noise-limited (SNL) linewidth of a laser locked to the NICE-OHMS signal. This plot shows the values in (a) transferred using equation (4.22). The minimal spectral width obtainable from a laser locked to this system is suggested by experiment to be a shot noise limited linewidth of $\Delta\nu = 40$ mHz. Adapted from [99].

probing power is $P_{in} = 180$ nW. The temperatures results in FWHM linewidths of $\Gamma_D = (4.2, 3.8, 3.8)$ MHz, and the power causes significant saturation broadening.

At low atom numbers the dispersion feature looks much like we would expect from the naive approach of figure 4.3, with a signal that is the sum of Doppler and saturated dispersions. At medium atom number the folding of the atomic and cavity dispersions causes a flattening of the Doppler feature around a detuning of $\Delta_{ce} = \pm 1$ MHz. This limits the maximal dispersion signal to around 0.8 mV. Finally in figure 4.7 (c), the atom number is sufficiently high that the phase response of the atoms is much larger than the linear range of the cavity dispersion, and the Doppler dispersion peaks seem to be flipped around some maximal signal amplitude. While the non-linearity at high phase-shifts is clear, the slope at resonance remains unchanged. As we shall see below, the effect can limit the peak-peak width of the central linear regime as the phase shift of the saturation feature also crosses the limits set by the cavity. This will in turn limit the dynamical range of a locking servo, as the frequency detuning range where one can expect a linear response decreases.

4.5.1 Projected frequency stability

Focusing first on the dispersion slope at resonance, we can find the phase slope from our theoretical curves as a function of the input power P_{in} . Such a dependency is shown in figure 4.8 (a). The plot includes seven data points that have been taken under similar experimental conditions. The variance in temperature $T = 4 \pm 1$ mK and atom number $N = 2.7 \cdot 10^7 \pm 5 \cdot 10^5$ has been used to find the extremum cases bounding the shaded region.

The phase slope is negative for most values, but becomes positive for $P_{in} \rightarrow 0$ as the atomic ensemble is no longer saturated and the Lorentzian dispersion

disappears. For very high input powers the saturation broadening causes the feature to flatten out and go to zero. Optimum power is on the order of $P_{in} = 5$ nW and lies just below the stable regime of our cavity lock. This seems like an issue at first glance, but would have put us in a regime where the SNR of the signal would be limited by the photonic shot-noise on the detector. From [67], [120] we can write an expression for the shot-noise-limited (SNL) linewidth of a laser stabilized to our dispersion signal.

$$\Delta\nu = \frac{\pi h\nu}{2\eta_{qe}P_{sig}} \left(\frac{d\phi}{d\nu} \right)^2 \left(1 + \frac{P_{sig}}{2P_{ref}} \right). \quad (4.22)$$

In our case the signal is the carrier power $P_{sig} = P_0$ and the reference is the first order sideband $P_{ref} = P_1$. The phase slope at resonance is given by $\frac{d\phi}{d\nu}$ and the quantum efficiency of the detector η_{qe} will be assumed to be unity for the moment. Applying this expression to the phase-slope results in figure 4.8 (b). Here we see that the functional form has changed significantly, as low input powers causes low output powers. This means that the shot noise will limit the attainable linewidth for an input power below $P_{in} \sim 10$ nW. At this level the linewidth stays approximately constant over a whole decade leading to power levels that are much easier to deal with experimentally. The lowest-lying point we have corresponds to a SNL linewidth of $\Delta\nu = 40$ mHz. This is at a very interesting level, where only few lasers have ever been realized [6], [48], [50]. Since our paper on this approach [99] was published in 2017, the world record has been pushed down by another order of magnitude [68], [92], [127].

4.5.2 Dynamical locking range limitations

For any real lock, noise in the system leads to probing of the error function away from atomic resonance as well. This means that the locking range, within which the slope of the error signal is constant, becomes an important factor for the robustness of the lock. We denote this as the dynamical locking range of the error signal, and define it mathematically as the range for which the sign of the slope is unchanged. For the parameters we saw in figures 4.7 this range is defined by the power broadened linewidth of the of the transition, as well as the Doppler width. The Doppler dispersion causes a pulling of the saturation dispersion feature as illustrated in figure 4.3. So for lower temperatures, the slope at resonance increases while the dynamical range is reduced [120]. As the phase-shift increases, we enter a regime where the power broadening no longer sets the limitation on the dynamical range.

In figure 4.9 (a) we plot the dynamical range as a function of atom numbers for an ensemble temperature of $T = 2.5$ mK and an input power of $P_{in} = 100$ nW. Three representative shapes of the dispersion signal are shown in figure 4.9 (a), with corresponding dots marked on 4.9 (a). Notice that we plot only the saturation dispersion feature here, and cannot see the full Doppler-broadened dispersion.

For an atom number of $N = 2.4 \cdot 10^7$ the saturation dispersion shape is only slightly distorted, and almost sinusoidal in behavior. The position of the extrema are essentially unchanged, resulting in a dynamical range of $\Delta_{dyn} \simeq 180$ kHz. As the atomic phase shift increases beyond the cavity limitation, an inversion of the

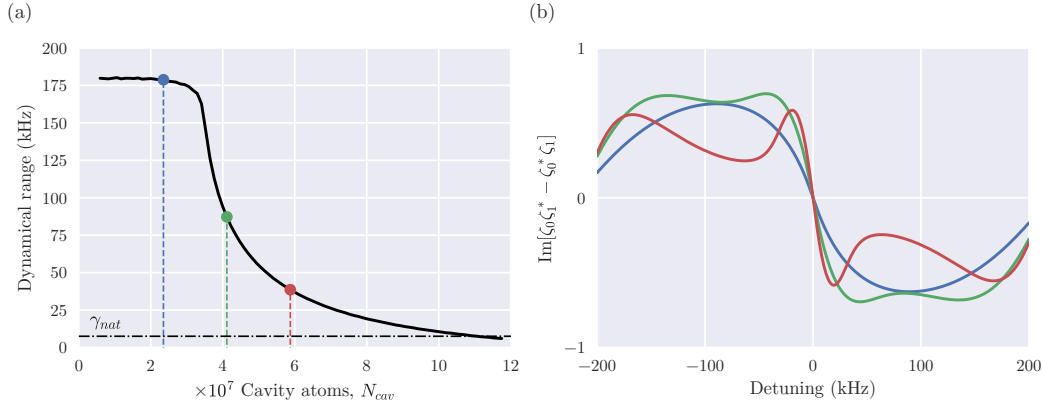


Figure 4.9: Limitations on the dynamical locking range of the dispersion signal. At high atom numbers the amplitude of the saturation dispersion feature increases beyond the cavity dispersion limitations. This results in a reduced linear range for frequency locking. **(a)** The full width of the dynamical locking range as a function of atom number. Above a threshold of $N = 3 \cdot 10^7$ atoms the dynamical range decreases. Even for a large initial power broadening of 180 kHz, the range eventually decreases below the natural linewidth of the transition. **(b)** Example curves showcasing the three levels marked by dots in (a). Only the central saturated dispersion feature is shown, for $N = 2.4 \cdot 10^7$ (blue), $N = 4.1 \cdot 10^7$ (green) and $N = 5.9 \cdot 10^7$ (orange) respectively. Adapted from [99].

dispersion signal occurs, resulting in a sudden drop in the dynamical range and a subsequent decrease towards zero. At an atom number of $N = 4.1 \cdot 10^7$ this inversion is just visible, resulting in two maxima rather than a single one for negative detuning. As the number of atoms reaches $N = 5.9 \cdot 10^7$ the inversion is very clear, and the dynamical range has dropped to around $\Delta_{dyn} = 40$ kHz. As we expect, the slope at resonance continues to increase. While the cavity dynamics does cause the sign of the phase-slope to flip, the sign of the phase itself will never change.

4.5.3 Cavity lock effects

In section 4.3 we assumed an ideal cavity lock, which resulted in the perfect transfer of phase information from the carrier frequency to the sideband field components. In any physical system we expect the cavity to have a finite response time which might result in deviations from the simple case of a purely real-valued ζ_0 .

Particularly, our experimental system relies on a cyclic operation in which a long loading time of up to $\tau_{load} = 800$ ms is followed by a much shorter interrogation time of $\tau_{probe} = 100$ μ s. As such, the cavity is not necessarily in a steady state when the atoms are probed, and we do not necessarily fulfill equation (4.9). If we write a general expression for the cavity phase

$$\begin{aligned}
 \phi_{cav}(\omega) &= n\pi - \phi_{init}(\omega) \\
 \phi_0(\omega) &= n\pi + \phi_D(\omega) + i\phi_A(\omega) - \phi_{init}(\omega) \\
 \phi_j(\omega) &= (n+j)\pi - \phi_{init}(\omega) \quad \text{for } j \neq 0,
 \end{aligned} \tag{4.23}$$

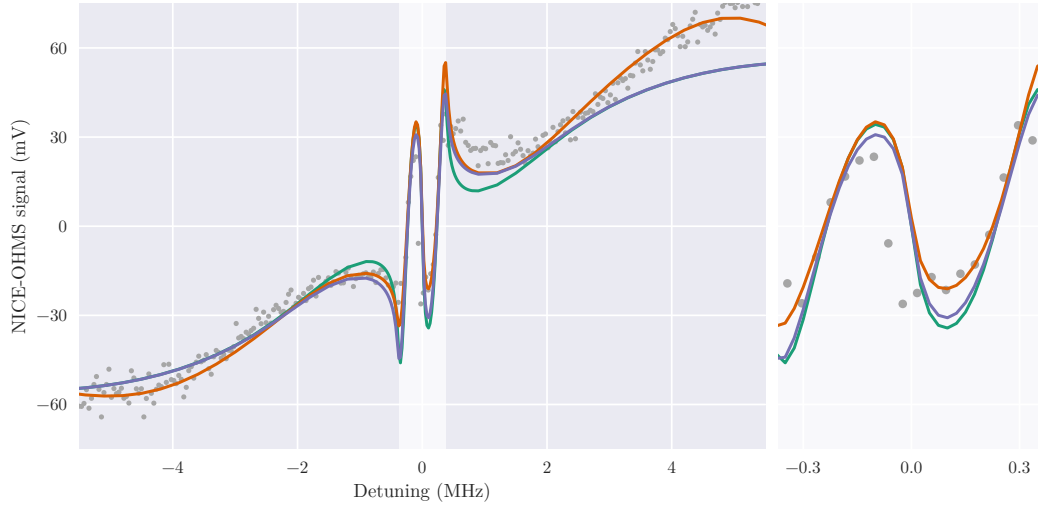


Figure 4.10: Sensitivity of the dispersion signal to the locking conditions of the cavity. We show an example scan of the dispersion feature (gray dots), with three separate theoretical curves, corresponding to varying conditions on the initial phase of the cavity $\phi_{cav}(\omega)$. In the case where the cavity-lock is independent on the presence of the atoms, $\phi_{cav}(\omega) = 0$, we obtain the green curve. Here the features are accentuated, as the atomic phase information will remain on the carrier frequency. If the cavity length follows the effective length with atoms included, $\phi_{cav}(\omega) = \phi_D(\omega)$, we obtain the blue curve. Here all atomic phase-information is transferred to the probe laser sidebands. The case where the cavity lock is not in a steady state, but has corrected for the phase response of atoms subjected to cooling lasers is shown in orange. Here a phase $\phi_{cav}(\omega) = \phi_{MOT}(\omega)$ is written on all frequency component of the probing laser. This condition causes an asymmetric dispersion signal due to the AC Stark shifted ground level under influence by the cooling beams. The side panel shows a zoom of the central saturation dispersion feature. Adapted from [99].

We can denote different cases by the value of the initial phase. In the ideal case described above, the cavity is fast, and follows the atom dynamics. This results in an initial phase of $\phi_{init} = \phi_D$ as per equation (4.9). If the cavity response is infinitely slow, we have an initial phase $\phi_{init} = 0$, and the cavity length follows that of the vacuum wavelength of the laser field. The most experimentally realistic case is an initial phase that can be close to the atomic dispersion but is modified by the fluctuations of the system.

In the present case, these phase fluctuations are highly predictable as the cavity is locked to the atom-trap system most of the time. When the trapping and cooling light is on, atoms are present inside the cavity, but the ground state of the atom will be shifted significantly due to the AC Stark shift caused by cooling beams. We can then write $\phi_{init} = \phi_{MOT}$. Whether we are dealing with an atom-independent lock, or a lock to some other phase $\phi_{init} \neq \phi_D$, the atomic dispersion will remain on the carrier component rather than being written onto the sidebands. On the other hand all frequency components j will have the initial cavity phase written onto them, as shown in equations (4.23).

This non-equilibrium case should be taken into account when calculating the semi-classical atom-field interaction. If the modification of the system is small, however, we can approximate the response to first order by simply adding in

the additional phase-shift manually. We show this for the three different initial conditions in figure 4.10. Here we show a dataset, and theoretical curves for $T = 2.8$ mK, $N = 2.5 \cdot 10^7$ and an input power of $P_{\text{in}} = 115$ nW. The blue, dashed curve corresponds to the ideal case of an infinitely fast cavity lock, the green curve is the atom-phase-independent cavity lock, and the orange corresponds to an initial phase set by the AC Stark shifted atomic ensemble ϕ_{MOT} .

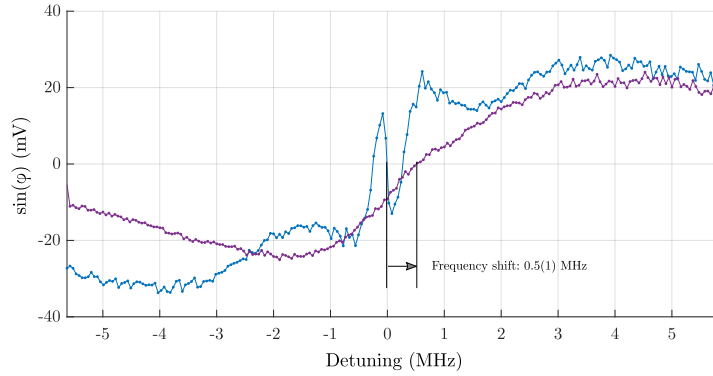


Figure 4.11: Dispersion features with (blue dots, orange line) and without (purple dots, yellow line) the cooling light on. We see that the scattering of cooling light causes the saturation feature to almost disappear and reduces the total amplitude of the Doppler dispersion. It also adds an AC Stark shift of about 0.5(1) MHz when measured against the fit, and with uncertainties derived from experimental variations over a number of different measurements. The purple dots are averages over four measurements. The red curve is a Gaussian derivative fitted to the dispersion with MOT light on. Some asymmetry is visible for large detunings, which could be caused by nonlinear AOM behavior.

The phase-shift ϕ_{MOT} from a cavity locked to atoms subjected to the cooling beams can be evaluated quite well. In order to measure this, we can make a similar phase-measurement, but leave the cooling beams on. See figure 4.11. In this case the steady-state assumption is fulfilled. This results in an approximately Gaussian dispersion feature with only a faint trace of saturation. Most importantly an AC Stark shift of about $\Delta_{ac} = 0.5$ MHz shifts the distribution, and breaks the symmetry of the response. The experimental AC Stark shift uncertainty is estimated from the measurement noise. We can find the expected shift using the dipole potential of the laser field as: [76]

$$\Delta_{ac} = \frac{\Delta E_i}{h} = \frac{3\pi c^2}{2\omega_0^3} \gamma \frac{-\Delta}{\Delta^2 + \left(\frac{\gamma}{2}\right)^2} I = 0.6 \text{ MHz}. \quad (4.24)$$

Here we have assumed that the laser detuning, Δ , is much larger than the transition linewidth, γ . We consider only the perturbation to the ground state due to the $^1S_0 \rightarrow ^1P_1$ transition at ω_0 , and thus use the associated values.

There is qualitatively very little difference between the three cases close to resonance. Notably the atom-phase-independent lock has sharper features, with a “deeper” inverted Doppler dispersion. The implementation of an initial cavity phase of ϕ_{MOT} results in an asymmetric behavior that agrees quite well with the

experiment - this is especially visible for large detunings $\Delta\nu > 2$ MHz. Figure 4.10 (b) shows a zoom on the saturation feature showcasing the asymmetry at low detunings.

4.6 Frequency stability

By using the dispersion signal as an error signal in a feedback loop, we can lock the frequency of the probe laser to the atomic transition. The current realization of the system is not optimized for this use. It has a long cycle time compared to the interrogation, which means that there will be a significant dead time when stabilizing the laser frequency. Dead time causes noise through the Dick effect [119], where undetected laser noise limits the effectiveness of the lock. The cooling laser causes fluctuations of atom number and temperature, which results in a noisy error signal. We have nevertheless made a first attempt at locking the probing laser frequency to show the feasibility of the approach.

We set up the system to run with a reduced cycle time of $\tau_0 = 200$ ms, and an increased probing time of $\tau_{probe} = 1$ ms. By removing some of the wait-time in the cycle we retain a sufficiently large atom number to be deep in the non-linear dispersion regime. The probing power is set to $P_{in} = 275$ nW resulting in a highly power-broadened saturation dispersion feature. In figure 4.12 (a) the dispersion signal for those parameters is shown. At the time these measurements were taken, we did not have the reference laser of chapter 3.2, so an out-of loop measurement of the system was not possible. This means that the only way of evaluating the system performance is the in-loop measurement of the error signal value.

Since this is the reference signal used in the lock, any common-mode noise there might be between probe-laser and atomic ensemble will not be measured. Any drift of the atomic reference or noise within the locking bandwidth, will not be detected either. The measurements thus serve primarily as a proof-of-principle, and as a first approach to identifying technical limitations of the system. Since the reference signal is measured as a voltage we use the scan over the dispersion signal in figure 4.12 (a) in order to estimate a conversion factor from voltage to frequency. We find this conversion in figure 4.12 (b) by numerically differentiating the dispersion signal in figure 4.12 (a). In order to reduce the noise on the differential signal, we calculate a running mean over five-point sets of the dispersion signal. In figures 4.12 (a) and (b) the measured values are shown as blue dots, whereas the running mean and its differential signal are shown in orange. At zero detuning, the maximal slope is found to be 518 mV/Hz. Using this value we obtain the time-series of frequency deviations shown in figure 4.12 (c).

We lock the probe laser for over two hours, and plot the Allan deviation of the measured frequency deviations in figure 4.13. The laser frequency is locked by an exclusively integrating servo, with a gain of 0.8. As one might expect from the width of figure 4.12 (c) the stability for an averaging time of $\tau = \tau_0$ is about $\sigma = 2$ kHz. As the averaging time increases we expect the frequency deviations to decrease, since drift and random walk of the reference is not detected with our measurement. Interestingly we see that the Allan deviation decreases as $1/\tau$ for times $1 \text{ s} \leq \tau \leq 100 \text{ s}$. This indicates that we are limited by phase-noise in this

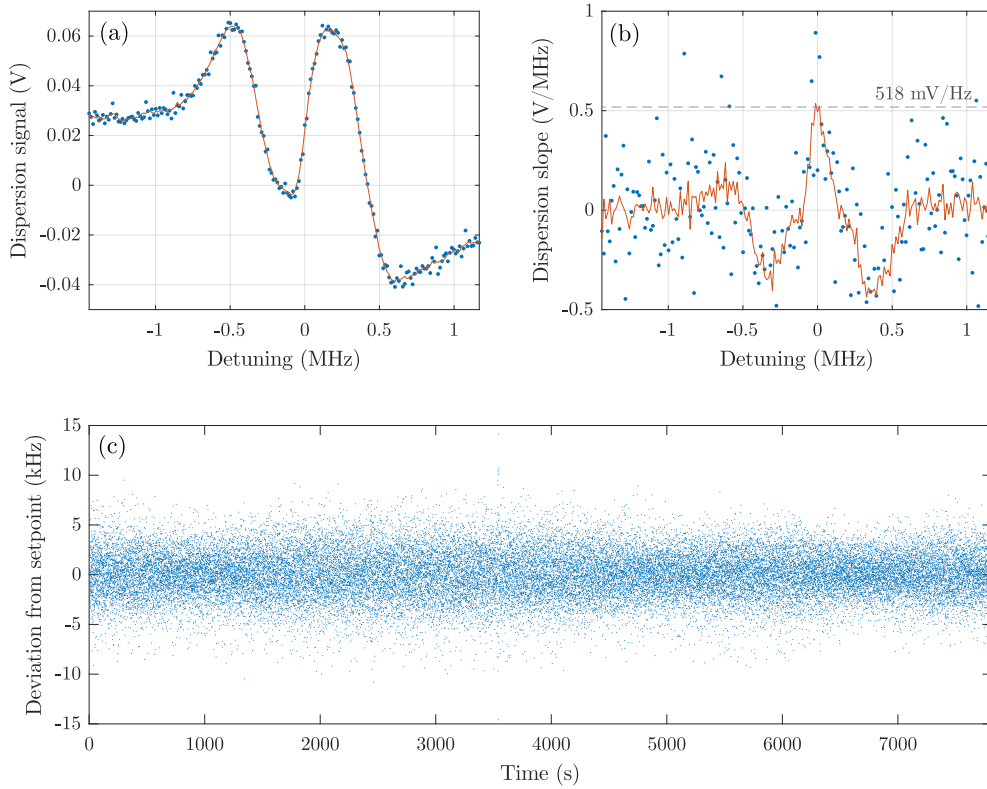


Figure 4.12: Data analysis of NICE-OHMS locking signal. The dispersion signal is used to find the voltage-to-frequency conversion factor necessary to interpret the measured error signal during locking as an effective frequency deviation of the probing laser. (a) The dispersion signal as a function of laser-atom detuning. A highly asymmetric dispersion signal in the deeply nonlinear phase regime. The saturation dispersion feature exhibits a linear frequency response between $\Delta\nu = \pm 100$ kHz, which is suitable for frequency locking. The signal is offset from zero by about 30 mV. Blue dots show the measured points, whereas the orange curve is a five-point running mean. (b) A numerical differentiation of the dispersion signal yields the conversion factor. We show the numerical differentiation of both the raw dispersion data (blue), and the numerical differentiation of the five-point running mean of the dispersion signal (orange). Using the maximal slope of the averaged dispersion, we find a conversion factor of 518 mV/Hz. (c) Using the conversion factor we can calculate a relative frequency deviation for each experimental cycle.

regime rather than white frequency noise as we see for longer times where the Allan deviation decreases as $1/\sqrt{\tau}$.

The phase noise is a sign that we are limited, not by the efficiency of the locking servo, but rather by noise in reference signal. Indeed this might be expected from the poor SNR we have observed when mapping out the dispersion signals. The white frequency noise level that we reach after $\tau = 100$ s is at $\sigma_{\text{white FM}} = 201 \text{ Hz}/\sqrt{\tau}$ which is somewhat higher than what we see from the prestabilized laser itself, see chapter 3.2. This is another sign that the limiting factor here is the reference signal. After 25 minutes of averaging the fractional frequency stability is at 10^{-14} , corresponding to 5 Hz in absolute stability.

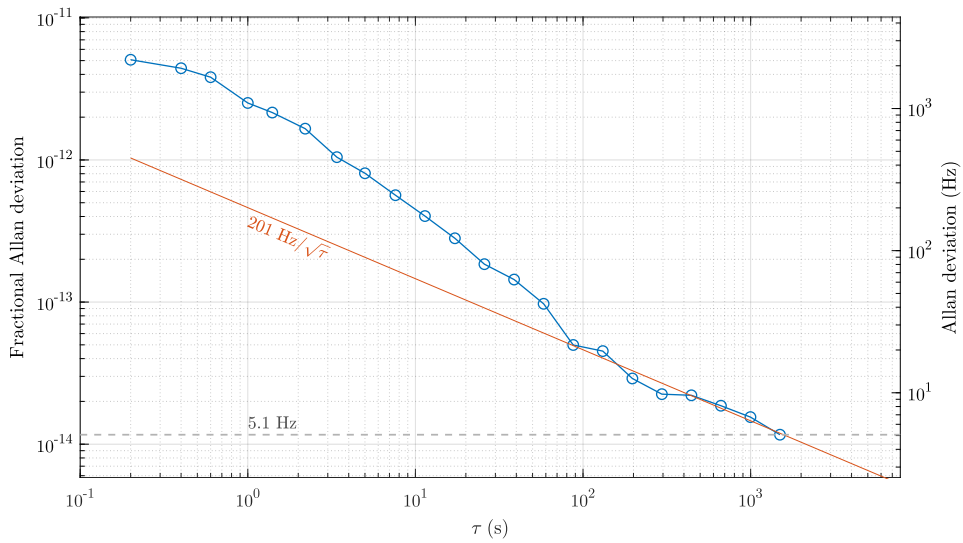


Figure 4.13: Allan deviation of the in-loop frequency measurements found in figure 4.12. The noise initially scales as phase noise, but reaches a white frequency noise floor around $\tau = 100$ s. The full measurements lasted for over two hours, and we see that we reach a fractional frequency stability level of 10^{-14} after 25 minutes. Because this is an in-loop measurement, drift of the reference frequency, as well as common-mode noise between probing laser and reference signal is not detected, and the true frequency instability of the system is likely larger.

Though we have shown that we can lock the probe laser frequency with the current signal, we expect significant improvements to the performance can be made by improving the SNR of the dispersion signal, reducing the probing power, increasing the fractional probing time in order to reduce the Dick effect, as well as optimization of the servo parameters.

A PULSED LASER IN THE CROSSOVER REGIME TO SUPERRADIANCE

Contents

5.1	Gain in an unconfined cold ensemble	60
5.1.1	Considerations for the excitation pulse	62
	Coherence scrambling	64
	Optimal excitation	64
	Technical noise and instabilities	65
5.2	Atom-cavity interaction	66
5.2.1	Expected lasing regimes	68
5.3	Lasing pulses	70
5.4	Lasing threshold	71
5.5	Time-evolution of the lasing pulses	73
	Randomly varying phase	75
	Killing the coherence	75
5.6	Seeded lasing	77
	Phase seeding	77
	Delay times under stimulated emission	77
	Amplifier properties	78
5.7	Spectral properties	80
5.8	Frequency stability	84

Generating laser light has become technically simple with the advent of diode lasers. Lasers for frequency stabilization are designed to be flexible in terms of frequency tuning and emission power. This is important if you want to be able to correct the frequency efficiently, and in that way reduce the inherent noise or drift

of the laser spectrum. However, highly adjustable lasers are only necessary because their spectral performance is insufficient by default.

In the perspective of atomic clocks, the insufficiency of classical lasers is primarily caused by two things: their frequency accuracy is very low, and they are prone to frequency drifts. One way to circumvent these issues is to build a laser that operates in a very different regime from classical lasers [17]. Characterizing lasers by their primary physical constituents: a gain medium and an enhancement cavity, the relation between the respective linewidths of these constituents greatly influences the lasing behavior. In the classical laser, the spectral width of the gain medium $\Delta\nu_G$ is typically broad compared to the linewidth of the enhancement cavity κ . This places these types of lasers in what is sometimes referred to as the “good-cavity” limit $\frac{\Delta\nu_G}{\kappa} \gg 1$ where the characteristic lifetime of a photon in the cavity is much greater than the lifetime of an excitation in the gain medium. At the other end of this scale we find the “bad-cavity” limit where the spontaneous emission rate of the gain medium is much smaller than the cavity decay rate. In this limit, the photons emitted into the lasing mode will be lost to the environment much faster than we would see the appearance of another spontaneously emitted photon from the gain medium into the cavity mode. This has also been called an “almost light-less laser” [116].

For a suitably chosen gain medium we can obtain a laser that is inherently accurate, and stable. This is achieved, e.g., by choosing one of the atomic transitions that might be traditionally used as the reference transition in an atomic clock. Direct laser generation on such a transition constitutes the essential part of an active optical clock [17], [73], [80], [98], where a well controlled environment will remove the need for externally controlling the frequency of the system. The high level of drift typically present in laser gain is thus suppressed in the gain medium. Another important source of frequency noise comes from the the cavity length fluctuations. Even highly engineered and stabilized reference cavities are limited by such length noise [21], [82], [92]. By placing the system in the bad cavity regime, such cavity noise is suppressed.

After an introduction to the experimental gain medium we will use here, we discuss the theoretical background for atom-cavity interaction in the context of superradiance. The experimentally realized measurement of lasing threshold in our system is characterized, and an investigation of the time evolution of a lasing pulse is performed. Subsequently we look at the spectral properties of these laser pulses, and attempt to characterize their initial frequency stability using the reference laser presented in chapter 3.2. We show that the system is on the limit between the good- and bad-cavity regimes, and find that the characteristics of the system change from one scaling to the other as we vary the number of atoms. Our experiments here thus place us in the crossover regime between classical lasing and superradiant lasing. This chapter is partially based on work presented in [100].

5.1 Gain in an unconfined cold ensemble

We use the experimental system described above with atoms trapped and cooled in a 3D MOT. By overlapping the trap center with the fundamental mode of an optical

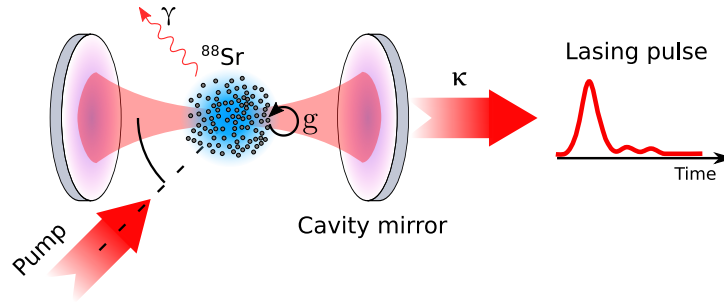


Figure 5.1: Schematic overview of the atomic ensemble coupled to a mode of an optical cavity. The atoms decay spontaneously with a rate γ and couple to the cavity field with the rate g . κ gives the decay rate of the cavity field to the environment.

cavity, we enable atom-to-atom coupling mediated by the cavity field. In figure 5.1 this system is shown schematically. The atoms can be excited from a pumping beam that is not coupled to the cavity mode, but incident from an angle of 45° . The atoms are then left in the excited state, where they decay spontaneously with a rate of γ , or couple to the cavity mode with a coupling factor g . The cavity field leaks out through the end mirrors with a rate κ .

For a very dense sample, interactions between atoms mediated by, e.g., dipole-dipole forces has to be taken into account. Here, we can trap up to $N = 10^8$ atoms, giving a peak density of $\rho_{max} \approx 1.2 \cdot 10^{10}$ atoms/cm $^{-3}$. The ensemble is sufficiently dilute that these forces are not relevant.

The gain medium for a conventional laser is typically spectrally wide, which ensures some level of tunability, as well as strong interaction between the lasing medium and the filter cavity. The spectral features of the laser are then narrowed by ensuring damping of most of the spectrum, which allows the lasing band to become highly amplified. This damping can happen intrinsically in a cavity which ensures that only resonant modes are allowed, or using an additional spectral filtering, e.g., in the form of a grating or an interference filter as in section 3.1.1. The gain medium acts only to amplify the radiation, whereas the spectral characteristics are determined by the interference components of the setup. Figure 5.2 shows a conceptual understanding of the good cavity regime contrasted to the bad cavity regime.

The bad cavity regime also supports lasing, but in some sense flips the role of gain medium and cavity. Here the gain medium is spectrally more narrow than the enhancement cavity. This means that emission of radiation simply cannot happen outside of the narrow range set by the gain medium, and the spectral properties of the cavity will be suppressed by approximately the ratio between the resonance linewidths $\xi = \frac{\Gamma}{\Gamma + \kappa}$. The system then becomes highly sensitive to the control of frequency noise in the gain medium, but insensitive to, e.g., noise in the length of the cavity.

For typical physically realizable systems the cavity linewidth can range from few kHz to tens of GHz, whereas the gain medium has a much wider range from

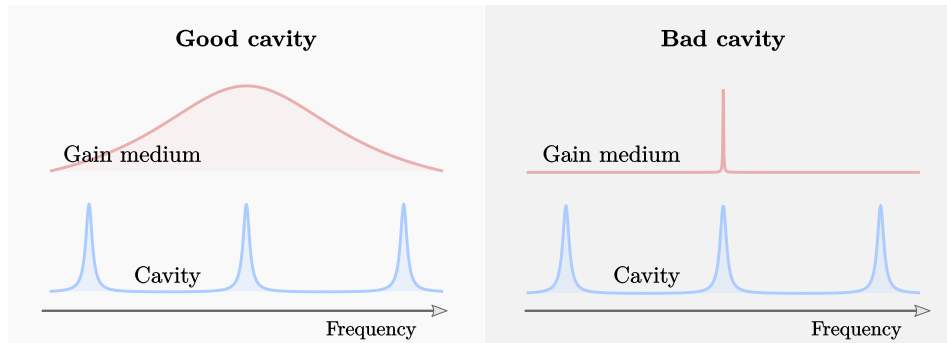


Figure 5.2: The good cavity and bad cavity regimes are named after the relative Q -values of the cavity and gain medium resonances. Here we illustrate the regimes with identical spectral linewidth for the cavity resonance to underline this fact. A bad cavity system could thus equally well be referred to as a narrow gain system.

solid state systems with widths of several tens of THz to narrow atomic transitions on the order of mHz [73]. This means we can choose a gain medium such as a narrow atomic transition, and take advantage of the well-defined spectrum this gives us.

Assuming perfect inversion in the system, the laser gain factor becomes proportional to the number of emitters N and their coupling rate to the lasing cavity g . For samples of cold atoms, the achievable atom number is often inversely proportional to the temperature of the atoms, and whereas we obtain samples of order 10^8 at mK temperatures, moving to hundreds of nK often results in a limitation of order 10^4 [70]. This is a very low atom number compared to solid state diode lasers which might have on the order of 10^{22} emitters. The narrow spectral features of the atomic transition, is a direct consequence of long lifetimes, and as a result the coupling rate to the cavity mode will be small as well. Typically, then, we can expect a much lower photon number both in the cavity and in the emission of bad cavity lasers based on cold atom systems.

5.1.1 Considerations for the excitation pulse

Since our experimental scheme relies on atoms initially in the excited state, we want to ensure a maximal number of atoms are pumped to that level. The phenomenologically most simple way to do this is a pi-pulse. A pi-pulse is a coherent excitation where resonant light interacts with an atom for a time t sufficient to place the atom in the excited state, according to equation (2.11). The decay rate of the atom will cause the Rabi oscillations to reduce in amplitude, and for an inversion close to 1, t needs to be much faster than the characteristic decay time of the energy level $1/\gamma$. By increasing the pumping power the Rabi frequency can be increased in an attempt to fulfill this requirement. A short excitation pulse causes a Fourier limited frequency linewidth of the excitation pulse, which in our case is approximately $\Delta\nu_{\text{Fourier}} \approx 0.9$ MHz, much broader than the natural linewidth of the atoms. Longer pulses reduce the excitation efficiency because of the decoherence rate of the collective atomic dipole. This decoherence rate is given by the inhomogeneous Doppler

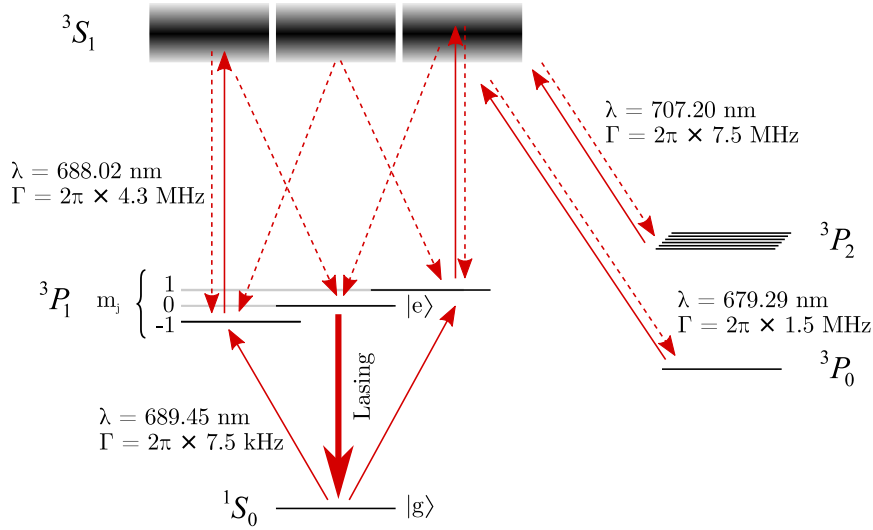


Figure 5.3: Incoherent excitation and repumping scheme that can be used to generate continuous lasing on the $^3P_1 \rightarrow ^1S_0$ transition without the need for accurately timed pulses. Due to decay from the 3S_1 levels to the remainder of the 3P manifold, the MOT repumping lasers at 679 nm and 707 nm are required to avoid substantial atom loss. Dashed lines indicate spontaneous emission, while full lines indicates pumping/repumping. Natural linewidths are indicated. The figure is not to scale.

broadening, $\Gamma_D = 2$ MHz, rather than the natural decay rate of the excited state.

Because some dephasing of the collective dipole will always be present during pumping, no coherent excitation can bring the entire ensemble to the fully excited state. If we consider a Bloch sphere of ensemble excitation some finite component along the equatorial plane will always be present as a phase written from the excitation laser to the atomic state. In addition to the average excitation being less than unity, the superposition state of a given atom will be both velocity- and position-dependent. In order to investigate a system whose subsequent evolution is completely independently of the pumping laser phase, we would prefer to avoid such phase-coherence. This can be done by ensuring that the excitation happens incoherently, e.g., via spontaneous decay from a higher-lying energy level. Such a scheme is in principle possible in our system, but inaccessible in our current experimental setup. A scheme was suggested in [81], and requires the use of the additional 688 nm laser as shown in figure 5.3. By applying a static magnetic field, the Zeeman levels of the 3P_1 state are no longer degenerate, and can be addressed individually. Choosing either of the $m_j = \pm 1$ states and using the 688 nm laser to further excite the atoms to the 3S_1 state allows spontaneous decay into the 3P_1 $m_j = 0$. This causes an inversion relative to the ground state, and a random phase of the atomic dipoles.

While we do use simple coherent pumping here, three effects wash out the possible coherence our atoms are prepared with: the inhomogeneous Doppler broadening, the incidence angle of our pumping pulse, and a cleaning pulse we apply after the pumping.

Coherence scrambling

In the case of an ensemble of atoms at finite temperatures, the Doppler shift of atomic resonance frequencies causes variable Rabi frequencies throughout the ensemble, and a reduction in the average excitation ratio follows. Along the pumping axis, this effect thus reduces the efficiency of our excitation – in particular for fast atoms. Since we do not pump along the cavity axis, but at a 45° angle (see figure 5.1) the effect parallel to the cavity-axis is different. Atoms with high velocities along the pumping axis do not necessarily have high velocities along the cavity axis. Velocity selective pumping is thus not very efficient. The variable speeds along the cavity axis means that the individual coupling efficiencies of the excited atoms to the cavity field is quickly scrambled. This can be seen from the term ζ_{LM}^j in equation (2.13).

For the case of stationary atoms, the 45° angle of the pumping beam with respect to the cavity axis further distorts the phase relation between the two. Since the pumping field and cavity mode has the same frequency, projecting the pumping field phase on the cavity axis scales the spatial evolution by a factor $\sqrt{2}$. In figure 5.4 (a) it can be seen that the phase-overlap between two such sine functions is quite poor. Plotting the two functions against each other in a parametric plot allows us to test the volume of phase-space that is mapped out. In figure 5.4 (b) this relation is seen to quickly maps out the entire phase space after only 20.5 wavelengths, and subsequently never overlaps with itself. Over the pumping beam size of about $2 \cdot 10^3 \cdot \lambda$ the phase space will thus essentially be completely filled. This effect means that the initial coherences along the cavity axis will not in general coincide with the cavity mode.

In addition we apply a short pulse of 461 nm light after the pumping pulse. Atoms in a superposition between ground and excited (3P_1) state will thus be projected onto either state, as ground-state atoms are cycled on the broad cooling transition $^1S_0 \leftrightarrow ^1P_1$. This "decoherence" pulse is delivered by the six MOT beams, and is thus detuned by $\Delta\nu = -41$ MHz and has an intensity of about 12 mW/cm². This is insufficient to saturate the transition, but for a pulse time of $\tau_{dec} = 500$ ns an average of about 1.4 photons per atom is scattered. This estimate assumes stationary atoms, whereas the finite ensemble temperature and omnidirectional beams, will effectively increase the scattering rate. Our pumping sequence is shown in figure 5.5.

Optimal excitation

The pumping sequence starts out with a cooling sequence lasting as little as $\tau_{MOT} = 50$ μ s. The cooling beams are turned off to allow atoms to decay into the ground 1S_0 state with a characteristic time of $\tau = 5$ ns. A strong pumping pulse with a power of $P_{pump} = 100$ mW drives the atomic ensemble for $\tau_p = 170$ ns to a maximal excitation of about $\eta_{MOT} = 55$ % limited primarily by the large dimensions of the total atomic ensemble with respect to the pumping pulse. If we consider only the atoms within $2w_0$ of the cavity mode, this number increases by 150% to about $\eta_{cav} = 85$ %. The decoherence pulse is then applied, and the ensemble is subsequently left to evolve freely for 10 – 20 μ s, before the cooling light is applied once more and the cycle starts over.

Figure 5.6 (a) shows the excited state population as a function of pumping time, t . The measurement is done by detecting the fluorescence level of the atomic

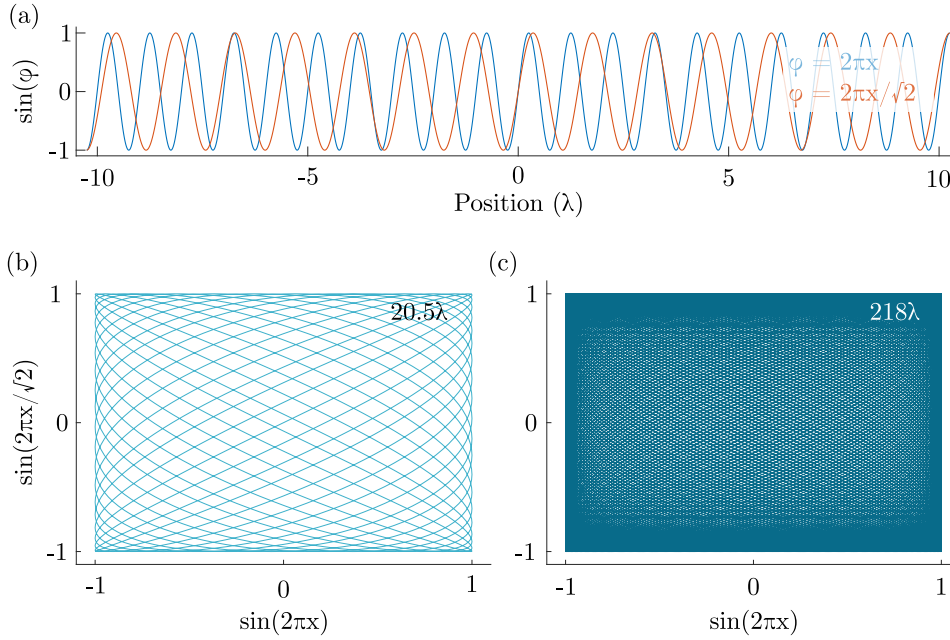


Figure 5.4: The phase relation between a standing wave in the cavity mode and a wave incident at an angle of 45° projected onto the cavity axis. (a) shows a plot of the two wave-evolutions along the cavity axis over 20.5 wavelengths. In (b) and (c) we see parametric plots of the two functions mapping most of the phase-space, and never overlapping with itself. The parametric plots are shown for 20.5 and 218 wavelengths respectively.

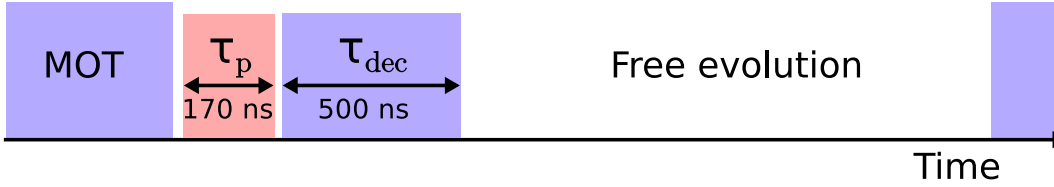


Figure 5.5: Operation cycle for atomic excitation and decoherence pulses. Cooling and trapping takes place during the MOT time. The cooling beams are turned off before applying a pumping beam during an interval τ_p , followed by a decoherence pulse during τ_{dec} . Finally the system is left to evolve freely before the cycle is repeated.

ensemble during the cooling time τ_{MOT} and decoherence pulse τ_{dec} respectively. The fluorescence ratio gives the ratio of atoms transferred to the excited 3P_1 state.

Technical noise and instabilities

Technical noise in the system causes fluctuations in the excitation ratio of the atoms for a given configuration. By keeping the full ensemble atom number constant, and plotting the integral of the cavity emitted lasing light against the ensemble excitation ratio, we obtain figure 5.6 (b). This configuration nominally gives about $N = 7 \cdot 10^7$ with a full ensemble excitation of $\eta_{MOT} = 45\%$, corresponding to a cavity excitation of $\eta_{cav} = 68\%$. We plot 5000 datasets in blue, and bin the points in excitation-intervals of 1%. The mean values of these bins are shown in orange, with statistical error-bars given by σ/\sqrt{n} where σ is the standard deviation within the

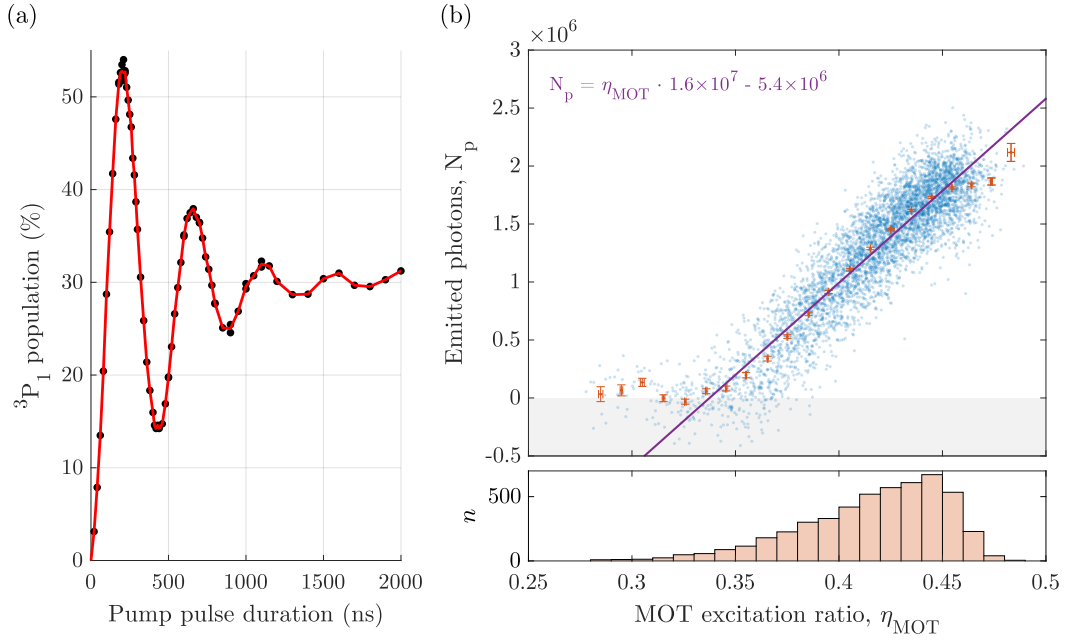


Figure 5.6: **(a)** Rabi flopping of the atomic excitation as a function of pumping pulse illumination time. The black dots are data, and the red line shows a 3-point moving average. **(b)** The excitation ratio of the full atomic ensemble is measured by switching off and on the MOT light. While the MOT light is off, a pumping pulse is applied for a time t , and the ratio of fluorescence before and after is measured. Here we used a pumping power of $P_p = 113$ mW and a waist size of $w_p = 3$ mm. Blue points are individual datasets, while orange points are mean values from 1%-intervals with error bars showing their statistical uncertainty. A linear fit and its associated expression in purple shows the slope of all $\eta_{MOT} > 0.33$. The lower plot shows the number of datasets, n , within a given bin.

interval, and n is the number of datasets. The lower plot shows a histogram of the number of datasets n for a given bin. The spread is relatively large, which means that proper characterization of the system behavior often requires post-processing of the individual datasets in order to filter for excitation ratio. Note that this spread in excitation ratio is independent of the absolute number of atoms in the ensemble. The number of emitted photons deviate significantly from zero for $\eta_{MOT} > 33\%$. This corresponds to the point of inversion within the cavity region $\eta_{cav} = 50\%$ as one might expect. We fit a linear behavior to datasets above this threshold as shown in purple.

5.2 Atom-cavity interaction

We model the ensemble of thermal atoms coupled to an optical mode of a cavity by a Tavis-Cummings model, following [100], modified from [108]. The atoms are considered as two-level units with ground state $|g\rangle$ and excited state $|e\rangle$. The model introduces some disorder in the system, by allowing position- and time-dependent atom-cavity couplings g_c^j for a given atom j . We also allow for a pumping field at frequency ω_p which couples to an atom at a rate of \mathcal{R}_p^j . The Hamiltonian for the system can initially be written as a generalized Dicke model:

$$\begin{aligned}
H &= \hbar\omega_c a^\dagger a + \sum_{j=1}^N \hbar\omega_e \sigma_{ee}^j \\
&+ \sum_{j=1}^N \hbar g_c^j (\sigma_{ge}^j + \sigma_{eg}^j) (a + a^\dagger) \\
&+ \sum_{j=1}^N \hbar \frac{\mathcal{R}_p^j}{2} (\sigma_{ge}^j + \sigma_{eg}^j) \left(e^{i\vec{k}_p \cdot \vec{r}_j - i\omega_p t} + e^{-i\vec{k}_p \cdot \vec{r}_j + i\omega_p t} \right).
\end{aligned} \tag{5.1}$$

We describe the cavity field with frequency ω_c by the raising (lowering) operator a^\dagger (a), and the atomic transition with frequency ω_e by the transition and population operators σ_{nm}^j for $n, m \in \{e, g\}$. The pumping field is modeled as a classical field with wave vector \vec{k}_p , and the atomic position is \vec{r}_j . The intensity distribution of the pumping field is found by directly measuring the experimental pumping field and using this profile in deriving the behavior of the Rabi frequency \mathcal{R}_p^j .

Since we are interested in modeling upwards of $N = 10^8$ atoms, we need to reduce the complexity of our Hamiltonian. We use an interaction picture in a frame rotating at the frequency of the pumping field ω_p and use the rotating wave approximation in order to cancel terms scaling with $\sigma_{eg}^j a$ and $\sigma_{ge}^j a^\dagger$. This corresponds to moving from the Dicke description to a generalized Tavis-Cummings model. This gives a set of equations that scales exponentially with the atom number N . We make the semi-classical approximation of factorizing all expectation values $\langle \sigma_{ge} a \rangle \equiv \langle \sigma_{ge} \rangle \langle a \rangle$. This results in a first order mean-field model which reduces the scaling from exponential to linear in N . This corresponds to neglecting all quantum fluctuations, and is justified by the large number of atoms present in the system. Since quantum noise scales as \sqrt{N} but the atomic signal scales as N .

We can then find the full time-evolution of the system by using three equations for the expectation values of our operators:

$$\begin{aligned}
\langle \dot{\sigma}_{ge}^j \rangle &= -\left(i\Delta_{ep} + \frac{\gamma}{2} \right) \langle \sigma_{ge}^j \rangle \\
&+ i \left(g_c^j \langle a \rangle + \frac{\mathcal{R}_p^j}{2} e^{-i\vec{k}_p \cdot \vec{r}_j} \right) (\langle \sigma_{ee}^j \rangle - \langle \sigma_{gg}^j \rangle) \\
\langle \dot{\sigma}_{ee}^j \rangle &= -\gamma \langle \sigma_{ee}^j \rangle + i \left(g_c^j \langle a^\dagger \rangle + \frac{\mathcal{R}_p^j}{2} e^{i\vec{k}_p \cdot \vec{r}_j} \right) \langle \sigma_{ge}^j \rangle \\
&- i \left(g_c^j \langle a \rangle + \frac{\mathcal{R}_p^j}{2} e^{-i\vec{k}_p \cdot \vec{r}_j} \right) \langle \sigma_{eg}^j \rangle. \\
\langle \dot{a} \rangle &= -\left(i\Delta_{cp} + \frac{\kappa}{2} \right) \langle a \rangle - \sum_{j=1}^N i g_c^j \langle \sigma_{ge}^j \rangle.
\end{aligned} \tag{5.2}$$

The detuning of field l with respect to the pumping field p is given by $\Delta_{lp} = \omega_l - \omega_p$. The spontaneous decay rate from atoms in the excited state is given by γ and we notice that there is no direct coupling of atomic spontaneous decay and the expectation value of the cavity field operators. Because of the semi-classical approximation, we can find the hermitian conjugates by taking the complex conjugate of the mean values, $\langle a^\dagger \rangle = \langle a \rangle^*$. And by using $\langle \sigma_{ee}^j \rangle + \langle \sigma_{gg}^j \rangle = 1$ we have all the necessary information. This leaves us with a total of $1 + 2N$ coupled differential equations.

If all atoms start out in the excited state we have $\langle \sigma_{ee}^j(t=0) \rangle = 1$ and $\langle \sigma_{eg}(t=0) \rangle = \langle \sigma_{ge}(t=0) \rangle = 0$. With an initially empty cavity mode, then, there can be no change to the cavity operator expectation values $\langle a^\dagger a \rangle$. This could be avoided by introducing some quantum noise, but here the system is initialized by the random coherence from the pumping field. Once this field is turned on $\langle \sigma_{ge}^j \rangle$ becomes nonzero, and a cavity field can build up.

The atom-cavity couplings g_c^j are given by equation (2.13). The pumping field drives the atomic transition with a Rabi frequency $\mathcal{R}_p^j = \mathcal{R}_p^0 \cdot \zeta_{BP} \cdot \zeta_B$. Here $\zeta_{BP}(r_j)$ and $\zeta_B(r_j)$ are scaling parameters given by the pumping beam profile and position in the magnetic field, whose values depend on the position of atom j . For uniform pumping and magnetic fields $\zeta_{BP}(r_j), \zeta_B(r_j) \rightarrow 1$. The position independent Rabi frequency is given by:

$$\mathcal{R}_p^0 = \sqrt{\frac{12c^2\gamma P_p(t)}{\hbar\omega_e^3 w_p^2}}. \quad (5.3)$$

The pumping power is $P_p(t)$ and is distributed over the beam profile whose area is proportional to w_p^2 for the case of a symmetric beam.

By numerically simulating this model, we can investigate a number of behaviors that are experimentally accessible to us. This is primarily related to the time evolution of the cavity field, measured by the transmission through the mirrors. We look at the time-evolution for varying atom number N and atom-cavity detuning Δ_{ce} . We take a Monte-Carlo approach to the simulations, and randomly distribute the position and velocities of the atoms. The atomic distribution is modeled as a 3D Gaussian with standard deviation $\sigma = 0.8$ mm, and allowed to evolve in time with Maxwell-Boltzmann distributed velocities. The ensemble temperature is estimated to be around $T = 5$ mK, and this value is used in all simulations of this section.

5.2.1 Expected lasing regimes

Our simulations indicate that there are two different regimes of lasing depending on how strongly the atoms are driven, as characterized by the Rabi frequency of the atom-cavity system \mathcal{R}_c . This frequency is proportional to the coupling factor $\mathcal{R}_c = 2g_c \sqrt{\langle a^\dagger a \rangle}$, where $\langle a^\dagger a \rangle$ is the mean photon number in the cavity. This makes the Rabi frequency atom- and time-dependent, and to ease interpretation we thus define an effective collective coupling rate $\Omega_N = \sum_j^{N_{cav}} \frac{g_c^j}{\sqrt{N_{cav}}}$ of atoms within the

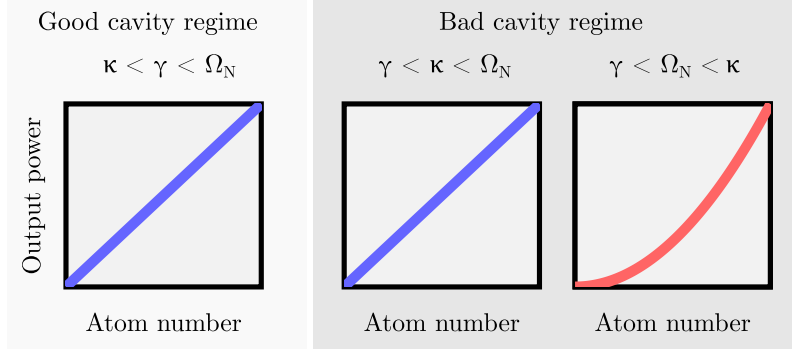


Figure 5.7: Power scaling dependency on the effective collective atom-cavity coupling Ω_N . For low atom numbers in the single-atom bad-cavity region, the output power scales quadratically with the number of atoms N . At higher atom numbers the effective collective coupling, causes the atoms to become coherently driven by the cavity field, and the output power scales linearly. γ denotes the natural decay rate of the atomic transition, and its relation to the cavity decay rate κ allows us to divide the behaviors into single-atom good- and bad-cavity regions. Figure adapted from [100].

waist of the cavity mode. This factor corresponds to the N -atom scaling appearing in the collective cooperativity $C_N = \frac{(2\Omega_N)^2}{\kappa\gamma}$. At low collective coupling $\Omega_N < \kappa$ the photon loss in the cavity mode is sufficiently large that the field inside the cavity does not appreciably alter the behavior of the atomic decay. As the collective coupling strength increases with increasing atom number we enter a regime where the strong emission of radiation during a single pulse can lead to multiple Rabi oscillations of the atomic excitation. This coherent oscillation is not directly observable in the experiment, but can be continually monitored in the simulations.

A consequence of this behavior seems to be that the scaling of the output power changes. As illustrated in figure 5.7, the peak power of the emitted lasing pulse scales either quadratically or linearly with the cavity atom number N_{cav} . At low atom numbers, then, we expect to observe a quadratic scaling of the output power. This is the scaling expected from ideal superradiant emission, as the lasing field E_{las} scales linearly with the atom number [39]. We associate the two bad-cavity regimes with a restrictive Born-Markov regime when the atom number fulfills the relation:

$$N_{cav} < N_{BM} = \sqrt{\frac{c}{\lambda\Gamma\mu}} = 1.1 \cdot 10^7 \quad \text{for} \quad \Gamma = \Gamma_D = 2\pi \cdot 2 \text{ MHz} \quad (5.4)$$

where $\mu = \frac{3\lambda^2}{8\pi\omega_0^2}$ is a value related to the solid angle of the lasing mode. And the Arrechi-Courstens regime for atom numbers above this number [39].

We also add the relation to the natural linewidth of the atomic transition γ to figure 5.7. This allows us to split the linear scaling into a good-cavity and a bad-cavity region that holds for the unbroadened case. It is possible to enter the single-atom bad-cavity region, while Doppler broadening still limits the ensemble to the good-cavity region. We do not consider the cases where single atom decay γ is larger than the collective coupling rate Ω_N . For a large atom number N_{cav} , such a system would couple primarily to the reservoir, and we expect no superradiant-like

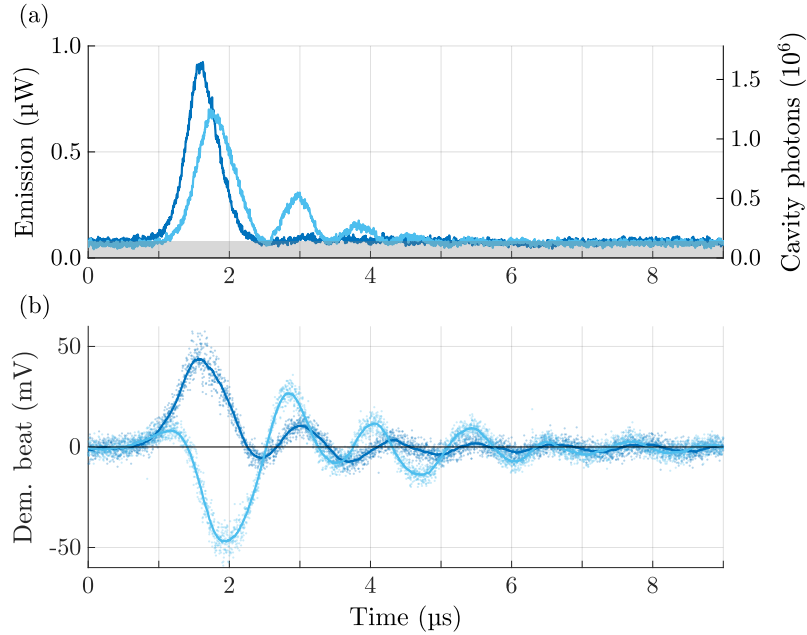


Figure 5.8: Time evolution of the cavity output field. After the pumping pulse ends at $t = 0$ s there is a characteristic delay of $\tau_D \sim 1.5 \mu\text{s}$ before a lasing pulse appears. The dark (light) blue curve corresponds to a cavity-atom detuning of $\Delta_{ce} = 0$ kHz ($\Delta_{ce} = 900$ kHz). (a) The power time-dynamics of the emitted lasing pulse is shown superimposed on a background originating from the off-resonant field that locks the cavity length. (b) Using the background signal as a reference, a demodulated beat-signal shows the evolution of the lasing E-field. Here the raw data from a single pulse is shown as dots, whereas the full lines are smoothed over 100 points to guide the eye. Figure adapted from [100].

behavior to occur. The collective cooperativity C_N would only be larger than unity deep in the single-atom good-cavity region, $\kappa \ll \gamma$.

5.3 Lasing pulses

When the experiment is set up correctly we are able to observe emission of lasing pulses during the free evolution time after pumping the atoms to the excited state. When there is initially no resonant light in the cavity, there will be a characteristic delay between the pumping pulse, and the lasing emission. For a total number of $N = 7.5 \cdot 10^7$ atoms in the MOT, we have an effective atom number $N_{cav} = N\eta_N \approx 1.6 \cdot 10^7$ atoms within the waist of the cavity mode, where $\eta_N \approx 0.22$. In figures 5.8 we show typical time-evolution of such laser pulses, when the cavity is resonant with the bare atomic frequency (dark blue) and when it is detuned by $\Delta_{ce} = 900$ kHz (light blue).

The lasing occurs as a pulse, as it is caused by the inversion of the atomic sample. Once the atoms decay, this inversion is depleted. Some of the light emitted into the cavity mode can nevertheless drive the atoms back to the excited state, restoring the inversion partially. This is particularly obvious for the case of a finite cavity-atom detuning, where multiple oscillations of the output power in figure 5.8 (a) after the

primary pulse are visible. Both signals in this figure are shown superimposed on a background of about $P_{ref} = 76$ nW. The background is a field detuned by one FSR of the cavity with respect to atomic resonance. This field does not interact with the atoms save for a constant AC Stark shift of the transition. It is used in order to obtain a PDH signal for locking the cavity length, and can additionally serve as a local reference for obtaining the E -field envelope and phase evolution of the lasing pulse.

Taking advantage of this, figure 5.8 (b) shows the E -field of the lasing pulse in a rotating frame. The signal is obtained by first considering the beat signal between the reference field and lasing pulse:

$$S_{\text{beat}}(t) = |E_{ref}|^2 + |E_{las}|^2 + |E_{ref}||E_{las}|\sin(\Delta_{ref-las}t + \phi). \quad (5.5)$$

By mixing down the signal with an RF field at $\Delta_{ref-las} \approx \nu_{FSR} = 781$ MHz and filtering it, the field magnitude and phase behavior can be extracted.

$$S_{\text{Dem. beat}}(t) = |E_{ref}||E_{las}|\sin(\phi). \quad (5.6)$$

Assuming a constant magnitude of the reference field, the signal can give us information about the phase- and frequency evolution of the lasing pulse. Here it becomes obvious that the oscillations in the ensemble population and cavity field occur for both the resonant and detuned case, as distinct oscillations are visible past $t = 9$ μ s. The phase evolves during the primary pulse envelope for the detuned case, indicating that the frequency of the emitted light might be shifted with respect to the cavity mode here. An effect caused by atomic pulling of the frequency.

5.4 Lasing threshold

The delay and amplitude of the primary lasing pulse changes when varying the atom number N in the MOT. This allows us to find a threshold behavior as shown in figure 5.9 (a). Here, no lasing pulses are visible for low atom numbers $N < 3.5 \cdot 10^7$. We have taken individual time series corresponding to those of figure 5.8 (a) and used the peak intensity of the pulse. The raw data has been divided into bins of 40 measurements, whose mean value and standard deviation are shown in black. At low atom number background noise peaks in the measurements causes non-zero values for the peak amplitude.

We expect the amplitude of the emitted lasing pulse to scale with the atom number in the cavity mode N_{cav} . As the system transitions from the restrictive Born-Markov regime to the less restrictive Arrechi-Courtens regime, we expect the pulse amplitude to transition from a quadratic to a linear atom number scaling. This behavior is seen to agree well with the derived number as the scaling changes around $N = 5.0 \cdot 10^7 \approx N_{BM}/\eta_N$.

The delay between excitation and lasing emission is plotted in figure 5.9 (b). This delay is a direct consequence of the time it takes to build up coherence in the system. We expect it to scale as the inverse of the number of atoms $\tau_D \propto 1/N$ right above threshold [39], and as the inverse square root $\tau_D \propto 1/\sqrt{N}$ for high atom

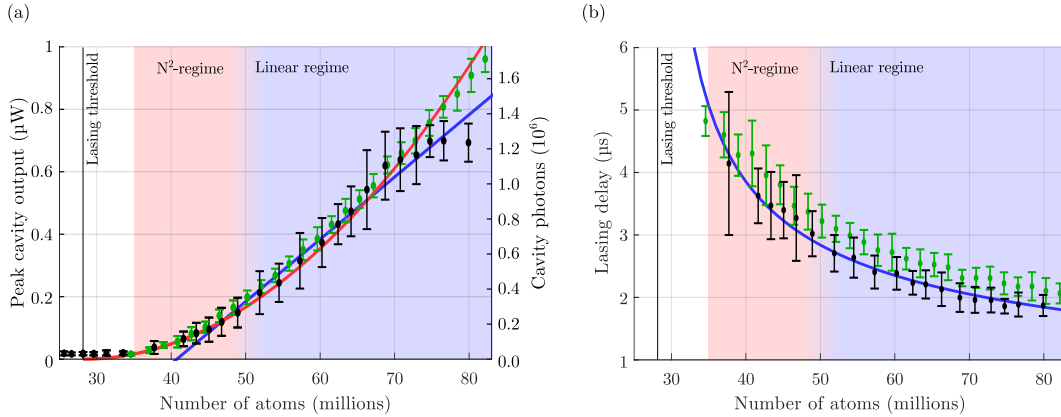


Figure 5.9: Lasing pulse dependency on atom number. **(a)** Shows the peak lasing pulse power detected in the cavity output as a function of MOT atom number. Approximate atom numbers within the cavity waist are given by $N_{cav} = 0.22 \cdot N_{MOT}$. The background field results in a noise level of about $P = 20 \text{ nW}$, visible below $N = 3.5 \cdot 10^7$. We fit a quadratic scaling (red) to the raw data in the $N = 3.5 \cdot 10^7$ to $N = 5.0 \cdot 10^7$ range, and a linear ($a \cdot (N - N_{offset})$) scaling (blue) for the following points up to $N = 7.0 \cdot 10^7$. The quadratic fit ($b \cdot (N - N_{th})^2$) gives us a lasing threshold at $N_{th} = 2.8 \cdot 10^7$. For high atom numbers a saturation in output power seems to occur. We interpret this as a breakdown of the linear scaling between atom number in the cavity and in the full ensemble. **(b)** The delay τ_D between atomic pumping and emission of the lasing pulse. This delay scales inversely with the atom number, and we fit a $\frac{c}{\sqrt{N-N_{th}}}$ curve in blue. Figure adapted from [100].

numbers [56]. We use the time of the peak pulse power, and see a behavior that agrees well with our expectations.

We have fitted quadratic and linear functions to the peak output power in two separate regimes as expected from section 5.2.1. The fits are made to the raw data, which is not displayed in the figure, and cover regions of 240 and 320 data points respectively. By fitting the quadratic fit to $3.5 \cdot 10^7 < N < 5.0 \cdot 10^7$ we find a zero-point at $N_{th} = 2.8 \cdot 10^7$, which is marked as the lasing threshold in figures 5.9. While the experimental data is explained well by the quadratic fit even for higher atom numbers, we chose to fit a linear curve to the region $5.0 \cdot 10^7 < N < 7.0 \cdot 10^7$. This linear fit does not explain the data well close to threshold, and we see the transition between a quadratic scaling and linear scaling according to the limit set by equation (5.4). For high atom numbers $N > 7.5 \cdot 10^7$ the output power seems to saturate. We believe this to be caused by an increase in total ensemble atom number N that is not mimicked by the cavity atom number N_{cav} . This linear relation can break down due to an inhomogeneous atomic distribution, as often observed experimentally. In this case the shape of the atomic cloud changes rather than the density increasing. The error bars increase in size with increasing power as they are, in part, an expression of experimental instabilities.

In addition to the experimental results, simulation results are plotted in green. These data agree well with the experimental data, and follow a clear linear trend at $N > 5.0 \cdot 10^7$ without saturation-like behavior. The model assumes a Gaussian density profile of the atoms which ensures that the linear relation $N_{cav} = N\eta_N$ holds at all times. The error bars are caused by randomly varying initial conditions

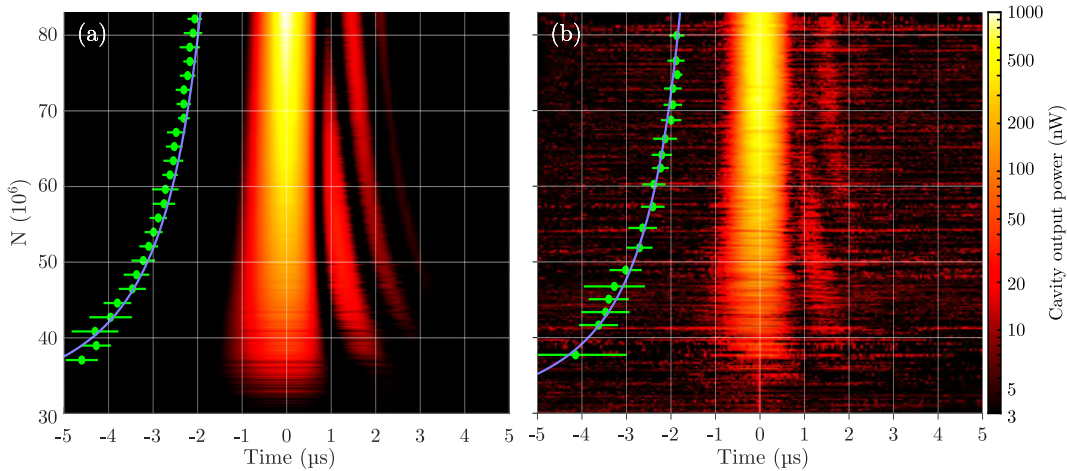


Figure 5.10: Pulse evolution with varying atom number N . All sequences are aligned with their maximum emission power at $t = 0$ in order to ease interpretation. The color scale is logarithmic with all values below $P = 3$ nW retaining the same color (black). The end of the pumping pulse can be found by the green points, which are binned, and shown with 1σ error bars. An inverse square root-dependency is fitted to them, and illustrates the pulse delay dependency on atom number. (a) Simulations. (b) Experimental measurements. These data have a finite background signal caused by the reference field in the cavity which has been subtracted for this figure, but adds significant zero-point-noise. Figure adapted from [100].

from the Monte-Carlo approach. The delay shown in figure 5.9 (b) is persistently longer in the simulation than in experiment. This could be caused by the lack of spontaneous emission into the cavity mode of the model.

5.5 Time-evolution of the lasing pulses

We map out the time evolution of the lasing pulses as a function of atom-cavity detuning and atom number. This behavior is compared with the numerically simulated time evolution in figures 5.10 and 5.11. Figure 5.10 shows the full time evolution of the lasing power as a function of atom number in the MOT. The primary pulse was used in figure 5.9 above to determine the lasing threshold. To ease interpretation of the plot, all time series are realigned, so that $t = 0$ μs corresponds to the pulse maximum rather than the end of the excitation pulse. This allows us to clearly identify the evolution of the coherent oscillations that follow the primary pulse. The time of the excitation pulse can still be seen as the binned green points. The color scale was chosen to reduce excessive noise from the experimental figure, and all values below $P = 3$ nW are black. In the experimental figure 5.10 (b) the mean background signal has been subtracted from the full signal, but its noise is visible at all times.

Just above lasing threshold, only the primary pulse is visible, but oscillations appear as the atom number is increased. We notice three separate effects. Firstly the primary pulse is broad at low N , and narrows as N increases. Both the FWHM, and the width at some absolute power value decreases. This is expected behavior as the increased gain also speeds up the evolution of the atomic decay into the

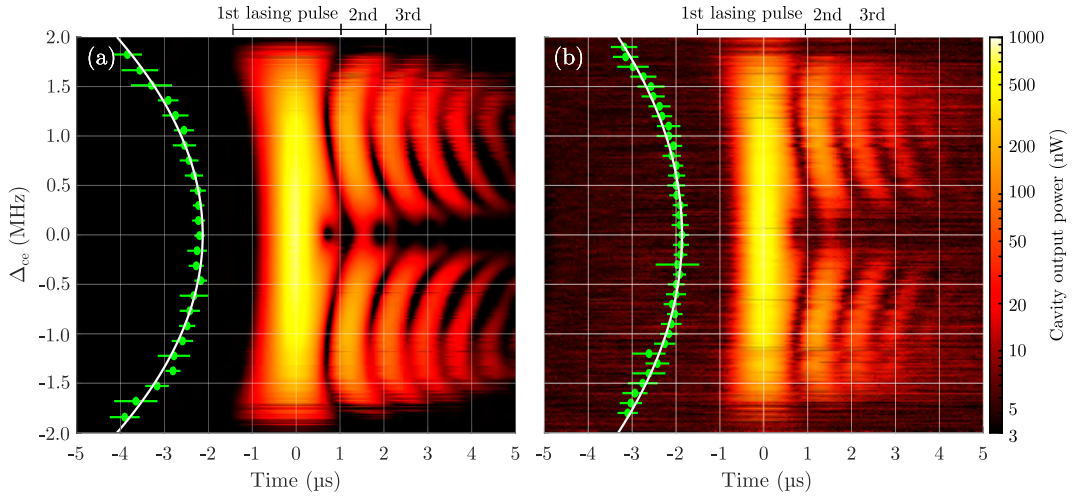


Figure 5.11: Pulse evolution with atom-cavity detuning Δ_{ce} . All sequences are aligned with their maximum emission power at $t = 0$ in order to ease interpretation. The color scale is logarithmic with all values below $P = 3$ nW retaining the same color (black). The end of the pumping pulse can be found by the green points, which are binned, and shown with 1σ error bars. A quadratic function is fitted to them, and illustrates the pulse delay dependency on cavity detuning. (a) Simulations. (b) Experimental measurements. These data have a finite background signal caused by the reference field in the cavity which has been subtracted for this figure, but adds significant zero-point-noise. Figure adapted from [100].

cavity mode. The collective evolution time is decreased as the collective coupling Ω_N increases, $\tau_{\text{coll}} = C_N \gamma$ [39].

Secondly the oscillations in power that follow the primary pulse increase in frequency with increasing N . We expect the existence of the oscillations to be caused by Rabi nutation of the excitons between cavity and atomic modes [9], [13]. At cavity resonance this Rabi frequency is intimately tied to the collective coupling factor Ω_N . At high atom number the first oscillation seems to be engulfed by the primary pulse as the oscillation period is matched to about $t = 0.75$ μs. At this particular delay time we observe zero emitted light independently of the atom number N .

Thirdly the symmetry of the primary pulse shifts as N is increased, becoming increasingly symmetric. For low atom numbers, the asymmetry could be explained by the accelerating decay rate during the emitted pulse, as predicted in pure super-radiant systems [25], [39]. As the atom number increases, the high Rabi frequency of the atom-cavity-field system causes multiple Rabi oscillations during the emitted pulse, as was indicated by simulations [108]. This causes a disruption of the accelerating behavior, and thus a less abrupt downward slope of the pulse.

We vary the atom-cavity detuning symmetrically around resonance in figure 5.11. At $\Delta_{ce} = 0$ we expect a behavior like that in figure 5.10 for $N = 7.5 \cdot 10^7$. For nonzero detuning the picture changes dramatically. The generalized Rabi frequency $\mathcal{R} = \sqrt{\mathcal{R}_0^2 + \Delta_{ce}^2}$ is proportional to the detuning of the cavity, and indeed we see oscillations with increasing frequencies. The full behavior is quite complicated as the bare Rabi frequency changes when the photon number changes in the system.

This happens both as a function of cavity detuning and time. The oscillations are much more pronounced for the case of a detuned cavity, and in both experimental and simulated data we here see 4 to 5 oscillations after the primary pulse. Unlike what we would expect from a generalized Rabi frequency picture, the oscillations do not seem to converge towards the value exhibited at $\Delta_{ce} = 0$. Instead there is an abrupt attenuation of the oscillations as the atom-cavity detuning is reduced towards zero, and for values $\Delta_{ce} < 200$ kHz the behavior of the oscillations seems to have changed. At large detunings the frequency of the oscillations decrease which could be explained by the low power in the system.

It is interesting that lasing is supported for quite a wide range of atom-cavity detunings. There are a number of effects that need to be taken into account to justify this behavior. Remembering the relation between broadening effects in the system, the Doppler width of the atomic ensemble at $T = 5$ mK is the largest feature with a width of $\Gamma_D \approx 2$ MHz. This inhomogeneous broadening of the ensemble means that significant gain, is available for the full width of the cavity line $\Delta\nu_G = \Gamma_D \approx \kappa$, and the range seen in figure 5.11. It places the atomic ensemble just on the border of the good- and bad-cavity regimes. Some mode-pulling by the cavity is expected, but suppressed as the system is not far into the good-cavity regime. Only a few photons are needed to start the lasing, and the cavity power build-up causes power broadening of the individual atoms. This effect thus acts to increase the resonance overlap between atoms and the cavity mode once lasing is initiated. This in turn increases the available gain. The emitted lasing power thus becomes more robust to atom-cavity detuning, and a nearly flat peak output power is seen for $|\Delta_{ce}| < 1$ MHz.

Randomly varying phase

Since each lasing pulse is initiated by random spontaneous emission we expect no phase-coherence between successive pulses. We can look at the beat signals in the dynamical regimes of varying atom number N and cavity detuning Δ_{ce} . On figures 5.12 (a) and (b) this behavior is plotted. The field emitted from the cavity is beaten against the cavity reference field, and mixed down to DC by the FSR frequency in order to show the phase-evolution within the pulses. The data was taken simultaneously with the data shown in figures 5.10 (b) and 5.11 (b). Here we show only the relevant section around the emitted pulse at $t = 0$ μ s. As can be seen from figure 5.12 (a) the overall sign of the phase-signal is random between pulses even within narrow ranges of N . In figure 5.12 (b) we notice that large detunings Δ_{ce} cause some pulling of the frequency, so that the signal is no longer at DC, but changes sign during a pulse. See, e.g., around $\Delta_{ce} = \pm 1.4$ MHz.

Killing the coherence

We can add significant decoherence of the atomic ground state by leaving the MOT-beams on during pulse emission. This results in a decoherence given by the scattering rate of equation (2.25) and destroys the oscillations that follow the primary pulse emission. In figure 5.13 (a) and (b) we show some 40 sample datasets of the pulse emission (top) and the phase-response. The average of all lasing pulses is shown in black, and in the background we plot the average MOT fluorescence and pumping pulse in gray full and dashed lines respectively. In figure 5.13 (a) there

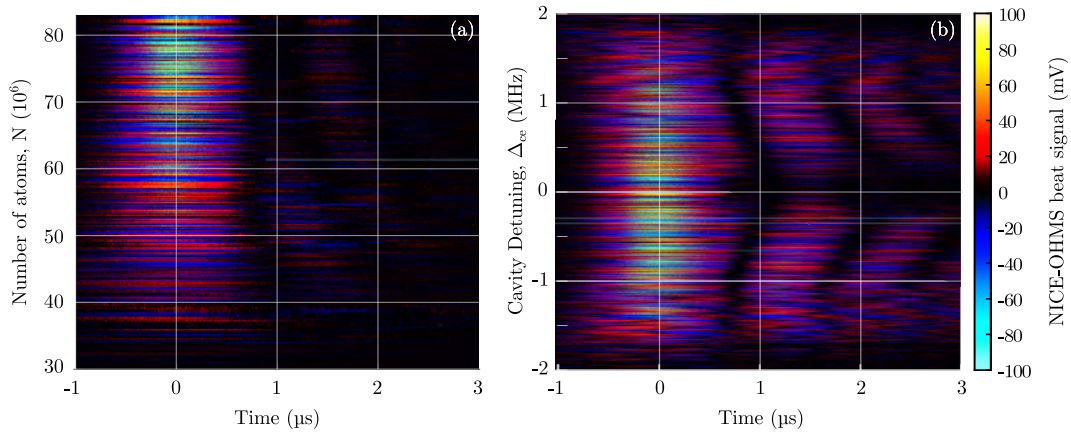


Figure 5.12: Superradiant emission dynamics with the associated NICE-OHMS beat signals. The emitted lasing pulse is beaten against the cavity reference field and mixed down to DC by the FSR frequency. The sign of the phase is seen to vary randomly between realizations. $t = 0$ is the maximum of the emitted pulse power. (a) The atom number N is varied. (b) Cavity detuning Δ_{ce} is varied. At large detunings the frequency pulling by the atomic resonance causes the beat-signal to change sign during a single pulse-envelope as it is no longer at DC.

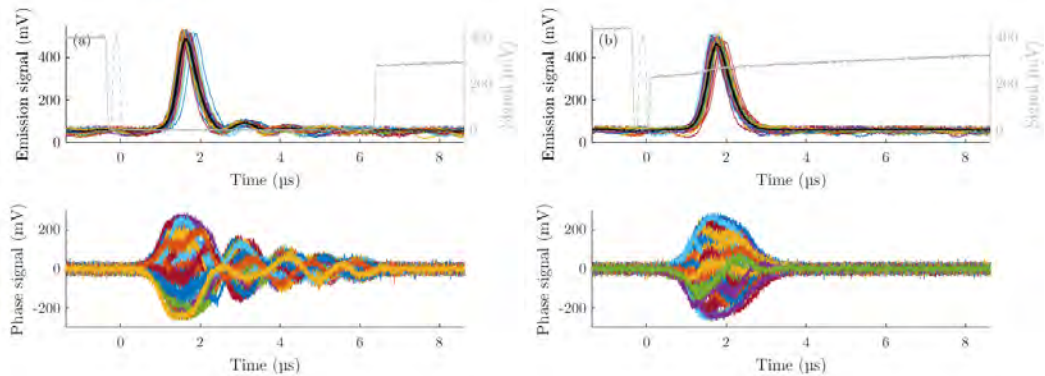


Figure 5.13: Laser pulses without (a) and with (b) decoherence induced by MOT beams. Emission intensities are plotted above the associated phase-behaviors. About 40 individual scans are plotted to showcase their variable DC phase. The mean lasing intensity is plotted as a thick black line in the upper figures and the mean MOT fluorescence and pumping pulse is also shown.

is no added decoherence, and the oscillations are clearly visible in the phase signal, ending abruptly around $t = 6.5$ μs as the MOT light is turned on again. In figure 5.13 (b) the MOT light is on throughout the lasing pulse, and no oscillations are visible after the primary pulse. The pulse amplitude itself is also reduced slightly.

We can use the configuration with the MOT light on during lasing to calibrate the atom number. Assuming that all atoms that decay to the ground state during the pulse emit only a single photon, the number of atoms participating in the emission process can be found as the integral of the laser pulse. The MOT fluorescence increases steadily as atoms within the full ensemble spontaneously decay to the ground state. During the emitted lasing pulse, however, this rate is increased. By noting the change in fluorescence caused by the emitted lasing pulse, then, the MOT

fluorescence can be calibrated to an atom number N .

5.6 Seeded lasing

We can run the system in a slightly different configuration if we allow for an input field to the cavity on resonance with the atomic transition ω_e . This field will seed the lasing by forcing stimulated emission of radiation from the excited atoms into the cavity mode. The emitted lasing pulse will then inherit the phase-properties of the seeding light, and act as an amplifier. Such an amplification scheme becomes interesting as it relies on exceedingly low input powers down to $P_{seed} = 8$ pW, yet can deliver several orders of magnitude of amplification. It is spectrally limited to the narrow range defined by the atomic transition, and in the present realization limited to the production of lasing pulses. With a continuous pumping scheme, the latter limitation can be overcome.

Phase seeding

In figure 5.14 (a) we show a schematic of the seeding configuration. Our reference laser is still detuned by one FSR and acts as both the reference of a beat signal on a fast photodetector and as a carrier for PDH-locking of the cavity length. Adding sidebands to this carrier frequency at $\omega_L \pm \omega_{FSR}$ allows us to lock the cavity length and have a seeding field for the lasing process independently of each other. We ensure $\omega_L + \omega_{FSR} = \omega_e$ by scanning the carrier frequency ω_L , and vary the seeding power by adjusting the modulation index of our EOM.

An advantage of this method is that the phase-relation and overall phase of the seed and reference fields is determined by the EOM modulation. When we detect and mix the beat signal down to DC, our mixing phase ϕ_M will be locked to the phase of the seed and reference fields. This should result in a well-defined DC-level of the beat signal. In figure 5.14 (b) we show a typical behavior of the laser pulse when seeded. The blue curve shows the emitted power, and the orange curve shows the DC beat signal. This data was taken with constant atom number and seeding power $P_{seed} = 90$ nW, but the excitation ratio varies due to technical noise in the system. This allows us to showcase the robustness of both the output power and phase over 84 datasets, whose mean values are plotted in color, with the standard deviations shown as a shaded gray area. Because the lasing pulse is seeded, the well-defined phase of the seeding signal is inherited, and we get a consistent evolution between consecutive pulses.

Delay times under stimulated emission

Introducing a seed field in the cavity mode means that the physical process changes. While the lasing process in the non-seeded version is based on coherence buildup between the atoms in the cavity mode, a seeded laser is controlled by stimulation from the seed field. This is analogous to passive hydrogen masers [117] used, e.g., in the ESA Galileo navigation satellites [30]. The phase dictation reduces the requirements on the atom number and lowers the threshold for laser emission $N_{th}^{seeded} < N_{th}$. For a pulsed system this fact shows itself in the delay τ_D between pumping and pulse emission. Since there is no longer a delay caused by coherence

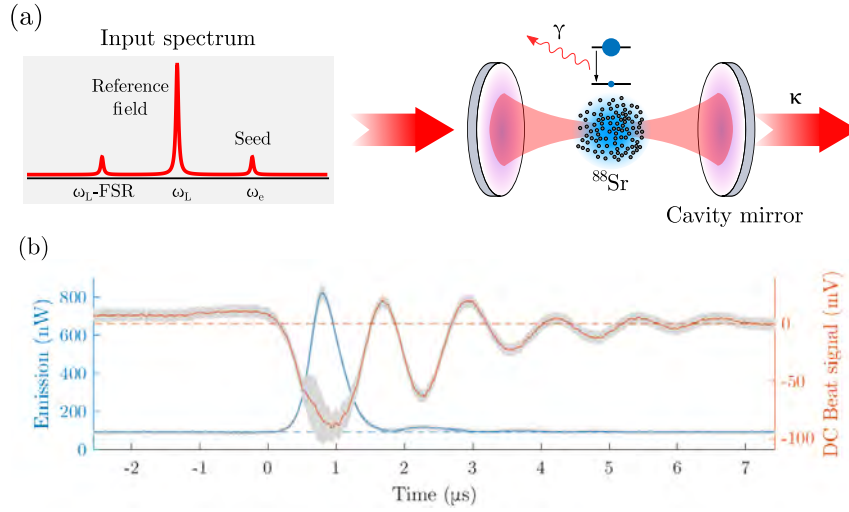


Figure 5.14: **(a)** Overview of a cold-atom based laser system with controllable seed power. The spectrum of the input field is composed of a carrier signal at ω_L which acts as a reference signal to lock the length of the cavity and to beat the lasing output against. Detuned by one FSR, a sideband at atomic resonance ω_e acts as the seeding light for the lasing pulse emitted from the cavity. The cavity is shown with its input, output rate κ and atoms. The atomic ground and excited state are pumped to population inversion and can emit spontaneously into the surrounding reservoir, or be stimulated into the cavity mode by the seeding light. **(b)** Experimental behavior of a seeded lasing pulse. A constant delay τ_D of the peak output power, and well-defined phase-evolution of the E-field as seen in the DC beat signal. Here we average over 84 datasets to showcase the repeatability of the signals. Standard deviations are shown by the gray areas.

buildup, emission can happen much faster. As the seeding field is reduced, the delay increases until we reach the self-lasing case. In figure 5.15 we see the pulse evolution as a function of the seeding power. Notice here that the seed power (ordinate) axis is logarithmic, and the delay thus decreases exponentially with increasing seed power, $\tau_D = \tau_0 \cdot e^{-A \cdot P_{seed}}$, indicated by the dashed trend line. For the lowest $P_{seed} = 8$ pW we obtain a pulse delay of $\tau_D = 2.4$ μ s, which is comparable to the non-seeded case.

As the seed power decreases so does the peak output power. While the seed power can go to zero, the laser pulse power never will as long as we are above N_{th} , where it simply reduces towards the self-lasing case. Here we have used $N = 5 \cdot 10^7 > N_{th}$ and converge towards a pulse power of $P_{pulse} \approx 250$ nW as the seed goes to zero.

Amplifier properties

If we consider this system as an amplifier, we are interested in the amplification factor and the accumulated phase-noise. The amplification factor is shown in figure 5.16 for individual pulse sequences as a function of the seed power. The amplification factor G is seen to scale as a monomial with a trend line shown at $G = 350 \cdot (P_{seed})^{-0.92}$. This is close to $G \propto \frac{1}{P_{seed}}$ which would be expected for a pulse power that is completely independent on the seed power. The total available gain in the system will be limited by the atom number N_{cav} and inversion. It is thus

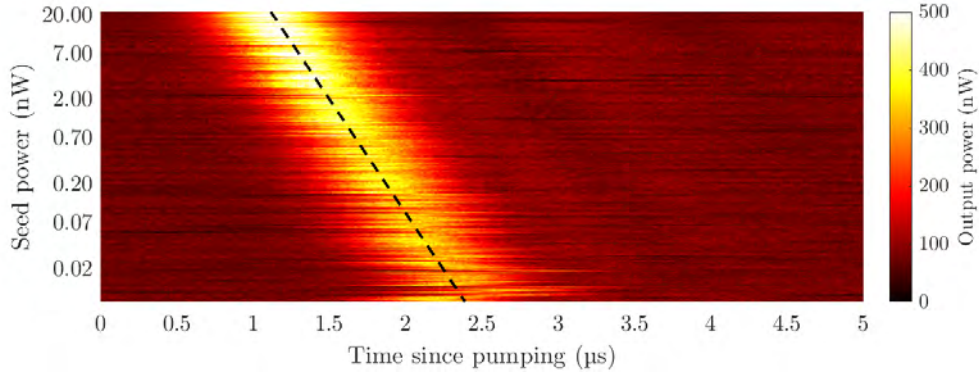


Figure 5.15: Heat map of the output power evolution of a lasing pulse when varying the seeding power P_{seed} . Notice that the ordinate axis is logarithmic. The linear appearance of the pulse peak time-dependence tells us that the delay scales as $\tau_D = \tau_0 \cdot e^{-A \cdot P_{seed}}$ as indicated by the dashed trend line. Individual pulse sequences are shown, with the seed power kept constant for 10-20 consecutive sequences.

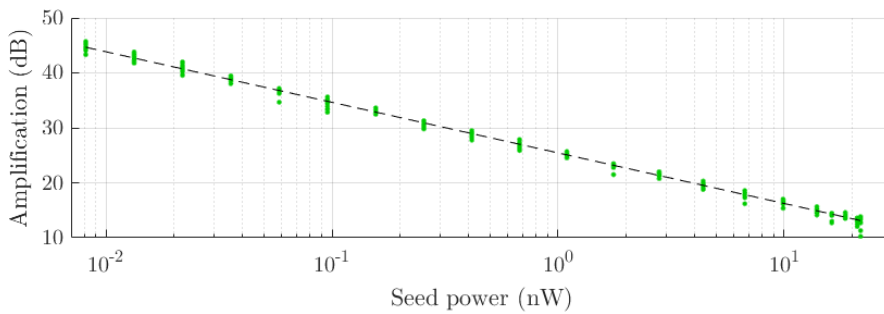


Figure 5.16: The amplification of the input seed power relative to the peak pulse power. The exponential behavior means that the amplification goes to infinity for $P_{seed} \rightarrow 0$. This is caused by the ability of the ensemble to emit lasing even without a seed. The trend line shows an amplification G that scales as $G = 350 \cdot (P_{seed})^{-0.92}$.

reasonable that the seed power can influence the total emitted power very little. We expect $G = 1$ for a seed power of $P_{seed} \approx 580$ nW. The amplification increases beyond 40 dB for $P_{seed} < 10$ pW. Though this is a pulsed system, it is intriguing that it allows such high amplification of pW signals.

The signal amplification is only interesting if we can preserve the spectral behavior of the signal as well as possible. We make a preliminary analysis of this by looking at the phase-behavior through the E-field evolution. The current system still has a great deal of technical noise and instabilities in the experimental parameters. In figure 5.17 we show the time-dynamics of the pulse power and E-field when all parameters are attempted to be kept constant. In particular the atom number N , and the atomic temperature T are kept constant. The efficiency of the pumping pulse is still seen to vary which causes a large variation in the inversion. As a result the power of the emitted lasing pulse varies, and we order the pulse sequences by their peak power. This allows for some visual averaging, without explicitly blurring the behavior by averaging over different pumping efficiencies.

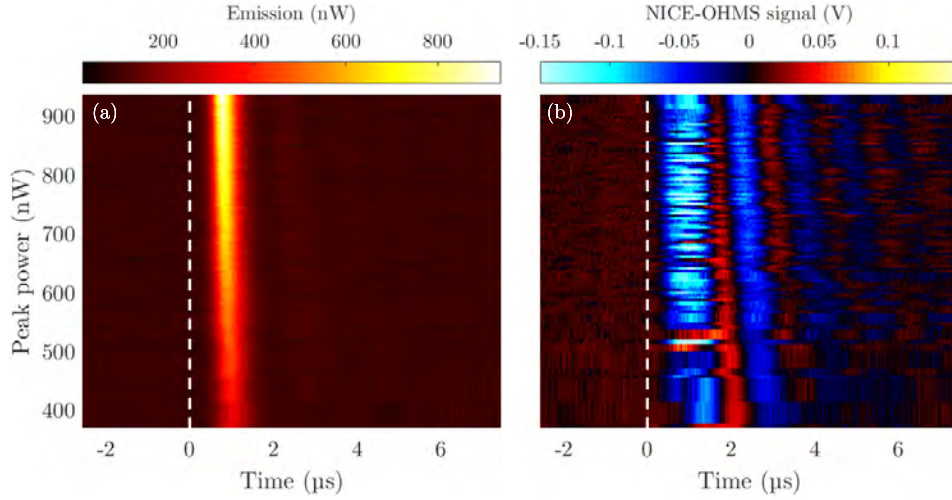


Figure 5.17: The emitted lasing pulse for a situation where the atomic inversion is unstable between sequences. We sort 256 datasets according to the lasing pulse peak power. The total atom number and seeding power $P_{seed} = 90$ nW is kept constant. **(a)** Emitted power from the lasing pulse. A non-zero background caused by the reference signal and the seeding is present, and not removed. **(b)** The E-field of the emitted pulse can be detected by down-mixing a beat signal to DC. This shows that the phase-evolution is quite consistent between pulses. We keep the ordering of **(a)** in order to not blur the evolution by averaging over different pulse delays.

The DC beat signal shown in figure 5.17 (b) is proportional to the time-dependent E-field in a frame rotating at the atomic transition frequency ω_e , namely $E_{pulse}(t)|_{\omega_e\text{-frame}} = A(t) \sin(\phi)$. Just as in figure 5.14 (b) we see a phase evolution that is highly reproducible between separate pulses that are not necessarily ordered in time. This well-defined phase means that we are able to preserve the phase-information from the seeding laser very well. Further investigations into the robustness of the phase-transfer will be presented in [101].

5.7 Spectral properties

We have used the DC beat signal to get information on the coherence of the signal. If we look at the generated beat signals directly or mixed down to some non-zero frequency $\omega \gg \frac{1}{\tau_L}$, where τ_L is the duration of the emitted lasing pulse, we can measure the frequency spectrum of a pulse. In section 5.8 we use that signal to investigate the frequency stability between consecutive pulses.

Figure 5.18 shows a beat signal at $\beta \approx 10$ MHz. The envelope is given by the time-dependent lasing amplitude $A(t)$, and we assume a the background field to be constant. Within the envelope the signal evolves as $S \propto \sum_{\beta} c_{\beta} \sin \beta t + \phi$. By Fourier transforming the signal we can then extract the distribution of the frequency components c_n .

In order to get information about the evolution of the spectrum, we analyze the Fourier frequency as a function of integration time t . An example of such an evolution for $\beta \approx 50$ MHz is shown in figure 5.19. We use a finite atom-cavity detuning of $\Delta_{ce} = -1.4$ MHz. This means that we have significant ringings after

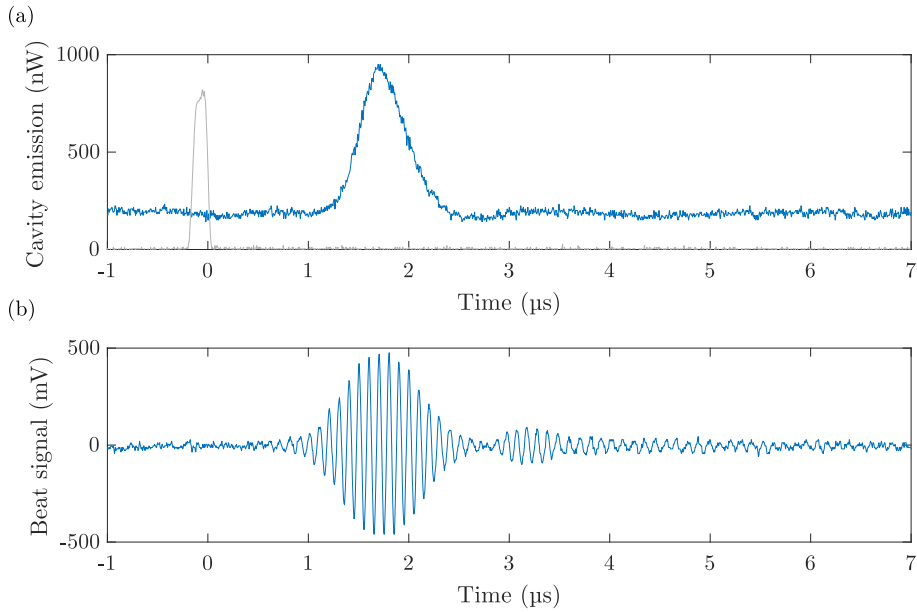


Figure 5.18: A single lasing pulse from an unseeded sample of atoms. **(a)** The ensemble is pumped (gray) at $t = 0$ s and a pulse is emitted after a delay $\tau_D = 1.7 \mu\text{s}$ (blue). Here the cavity is kept on resonance with the atomic transition by the large noisy background field around 200 nW. **(b)** The beat signal mixed down to 10 MHz in order to visualize the oscillations used for determining the average frequency and spectral properties. While the spectrum can be found by Fourier transforming, a simple method such as counting zero-crossings can be used for determining the average frequency.

the primary pulse, and it turns out that these ringings are highly interesting for the spectral evolution. They provide an extended period of significant signal, compared to the resonant case where the ringings are negligible. This reduces the Fourier limitation on the spectral resolution. It also appears that with each ringing, new features appear in the spectrum. In figure 5.19 this is evident, e.g., around $t = 3 \mu\text{s}$, $t = 4 \mu\text{s}$, and $t = 4.4 \mu\text{s}$. For $2 \mu\text{s} < t < 3 \mu\text{s}$ the primary pulse is emitted, and a single symmetrical spectral feature is seen in figure 5.19 (a). At $t = 3 \mu\text{s}$ the primary pulse ends, and the spectrum is seen to bifurcate into two branches. At the second ringing the bifurcation is repeated with a clear asymmetry between the spectral density of the two primary branches of the spectrum. The asymmetry is caused by the offset between cavity resonance – which appears to dictate the initial pulse frequency – and the bare atomic frequency. The emitted spectrum is thus pulled from cavity resonance towards the atomic resonance as the emission is left to evolve.

In the case of a resonant cavity, $\Delta_{ce} = 0$, the symmetry between red- and blue-detuned lasing is not broken, while the oscillations will still cause bifurcation, there is no significant frequency-pulling.

By taking the Fourier spectrum for a range of different atom–cavity-detunings we can look at the frequency pulling factor across various Δ_{ce} . This results in a slope of 1 when there is no frequency pulling, but which can in general be time- and detuning-dependent. We look at this behavior for three different integration

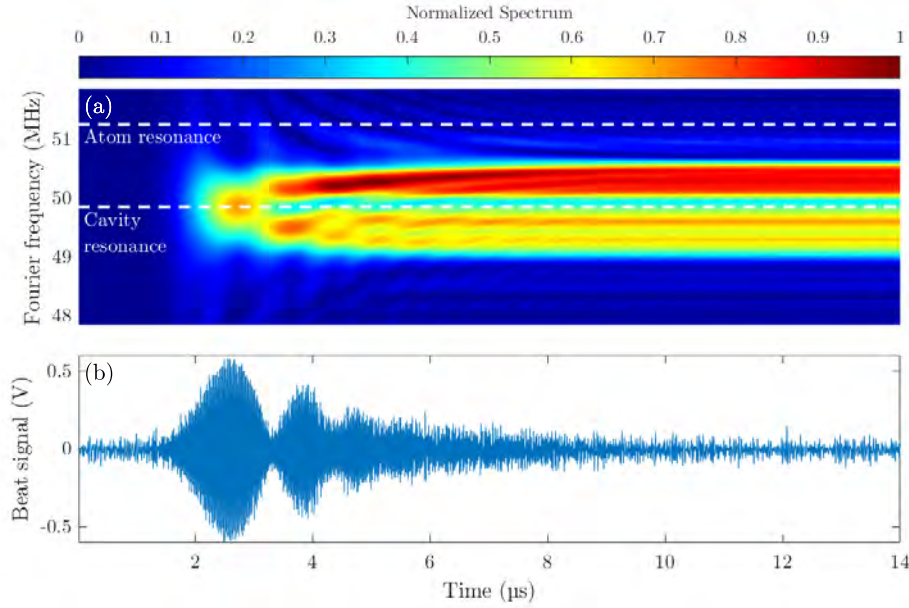


Figure 5.19: Lasing pulse at $\Delta_{ce} = -1.4$ MHz. (a) Spectral behavior of a single lasing pulse during its time-evolution as a function of integration time t . The dashed lines indicate the cavity resonance and bare atomic resonance frequencies. The beat-signal is down-sampled from 169 MHz to about 50 MHz by mixing with a constant RF signal. The spectrum is normalized to the maximal value over the whole spectrum. (b) Time-evolution of the beat-signal.

times t in figure 5.20. During the first pulse at time $t = 2.5$ μs , figure 5.20 (a), the spectrum follows approximately the dash-dotted line of unity slope. This indicates the tendency of the first pulse to follow the cavity frequency. The cavity-pulling factor of the frequency is given by the inverse slope of this line. Initially, then, it looks a lot like a good-cavity case with a cavity-pulling factor of one.

At a later time, $t = 3.6$ μs – figure 5.20 (b), a single ringing has developed, and the spectrum is now seen to split into two branches across most cavity-detunings. We interpret the lack of spectral density along the cavity frequency (dash-dotted line) as an expression of light resonant with the cavity being largely reabsorbed by the atoms. Finally when most of the ringings are over, at $t = 7$ μs – figure 5.20 (c), the steepest branch has reached a slope of about 3 corresponding to a cavity pulling factor of $\zeta_{CP} = 1/3$.

A cavity pulling factor ζ_{CP} below unity is a hallmark of the bad-cavity regime. It is desirable for the realization of a noise-resistant laser because it is an indication that noise in the cavity resonance frequency will be suppressed in the frequency of the laser light. However, it seems that the slope in a narrow region around $\Delta_{ce} = 0$ remains unity. This region coincides with the region of suppressed ringings in figure 5.11.

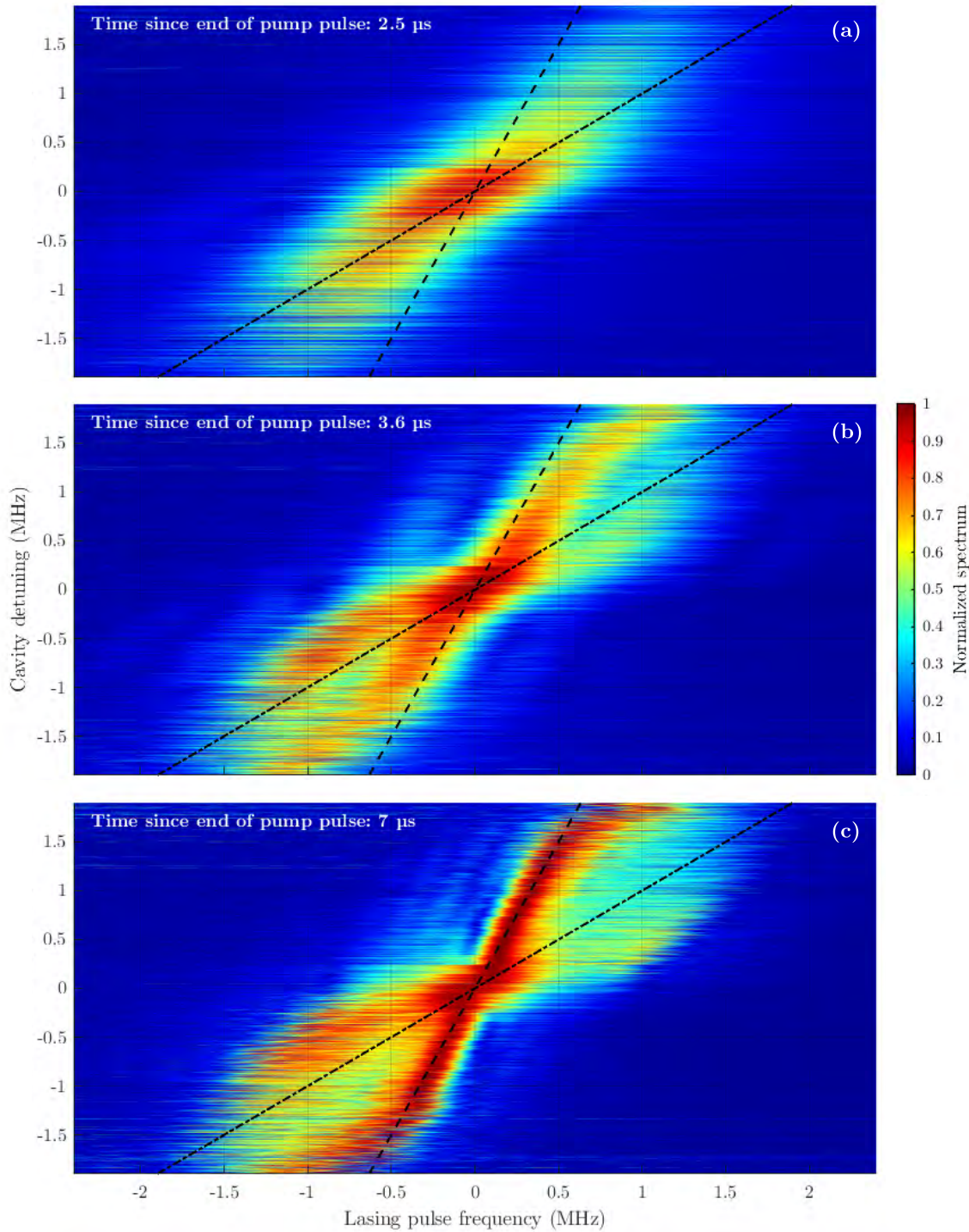


Figure 5.20: Spectral line pulling by the atomic resonance. The normalized Fourier spectrum of the pulse sequence is found for different integration periods, and is here shown for data from $t = 0 \mu\text{s}$ to (a) $t = 2.5 \mu\text{s}$, (b) $t = 3.6 \mu\text{s}$, and (c) $t = 7 \mu\text{s}$, corresponding approximately to the primary pulse, up to and including the second pulse, or all visible pulses. The dash-dotted line shows a slope of unity, corresponding to the lasing frequency directly following of the cavity resonance. The dashed line shows the attained atomic line-pulling during the ringings of $\zeta_{CP} = 1/3$.

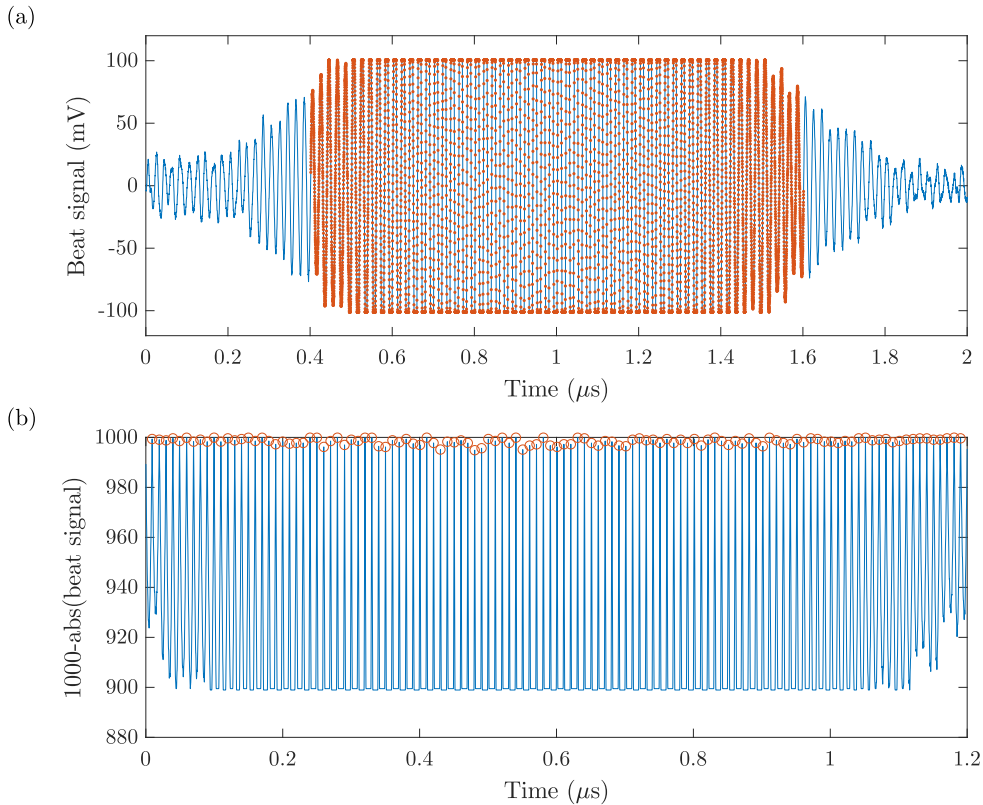


Figure 5.21: Data analysis of a single pulse beat signal. **(a)** The beat signal at around 50 MHz is recorded with a 100 ps sample rate. A window of integration, shown with orange points, is chosen in order to exclude noisy regions of small or no signal that will reduce the confidence of the frequency count. **(b)** An algorithm is used to find the number of zero crossings by detecting peaks in the negative absolute signal. During the integration time, the delay between subsequent zero-crossings is found and an average frequency recorded.

5.8 Frequency stability

We estimate the laser's performance as a frequency reference, and are interested in the frequency stability of the lasing pulses. Here we measure the frequency by counting zero-crossings of the beat oscillations which results in a single number for the frequency of each emitted pulse. A traditional counter-device relies on continuous signals and cannot be used here. Instead we record the full beat signal of a large number of pulses, and subsequently count the frequency in post-processing. This method is shown in figure 5.21 where a counting window is initially chosen from the recorded pulse-sequence, 5.21 (a). The zero crossings are then found by locating peaks in the negative square of the beat signal, 5.21 (b), and the inverse time difference between these zero crossings is used to find the average frequency.

We have seen in the above analyses that we are on the border of the bad-cavity regime, and that in particular for small Δ_{ce} it appears that the spectrum is dictated by the cavity resonance. In this case we expect the frequency stability to be limited by the cavity noise of our system. We measure the frequency stability in two different ways. The first method takes advantage of the reference light used to stabilize the

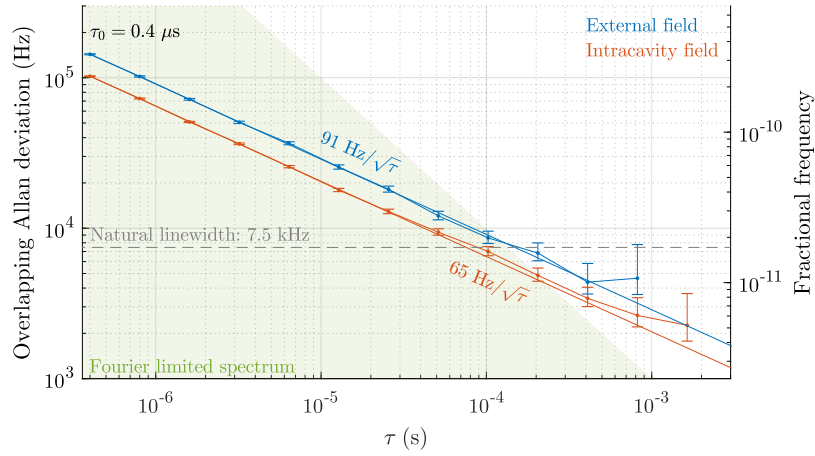


Figure 5.22: Overlapping Allan deviation showing the mean frequency stability of lasing pulses when the cavity is set to resonance $\Delta_{ce} = 0$. The beat is measured against the intracavity field used for locking the cavity length (orange), and against an external reference laser (blue). In orange the frequency stability is measured over 17609 pulses taken in four sections of 5 s with repetition rates of $t_{rep} = 1$ ms during a 10 minute interval. In blue 10094 pulses were taken in eight sections of 0.5 s with repetition rates of $t_{rep} = 0.5$ ms during a 10 minute interval. Both measurements use a gate time of $\tau_0 = 0.4$ μ s. The beat signals used to derive mean pulse frequency was recorded with reference to the cavity locking laser detuned at 781 MHz and mixed down to 50 MHz (orange) and the external reference laser of section 3.2.2 beating at 129 MHz and mixed down to 50 MHz (blue). Lines following a $\tau^{-\frac{1}{2}}$ dependency are fitted to the first seven points of each dataset. The frequency stability is better than the Fourier limited spectral linewidth within the green area.

cavity length. A beat between the laser pulse and this field could be expected to have most of the cavity noise and drift as a common mode. The intrinsic noise of the laser would, however, still show up in the beat signal. The second method relies on a beat with an external field that is independent on both the cavity locking reference and the generation of the pulse. For this method we use the reference laser described in section 3.2.2.

The overlapping Allan deviations of the two measurement methods are shown in figure 5.22. The cavity is stabilized as close as possible to atomic resonance $\Delta_{ce} = 0$. We use a gate time of $\tau_0 = 0.4$ μ s for both of our measurements, which ensures that we only count the pulse frequency when its signal-to-noise ratio is high. When measuring against the intracavity field, the pulse-to-pulse frequency deviation is about 100 kHz. At short times the overlapping Allan deviation is seen to scale as $\tau^{-\frac{1}{2}}$ which is an indication that the frequency distribution is Gaussian, and we are dealing with white frequency noise. We find the indication of a possible noise floor at an integrated pulse time of about $\tau = 2$ ms to be $\Gamma_{lasing} = 2$ kHz. This noise floor becomes visible as we exit the Fourier limited region marked in green on figure 5.22.

The limiting linewidths of this system are the inhomogeneous Doppler broadening $\Gamma_D = 2$ MHz, the cavity linewidth $\kappa = 620$ kHz, and the natural linewidth of the atomic transition itself, $\gamma = 7.5$ kHz. The stability is about a factor of two below

the natural linewidth, demonstrating that the laser linewidth can be more narrow than the transition it is derived from.

When using the external field we see that the entire noise-level increases approximately by 50%. The resulting noise floor agrees with the natural linewidth of the lasing transition to within 1σ . There is significant noise on the cavity caused by a poor lock to the stabilizing laser. With an ideal cavity lock and no atomic frequency pulling on the laser pulse frequency around resonance, we would expect an Allan deviation that did not hit a noise floor, but simply continued to average down as $\tau^{-\frac{1}{2}}$. In addition the instability goes to zero at all times for an infinite bandwidth. For some finite locking bandwidth, the deviations become non-zero. The difference between the Allan deviation derived from the intracavity field and that derived from the external field can then be seen as the locking efficiency of the cavity. Since the locking bandwidth of the cavity is exceedingly low (few Hz), and the resonance frequency is noisy, barely any noise suppression is observed.

This Allan deviation does not correctly present the behavior of the current machine if it were used directly as a frequency reference. We are ignoring the dead time of order 1 ms between each pulse, and simply defining the timescale as the "pulse-light-time" needed for a given stability to be reached. Because we ignore the dead time, the time-scale at which we start to see frequency drift and random walk of corresponds to a significantly different laboratory-timescale. The drift happens thus on the scale of seconds to minutes, and is aliased down to ms. Extrapolating the white frequency noise floor to $\tau = 1$ s will give us a laser linewidth of about 100 Hz – comparable to our prestabilized laboratory lasers shown in section 3.2.

The main limitation to the attainable linewidth of the lasing pulses is the cavity noise. The measurement against the intracavity field rejects all common-mode fluctuations, but because the cavity lock is exceedingly poor, this barely improves the frequency stability. To remove this limitation there are two approaches: reducing the fluctuations, or reducing the sensitivity to the fluctuations. The first approach is a technical problem, and will be pursued in the laboratory imminently. The second approach is what motivated the idea of a superradiant laser, and consists in pushing the physical system well into the bad cavity regime. This can be realized by significantly reducing the cooperativity C_0 , or by significantly reducing the ensemble linewidth. A reduction of the ensemble linewidth by cooling the ensemble down to μK level is already under way in both a further development of the current setup, and a newly designed continuous approach.

YTTERBIUM OPTICAL LATTICE CLOCKS AT NIST

Contents

6.1	Electronic sideband locking to a multi-color cavity	90
6.2	Lattice laser	91
6.3	BBR shift from localized heating in a window	93
6.4	DC Stark shift measurement and cancellation	95
6.5	Frequency evaluations	97
6.5.1	Systematic fractional frequency uncertainty of $1.4 \cdot 10^{-18}$	97
6.5.2	Fractional frequency stability at the 10^{-19} level	99
6.5.3	Remote inter-species atomic clock comparisons	99
	Absolute frequency measurement	100
	Loop closures	100
	Optical comparison stability	101

In this chapter, we will look at a very different system from the previous chapters. We will see some of the work I was part of on two ytterbium optical lattice clocks. These clocks rely on a much more mature methods, and represent the state of the art. While previous chapters have focused on investigating new paths, this will be focused on recent progress in what is currently recognized as the canonical approach. The ytterbium optical lattice clocks at the U.S. National Institute for Standards and Technology (NIST), Boulder are some of the best performing atomic clocks in the world [70], [71]. The two clocks are based on interrogation of the $(6s)^2\ ^1S_0 \leftrightarrow (6s6p)\ ^3P_0$ transition at $\lambda_{clock} = 578$ nm in neutral ^{171}Yb atoms trapped in a vertical one-dimensional optical lattice. The energy level scheme of ytterbium is very similar to strontium because of the two electrons in the outer shell, see

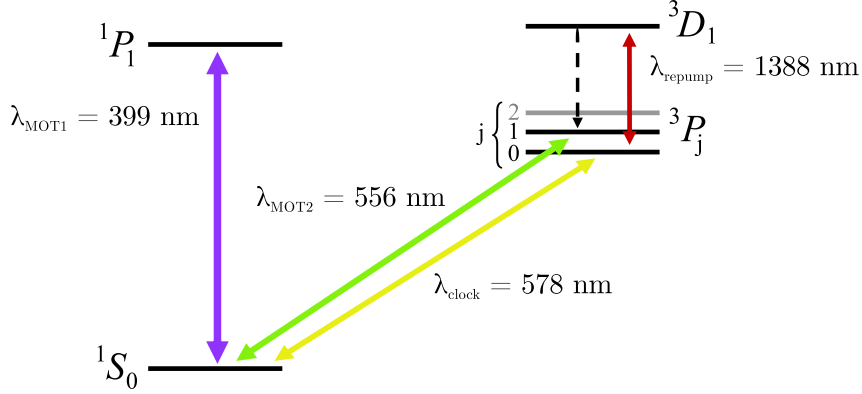


Figure 6.1: Simplified level structure of Yb. Here we show level structure and approximate wavelengths of the relevant transitions to the Yb optical lattice clock. The hyperfine structure is not shown.

figure 6.1. The nuclear spin is $I = \frac{1}{2}$ resulting in a simple hyperfine level structure when compared to the commonly used ^{87}Sr , $I = \frac{9}{2}$ isotope. The clock transition is spin-forbidden just like it is forbidden by the electronic angular momenta of the transition resulting in a natural linewidth of 7 mHz. An excellent introduction to optical lattice clocks can be found in [65].

The experimental system relies on atoms that are cooled using several stages of 3D MOT cooling. First they are slowed, and trapped using the 29 MHz wide $(6s)^2 1S_0 \leftrightarrow (6s6p) 1P_1$ transition at $\lambda_{MOT1} = 399 \text{ nm}$. The atoms are then further cooled in three consecutive traps on the spin forbidden 180 kHz wide $(6s)^2 1S_0 \leftrightarrow (6s6p) 3P_1$ transition at $\lambda_{MOT2} = 556 \text{ nm}$ before they can be loaded into the optical lattice. The lattice is run at the operational magical wavelength [15] near $\lambda_{\text{lattice}} = 759 \text{ nm}$, in order to effectively cancel lattice induced Stark shifts. The lattice traps on the order of 10^3 atoms in a trapping potential that is $50E_r$ deep, where $E_r = \hbar^2/(2m\lambda_{\text{lattice}}^2)$ is the lattice photon recoil energy, for an atom of mass m . This trapping depth ensures that the atoms are in the Lamb-Dicke regime, where the atomic motion becomes quantized. Here it is possible to resolve, and thus suppress the interaction with, atoms with different momentum quanta. See [3], [46], [47], [58], [59], [96] for an overview of the development of the Yb clocks at NIST.

In the optical lattice, spin-polarization is performed to purify the spin state of the atomic ensemble and quenched sideband cooling [89] allows us to reach temperatures of $T_{\parallel} = 500 \text{ nK}$ along the lattice axis, or maximal total temperatures of $T = 4.8 \text{ } \mu\text{K}$. This results in a sample of very well controlled atoms, isolated from most external perturbations, and allowing detailed measurements of the remaining systematic shifts and uncertainties of the resonance frequency. The atoms can then be used to synchronize a probing laser with the clock transition.

The probing laser is used to excite the atomic ensemble using either Rabi or Ramsey spectroscopy. When using Rabi spectroscopy we have a typical probing time of $\tau_{\text{probe}} = 560 \text{ ms}$ which corresponds to a full 65% of the total cycle time $\tau_{\text{cycle}} = 860 \text{ ms}$. The long interrogation time results in a Fourier-limited linewidth of the clock transition of 1.4 Hz as illustrated in figure 6.2. The high percentage of

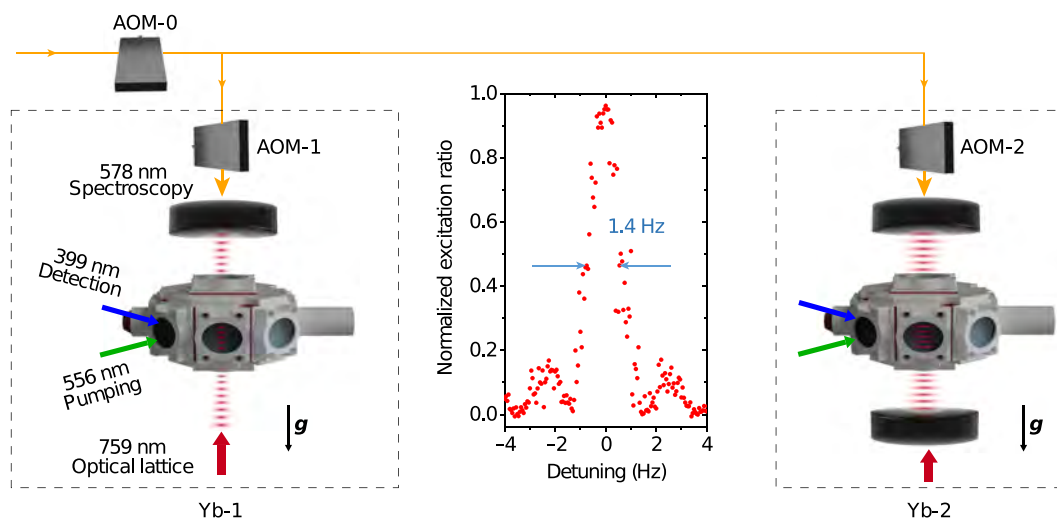


Figure 6.2: Conceptual sketch of the comparison of the two Yb clocks at NIST, and their Fourier-limited clock transition spectrum. The probing laser is derived from the same source, but distributed to the two systems, Yb-1 and Yb-2, through AOMs 0, 1, and 2. The laser frequency can then be locked to the atomic transition either by locking AOMs 1 and 2 to the respective clocks, or by locking the probing laser to one system via AOM-0, and recording the error signal on the other system. Once atoms are cooled and trapped in the optical lattice, spin polarization is done by the green $\lambda_{\text{MOT}2} = 556 \text{ nm}$ light, and sideband cooling via the narrow $\lambda_{\text{clock}} = 578 \text{ nm}$. Spectroscopy on λ_{clock} shelves the electrons in the clock state and detection is done subsequently using blue light, $\lambda_{\text{MOT}1} = 399 \text{ nm}$. An important difference between the two clocks is the lattice, formed by a retro-reflecting mirror in Yb-1 and a build-up cavity in Yb-2. The central plot shows the typical spectrum for Fourier-limited Rabi spectroscopy over $\tau_{\text{probe}} = 560 \text{ ms}$ with a FWHM of 1.4 Hz. The figure is taken from [70].

cycle time used for interrogation aids in reducing the influence of the Dick effect on the laser stability [119]. Measurements using Ramsey spectroscopy have been performed using a probe free evolution time of $\tau = 510 \text{ ms}$. Because both clocks use the same local oscillator, frequency corrections can be applied in two separate ways. i: to each probing arm independently through AOM-1 and AOM-2, or ii: only from Yb1 to AOM-0. In case i, the frequencies of the two systems are directly recorded via the servo signal, whereas case ii uses Yb2 as an external frequency discriminator.

While at NIST I had the pleasure of becoming a part of the clock team, and take part in a number of clock characterizations and frequency measurements. In addition I worked on a number of projects to improve the clock infrastructure. In the following I will briefly present some of this work. We will first look at some of the upgrades, and then the clock characterizations we made during my stay. Finally the current status of the frequency stability and accuracy as published in [70], [71] will be presented.

6.1 Electronic sideband locking to a multi-color cavity

In an effort to improve the reliability of the laser systems the performance of a multi-color reference cavity was investigated. The idea is to use a single reference cavity to lock several of the relevant laser systems. In order to improve the flexibility of such a setup we employ offset locking of the lasers by using electronic sideband modulation. This exploits PDH signals generated on first order sidebands by means of phase modulation or multiple frequency modulation in the EOM. It replaces the use of an AOM to patch the frequency detuning between the cavity resonance and the required laser frequency, and has the advantage of a very flexible tuning range over several GHz.

The cavity is designed to have a medium high finesse of about $F = 5 - 10 \cdot 10^3$ for a very large frequency range. This results in a cavity that can be used to lock lasers with wavelengths starting in the green and ending somewhere in the NIR. We tested the performance when locking three different colors at $\lambda_{\text{repump}} = 1388$ nm, $\lambda_{\text{lattice}} = 759$ nm and $\lambda_{\text{MOT2}} = 556$ nm. Light at λ_{MOT1} is frequency locked using modulation transfer spectroscopy on a Yb hollow cathode cell, whereas the clock light λ_{clock} is locked to an ultra stable cavity. Though the multi-color reference cavity is functional for all three wavelength, locking three different systems to the same cavity requires some planning. We choose to lock the lasers using the PDH technique and a combination of optical and RF filtering. Using different modulation frequencies for the lasers allows us to isolate a single laser error signal by filtering of the detected RF signal. This method can be generalized to any number of independent locks, limited only by the SNR reduction for each signal splitting, and the required locking bandwidth per lock. Figure 6.3 illustrates the setup.

Offset locking relies on the ability to lock a sideband rather than the carrier frequency of the signal. A sideband that is resonant with the cavity is generated by phase-modulation of the laser light. The phase modulation is done in an EOM with a pure RF frequency – typically in the hundreds of MHz. The locking signal for a PDH scheme could be obtained by adding a secondary RF signal to the same, or a subsequent EOM. This will result in PDH signals at both the primary carrier, and each of the primary sidebands. An alternative method relies on phase-modulation of the RF signal, that is, electronic sidebands. This results in a carrier-and-sidebands RF spectrum in the EOM rather than two distinct RF frequencies, see figure 6.4. The resulting electric field, E_{ESB} , of the modulated laser light becomes [111]

$$E_{\text{ESB}} = \sqrt{P_0} \exp \left\{ i \left[\omega_l t + \beta_1 \sin \left(\Omega t + \beta_2 \sin \Delta\phi t \right) \right] \right\}, \quad (6.1)$$

where ω_l is the laser carrier frequency and β_j is the modulation index of the optical and electronic sidebands respectively. The offset frequency is set by Ω which is the RF carrier frequency, and the sideband detunings are set by the RF phase modulation frequency $\Delta\phi$. The frequency of the original laser, ω_l , can then be tuned by adjusting Ω . The PDH signal is obtained by demodulating at $\Delta\phi$.

We were able to show that electronic sideband locking of multiple lasers at different frequencies to a single optical reference cavity was feasible, and the approach has now been fully implemented. One challenge was dealing with a large uncompensated residual amplitude modulation (RAM) in the fiber-coupled EOMs,

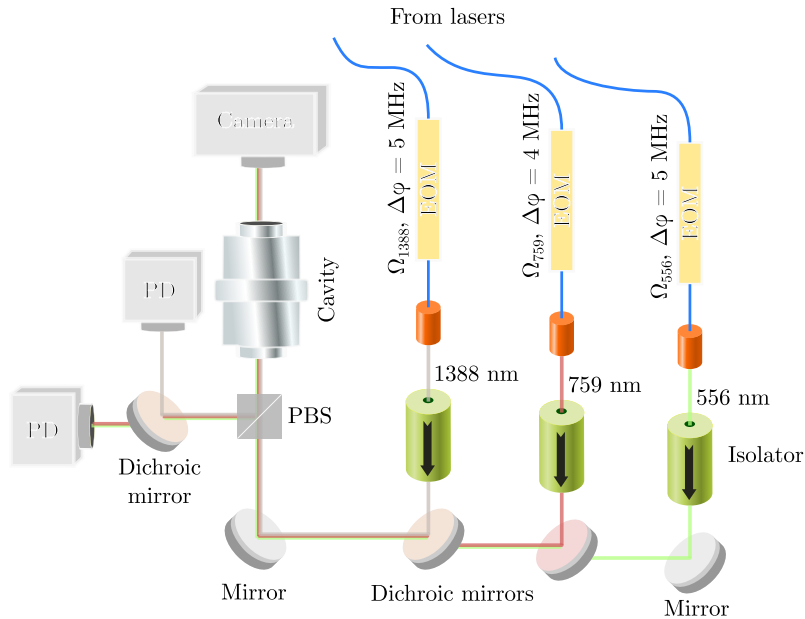


Figure 6.3: Multiple lasers locked to a single Fabry-Perot Cavity. Because of the incompatibility of detecting both 556 nm and 1388 nm on a single detector type, we split the reflected signal from the cavity between two detectors (Si and InGaAs based). This allows us to use identical PDH frequencies for two of the three lasers. The laser frequencies are locked to the cavity by means of electronic sideband locking (ESB). Phase modulation ($\Delta\phi$) of the RF-carrier signal (Ω) is thus used to generate the PDH signal.

which is particularly severe at high offset frequencies. For the broadband 1388 nm repumper, this was alleviated by doing the PDH modulation directly on the laser diode current.

6.2 Lattice laser

The NIST laboratory has two running Yb clocks, which have several similarities and several differences. Having two clocks is essential in order to be able to evaluate their frequency stability - especially when that stability starts to exceed everything else. It also allows asynchronously scheduled improvements of the setups, without complete down-time. Finally, having two clocks allows the efficient mapping of systematic effects in the two setups. In principle two clocks can be located within a single vacuum chamber, and have everything but the atoms in common [16]. When atomic clocks are compared, however, common mode noise in the two systems will go undetected. A reliable clock comparison, is thus a comparison in which the clocks are as independent of each other as possible.

Since the two Yb clocks were sharing a single lattice laser, an effort to make the atomic clocks more independent of each other was made by preparing a second lattice laser. The required power levels of the lattice laser is in the few W regime. For this a Ti:Sapphire laser pumped by 10 W of 532 nm laser light is used. In figure 6.5 a schematic of the lattice laser is shown, as well as the seeding light

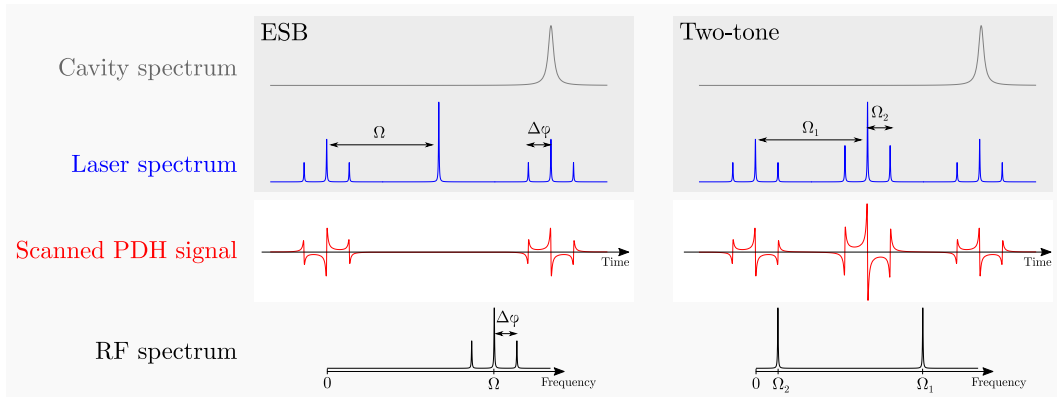


Figure 6.4: Overview of the electronic sideband (ESB) PDH scheme in contrast to a simple two-tone generated offset PDH locking. The ESB scheme relies on phase-modulation of the RF signal. The resulting error signal has PDH features of opposite signs at the first order sidebands ($\pm\Omega$). In contrast the two-tone scheme generates PDH features that all have the same sign. In addition the laser carrier frequency will also have a PDH signal. The ESB scheme thus results in a simpler error signal spectrum.

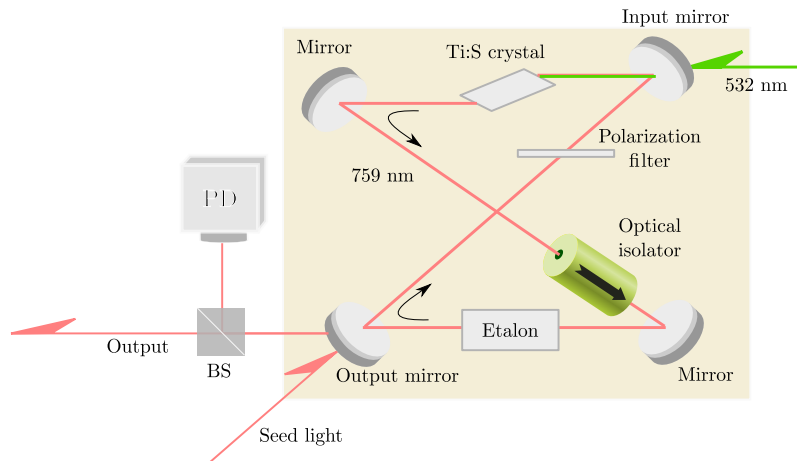


Figure 6.5: Injection locking of a Ti:Sapphire lattice laser. The laser cavity itself is a commercial product, where a titanium-doped sapphire crystal (Ti:S) is pumped and used as a gain medium, within a unidirectional traveling-wave cavity. The unusual PDH-configuration where transmission and reflection from the cavity is superimposed on each other has enhanced signal because of the cavity gain. the seed light is derived from a second, commercial ECDL laser, stabilized to the multi-color cavity described in 6.1.

and cavity locking scheme used. The Ti:Sapphire laser consists of a bow-tie cavity configuration. The pumping light is sent in through an input mirror, and creates inversion in the Ti:Sapphire crystal. Some systems use mode cleaning by means of polarization filtering, isolation of the direction of propagation, and an optical etalon to control the spectrum, but our system relies solely on the seed field in order to achieve single-mode operation at a well-controlled frequency. The seeding laser is based on an ECDL construction frequency stabilized to an external reference cavity as described in section 6.1.

The cavity length is stabilized to ensure resonance with the seed laser by means of a PDH signal. In contrast to traditional PDH stabilization, a traveling-wave cavity spatially separates the input beam from the reflected beam. The PDH signal is thus detected in the output arm of the cavity, where the carrier frequency has experienced considerable gain. This acts to amplify the signal size, and thus improves the cavity lock. While the lock of the seed light frequency to the multi-color reference cavity attained a bandwidth of 900 kHz, the Ti:S cavity piezo lock reached a bandwidth in the tens of kHz. The secondary lattice laser was successfully made ready for operation with an output power of $P_{out} \sim 4$ W.

The current lattice configurations are shown in figure 6.2. It is a one-dimensional vertical red-detuned lattice, leading to high confinement along the probing axis, with looser constraints on the radial dimension. In Yb-1 the retro-reflected standing wave can result in some traveling-wave component whenever an imbalance between incident and reflected beams occur. This degrades the lattice contrast, and leads to a finite shift of the clock transition. The reflecting mirror is also used as a reference surface for phase/fiber noise cancellation (FNC) of the λ_{clock} probing beam, in order to cancel any first-order Doppler shifts induced by shaking of the lattice standing wave. The waist radius at the atoms is $w_0 = 70$ μm . Yb-2 uses a build-up cavity which allows a reduction of the incident power. It also ensures that there is no traveling wave component in the lattice standing wave. In this setup the cavity mode is large, leading to a Gaussian waist radius of $w_0 = 175$ μm . In Yb-2 the top cavity mirror is used as reference surface for the probing laser FNC.

6.3 BBR shift from localized heating in a window

Of the many perturbations to the atomic clock frequency, the largest uncanceled absolute shift and limiting uncertainty is caused by the finite temperature of the atoms surroundings. This results in black body radiation (BBR) which in turn leads to an electromagnetic field that shifts the energy levels of the atom. An electronic energy level experiences a shift in energy [88] $\Delta E_g \propto (k_B T)^4 \alpha_0$, where k_B is the Boltzmann constant, T is the environment temperature and α_0 is the level polarizability. This means that an increase in temperature of the atomic surroundings can have severe influences on the shift of the atomic level. In order to reduce this effect, one approach is to place the atoms inside of a cryogenically cooled enclosure when probing them [78]. This reduces the absolute temperature of the field of view, and thus the total BBR shift of the atomic ensemble. At NIST the approach has been to use an enclosure kept at room temperature, but with a highly uniform temperature distribution, see figure 6.6 (a). The presence of several temperature sensors at representative geometrical positions, allow real-time monitoring of the temperature and highly precise corrections to the ensemble frequency. An earlier generation of this enclosure was described in [3].

The enclosure is a single piece of copper, internally coated with a highly absorptive layer of carbon nanotubes. These ensure that the radiation inside the enclosure can be described well as BBR and need not include stray reflections. There are two direct-access holes to allow the atoms to enter and exit the enclosure, and seven optically coated viewports for access of trapping, cooling and probing

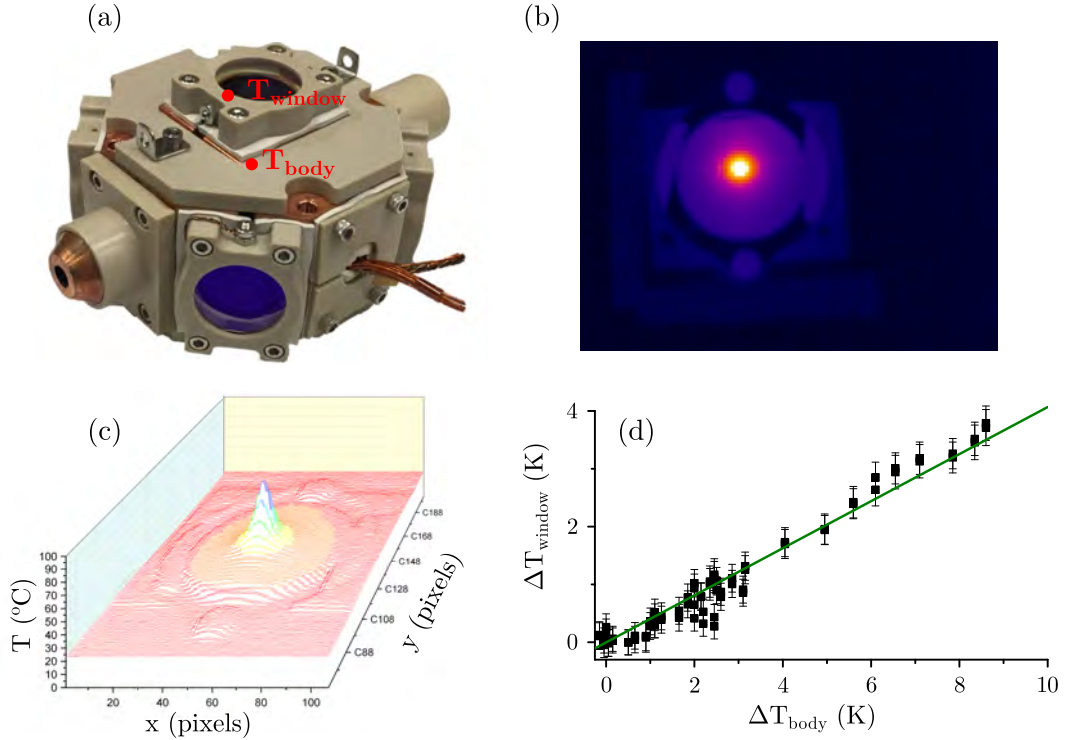


Figure 6.6: BBR enclosure and details of window heating measurements (a) The copper BBR enclosure used in both Yb-1 and Yb-2 systems. The enclosure fully encapsulates the atoms except for an entry (exit) hole at the bottom left (top right) corner of the picture. Temperature sensors are placed in a number of representative places, and here the approximate position of the window (T_{window}) and enclosure body (T_{body}) sensors are marked. The figure was taken from [4]. (b)-(d) A test setup is used to estimate localized heating of the window due to the lattice laser beams, using both green 532 nm light and λ_{lattice} light. (b)-(c) The temperature distribution across the window is recorded with a thermal camera, and (d) a dependency of the true window temperature discrepancy on the measured difference of the probes in (a) is found.

light. The high-intensity lattice beam also travels through these windows, causing a measurable heating on the associated temperature probes. Since we cannot have temperature probes on the window surface, the window temperature is measured by attaching a temperature probe to its edge. Because the BBR shift is so highly temperature dependent, a localized heating of the window could go undetected, and cause deviations from the modeled BBR environment.

In order to estimate the effect of local heating, test measurements of the thermal distribution across identical window samples were made. In order to avoid thermal conductance by air, a primitive ultra-low-vacuum chamber ($P = 1$ mBar) was constructed to house the measurements. A thermal camera was then used to measure the temperature distribution. An example picture of a laser-heated window can be seen in figure 6.6 (b). Measurements were made using up to 650 mW of lattice light, and up to 10 W of 532 nm light. Mapping out the temperature distribution over a window with an intense laser beam reveals a sharp temperature peak at the laser beam incidence, see figure 6.6 (c).

We can make a simple model for the temperature distribution by considering the window as a cylindrical disk of radius R and thickness t . Once the window temperature reaches a steady state, it will satisfy Laplace's equation $\nabla^2 T = 0$. The solution gives us the temperature distribution. In our geometry the temperature will be purely dependent on the radial coordinate ρ , and the window edge will have a temperature T_0 ,

$$T(\rho) = -\frac{\dot{Q}}{2\pi kt} \ln\left(\frac{\rho}{R}\right) + T_0. \quad (6.2)$$

The heat rate into and out of the window is \dot{Q} and k is the thermal conductivity of the material. The average temperature over the surface can then be found. Since the window is flat and relatively close to the atoms, we should integrate over the solid angle extended by the window rather than its area¹. Experimentally we mapped out the difference in measured window temperature and average window temperature (ΔT_{window}) against the temperature difference between the window edge and enclosure body (ΔT_{body}), see figure 6.6 (d). The measured window temperature and enclosure body are found with RTD's on the window edge and body respectively, whereas the average window temperature is found from the thermal imager. This gives a linear dependency, that is then used to deduce the resulting correction in the BBR shift on the two lattice clocks, and the added uncertainty.

The lattice configuration of the two clocks is slightly different, as one (Yb-1) relies on a simple retro-reflected lattice beam, whereas the other (Yb-2) has a build-up cavity. The build-up cavity increases homogeneity of the wavefront, and results in a broader lattice. The retro-reflection avoids a number of loss factors and results in less optical power absorbed in the enclosure windows. Typical temperature differences between enclosure body and window on the two setups (1,2) were $\Delta T_{window} = (85, 440)$ mK, resulting in added fractional frequency shifts of $(-1.2, -6.1) \cdot 10^{-19}$ and relative uncertainties of $(0.33, 2.8) \cdot 10^{-19}$. This corresponds to a factor of $(0.04, 0.28)$ of the total BBR shift uncertainty on the two systems [70]. The effect is thus not entirely negligible in Yb-2 where an estimate with improved uncertainties might be warranted.

6.4 DC Stark shift measurement and cancellation

The atom enclosure in figure 6.6 (a), not only acts as a homogeneous BBR enclosure, but also serves as a Faraday cage. The structure itself is made from copper internally coated with electrically conductive carbon nanotubes, and each window is coated on the inner surface with a thin conductive indium-tin-oxide (ITO) layer. This Faraday cage isolates the atoms from external electric fields which can cause DC Stark shifts of the atomic energy levels. External charges will in general cause shifts proportional to the square of the electric field. For a uniform electric field a frequency shift of $\delta\nu = kE^2$ will be introduced. Here E is the field magnitude, and k is a transition-dependent value. For non-uniform fields, the spatial distribution

¹This turns out to account for a correction factor of about 1.29.

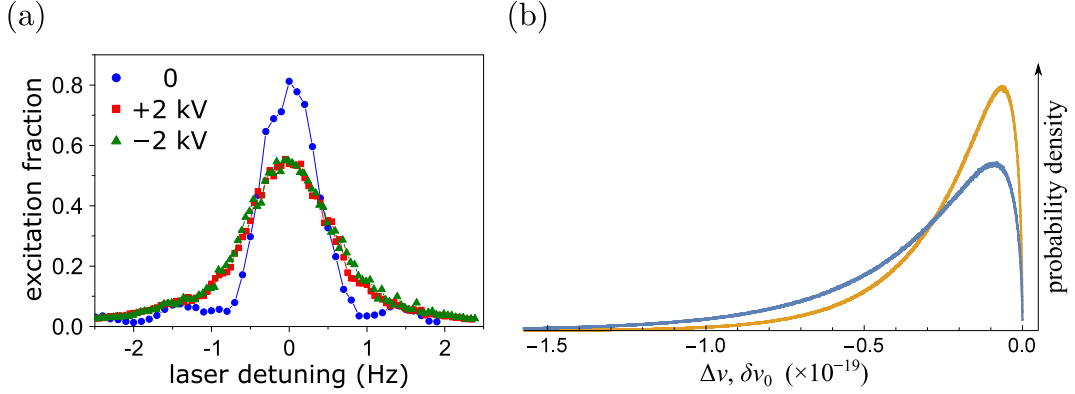


Figure 6.7: DC Stark shift measurements. (a) Spectroscopy of the clock transition. When a large electric field is applied to the windows of the BBR enclosure (figure 6.6 (a)), a DC Stark shift of the clock transition occurs. Here we subtract that shift to show the broadening with respect to the case of a fully grounded enclosure (blue). Red and green curves show the cases of ± 2 kV and ∓ 2 kV applied to the vertical-axis windows. The symmetry between the cases indicate the lack of any stray field gradient. (b) Through Monte Carlo modeling of the stray field-induced shift the yellow and blue probability distributions of homogeneous ($\Delta\nu$) and total stray-field shift ($\delta\nu_0$) respectively, are found. Figures are taken from [4]

of atoms within the optical lattice will cause an inhomogeneous broadening of the spectroscopic feature.

While one method to avoid DC Stark shifts is to measure and actively try and compensate for the stray fields present [8], [31], [64], [79], [80] a perfect reversal of the stray field distribution can be hard to achieve. Instead, the Faraday cage approach aims to passively reduce any stray electric fields [3], [54], [78], [113]. We show in [4] that this approach is sufficient to constrain the fractional DC Stark frequency shift of our Yb clocks to the 10^{-20} level.

The conductive window surfaces are isolated from the enclosure body, and can be individually electrically accessed outside the vacuum chamber. We can use them in order to artificially add electric fields across the atomic ensemble, and measure the resulting shift and broadening of the clock transition relative to an unperturbed atomic ensemble. Opposing windows of the enclosure in figure 6.6 (a) along the three spatial axes, form a basis that can be used to map out the full spatial dependence. We add electrical potentials of up to $V_i = \pm 2$ kV across the window surfaces, and measure the resulting shift and broadening of the transition line, see figure 6.7 (a).

For a total electric field consisting of some stray field \vec{E}_0 to be characterized, and a sum of applied fields $\vec{E}_i \propto V_i$, the total clock shift can be described by [4]

$$\delta\nu(V_1, V_2, V_3) = \delta\nu_0 + \sum_i a_i V_i + \sum_{ij} b_{ij} V_i V_j, \quad (6.3)$$

where the stray field shift is given by $\delta\nu_0 = k\langle E_0^2 \rangle$, the applied fields are responsible for the last term $b_{ij} V_i V_j = k\langle \vec{E}_i \cdot \vec{E}_j \rangle$, and a cross term given by $a_i V_i = 2k\langle \vec{E}_0 \cdot \vec{E}_i \rangle$. Applying controllable fields to the window faces thus allows an increased sensitivity

to the stray fields of the system through the cross term. The total stray field frequency shift $\delta\nu_0 = \Delta\nu + \delta\nu^*$ is given by a homogeneous component $\Delta\nu$ and an inhomogeneous component $\delta\nu^*$ caused by the finite extent of the atoms. By applying voltages to the windows and subsequently reversing their polarity, we can map out $\Delta\nu = \sum_i \frac{a_i^2}{4b_{ii}}$, and find that it is consistent with zero for all measurements. Using a Monte Carlo approach we find a 95.5% confidence intervals of $-6.7 \cdot 10^{-20} < \Delta\nu < 0$, see yellow distribution of figure 6.7 (b).

The blue curve in figure 6.7 (a) shows the clock transition in the case where all windows are grounded. Here, only left over stray fields are present, and we see a Fourier-limited transition linewidth of ~ 1 Hz. By applying $V_i = \pm 2$ kV – here done over the vertical direction (red and green curves) – broadening of the transition proportional to the stray and applied field gradients is expected. If the applied field anti-aligns with a stray field, the broadening is expected to be reduced as the effective potential seen by the atoms will be reduced. After adding uncertainties due to geometrical considerations of the experiment, a total systematic uncertainty (95.5% confidence) of $-1.0 \cdot 10^{-19} < \delta\nu_0 < 0$ is found – see the blue curve of figure 6.7 (b).

6.5 Frequency evaluations

Throughout my stay at NIST we ran comparison campaigns of the two Yb clocks. In order to estimate systematic uncertainties on one clock, the other is often used as a reference where the parameter under investigation is kept constant. In a similar fashion we compare the two clock frequencies to each other while keeping all parameters constant. This allows us to estimate the frequency stability of the systems under operational conditions. When a reference clock is being used to map out systematic effects on the other clock, it can also be used to compare its frequency with an external reference. During several campaigns, the ^{171}Yb clocks were compared to an off-site ^{87}Sr optical lattice clock, an on-site $^{27}\text{Al}^+$ ion clock as well as international ^{133}Cs and ^{87}Rb frequency standards through satellite time and frequency transfer and a local ensemble of H-masers.

6.5.1 Systematic fractional frequency uncertainty of $1.4 \cdot 10^{-18}$

In [70] we present the full uncertainty budget for the two Yb atomic clocks. Mapping out the total uncertainty budget is a large task where methods and equipment is incrementally improved over a long period of time. The final budget presented is thus the culmination of several years of research, and the effort of a large number of researchers. Above we discussed a few of the sources of uncertainty, namely the BBR shift and the DC stark shift. A number of AC stark shifts, magnetic shifts and collisional shifts also have to be taken into account, just like technically introduced errors via the servos. A thorough investigation of these effects can be found in [4], [15], [70]. The current low levels of uncertainty necessitate some level of real-time correction to the atomic clock frequency. As such both the Zeeman shift and BBR shifts are measured throughout the session, and while the Zeeman shift is canceled

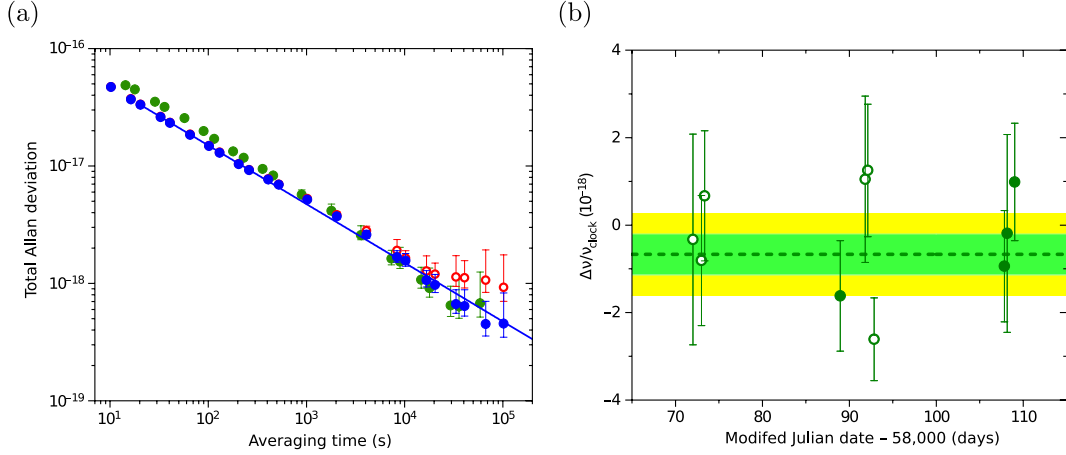


Figure 6.8: Clock performance. **(a)** Total Allan deviation of the comparison of the two Yb clocks, showing a fractional frequency instability below 10^{-18} . Blue and red points represent a single measurement session using synchronized Rabi interrogation in the two Yb clocks. Green points are from a separate measurement session using unsynchronized Ramsey spectroscopy. The BBR shift is measured in real-time and each frequency measurement is corrected for the time-dependent shift in the blue and green datasets. Red points are not corrected. **(b)** The reproducibility of the systems are shown by the frequency differences for 10 blinded measurement sessions. Each measurement session is taken in either configuration i (filled circles) or ii (empty circles), as described at the beginning of the chapter and in figure 6.2. The mean value is given by the dashed line with green and yellow areas showing the statistical and total 1σ uncertainty respectively: $(\nu_{Yb2} - \nu_{Yb1})/\nu_{\text{clock}} = (-7 \pm 5_{\text{stat}} \pm 8_{\text{sys}}) \cdot 10^{-19}$. Errorbars represent the 1σ uncertainty obtained from the total Allan deviation of the given session. The figures are taken from [70].

by means of the measurement protocol, the BBR shift is currently corrected in post-processing. Figure 6.8 (a) shows frequency stabilities of the system with (blue) and without (red) measurement-by-measurement compensation for the BBR shift.

As a result of these investigations we were able to present two independent Yb optical lattice clocks, each with a fractional frequency uncertainty of $1.4 \cdot 10^{-18}$. At the time of writing this constitutes the lowest frequency uncertainty yet on any clock. The low 10^{-18} range of fractional frequency uncertainty is interesting in that it marks the limit of performance for accurate determination of the gravitational frequency shift uncertainty as measured across long baselines. Because time moves slower in high gravitational potentials relative to an external observer, the altitude with respect to the earth geoid can have a rather large influence on the frequency measured by a clock [40]. The fractional frequency change $\Delta\nu/\nu$ for a given height difference h close to the geoid is given by

$$\frac{\Delta\nu}{\nu} \approx -\frac{gh}{c^2}, \quad (6.4)$$

where g is the acceleration due to gravity, and c is the speed of light. Modern geopotential measurement rely on the global navigation satellite system (GNSS) and preexisting geoid models, and are reliable down to an accuracy of two centimeters in height [24], corresponding to a fractional frequency uncertainty of $2.2 \cdot 10^{-18}$. If a relative height measurement between closely located points is desired, classical

spirit leveling methods can reach even higher accuracies at the millimeter level. The absolute uncertainty of the NIST Yb clocks is thus better than the uncertainty on the geopotential of the system, which is $6 \cdot 10^{-18}$ and realized by geodetic measurements from the Terrestrial Time reference surface. With an absolute uncertainty of 1.3 cm, these atomic clocks are thus better geopotential measurement tools than the preexisting methods.

Over the course of over a month, the clock frequencies have been compared, in order to verify the consistency of the measurements. Figure 6.8 (b) shows ten such blinded measurements, where the frequency difference was kept from the operators of the clocks during each measurement session in order to avoid any operator-bias. The comparisons show an average frequency deviation between the two clocks of $7 \cdot 10^{-19}$. This is consistent with zero within the systematic uncertainty between the two systems of $\pm 8 \cdot 10^{-19}$, and shows a statistical uncertainty of $\pm 5 \cdot 10^{-19}$.

6.5.2 Fractional frequency stability at the 10^{-19} level

In figure 6.8 (a) we show the total Allan deviation from two comparison sessions between the two Yb clocks. The blue and red dots are from a 72-hour synchronous measurement on the two systems using $\tau = 560$ ms Rabi spectroscopy, whereas the green dots are from an unsynchronized $\tau = 510$ ms Ramsey interrogation. Both measurements show measurement instabilities below 10^{-18} with a single clock instability of $4.5 \cdot 10^{-19}$ reached after 36 hours, and an extrapolated $3.2 \cdot 10^{-19}$ after the full measurement time. This is the lowest instability recorded for an atomic clock. It underscores the degree of control over drifts and indicates for this particular measurement that the limiting frequency uncertainty is not caused by insufficient control of the system parameters.

The total Allan deviation of figure 6.8 (a) shows no signs of flattening, but decreases with $\tau^{-1/2}$ as expected from white frequency noise. The averaging time is thus limited by the 1 s stability of the interrogation laser, and introducing an interrogation laser with even higher stability [68], [83], [92] will immediately reduce the required integration time to reach a given instability. The high precision shown here would allow *local* gravity comparisons of the clocks equivalent to 3 mm of change in the gravitational potential.

6.5.3 Remote inter-species atomic clock comparisons

While primary frequency standards are based on ^{133}Cs in accordance with the SI definition of the second, the International Committee for Weights and Measures (CIPM) has also classified a number of secondary frequency standards. Yb is currently a secondary frequency standard and is one of the possible candidates for a new definition of the second [7]. NIST is currently working to incorporate the clocks into their time scale [123], [124].

Besides in-lab comparisons between the two Yb atomic clocks, several external comparisons were made. These span comparisons to the SI definition of time, realized by the International Atomic Time (TAI) [71], a local comparison to the NIST Al^+ ion clock [14], [42], as well as a remote comparison to the Sr optical lattice clock at JILA were performed [12], [60], [83]. ^{87}Sr and $^{27}\text{Al}^+$ are both recognized as

secondary representations of the SI second. Frequency comparisons with the optical atomic clocks have not yet been finalized, but manuscripts are in preparation. These were performed, at least partially, as three-way comparisons, with all atomic clocks operating simultaneously, and comparisons being made locally at NIST through frequency combs [61].

Comparisons of the Yb clocks to international atomic clocks are made by means of satellite time and frequency transfer. At NIST, Boulder, an ensemble of hydrogen masers realize a timescale denoted AT1. Sensitivity to environmental perturbations can be reduced by modifying the weighting of the masers in the ensemble. This creates a post-processed timescale AT1E with increased stability. This timescale is steered to the TAI timescale in order to improve long-term stability. Locally this time scale can be continuously compared to the Yb clock frequency. The International Bureau for Weights and Measures (BIPM) makes comparisons of the AT1 timescale and TAI, and also publishes timescale measurements made with international primary and secondary frequency standards (PSFS).

Absolute frequency measurement

During parts of the Yb clock operation, both Cs and Rb frequency references were reported as part of the PSFS. This allowed us to make high-accuracy comparisons with both atomic species. Cs and Rb atomic clocks are microwave clocks that both have higher fractional frequency uncertainties than the Yb clocks. Nevertheless, because of the SI definition of the second, an absolute frequency measurement of Yb must be made with respect to Cs clocks. The fact that optical atomic clocks are performing much better in terms of both accuracy and stability than their microwave counterparts, means that the second must eventually be redefined [7]. In order to ensure reliability of that redefinition as well as a smooth transition it is required that absolute frequency measurements of the contestants for a redefinition are limited by the uncertainties of the Cs clocks. In addition frequency comparisons between different optical references must also be realized to at least the uncertainty of the current definition. Previous fiber [40], [78], [105] and satellite-based [35] comparisons of ^{171}Yb and ^{87}Sr have shown uncertainties below the 10^{-16} -level – a feat that Cs clocks have not yet been able to do.

Figure 6.9 (a) shows the measured absolute frequency deviations of Yb for different atomic clocks, with the NIST clock in blue. The most recent measurement agrees well with the mean of previous reported values, and to within 2σ of the previous measurement reported by NIST [59]. Contributions to this measurement were made during an eight-month long campaign, whose monthly values are shown in the blow-up. As reported in [71] the result was a measured absolute Yb frequency of 518 295 836 590 863.71(11) Hz with a fractional frequency uncertainty of $2.1 \cdot 10^{-16}$. This absolute frequency measurement is limited by the uncertainty of the primary frequency standards, and also constitutes the most accurate absolute frequency measurement of any species.

Loop closures

The absolute frequency measurement of Yb allows an improved uncertainty on the loop-closure of frequency comparisons. This is a consistency check of the pairwise

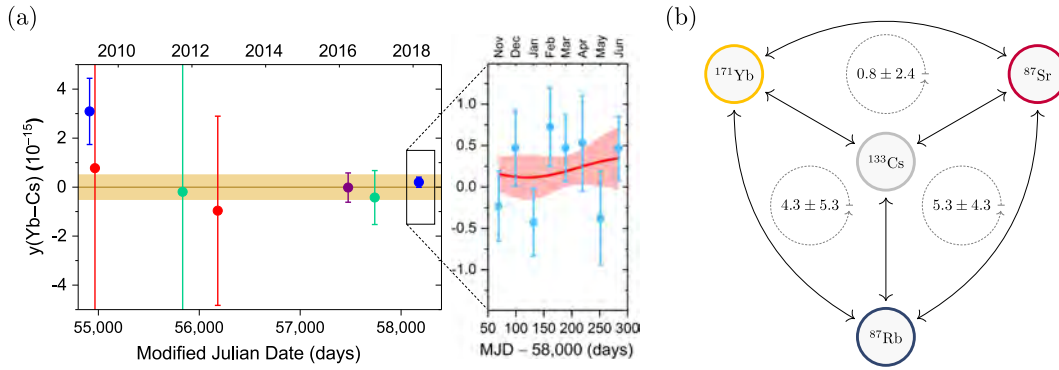


Figure 6.9: Absolute frequency measurement and comparison-loop closures. **(a)** Seven absolute frequency measurements of the clock transition in ^{171}Yb spread over almost 10 years. Red points are from measurements done by the National Metrological Institute of Japan (NMIJ) [52], [125], green points are from the Korea Research Institute of Standards and Science (KRISS) [51], [85], purple is from the Italian Istituto Nazionale di Riserca Metrologica (INRiM) [87], and the blue points are from NIST [59], [71]. The final point represents the current measurements taken over eight months as detailed in the inset. **(b)** Absolute frequency measurements together with optical frequency ratios allows comparison-loop closures that can serve as consistency checks. The work presented in [71] leads to two new loop closures with Yb. The numbers indicated are fractional frequency misclosures of the loops given as parts in 10^{16} . The figures are taken from [71]

frequency comparisons that is typically done between clocks. All combinations of frequency comparisons in the Cs-Sr-Yb-Cs chain have previously been made, but with the improved measurement of the Yb frequency we obtain an accumulated fractional frequency difference of $(0.8 \pm 2.4) \cdot 10^{-16}$. This misclosure is calculated from the relative difference between an optically measured frequency ratio ($\nu_{\text{Yb}/\text{Sr}}$) and the frequency ratio derived from absolute measurements (ν_{Yb} and ν_{Sr} ,

$$\text{misclosure} = \frac{\nu_{\text{Yb}}/\nu_{\text{Sr}} - \nu_{\text{Yb}/\text{Sr}} \left(\pm \sqrt{\Delta(\nu_{\text{Yb}}/\nu_{\text{Sr}})^2 - \Delta\nu_{\text{Yb}/\text{Sr}}^2} \right)}{\langle \nu \rangle} \quad (6.5)$$

where $\langle \nu \rangle$ is the average frequency of the ratio, which is important only to the precision of a few digits. An additional loop-closure of the Rb-Sr-Yb-Rb chain was afforded by the contribution of frequency measurements by LNE-SYRTE with a Rb fountain to TAI in the given period. This loop yields a difference of $(4.3 \pm 5.3) \cdot 10^{-16}$. Both loop residuals are consistent with zero to within 1σ , and are illustrated in figure 6.9 (b). The final loop residual shown in the figure is enabled by a Sr/Rb ratio measurement [63] with the same Rb fountain clock at LNE-SYRTE.

Optical comparison stability

The three-way comparison of optical frequencies performed between NIST and JILA, was done through 1.5 km of optical fiber on two separate frequency combs, as well as through free-space frequency transfer. This redundancy in the comparison allows characterization of the instability in the comparison modules themselves in addition to the three optical ratios. In figure 6.10 we show the typical daily fractional frequency instability for all components of the comparison. The free-space link and fiber link (Boulder Research and Administration Network – BRAN)

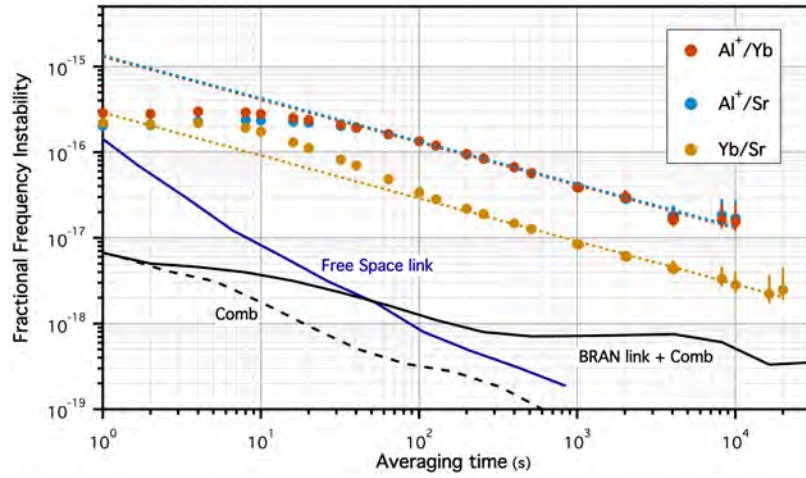


Figure 6.10: Preliminary plot of the fractional frequency instability of optical comparisons between the ^{171}Yb , ^{87}Sr and $^{27}\text{Al}^+$ optical clocks at NIST and JILA. The dashed lines are weighted fits to all points above 100 s, indicating ratio uncertainties of $3.6 \cdot 10^{-16} / \sqrt{\tau}$ for the Yb/Sr comparison and $1.4 \cdot 10^{-15} / \sqrt{\tau}$ for the Al $^+$ /Yb and Al $^+$ /Sr comparisons. Also shown are instabilities of the measurement systems that are shown not to limit the comparisons. The figure taken from [60].

show instabilities well below the ratio measurements, just as the frequency combs are not a limitation.

The three clock comparisons show exceedingly low instabilities after about 3-4 hours of averaging. The comparisons with Al $^+$ are limited by the quantum projection noise of the single ion, to the 10^{-17} -level. The $^{171}\text{Yb}/^{87}\text{Sr}$ comparison reaches an instability of $2 \cdot 10^{-18}$. This is the first time inter-species optical comparisons have been made with such high stability, which showcases how the measurements are now limited by and significantly outperform the current Cs fountain clock standard.

CONCLUSIONS AND OUTLOOK

This thesis presents a number of experiments on cavity-enhanced atomic systems as the basis of new atomic clocks. These systems rely on cold strontium atoms which are currently one of the best-performing atomic species used in optical lattice clocks. We emphasize simplicity and use thermal atomic ensembles in order to create proof-of-principle demonstrations of the capabilities of the systems. The use of a broad clock transition (in the world of atomic clocks) reduces the ultimate performance of our experimental realizations, but promises more compact solutions than would be possible otherwise.

The chapters on systems with cavity-enhanced interactions relied on strontium, whereas a final chapter on the current performance of a state-of-the-art atomic clock at NIST is based on a second favored atomic species for optical lattice clocks, ytterbium. This chapter shows the great deal of effort necessary to realize a high-accuracy clock. A characterization effort whose results can hopefully be transferred by a high degree to new systems relying on these atomic species.

7.1 Prospects for a NICE-OHMS clock

The preliminary investigation of the NICE-OHMS technique with cold strontium looks promising in terms of expected laser linewidths in the tens of mHz range. It relies on the resonant dispersive measurement of a saturated absorption signal, which can be used directly as an error signal for an interrogation laser.

The signal-to-noise ratio of the current experimental setup is too poor for efficient locking, and an improvement of this system is necessary in order to realize frequency stabilities that are relevant in the current efforts of atomic clocks. So far we have used the system as a testbed for the physical models, in order to improve our understanding of the physical behavior. Initial measurements indicated good agreement of the experiments with the model and simulations [112], [120], but we found that a modification of the cavity interaction was necessary [18]. As system parameters were upgraded, the increased optical density resulted in severely dis-

torted dispersion signals that agreed only with the modified theory, as presented in chapter 4 and [99].

These proof-of-principle measurements and characterizations of the system has thus yielded a good understanding of the physics in the system, and a great foundation for the further improvement towards a functioning frequency reference. In order to realize the system as an atomic clock, some important points needs to be addressed: the frequency accuracy, the signal-to-noise ratio, and the interrogation deadline.

Rigorous investigation of *frequency shifts* in the system is necessary in order to consider the system as an atomic clock of any level. Here the simplicity of the setup is a double-edged sword. Since there is no confining lattice like in an optical lattice clock, light shifts from the trapping potential is not an issue. However, the high temperature of the atoms results in a number of shifts and broadening effects that will need to be taken into account. Though the technique relies on Doppler-free spectroscopy, second-order Doppler shifts and collisional broadening or shifts will become relevant.

The low *signal-to-noise ratio* of the atom spectroscopy is currently adding noise to the laser frequency when locking. At $\tau = 1$ s this noise is at least an order of magnitude above the laser stability. The noise in the spectroscopic signal is caused by both electronic noise and loss in detection scheme and by variations in the atomic parameters. Noise in the enhancement cavity and atom number means that the spectroscopic conditions vary from shot to shot, effectively reducing the signal contrast. This necessitates high probing powers which will increase the signal size, but also leads to significant power-broadening of the saturated dispersion signal.

Interrogation *deadline* is problematic as it allows the clock laser to evolve freely between corrections. This means that laser frequency noise can be uncompensated for large ratios of the clock cycle. Our simple setup allows very short cycle times ($< 100 \mu\text{s}$), but also severely restricts the probing time.

We are currently following two roads to improve the experimental parameters. One approach is to reduce the atomic temperature by adding a second-stage red MOT. This would reduce the atomic temperature to the 10–100 μK range. This adds more atoms to the “zero-velocity” class and as a result the dispersion slope increases significantly. This approach is currently being taken on the Sr-1 3D MOT machine. A second machine (Sr-2) is being constructed in order to feed a continuous beam of mK temperature atoms through a medium-to-high finesse cavity. The increased cavity finesse results in an increased dispersion slope, but shot-noise limitations on the detection might necessitate a significant amount of transition power-broadening. A continuously fed cavity also yield a continuous error-signal. This in turn promises the possibility of zero-deadtime clock operation, and severely suppresses the free wander of the reference laser.

7.2 Prospects for a superradiant clock

The second road we have followed here is the investigation of an active optical clock based on bad-cavity lasing. This approach utilized the same atomic ensemble as the NICE-OHMS experiment. The goal has been a superradiant laser, but in

the present investigations we are in the crossover regime between a good- and a bad-cavity laser. Only deep in the bad-cavity regime can we truly call the system a superradiant laser.

We have shown that the cooperative interaction of the atoms result in pulsed lasing into the cavity mode, and have characterized the time evolution of the system under a range of different circumstances. The lasing threshold was shown to exhibit a quadratic scaling of output power with atom number, as expected from a superradiant system. At increased atom numbers this scaling becomes linear, due to increased power in the cavity mode. The coherence of the system thus switches between being preserved primarily by the atomic ensemble, and the cavity mode. A mean-field theory simulation of the system showed excellent agreement with the experimental results. This is a precious tool, that has allowed considerable insight into the dynamics of the atomic evolution. It remains a semi-classical approach though, and as the system is pushed deeper into the low-photon-number regime, more quantum behavior will have to be taken into account.

The cyclic experiment currently has no excited-state repumping, and the pulse length is thus determined by the cooperative enhancement of the spontaneous decay rate. This in turn Fourier limits the spectral linewidth that we can obtain. Accordingly the frequency stability is considerably worse than what we would expect from a continuous system. The investigation of the spectral properties of the system is currently being prepared for publication [107].

Seeding the atomic ensemble with an external optical field, allowed more than 40 dB of amplification of $P_{seed} < 10$ pW light. We made preliminary investigations of the phase-quality in the amplifier configuration, and will investigate this approach further in the future [101].

In order to realize a superradiant frequency reference we need to reduce the amount of noise in the system, reduce the spectral sensitivity to cavity fluctuations, and attain continuous operation. The reduction of noise is a technical challenge which must improve the overall reliability of the system and reduce both mechanical vibrations and electronic noise in the cavity length. Spectral sensitivity to cavity noise is given by the cavity pulling factor $\xi = \frac{\Gamma}{\Gamma + \kappa}$, and is reduced by moving further into the bad-cavity regime. In order to retain superradiant lasing this must be done by cooling the atomic ensemble below mK. While a first approach to continuous operation could be done by repumping the atomic ensemble, atoms are lost after ~ 1 ms because of their thermal velocity. A truly continuous laser must then be realized using a continuously flowing beam of excited-state atoms.

Both *technical improvements and reduction of temperature* will be pursued in the current setup. Laser systems are currently being improved, and the cavity electronics will be thoroughly reworked. A second-stage red MOT on the lasing transition will be constructed in order to reduce the atom temperature by one or two orders of magnitude. The result should be reduced decoherence in addition to a reduced cavity-noise sensitivity of the system. *Repumping* will also be implemented in order to prolong the lasing duration. To realize a clock the accuracy of the final system must also be carefully investigated.

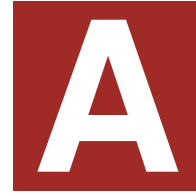
Finally a *truly continuous* system for superradiant lasing (Sr-3) is being developed in collaboration with the iqClock consortium. This system will deliver a continuous

dipole-trap-confined beam of cold atoms to a lasing cavity. The atoms will be continuously fed through the cavity with a temperature along the cavity axis of order $10\ \mu\text{K}$. The atoms will be cooled through several MOT and optical molasses steps before entering the cavity mode in the excited state. Here they will emit collectively into the cavity mode while repumping of ground-state atoms is performed to further increase the effective atom number. The low temperatures in combination with an increased cavity linewidth will ensure that the system is well within the bad-cavity regime. Noise in the cavity mode will also be suppressed by careful design of chamber and mounting mechanisms.

The investigations presented here thus provide an important stepping stone for further development of superradiant lasers. While we do not expect a superradiant laser based on the $7.5\ \text{kHz}\ ^1\text{S}_0 \rightarrow ^3\text{P}_1$ transition to perform as well as a state-of-the-art optical lattice clock, it could afford an excellent alternative for mid-range performance in the low 10^{-15} fractional frequency stability. Such a system might be realized much sooner than a truly continuous superradiant laser on the narrow clock transitions offered by, e.g., Sr and Yb.

Traditional optical lattice clocks have been rapidly improving for years, and as the systems start to move towards higher levels of control the quantum limitations become increasingly important. As traditional atomic clocks continue to improve they incorporate techniques previously seen in other areas of atomic physics. These techniques include 3D lattices [16], cavity-enhanced readout [114] and entanglement of atoms [49], [55]. The two new approaches we have taken here are manifestations of this tendency. Isolated, they could allow for more compact schemes. As hybridizations with traditional atomic clocks, they might prove to be the next step in the evolution of optical atomic clocks.





DESIGN DETAILS FOR A CONTINUOUS COLD-ATOM MACHINE AT NBI

Contents

A.1	Oven design	108
A.2	MOT coils	108
A.3	Interference filter laser	110
A.4	Some cavity designs	113
	A.4.1 Sr-2 probing cavity	113
	A.4.2 Transfer cavity	115

All initiatives presented in this thesis rely on the cyclic operation of a cold-atoms machine that traps and loads atoms within the interrogation or physics zone. This results in significant deadtime in between probing sequences, though the techniques themselves should work continuously. If cold atoms can be loaded continuously without suffering the perturbations and decoherence caused by cooling beams this would thus significantly improve the systems. We currently have two parallel efforts towards continuous cold strontium machines. The first machine is being built in Copenhagen with the purpose of delivering mK-temperature atoms from a 2D blue MOT directly to the physics cavity. This system – Sr-2 – will not see an improvement in the thermal properties of the atoms, but will simply mark the shift from cyclic to continuous.

In addition a third system – Sr-3 – is under development in collaboration with Florian Schreck at the University of Amsterdam and the iqClock consortium under the EU Quantum Flagship initiative. This system will be developed with the primary goal of creating a continuous superradiant laser. The main experimental facilities are being constructed in Amsterdam, with Copenhagen driving the investigations on how to achieve superradiance, and constructing the physics chamber.



Figure A.1: Picture of the capillary tube holder for the Sr-2 oven, with tubes mounted.

This system will use continuous atom cooling techniques that university of Amsterdam are experts in, and will subsequently be transported to Copenhagen.

Here we will show some of the designs and characteristics of the Copenhagen Sr-2 machine. This includes photos of current assemblies and technical drawings of the design. This appendix is primarily for future reference of people working on said experiment.

A.1 Oven design

Our previous machines and reference oven have all relied on simple ovens with a single central hole of 1 – 2 mm in diameter. In order to reduce coating of the oven chamber windows which will be used for 2D molasses, we designed a simple oven lid with micro-capillary tubes. These tubes serve to retain the atoms with large transverse velocities inside the oven, and results in a more collimated output beam. Here we show the design merely for future reference.

The oven lid clamps onto a separate tube holder as pictured in figure A.1. The holder is circular with an inner circular aperture of 4 mm in diameter, and a slit to provide some elasticity for holding the tubes in place. Mounted with the capillary tubes it holds a total of 132 tubes. Because of the circular geometry a triangular packing is not possible, and the tubes will be loose in some regions. To avoid large gaps and tubes falling out, slivers of metal are wedged in between the tubes to fasten them. The tubes themselves are 8 mm in length and have an inner diameter of 150 μm with an outer diameter of 300 μm .

A.2 MOT coils

The Sr-2 system is designed around welded vacuum parts, and use a 2D MOT in order to transversely cool the atomic beam and simultaneously deflect it out of the longitudinal Zeeman cooling beam. The model in figure A.2 shows the end of the coil-wound Zeeman slower at the lower left corner, followed by a 7-way cross in the center where the 2D MOT will be. A thin tube for the atoms extend back to the

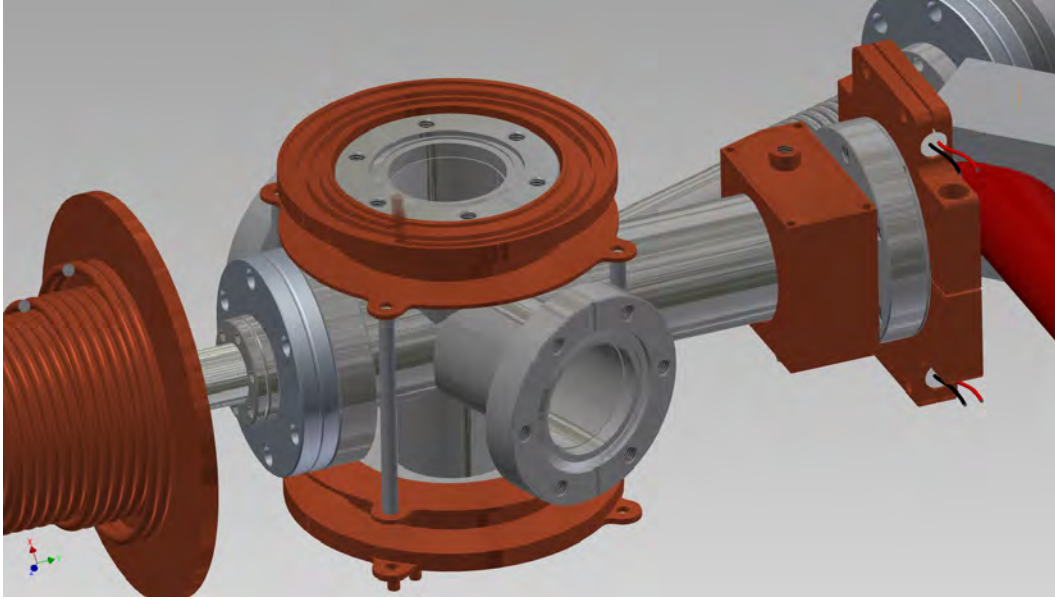


Figure A.2: Model of 2D MOT section in Sr-2 machine. Vacuum chambers are shown in gray, and made of stainless steel. External heaters and coolers are all made from copper, and shown in brown. In the center the 2D MOT chamber is shown with its magnetic coils on top and bottom. Lower left shows end of the Zeeman coil, and right in front shown the Zeeman window with heater and cooler. The heater increases the temperature of a sapphire window in order to avoid strontium coating deposits. In the upper right back, the atoms are led towards the physics chamber.

upper right corner of the drawing and an arm for the Zeeman viewport stretches to the right. The Zeeman window is made of sapphire and mounted with a copper heating element on the DN40CF window flange, and a block for water cooling immediately before.

The MOT coils are mounted on two holders shown in the center of the model. They are made out of copper and arranged in an anti-Helmholtz configuration. The holders both feature cut-outs for water cooling on one side, with the lids removed in figure A.2 for visualization. A temporary build with the MOT coils mounted on a vacuum chamber was used to map out the axial magnetic field of the coils as shown in figure A.3. We used about 135 windings on each coil, and the wire has a cross-sectional diameter of 1.2 mm. The top and bottom coil have respective resistances of (647, 665) m Ω at $I = 17.37$ A.

The magnetic field of the MOT controls the position-dependence of the force, and we are thus interested in an anti-symmetric field around the center. We plot the magnetic field for three different cases in figure A.3 (a). In orange and blue we show the field of the coils without a vacuum-chamber between the coils. The orange plot corresponds to a case where the current running through the two coils is identical, whereas the blue plot are parameters optimized for blue MOT fluorescence in the assembled system. The yellow curve was done when the coils are mounted on a vacuum-chamber in order to more closely mimic the experimental conditions. We see a slight pinching of the field close to the peak values when the vacuum chamber is included. The peak positions correspond to the height of the MOT

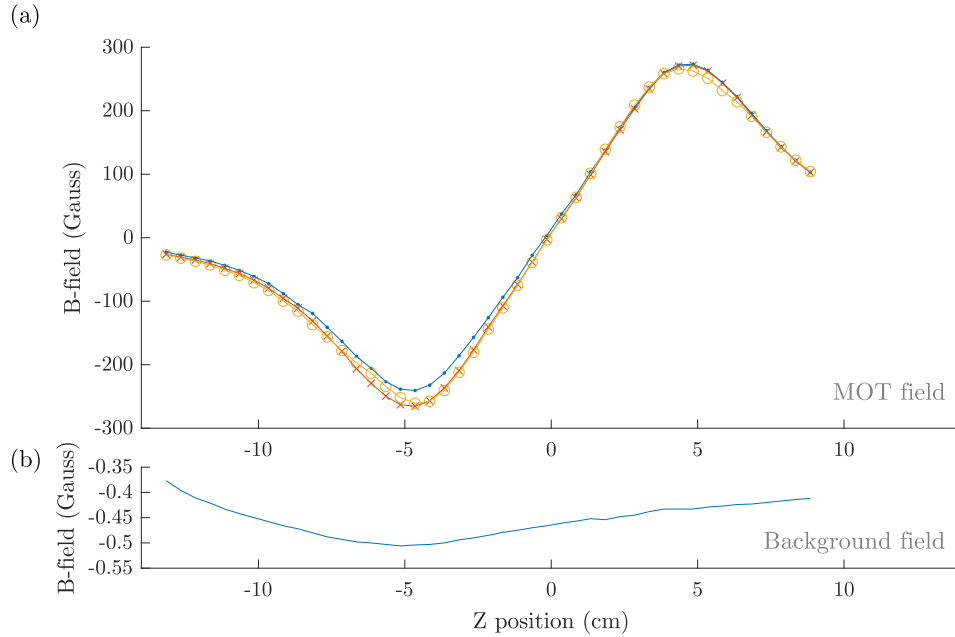


Figure A.3: Magnetic field along the vertical axis of the MOT. **(a)** shows the MOT fields with current in the coils. The balanced current measurement (orange crosses) and run parameter measurement (blue dots) are done with the coils in free space, whereas an additional measurement with balanced current (yellow circles) is done with the coils mounted on a 6-way cross. **(b)** The measured background field which has been subtracted from all plots.

Table A.1: MOT current configurations for figure A.3.

	MOT coil:	Top	Bottom
In free space	Balanced current	17.37 A	17.37 A
	Experimental parameters	17.37 A	15.90 A
With vacuum chamber installed	Balanced current	17.37 A	17.37 A

coils, and we see that the optimized parameters (blue) appear slightly asymmetric. The magnetic field slopes fall in the range of 65 G/cm to 70 G/cm with the lowest slope corresponding to the optimized parameter. Inclusion of the vacuum chamber slightly increases the slope at the center position. In figure A.3 (b) we show the background field which has been subtracted from all measurements. Currents in the coils can be seen from table A.1.

A.3 Interference filter laser

One of my first actions in the lab was to design an interference-filter based ECDL of the Cateye type shown in figure 3.1. At the time we wanted to design a new cooling laser system at 461 nm to be used in a future setup such as the Sr-2 machine. The technical drawing of this design is shown in figure A.4. The design relies on a very large thermal mass for the ECDL base, and a smaller, individually temperature-controlled holder for the laser diode. The diode holder is temperature controlled

with a peltier element, whose reservoir is the ECDL base. The base incorporates a full-size 1-inch kinematic mirror mount for the end-mirror. An interference filter can be installed in the central kinematic mount, which rests on a rotation plate. Finally two simple lens-holders are placed before and after the end-mirror to facilitate a cat-eye configuration.

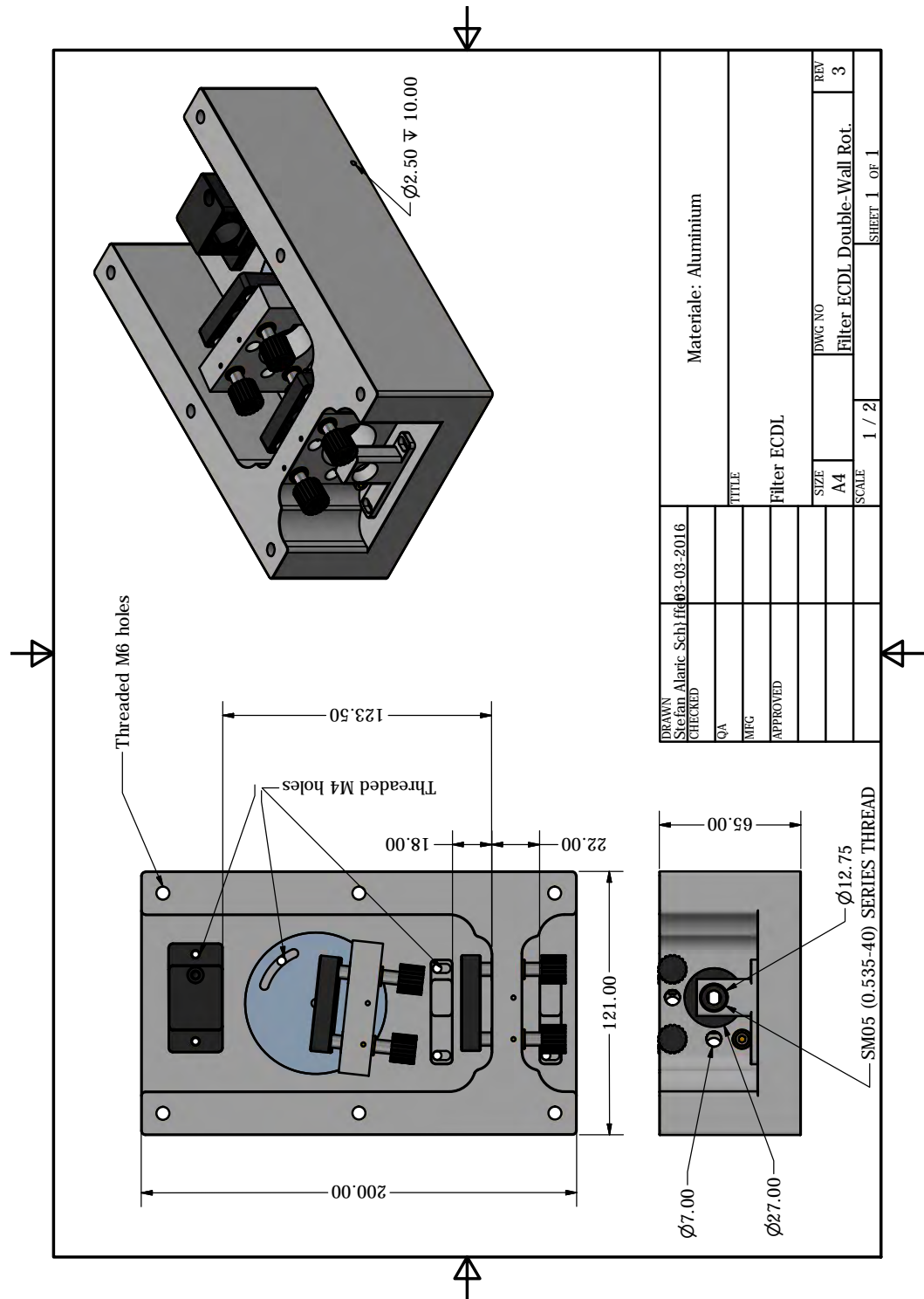


Figure A.4: Design for an interference-filter based ECDL.

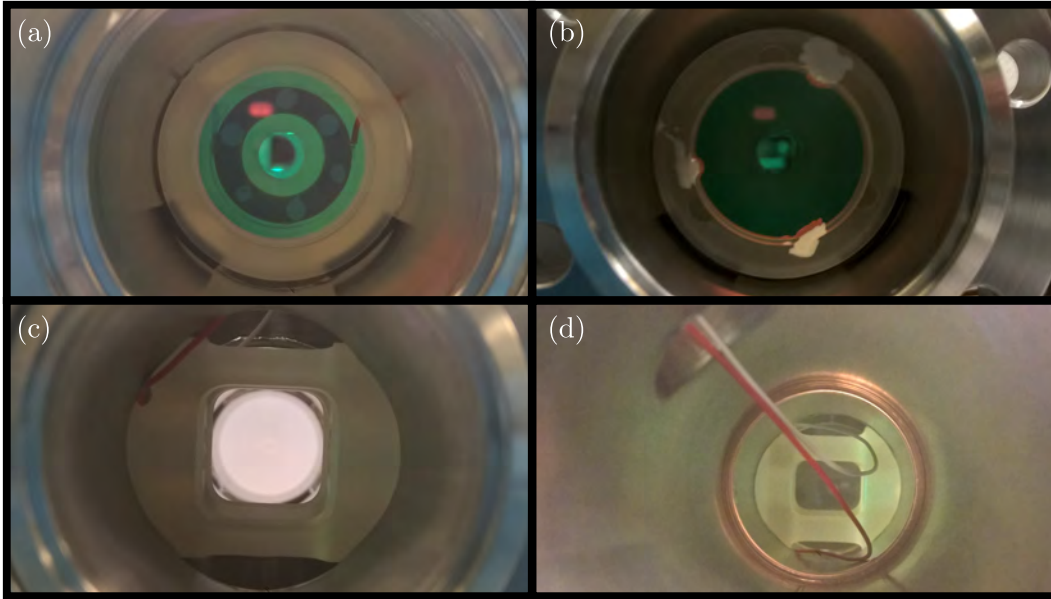


Figure A.5: The interrogation cavity shown inside a welded DN40CF 6-way cross. (a) and (b) show the mirror sides with piezo mounted on one end. The Viton rods used for support are visible. (c) shows the horizontal plane where atoms pass through the interrogation cavity. (d) show the vertical axis with optical access to the cavity mode. The optical access is also possible from the bottom of the cavity. Visible piezo wires are from the test setup.

A.4 Some cavity designs

We use a wide array of cavities in our experiments in order to stabilize laser frequencies or enhance atom-field interactions. Here two designs for the Sr-2 system are presented.

A.4.1 Sr-2 probing cavity

The probing or interrogation cavity in Sr-2 was designed as a short Zerodur rod resting on viton spacers directly inside a DN40CF 6-way cross vacuum tube. The spacer diameter is designed to be naturally center the cavity in the tube cross-section while its length is decided by the necessary reach to have support points within the tubes of the vacuum chamber. The transverse directions of the spacer has holes to permit atoms to pass through the cavity mode in the horizontal plane, and allows laser access for repumping, or optical access for fluorescence detection along the vertical axis. Figure A.5 shows pictures of the cavity in a test-mount. The technical drawing is shown in figure A.6. Here holes for piezo-wires as well as grooves for viton O-rings are visible. We use two pieces of cut O-rings at each end as support.

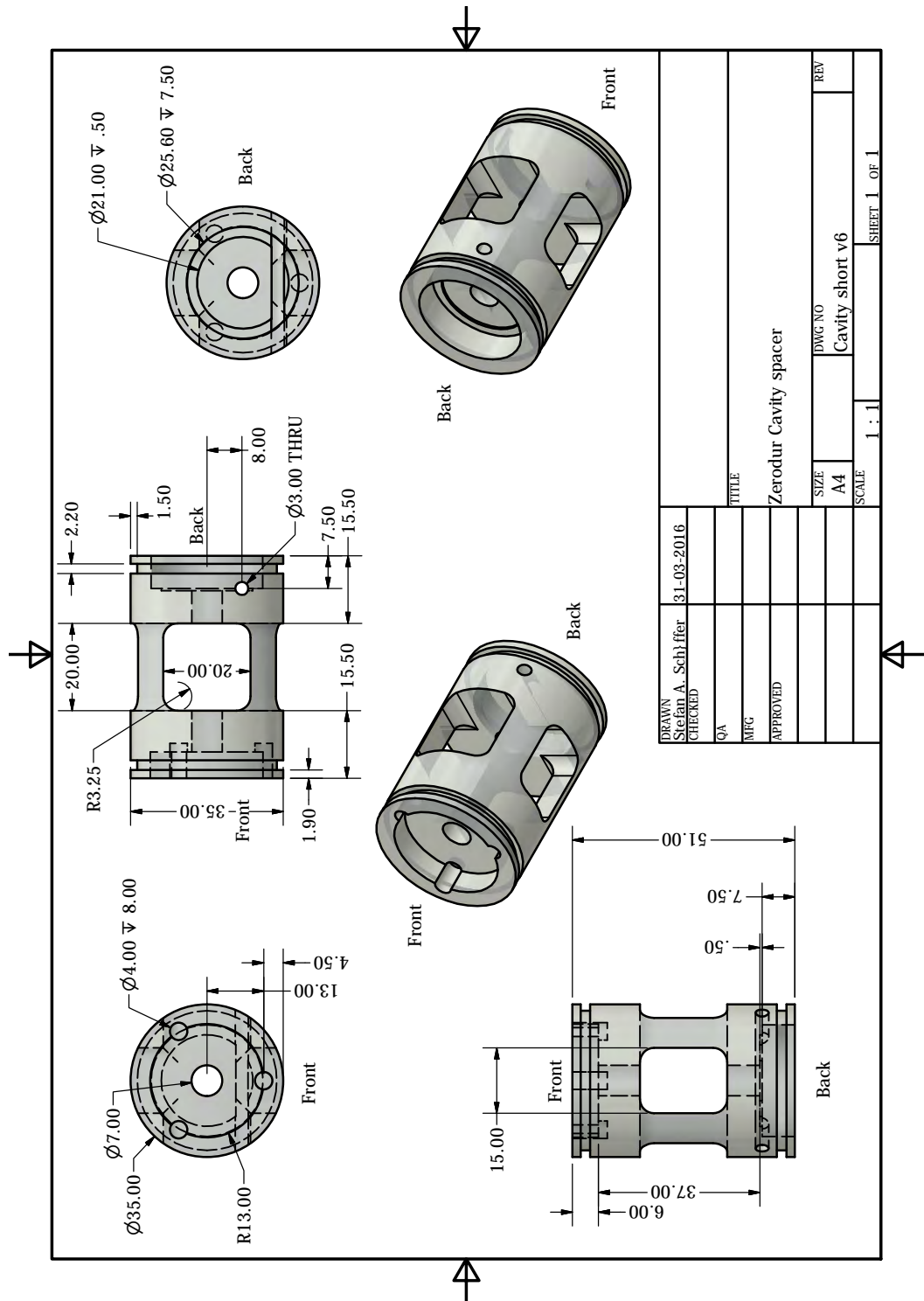


Figure A.6: Technical drawing of Zerodur cavity spacer used in Sr-II machine for atom interrogation.

A.4.2 Transfer cavity

A transfer-cavity for locking the repumping lasers at 679 nm, 688 nm, and 707 nm was constructed in order to allow offset frequency stabilization of all repumping wavelengths to the clock laser at 689 nm. The cavity spacer and mirrors are identical to the interrogation cavity of Sr-1. The technical drawing of the cavity spacer can be seen in figure A.7. The spacer length is 19 mm and the mirrors have power reflectivities of $R = 99.8$ and radius of curvature of $ROC = 9$ m. This results in a cavity linewidth of about $\kappa = 2\pi \cdot 520$ kHz.

The cavity spacer is mounted with a ring-piezo on one of the end mirrors in order to enable frequency tuning. The spacer is mounted in the vacuum chamber by means of two stainless steel rings mounted 3 cm from each end of the spacer, see figure A.8. The rings have holes in order to facilitate vacuum pumping, and provide mechanical isolation of the cavity spacer from the vacuum chamber through Viton rods. The Viton is placed so that the cavity spacer and mounting rings rest on two rods each. A technical drawing is shown in figure A.9.

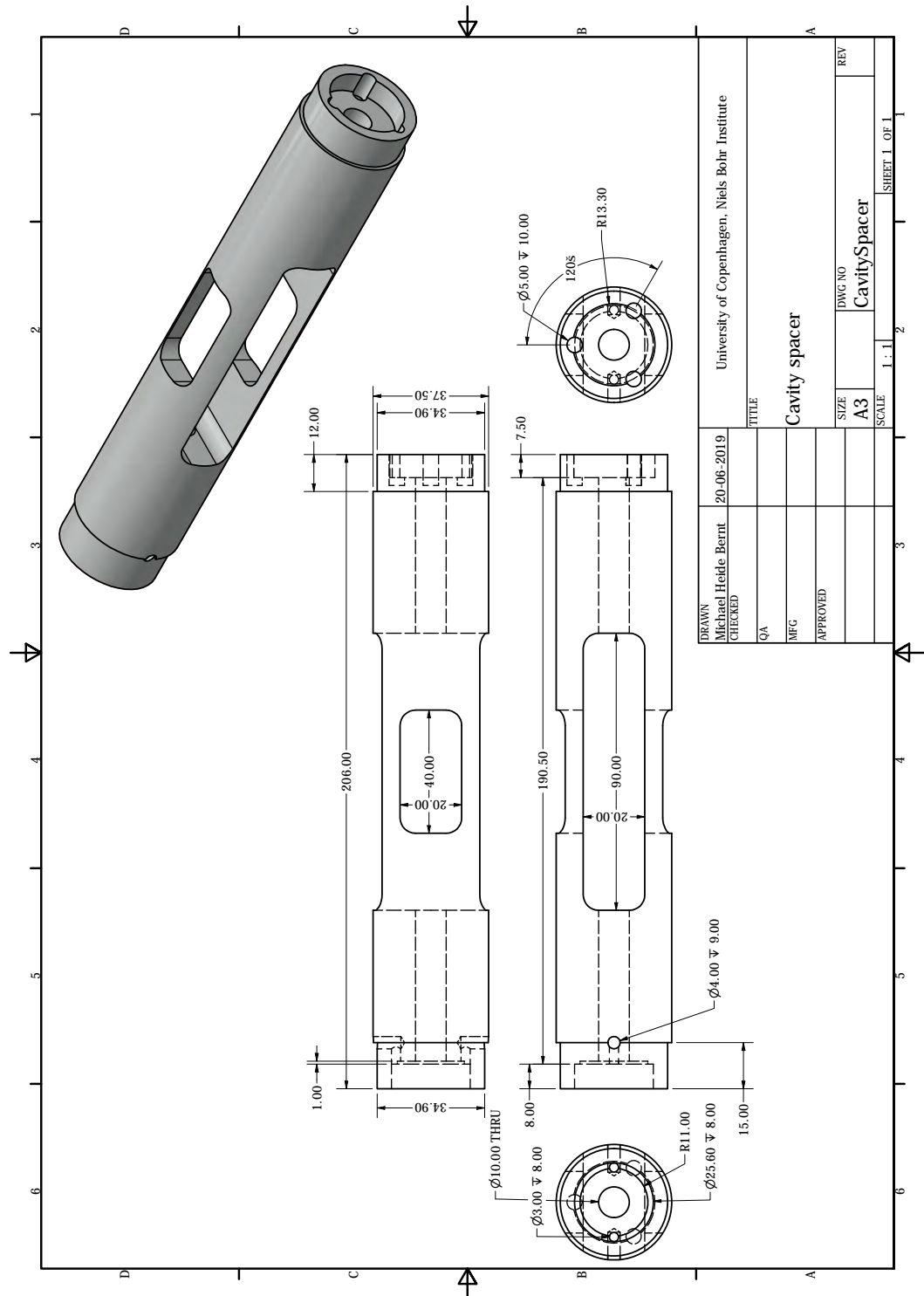


Figure A.7: The cavity spacer used in the transfer-cavity as well as the interrogation cavity for Sr-1. The orthogonal cutouts in the center are designed for passage of MOT beams, fluorescence and atoms.

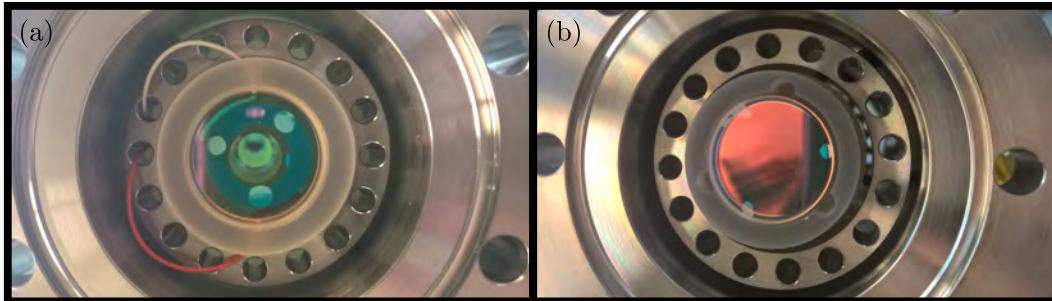


Figure A.8: Mounting of the transfer cavity within the vacuum chamber. The two ends of the cavity spacer rests on two rods of viton inside the support rings. (a) shows the ring-piezo mounted behind the cavity mirror, with wires in red and white going through the supports rings.

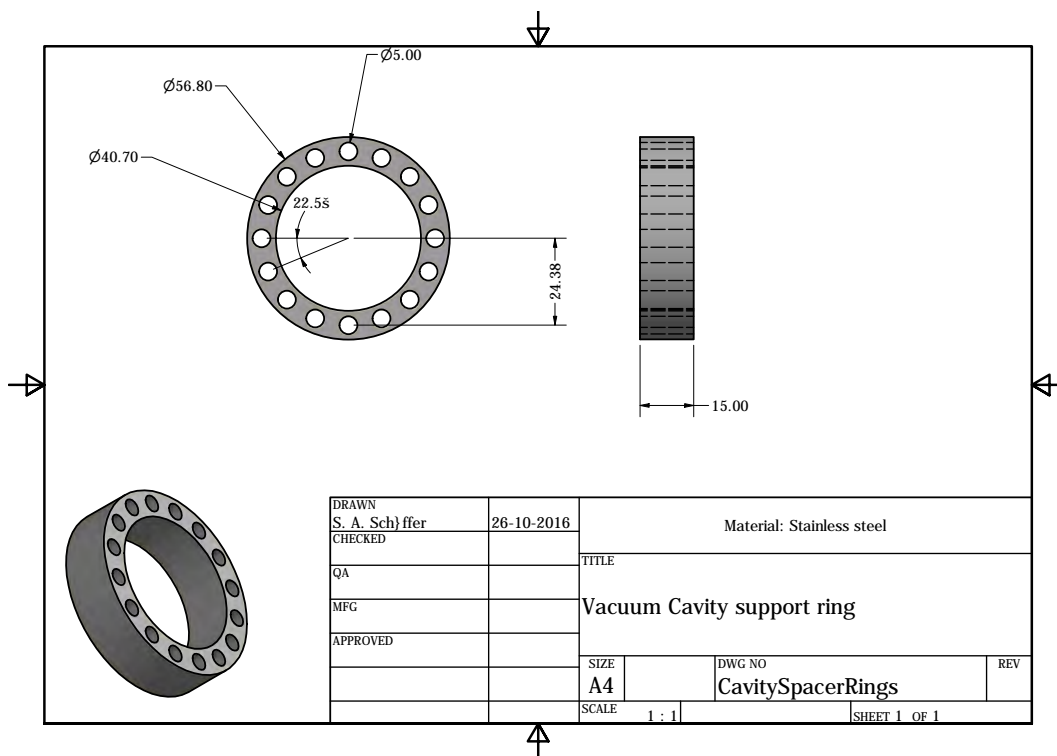


Figure A.9: Support rings for mounting the transfer cavity.



ENVIRONMENTAL NOISE

Contents

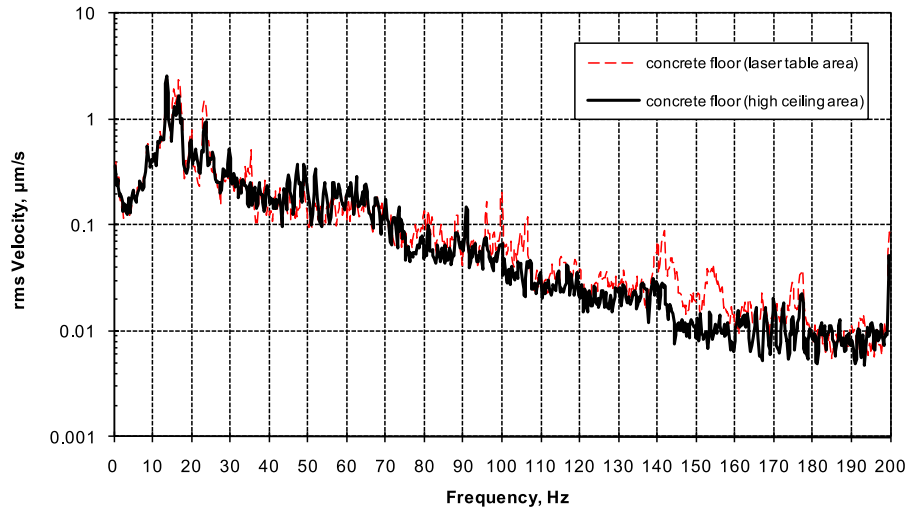
B.1	Vibration measurements	119
B.2	Acoustic measurements	121

Here we show two different characterizations of the laboratory environment noise: the floor vibration and the room acoustic measurements. The floor vibrations were measured by an independent consulting company: Colin Gordon Associates Inc. in 2011. The measurements were made in connection with the planning of a new building for the Niels Bohr Institute, and show excellent stability. The Acoustic measurements have been made with in-house equipment with the aid of Claus B. Sørensen in 2019. This was done in order to find the most appropriate place to install our stable reference cavity.

B.1 Vibration measurements

Figure QO-Uk1C-12: Survey of Lab Vibrations for NBSP Project - 19 May 2011
Niels Bohr Institute, Room 06-01-Hk1, Vertical, Maximum RMS Ambient

a) Narrowband (Bandwidth = 0.375 Hz) Velocity



b) One-Third Octave Band Velocity

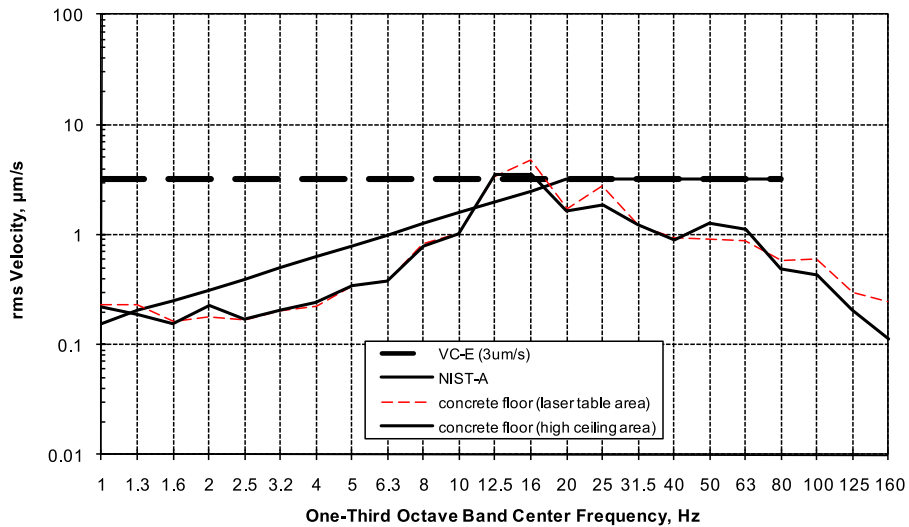


Figure B.1: Vibration level of laboratory floor. Outtake from a report done by Colin Gordon Associates Inc. in 2011. (a) The vibrations of the laboratory floor at two separate positions, when exposed to ambient sources such as vehicles on the road outside the building. The maximal rms velocity spectrum peaks between 10 – 20 Hz at around 1 $\mu\text{m/s}$. (b) The vibration level agrees well with the NIST-A standard with a peak around 16 Hz, and is always below the VC-E standard. These are some of the highest standards, and vibration through the floor should not be a problem for us.

B.2 Acoustic measurements

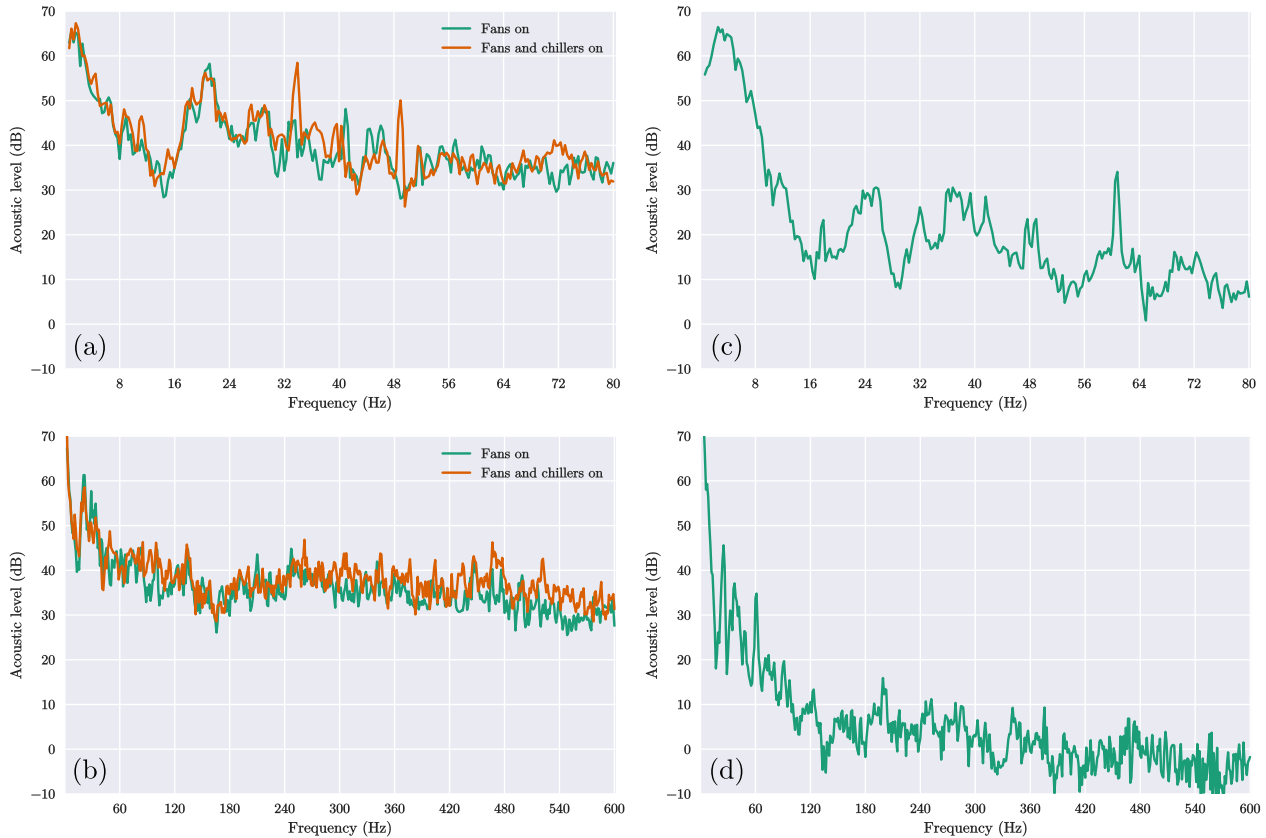


Figure B.2: Acoustic levels for our laboratories. **(a)-(b)** Acoustics in the main laboratory, where the clock laser is kept for two different frequency ranges. This room has a range of technical equipment that is always on. Here we show the acoustic environment in the case where only the electrical apparatuses are on (green), and in the case where we also allow the chillers to be on (orange). Under typical experimental conditions we expect the chillers to be on. The chillers add significant noise spikes 35 Hz and 50 Hz. **(c)-(d)** Acoustics in the separate silent room where we installed the reference laser. Here there is no other equipment than that used to drive the lasers with, which was not included in this measurement. We see that the noise level is always lower than in the main laboratory for frequencies above 8 Hz. The noise level is 30 – 40 dB reduced for frequencies above 100 Hz.

INCLUDED PAPERS

Contents

Dynamics of bad-cavity-enhanced interaction with cold Sr atoms for laser stabilization [99]	123
Towards passive and active laser stabilization using cavity-enhanced atomic interaction [98]	134
Lasing on a narrow transition in a cold thermal strontium ensemble [100]	141

This appendix contains the three papers that are submitted with the PhD thesis. All three papers are first-author papers. [99] and [98] are published at the time of submission, while [100] is still under review in Physical Review A.

Chapter 4 is based on the results presented in [99], while chapter 5 is based partly on [100]. The discussion in [98] is more fundamental in nature, and serves as a motivation and comparison of the methods in [99] and [100].

Dynamics of bad-cavity-enhanced interaction with cold Sr atoms for laser stabilization

S. A. Schäffer,^{*} B. T. R. Christensen, M. R. Henriksen,[†] and J. W. Thomsen
Niels Bohr Institute, University of Copenhagen, Blegdamsvej 17, 2100 Copenhagen, Denmark
 (Received 22 April 2017; published 24 July 2017)

Hybrid systems of cold atoms and optical cavities are promising systems for increasing the stability of laser oscillators used in quantum metrology and atomic clocks. In this paper we map out the atom-cavity dynamics in such a system and demonstrate limitations as well as robustness of the approach. We investigate the phase response of an ensemble of cold ⁸⁸Sr atoms inside an optical cavity for use as an error signal in laser frequency stabilization. With this system we realize a regime where the high atomic phase shift limits the dynamical locking range. The limitation is caused by the cavity transfer function relating input field to output field. The cavity dynamics is shown to have only little influence on the prospects for laser stabilization, making the system robust towards cavity fluctuations and ideal for the improvement of future narrow linewidth lasers.

DOI: [10.1103/PhysRevA.96.013847](https://doi.org/10.1103/PhysRevA.96.013847)

I. INTRODUCTION

Optical atomic clocks have undergone an immense development, and are continuously improving, with increased stability and accuracy every year [1–4]. The ability to reach exceedingly high accuracies within a reasonable time is made possible by the correspondingly huge effort to bring down the frequency noise in ultrastable laser sources [5–8].

The full potential of the high Q factor atomic transitions used in many optical atomic clocks can be reached only through improvements in the stability of the interrogation laser. Traditionally such interrogation lasers are stabilized to highly isolated optical reference cavities. This stabilization method is mainly limited by thermal fluctuations in the optical coating, mirror substrate, and cavity spacer [8–11], demanding considerable experimental effort in order to construct cryogenically cooled monocrystalline cavities and crystalline mirror coatings [5, 8]. Several new approaches are being pursued in the so-called bad-cavity regime [12], in order to significantly suppress thermally induced length fluctuations. They use a combination of narrow linewidth $\delta\nu$ atoms and optical cavities. These atomic systems have strongly forbidden transitions at optical frequencies ν , resulting in high Q factors, $Q = \frac{\nu}{\delta\nu}$. By exploiting the high Q factor of the atomic transitions and using cavities with comparatively low Q factors the systems are far less sensitive to thermal fluctuations of the cavity components, and the experimental requirements are simplified. In these approaches active as well as passive atomic systems have been suggested [13–18]. The active atomic systems are optical equivalents of the maser, relying on cooperative quantum phenomena such as superradiance or superfluorescence of atoms inside the cavity mode. Several pioneering experiments have already demonstrated lasing under such conditions [19–23]. In the passive approach the atom-cavity system is used as a reference for laser stabilization where the narrow linewidth atomic transitions are interrogated inside an optical cavity. One proof-of-principle approach to this is based on

using the noise-immune cavity-enhanced optical heterodyne molecular spectroscopy (NICE-OHMS) technique [24, 25] for generating sub-Doppler dispersion signals [26]. This has shown promising results for laser stabilization that could be able to compete with traditional cavity-only stabilization techniques [27–29].

By employing an optical cavity the coupling between atoms and optical field is improved by a factor of the cavity finesse, which significantly increases the total phase shift experienced by the optical field. As the total phase shift is increased, however, this limits the frequency range of linear behavior and thus the dynamical range of a servo locking the laser frequency. Additionally, the cavity servo response time might limit the signal quality if the condition of constant laser-to-cavity resonance must be strictly met.

In this paper we show experimentally that the large total phase shift of the system not only improves the resonance slope but also distorts the dispersion signal off atomic resonance. This becomes relevant for the interest of servo optimization in such a system [30] as it can limit the dynamical range of a servo lock. We show that this distortion originates from the transfer function of the cavity itself, and thus cannot be circumvented. We have realized a system with a theoretically attainable shot-noise limited (SNL) laser linewidth of $\Delta\nu \approx 40$ mHz, possibly allowing laser performance at the level of the state-of-the-art reported values [5–8]. We use the system to map out the dynamical range and investigate the consequences of an imperfect cavity servo, which causes a mismatch of the cavity resonance with respect to the laser frequency. Due to the bad-cavity regime much looser bounds on the cavity resonance are allowed, as expected. This opens the possibility of using cavities with quasistationary lengths, and simultaneously underlines the insensitivity to cavity fluctuations.

II. EXPERIMENTAL SYSTEM

The experimental system investigated here consists of an ensemble of cold ⁸⁸Sr atoms cooled to a temperature of $T \approx 5$ mK. The atoms are trapped in a magneto-optical trap (MOT) at the center of a TEM₀₀ Gaussian mode of an optical cavity (see Fig. 1). The cavity has a finesse of $F = 1240$ and a linewidth of $\kappa = 2\pi \times 630$ kHz at $\lambda = 689$ nm. A laser beam probing the narrow $(5s^2)^1S_0 \rightarrow (5s5p)^3P_1$ transition of ⁸⁸Sr

^{*}schaffer@nbi.dk

[†]Also at SPOC, Technical University of Denmark, DTU Fotonik, Ørstedes Plads, building 343, 2800 Kgs. Lyngby, Denmark.

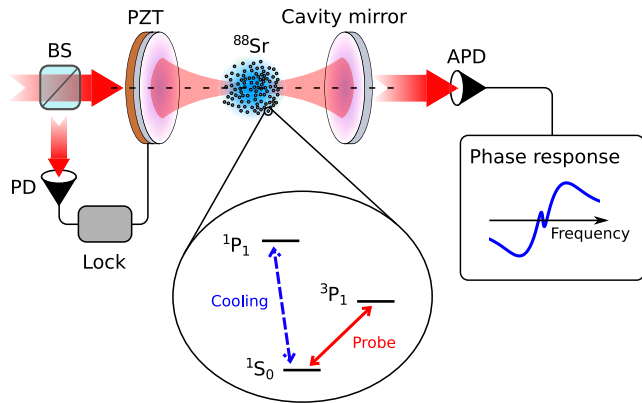


FIG. 1. Experimental system. The probe laser has a single carrier frequency as well as sidebands detuned an integer number of the cavity free spectral range. The light is coupled into the cavity by adjusting the cavity length to ensure resonance between the atom-cavity system and the probing laser at all times. This resonance is ensured by a Pound-Drever-Hall lock from the reflected light using the beamsplitter (BS), photodetector (PD), and locking circuit acting on the piezoelectric element (PZT) on one of the cavity mirrors. The sidebands do not interact with the atoms inside the cavity and act as references in the subsequent heterodyne measurement of the transmission signal on the fast avalanche photodiode (APD). The cooling transition for the MOT and the probe transitions are shown. During measurements the cooling light (blue) is turned off.

is coupled into the cavity mode, and the cavity resonance is locked to the probe laser frequency at all times.

Before entering the cavity the probe light is phase modulated using a fiber-coupled electro-optical modulator (EOM) in order to perform heterodyne detection of the transmitted signal. The modulation frequency is equal to the free spectral range (FSR) of the cavity, resulting in sidebands at $\omega_0 \pm j\Omega$ for integer j and $\Omega = 2\pi \times 781.14$ MHz. The sidebands are far detuned with respect to the $(5s^2)^1S_0 \rightarrow (5s5p)^3P_1$ transition which has a linewidth of $\gamma_{\text{nat}} = 2\pi \times 7.5$ kHz, and the interaction between the sidebands and the atoms can thus be neglected. This system is interrogated using a heterodyne measurement between the carrier and sideband frequencies in order to extract the dispersion signal of the atom-cavity system, which can be used as an error signal to lock the probe laser frequency to resonance with the atoms. We operate in the bad-cavity regime where any cavity fluctuations are suppressed in the atom-cavity signal by a factor of $\frac{\kappa}{\gamma_{\text{nat}}}$, here about 100.

The field transmitted through the cavity is split and simultaneously recorded on a low bandwidth (50 MHz) photodiode and a high bandwidth (1 GHz) avalanche photodiode (APD). The low bandwidth signal records the total transmission intensity of the cavity. The high bandwidth signal is filtered around the modulation frequency Ω and demodulated in order to record the atom induced phase shift of the sideband relative to the carrier frequencies.

The measurements are performed in a cyclic operation as the intense cooling light of the MOT results in an ac Stark shift of the 3P_1 level and washes out coherence of the probing transition. The cooling light is thus shut off before each measurement, and the probing light then recorded for an

interrogation period of $100 \mu\text{s}$. At this time scale the probing laser has a linewidth of $\Gamma_1 = 2\pi \times 800$ Hz, which is much narrower than the natural linewidth of the probing transition $\gamma_{\text{nat}} = 2\pi \times 7.5$ kHz. This transition linewidth places us deep in the bad-cavity regime, where the cavity linewidth is much broader than the atomic linewidth $\kappa \gg \gamma$. This means that the system is much less sensitive to variations in the cavity resonance frequency which can originate from, e.g., temperature fluctuations in the cavity components.

Only a single measurement is performed before reloading the trap with new atoms, since atom loss due to the finite temperature of the atoms becomes measurable after $500 \mu\text{s}$. This results in a cyclic operation where the dispersion is measured only for a single frequency detuning of the interrogation laser at a time. Varying the loading time of the MOT allows control over the atom number and typically ranges from 50 to 800 ms for intracavity numbers of $N = 2 \times 10^6$ to 4×10^7 .

III. THEORY OF MEASUREMENT

We investigate theoretically a system consisting of an ensemble of N atoms coupled to a single mode of an optical cavity in order to describe the experimental system presented in this paper. The NICE-OHMS technique as it is used here relies on the transmitted signal of the atom-cavity system, and is a heterodyne measurement between the carrier laser frequency and its sidebands. The input laser field before the cavity can then be described by

$$E_{\text{in}} = E_0 \sum_{j=-\infty}^{\infty} J_j(y) e^{i(\omega_l + j\Omega)t}, \quad (1)$$

where E_0 is the amplitude of the electric field and $J_j(y)$ is the j th-order Bessel function of the first kind, with the modulation index y . The laser carrier frequency is ω_l , whereas Ω is the modulation frequency applied in the EOM.

The interaction of the light with the atom-cavity system may be described by using a Born-Markov master equation as described in the Appendix following [27,29]. The approach is based on a many-particle Hamiltonian \hat{H} and a derived set of complex Langevin equations that includes the Doppler effect from the finite velocity of the atoms.

Classically we may relate the input and output fields with a complex transfer function $\chi[\theta(E_{\text{in}})]$. The field-dependent complex atomic phase experienced by the light when interacting with the atom-cavity system $\theta(E_{\text{in}})$ is found by means of the full quantum-mechanical theory of the Appendix. In order to cast the behavior of our system in terms of measurable quantities, we assume that the relation between the quantum-mechanical phase $\theta(E_{\text{in}})$ and the measured output power can be described by a linear model such that $E_{\text{out}} = \chi(\theta)E_{\text{in}}$. We then insert the theoretical value of $\theta(E_{\text{in}})$ into the transfer function.

Here we are mainly interested in the properties of such a transfer function. By increasing the finesse of the cavity with respect to the numbers reported in [28] we enable the system to move between a low-phase-shift regime and a high-phase-shift regime. Figure 2 shows typical dispersion scans where the theoretical model incorporating a cavity transfer function

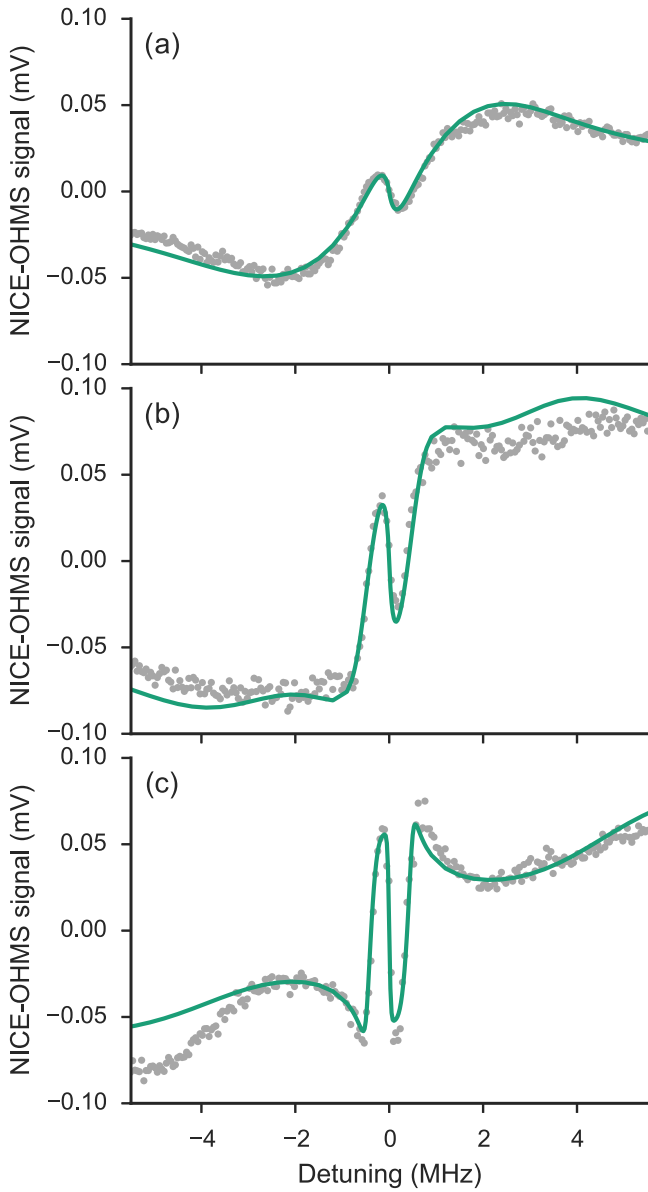


FIG. 2. Phase response of the atom-cavity system using the NICE-OHMS technique. We show the transition from low to high phase response by changing the number of atoms interacting with the cavity mode. Here the gray dots indicate recorded data, whereas the full green curve is a theoretical calculation using the experimental parameters. As the absolute phase increases, the transfer function reaches its maximal value and first flattens, then inverts the signal slope. (a) Cavity atom number of $N = 3.8 \times 10^6$, and a temperature of $T = 16$ mK. Due to the short loading time used the atoms are slightly warmer here. (b) Cavity atom number of $N = 1.4 \times 10^7$, and a temperature of $T = 13$ mK. Distortion in the dispersion signal is evident from ± 1 to ± 4 MHz. (c) Atom number of $N = 4 \times 10^7$, and a temperature of $T = 13$ mK. Here we clearly see a slope inversion initiating at ± 1 MHz. The maximal absolute value of the dispersion is not constant over the whole scan, as it depends on the absorption which is itself dependent on the detuning. This also causes the dispersion to retain a large absolute value for relatively high detuning.

(see [28]) has been plotted using the known experimental parameters. The dispersion signal serves as an error signal

for all values of the atom number N , but is distorted when detuned from resonance at higher values of N . This distortion is not caused by the atomic phase response itself, but rather by the classical conditions of the transfer function imposed by the cavity.

A. Dispersion signal

Only a single frequency component of the modulated light, namely, the carrier component $j = 0$, interacts with the atoms. This means that we can simplify the description of our system by defining a transfer function for each frequency component j of the light as it passes through the cavity [31]:

$$\chi_j = \frac{T e^{i\phi_j}}{1 - R e^{2i\phi_j}}, \quad (2)$$

where T (R) is the power transmission (reflectivity) of a single cavity mirror, and ϕ_j is the complex phase experienced by the j th component of the interrogation laser. We assume identical mirrors with no losses. The real part of the transfer function corresponds to the transmitted amplitude of the E field in the system, while the imaginary part corresponds to the dispersion. Due to energy conservation the absolute-squared value of the complex transfer function cannot exceed 1, $|\chi|^2 \leq 1$, for a system with no gain or frequency conversions. This classical condition thus imposes a maximal value on the dispersion signal which is independent of the nature of the phase delay inside the cavity. We can describe the complex phase for any sideband component as simply the phase shift experienced by a single-passage interaction with the cavity $\phi_j = \phi_{\text{cav}}^j$ for $j \neq 0$, while the carrier component of the light experiences the atomic phase as well:

$$\phi_0 = \phi_{\text{cav}}^0 + \phi_D + i\phi_A, \quad (3)$$

where ϕ_D and ϕ_A are the phase components caused by atomic dispersion and absorption from a single passage of the cavity. In the case of a medium with no gain, we have $\phi_A \geq 0$. The cavity phase shift is given by $\phi_{\text{cav}}^j = \phi_{\text{cav}} + j\pi$, and the cavity locking condition of the experiment defines ϕ_{cav} .

The output field can now be expressed by a superposition of frequency components and corresponding transfer functions:

$$E_{\text{out}} = E_0 \sum_{j=-\infty}^{\infty} J_j(y) \chi_j e^{i(\omega_0 + j\Omega)t}, \quad (4)$$

where E_0 contains any overall phase. By recording the intensity on a photodetector we can filter out the beat signal between sideband and carrier by demodulating at the modulation frequency Ω . By optimizing the phase of the demodulation signal to record the imaginary part of the transfer function and subsequently pass the signal through a 2-MHz low-pass filter we obtain a dc signal:

$$S_{\Omega} \propto 2i |E_0|^2 J_0(y) J_1(y) (\chi_0 \chi_1^* - \chi_0^* \chi_1), \quad (5)$$

which is a purely real number. We have only included up to second-order sidebands, and used $\chi_j = (-1)^{|j|-1} \chi_1$ for $j \neq 0$. Higher-order sidebands are negligible for modulation indices up to $y \simeq 1$.

If we assume that the system is in a steady state the cavity locking condition dictates that the cavity is on resonance with

the carrier frequency at all times, corresponding to that used in [28]. This gives us

$$\phi_{\text{cav}} + \phi_D = n\pi \quad (6)$$

for integer n . The complex transfer function of the carrier then becomes solely dependent on the absorption,

$$\chi_0 = \frac{T e^{-\phi_A}}{1 - R e^{-2\phi_A}}, \quad (7)$$

whereas the sideband transfer functions have the phase information of the atomic interaction written onto them by the cavity lock:

$$\begin{aligned} \phi_j &= \phi_{\text{cav}}^j = \phi_{\text{cav}} + j\pi \quad \text{for } j \neq 0 \\ &= n\pi - \phi_D + j\pi. \end{aligned} \quad (8)$$

Ignoring an overall sign from $e^{in\pi}$ we get

$$\chi_j = \frac{T e^{i(j\pi - \phi_D)}}{1 - R e^{2i(j\pi - \phi_D)}} \quad \text{for } j \neq 0. \quad (9)$$

Since χ_0 is purely real we can write the signal as

$$S_\Omega \propto J_0(y) J_1(y) \chi_0 \text{Im}(\chi_1). \quad (10)$$

We are thus particularly interested in the properties of the imaginary part of the transfer function if we wish to understand the behavior of our error signal.

B. Transfer function properties

Having understood the behavior of our system we can now investigate why we see the folding behavior depicted in Figs. 2(b) and 2(c). If we ignore the origin of the phases it is clear that a cavity transfer function such as the one in Eq. (2) must have a periodicity of 2π as a function of the phase shift experienced by the light inside the cavity. In the context of locking a laser to an atom-cavity system we are mainly interested in the phase slope around atomic resonance where the absolute phase is zero, but the phase slope can be very steep.

Very close to atomic resonance, the transfer function is proportional to $\sin(\phi) \approx \phi$ for small phase shifts [28] and we can treat the transfer function as linear in phase. For a slightly larger frequency detuning, however, the existence of a maximal value for the transfer function results in some interesting behavior for a system with large total phase shift. In Fig. 3 the imaginary part of a phase-dependent transfer function χ_j is shown with varying single-passage phase shift and mirror reflectivity R . We see that the imaginary part of the transfer function itself behaves in a dispersionlike manner for a linearly varying phase. In this figure we have assumed that there are no losses in the cavity mirrors ($T + R = 1$) and that there is no absorption in the cavity $\text{Im}[\phi] = 0$ which would not be the case close to an atomic resonance. If the effect of absorption in the medium is taken into account, this reduces the maximal value of transfer function $|\chi|_{\text{max}}$ further. For $\text{Im}[\phi] = \phi_A > 0$ we will thus have $|\chi|_{\text{max}} < 1$ asymptotically decreasing towards zero as a function of ϕ_A . As an aside, including absorption also decreases the phase slope at resonance. This slope will nevertheless still increase linearly with atom number when the saturation condition is fulfilled.

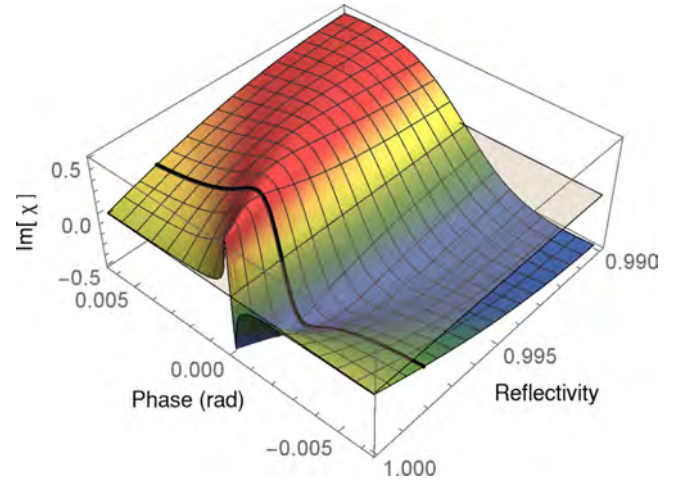


FIG. 3. The imaginary part of a transfer function as given in Eq. (2) as a function of phase ϕ and single mirror power reflectivity R . Here we have assumed that the phase ϕ is purely real, and that the cavity is symmetrical. Close to zero phase the function is approximately linear, and the values of the phase and the transfer function are proportional. As the phase increases, however, a maximal value for the transfer function is reached, and the transfer function slope is inverted. The black line indicates the mirror reflectance of our system ($R = 0.998$) and the transparent plane indicates $\chi = 0$.

As the reflectivity of the mirrors (R) is increased the light is stored in the cavity for longer and thus experiences a larger total phase shift. This increases the phase slope on resonance proportionally to the finesse F of the cavity and in turn leads to a decrease in the phase range where the transfer function χ is linear (see Fig. 3). This insight tells us that the dispersion signal observed from the atom-cavity transfer function will be distorted and even change the sign of the slope for detunings at which the value of the total phase shift is large.

This sets a limit to the maximal *dynamical range* that we can expect of a locking mechanism based on this dispersion signal S_Ω . It results in an inversion of the dispersion slope for large absolute phase shifts. Here the boundaries on the transfer function act to fold down the signal in a nonlinear manner. While the sign of the slope is thus inverted the sign of the signal itself never changes with respect to that of the phase. The linear-phase regime decreases in size linearly towards zero as a function of the mirror reflectivity R in the regime where the cavity linewidth $\kappa \ll \text{FSR}$ ($F \gg 1$). A maximal dynamical range of $\phi = \pi$ is reached for $R \lesssim 0.17$. For systems with much larger atom number (and thus larger phase shift) it could thus be an advantage to go towards lower mirror reflectivity, and thus deeper into the bad-cavity regime. This would further reduce the sensitivity to cavity perturbations. For systems using much broader atomic transitions where the cavity might naturally have lower finesse [13], these effects would only be visible for very large samples.

The absolute phase value at which such mirroring occurs typically increases with larger detuning from the resonance. This effect is caused by the decrease in atomic absorption for increased detuning. This causes the phase value necessary for the slope inversion of the transfer function to increase. Away from resonance the dispersion is thus highly distorted, with

respect to the atomic phase, due to the functional form of the cavity transfer function.

IV. RESULTS AND DISCUSSION

We now look at the phase response of the system when operating in a regime of high phase shift due to a combination of large atom numbers N and high reflectance of the cavity mirrors. At small frequency detuning we see a linear scaling of the dispersion slope with respect to the phase slope, which gives us a limit on the ultimate frequency linewidth of a laser locked to such a system [17,28]. The dynamical range of a laser frequency lock to the atom-cavity system becomes limited at high absolute phase shifts. This is caused by the characteristics of the transfer function the behavior of which will then dominate over the power broadened transition linewidth γ_{power} . We quantify this limitation and its implications for laser frequency locking. We have also investigated the effects of having a cavity resonance lock with nonoptimal conditions. The modification of such locking conditions is of interest to any experimental realization of the frequency lock.

A. Phase slope and projected shot-noise limited linewidth

In the context of locking the frequency of a laser to the atom-cavity system, we are interested in obtaining an error signal that we can use as a feedback signal, which must have a large relative slope and a large signal-to-noise ratio. The first condition is limited by the physical system, and is given by the phase slope present at resonance. The second condition is limited by the noise present in the experimental system, and is to a high degree limited by technical circumstances that may be significantly reduced. The technical contributions to the noise include residual amplitude modulation of the laser sideband components, atom number fluctuations, and noise in the detectors. Because of this fundamental difference in the two conditions, we wish to focus on the limitations set by the physical system initially, namely, the phase slope at resonance.

In Fig. 4(a) the slope of the atomic induced phase shift at resonance is plotted as a function of the input power on a logarithmic scale for $N = 2.7 \times 10^7$. It was shown in [27] that the slope at resonance scales linearly with the number of atoms N in the cavity mode. This is still the case in our regime of $N \approx 1\text{--}5 \times 10^7$ and $P_{\text{in}} \simeq 100$ nW [32], and we will thus focus on the strongly nonlinear scaling with laser power here. This scaling was shown for a cavity finesse of $\mathcal{F} = 75$ in [28]. Here we show results for a system with finesse of $\mathcal{F} = 1240$, and confirm that the theory scales well with cavity finesse.

The very nonlinear behavior of the phase slope shows a clear optimum in absolute phase slope for input powers of about 8 nW and a subsequent decrease in the absolute slope towards zero. While the phase slope is small for low powers due to the reduced saturation of the atoms, the saturation feature becomes power broadened for higher powers, once more leading to a reduction in the slope. The optimal phase slope is thus obtained for very low input powers; however, as we shall see below, this is not the optimal value for laser stabilization.

The shaded region in Fig. 4(a) is a theoretical plot including experimental uncertainties and we indicate a number of different input powers with green dots. At these powers

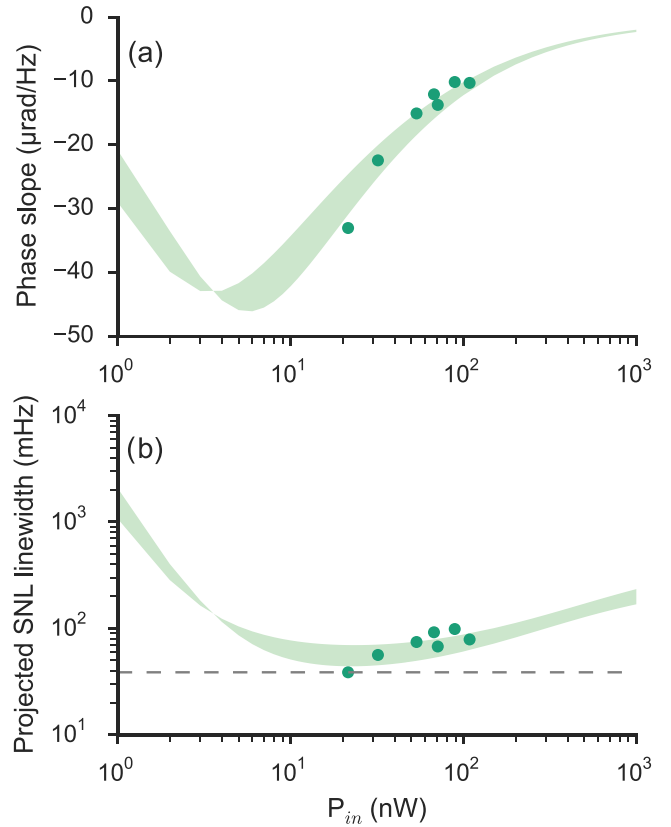


FIG. 4. (a) Semilogarithmic plot of the slope of the atomically induced phase slope at resonance, $\frac{d\phi}{d\nu}$, as a function of input power. The shaded area is the range between theoretical predictions for experimental parameters at a temperature $T = 3.6 \pm 1$ mK and $N = 2.7 \times 10^7 \pm 5 \times 10^5$ atoms overlapping with the cavity mode. This represents the uncertainty in atom number due to shot-to-shot variations, as well as the uncertainty in temperature mainly caused by power fluctuations of the cooling laser. For a number of different input powers we measured the dispersion and found the phase slope of the theoretical fit. The uncertainty in input power P_{in} is less than or equal to the dot size. (b) Projected SNL linewidth achievable for the system under ideal circumstances. The dots are calculated values corresponding to the slopes found in panel (a). The single-sideband-to-carrier power ratio is 0.5. We see a minimal SNL linewidth of $\Delta\nu \approx 40$ mHz which is comparable to the current state-of-the-art results.

we have performed scans of the atom-cavity spectrum and compared them to the theoretical model, in order to obtain a noise-free value for the phase slope at resonance. The fact that we see fluctuations of power, atom number, and technical noise or drift in the experiment is reflected by the misalignment between the dots and the theoretical behavior.

Using the phase slope it is possible to calculate the theoretically obtainable SNL linewidth of a laser locked to the system. Here we find the minimal achievable linewidth by assuming that the detector efficiency is unity, and the lock is perfect. This can be found theoretically by using the expression [17,32]

$$\Delta\nu = \frac{\pi h\nu}{2\eta_{\text{qe}} P_{\text{sig}} \left(\frac{d\phi}{d\nu}\right)^2} \left(1 + \frac{P_{\text{sig}}}{2P_{\text{ref}}}\right) \quad (11)$$

where $\frac{d\phi}{d\nu}$ is the phase slope at resonance, P_{sig} is the carrier power, and P_{ref} is the reference power, which in our case is the power in the first-order sidebands. η_{qe} is the quantum efficiency of the detector which we assume here is 1.

In Fig. 4(b) we calculate this SNL linewidth $\Delta\nu$ and plot the curve corresponding to the slope of Fig. 4(a). We see that the optimum value of input power changes when we consider the SNL linewidth. For low powers the SNL linewidth increases dramatically as the shot noise starts to dominate the signal. This results in a relatively flat region around the optimum power spanning about an order of magnitude from $P_{\text{in}} \simeq 10$ to 100 nW. The minimal value of $\Delta\nu$ is highly dependent on the ratio between sideband and carrier power. The optimal ratio of $\frac{P_{\text{carrier}}}{2P_{\text{sideband}}} = 1$ was used in these experiments. For these parameters we predict a minimal value of $\Delta\nu \approx 40$ mHz which is comparable to the smallest laser linewidths ever reported [5–7]. By increasing the atom number it is possible to simultaneously decrease the projected linewidth of the locked laser, and increase the optimal operation power P_{in} .

B. Dynamical range

In Fig. 2 the recorded signal S_{Ω} is shown for three different regimes where the maximal atomic phase shift is below, at, or above that corresponding to the maximal value of the transfer function. This shows the transition from a regime where the dispersion is largely unperturbed and represents the phase response of the atoms well, to a regime where the response is significantly modified by the cavity transfer function.

At small phase shifts we see a linear increase of the size of the signal proportional to the phase. At larger phase shifts, however, the functional form of the cavity transfer function results in a mirroring effect of the dispersion signal for detunings above γ_{power} where the phase shift is maximal. This has no influence on the slope around resonance, and will thus not affect the performance of an ideal frequency lock. It could, however, still limit the performance of a real servo system where the response time is not infinitely fast.

We define the dynamical range of a lock to the dispersion signal as the range around resonance within which the dispersion *slope* has constant sign. This range is dictated by the full width at half maximum of the power broadened transition linewidth. This corresponds to the width of the Lamb dip in the case of simple saturated absorption spectroscopy. The width, however, is modified by the slope of the Doppler-broadened Gaussian dispersion feature. This dispersion causes line pulling and thus decreases the dynamical range further. Lower temperatures will cause more pronounced line pulling than higher temperature as the Doppler-broadened dispersion slope increases. While this effect actually causes a decrease in resonance slope it turns out that the fractional increase in the number of saturated (cold) atoms N_{sat} outweighs this effect and the resonance slope is thus effectively increased for decreasing temperatures T .

Finally the signal is modified by the cavity transfer function. Below the threshold in maximal phase deviation set by this transfer function this is simply a phase-dependent scaling of constant sign and will thus not modify the dynamical range. Above this threshold, which becomes relevant in high N

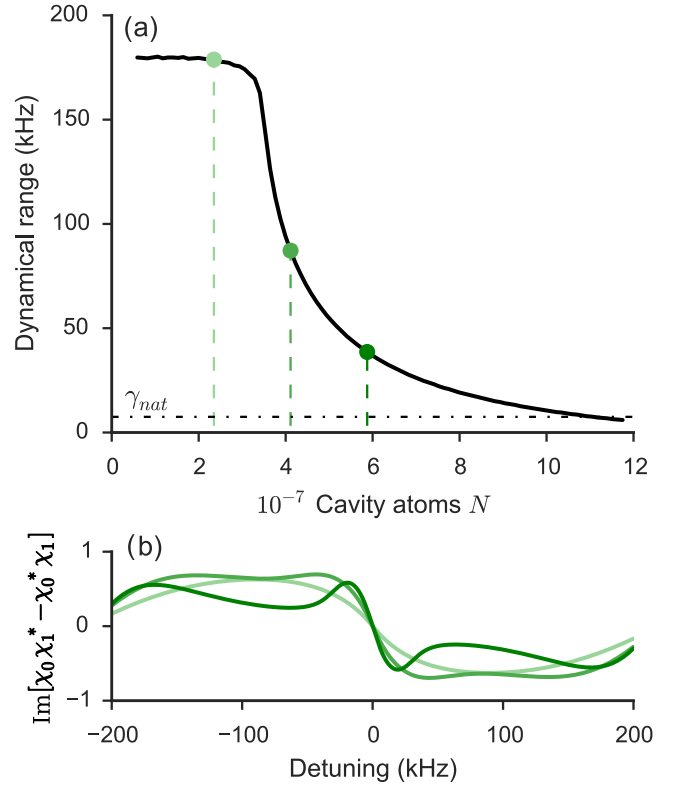


FIG. 5. (a) Dynamical range of the dispersion signal as a function of the intracavity atom number $N \times 10^{-7}$. The dynamical range is the range around resonance where the sign of the dispersion slope is constant. The black dash-dotted line indicates the width of the dispersion if it was uniquely determined by the natural linewidth of the transition γ_{nat} . Three examples of the saturation dispersion are shown in panel (b) and indicated by the dots on dashed lines in panel (a). The three examples correspond to atom numbers of $N = 2.4 \times 10^7$ (light green), $N = 4.1 \times 10^7$ (medium green), and $N = 5.9 \times 10^7$ (dark green), respectively. The recorded scans in Fig. 2 do not exceed $N = 2 \times 10^7$ and are thus not limited by this effect. In panel (b) the vertical axis, $\text{Im}[\chi_0 \chi_1^* - \chi_0^* \chi_1]$, is the unitless signal transfer function proportional to Eq. (5), and is thus linear proportional to the recorded signal.

systems such as the one reported here, we see a decrease of the dynamical range due to the slope-sign inversion dictated by the transfer function. A higher atom number N increases the total phase, and thus pushes the system further beyond the threshold set by the transfer function boundaries. Figure 5 shows the dependency on cavity atom number of the dynamical range for an in-coupling power of $P_{\text{in}} = 100$ nW and a temperature of $T = 2.5$ mK. This shows the initial dynamical range of $\Delta_{\text{dyn}} \simeq 180$ kHz below threshold and a drop to a few tens of kHz above the threshold. For typical atom numbers in our system we rarely exceed this threshold. For very high atom numbers, however, the range decreases asymptotically towards zero.

The dynamical range of a frequency locking scheme will be limited by the power broadened transition linewidth γ_{power} in all cases of Fig. 2. For higher atom numbers N , then, we will see another inversion within the narrow saturation dispersion [see Fig. 5(b)]. Such an inversion will bring us into a regime

where the dynamical range is limited by the properties of the transfer function χ rather than the power broadened transition linewidth γ_{power} . Notice that this is only true if we require the sign on the slope to be constant. The sign of the signal itself will never change, and thus some degree of locking can still be possible for a flexible servo system.

The dynamical range is of interest in particular regarding stability requirements for the interrogation laser. A standard requirement for the interrogation laser is that the interrogation laser linewidth should be smaller than the transition linewidth of the sample in order to resolve the line. If our initial interrogation laser linewidth is of the order of the natural linewidth ($\gamma_{\text{nat}} = 2\pi \times 7.5 \text{ kHz}$) this is well within the dynamical range below threshold. For very high atom numbers $N \gtrsim 1.1 \times 10^8$, however, the dynamical range decreases below the natural transition linewidth of the atoms. It is thus important that the interrogation laser is prestabilized to well within this dynamical range, before the atom-cavity error signal can be optimally utilized.

The aspect of the dynamical range considered here indicates that there is some optimal atom number depending on how efficient the servo can be made. While the slope around resonance increases linearly with the number of atoms N , and the dynamical range decreases severely above $N \approx 2.5 \times 10^7$, an intermediate error signal could be preferable. Such a signal, like the intermediate (medium green) signal of Fig. 5(b), provides the largest area under the error curve of the three shown. The preferred signal will depend on the particular experimental servo parameters.

C. Locking condition effects

Since our experimental realization is based on a cyclic operation, the cavity lock causes the length of the cavity to change dynamically throughout the experimental cycle. If the cavity dynamics is slower than required to obtain perfect locking, we see a small correction compared to the ideal locking signal of Eq. (10). This causes large deviations in the dc transmission signal but has a relatively small effect on the phase response. When the cavity lock responsiveness is too slow the condition of constant resonance between the cavity and the laser carrier frequency will no longer be fulfilled. The atomic dispersion information will no longer be fully written onto the sideband frequencies but remains, in part or fully, on the carrier frequency. This means that χ_0 is no longer purely real, and the dispersion term of the atomic phase shift affects the transmission. For high atomic phase shifts, then, the transmission of the carrier component will be significantly reduced as the resonance condition is no longer necessarily fulfilled.

The locking condition determines some initial phase ϕ_{init} written onto the cavity phase

$$\phi_{\text{cav}} = n\pi - \phi_{\text{init}}. \quad (12)$$

Here we investigate three different cases. For the case of a fast cavity lock that can follow the system dynamics we have $\phi_{\text{init}} = \phi_{\text{D}}$ as shown in Eq. (6). A second idealized case is where the cavity lock is independent of the atoms inside the cavity $\phi_{\text{init}} = 0$. This means that the length of the cavity simply follows the vacuum wavelength of the interrogation laser $L = n \frac{\lambda_{\text{vac}}}{2}$. The third, and the more realistic, case is where we

have some perturbed phase due to the experimental conditions. In our case, the fact that the locking dynamics are relatively slow results in an initial phase given by the atoms under the influence of the cooling light $\phi_{\text{init}} = \phi_{\text{MOT}}$. The phase shifts of the field components then become

$$\phi_0 = n\pi + \phi_{\text{D}} + i\phi_{\text{A}} - \phi_{\text{init}}, \quad (13)$$

$$\phi_j = (n + j)\pi - \phi_{\text{init}} \quad \text{for } j \neq 0, \quad (14)$$

for some integer n .

Since the first case has already been described above, we look at the second case of an atom-independent cavity lock. Here the cavity length ensures resonance with the laser beam assuming that there is only vacuum in the cavity. In this case the sidebands ($j \neq 0$) are always resonant, but the carrier frequency ($j = 0$) will be affected only by the atomic phase. In the limit of a very broad cavity linewidth κ this situation is equivalent to having no active lock on the cavity length. The behavior under this condition thus gives us some insight into the case of a system operating in the deep bad-cavity limit with stationary mirrors but resonant with the atomic transition.

In the third case, relevant to our current system, a slow lock means that we lock to the atoms in the MOT while the cooling light is still on. The carrier frequency thus experiences some phase shift from the ac Stark shifted atoms (ϕ_{MOT}), and this phase is written on the cavity length. Since the cavity cannot respond sufficiently fast to the subsequent conditions where the MOT light is turned off, this modifies the phase of all χ_j with ϕ_{MOT} . The phase information from the nonperturbed atoms is now only on the carrier component. This heavily modifies the dc transmission, and also causes the antisymmetric behavior of the signal to be lifted as ϕ_{MOT} is not symmetric with respect to ϕ_{D} . The carrier phase becomes

$$\phi_0 = n\pi - \phi_{\text{MOT}} + \phi_{\text{D}} + i\phi_{\text{A}} \quad (15)$$

for integer n , and the sideband phases retain the phase written on the lock $\phi_{j \neq 0} = (n + j)\pi - \phi_{\text{MOT}}$. In this case χ_0 is no longer a purely real quantity, and this modifies the signal. We have implemented this to first order by manually adding the measured phase shift ϕ_{MOT} of the system to the transfer functions of the carrier and sideband frequencies. A full description must include the modified atom-light interaction in the cavity caused by this effective cavity detuning during the probing time.

In Fig. 6 we show an example of a NICE-OHMS signal giving the dispersive response of the system. The NICE-OHMS signal has the expected features for a system with a large number of atoms in the cavity $N = 2.5 \times 10^7$ where sharp features occur due to the limitations set by the transfer function. Three theoretical curves are plotted, which shows the theoretical behavior of the system assuming a fast cavity lock (black), a cavity locked independently of atoms (dashed blue), and a cavity locked to the ac Stark shifted atoms in the MOT (light red). While these different approaches only cause slight variations close to resonance, they are necessary to include in order to explain the signal for larger detunings. As expected, the features are slightly sharper in the case of a fast cavity lock.

The consequences of a nonoptimal cavity locking condition on a laser lock is also considered here. Figure 7 shows

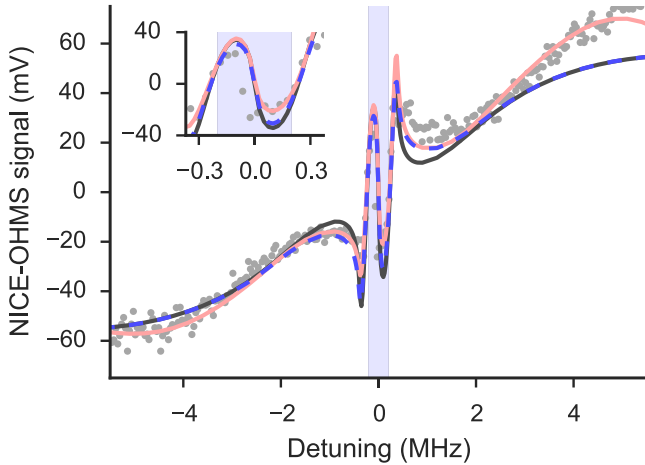


FIG. 6. NICE-OHMS dispersion signal with asymmetry due to an ac Stark shift asymmetric with respect to the probe transition. Gray dots indicate data points, whereas the curves are theoretical plots using experimental system parameters. The black curve is plotted assuming a fast lock compared to the measurement dynamics, $\phi_{\text{init}} = \phi_D$, which is the optimal case of the atom-cavity system locked to the carrier frequency of the laser. The dashed blue curve represents the case where the cavity is locked to resonance with the laser independently of the atoms, $\phi_{\text{init}} = 0$. This primarily changes the absolute size of the phase. The light red curve includes a first-order correction for the ac Stark shifted atomic phase present in the cavity when the MOT beams are on $\phi_{\text{init}} = \phi_{\text{MOT}}$. This has large effects far away from resonance, but only little effect close to resonance. The parameters used are cavity atom number $N = 2.5 \times 10^7$, temperature $T = 2.8$ mK, and an input power of $P_{\text{in}} = 115$ nW. The light blue area marks the detuning range plotted in Fig. 5(b).

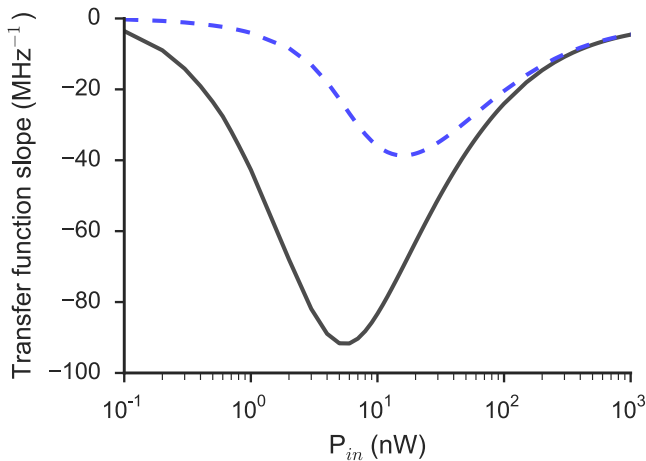


FIG. 7. Semilogarithmic plot of the transfer function slope at resonance as a function of input power. The curves are theoretical slopes of the transfer function of the system. The dashed blue curve indicates the expected behavior if the cavity was locked to resonance with the laser independently of the atoms. The black curve is the expected behavior if the cavity lock is ideal, and the full cavity-atom resonance is tuned to the laser frequency. We see a decrease in slope for nonoptimal cavity locking at all values of the input power P_{in} , as well as a distortion of the functional form which changes the position of the optimal slope.

two theoretical curves corresponding to optimal, fast locking conditions (black), and atom-independent locking (dashed blue). In the case of optimal locking the system is close to a steady state. This can be realized either when the cavity lock is fast enough to follow the shift caused by turning off the trapping light, or by using a system operating in a continuous fashion. For the parameters used here ($T = 2.5$ mK and $N = 2.7 \times 10^7$) we see an optimal phase slope with the fast lock, for powers of about $P_{\text{in}}^{\text{opt}} = 8$ nW. The phase slope is reduced for all values of the input power in the case of an atom-independent locking. The functional shape also changes, and the optimal input power is increased to about $P_{\text{in}}^{\text{opt}} = 25$ nW. Notice that while the slope is definitely reduced it is at or below a factor of 2 for powers relevant to laser locking. The optimal power also becomes more experimentally accessible, and the two cases are seen to give approximately identical slopes for powers larger than $P_{\text{in}} = 400$ nW. This indicates that the performance of the cavity lock might not be of detrimental importance to the ultimate performance of the system within technically relevant parameter regimes.

V. CONCLUSION

We have experimentally investigated an atomic ensemble of cold ^{88}Sr atoms in an optical cavity in the regime of high atomic phase shift. The phase response of the system is recorded using the NICE-OHMS technique, and has promising features for frequency stabilization.

The system operates in the bad-cavity regime which suppresses the fluctuations caused by the finite temperature of the cavity. For the case of a narrow atomic transition, the bad-cavity regime can still permit a high cavity finesse which yields a large number of photon round trips. This causes the accumulated phase to grow beyond the approximately linear regime of the cavity transfer function, and mirroring effects of the phase response can occur. These mirroring effects nonlinearly flip the slope of the dispersion signal around some maximal value. We experimentally mapped out the transition from the regime where the dispersion signal is an approximately linear representation of the atomic phase shift, to the regime where this representation is highly distorted by the cavity transfer function properties. We investigated the limitations this might have on an error signal for frequency locking of a laser. The mirroring effect causes a limitation of the dynamical range of a servo lock which must be included in the optimization of future servo systems operating using this technique.

We also investigated the ultimate performance of a laser stabilized to such a system and saw predictions consistent with earlier work [29]. These predictions rely on investigations of the phase slope achievable at resonance and do not take into account the limitations on a servo loop such as the dynamical range limitations that occur. We saw that the degradation of the signal slope caused by nonoptimal cavity locking was not detrimental to the system and amounted to a factor of 2 for realistic experimental parameters. This means that even a slow cavity lock could produce promising results for laser stabilization, and opens the possibility of leaving out the cavity lock entirely as long as the system is deep in the bad-cavity regime.

ACKNOWLEDGMENTS

We acknowledge support by the European Space Agency Contract No. 4000108303/13/NL/PA-NPI272-2012 and funding under 15SIB03 OC18 from the EMPIR programme co-financed by the Participating States.

APPENDIX: THEORY

Here we give a very brief overview of the theory used to model the interaction of the light with the atom-cavity system. We follow [27,29] and model the system by using a Born-Markov master equation to describe the evolution of the system's density matrix $\hat{\rho}$. This evolution can be written as

$$\frac{d}{dt}\hat{\rho} = \frac{1}{i\hbar}[\hat{H}, \hat{\rho}] + \hat{\mathcal{L}}[\hat{\rho}]. \quad (\text{A1})$$

The many-particle Hamiltonian describing the coherent evolution in a rotating interaction picture is given by

$$\begin{aligned} \hat{H} = & \frac{\hbar\Delta}{2} \sum_{l=1}^N \hat{\sigma}_l^z + \hbar\eta(\hat{a}^\dagger + \hat{a}) \\ & + \hbar \sum_{l=1}^N g_l(t)(\hat{a}^\dagger \hat{\sigma}_l^- + \hat{\sigma}_l^+ \hat{a}) \end{aligned} \quad (\text{A2})$$

where $\Delta = \omega_a - \omega_c$ is the atom-cavity detuning, $\hat{\sigma}^{+, -, z}$ are the Pauli spin matrices, and $\eta = \sqrt{\frac{2\pi\kappa P_{\text{in}}}{\hbar\omega_c}}$ is the classical drive amplitude. \hat{a} and \hat{a}^\dagger denote the annihilation and creation operators of the cavity mode, respectively. The coupling rate

between atoms and cavity is given by

$$g_l(t) = g_0 \cos(kz_l - \delta_l t) e^{-r_l^2/w_0^2}, \quad (\text{A3})$$

where g_0 is the vacuum Rabi frequency, k is the wave number of the cavity mode, z_l and r_l denote the longitudinal and axial positions of the l th atom, $\delta_l = kv_l$ is the Doppler shift contingent on the atom velocity v_l , and finally w_0 is the radial waist size of the cavity mode. Here the probing laser is assumed on resonance with the cavity at all times, $\omega_l = \omega_c$.

The incoherent evolution is described by the Liouvillian $\hat{\mathcal{L}}[\hat{\rho}]$ and is given by

$$\begin{aligned} \hat{\mathcal{L}}[\hat{\rho}] = & -\frac{\kappa}{2}\{\hat{a}^\dagger \hat{a} \hat{\rho} + \hat{\rho} \hat{a}^\dagger \hat{a} - 2\hat{a} \hat{\rho} \hat{a}^\dagger\} \\ & - \frac{\gamma_{\text{nat}}}{2} \sum_{l=1}^N \{\hat{\sigma}_l^+ \hat{\sigma}_l^- \hat{\rho} + \hat{\rho} \hat{\sigma}_l^+ \hat{\sigma}_l^- - 2\hat{\sigma}_l^- \hat{\rho} \hat{\sigma}_l^+\} \\ & + \frac{1}{2T_2} \sum_{l=1}^N \{\hat{\sigma}_l^z \hat{\rho} \hat{\sigma}_l^z - \hat{\rho}\}, \end{aligned} \quad (\text{A4})$$

where κ is the cavity decay rate, γ_{nat} is the atomic transition linewidth, and $\frac{1}{2T_2}$ is the inhomogeneous dephasing of the atomic dipole. The approach is thus based on a many-particle Hamiltonian \hat{H} and a derived set of complex Langevin equations that includes the Doppler effect from the finite velocity of the atoms. The evolution is found by means of a Floquet analysis and solved for the steady-state case. This will not be investigated further here; the interested reader is referred to [27,29].

-
- [1] B. J. Bloom, T. L. Nicholson, J. R. Williams, S. L. Campbell, M. Bishof, X. Zhang, W. Zhang, S. L. Bromley, and J. Ye, *Nature (London)* **506**, 71 (2014).
- [2] N. Hinkley, J. A. Sherman, N. B. Phillips, M. Schioppa, N. D. Lemke, K. Beloy, M. Pizzocaro, C. W. Oates, and A. D. Ludlow, *Science* **341**, 1215 (2013).
- [3] R. Le Targat *et al.*, *Nat. Commun.* **4**, 2109 (2013).
- [4] I. Ushijima, M. Takamoto, M. Das, T. Ohkubo, and H. Katori, *Nat. Phot.* **9**, 185 (2015).
- [5] T. Kessler, C. Hagemann, C. Grebing, T. Legero, U. Sterr, F. Riehle, M. J. Martin, L. Chen, and J. Ye, *Nat. Phot.* **6**, 687 (2012).
- [6] M. Bishof, X. Zhang, M. J. Martin, and J. Ye, *Phys. Rev. Lett.* **111**, 093604 (2013).
- [7] S. Häfner, S. Falke, C. Grebing, S. Vogt, T. Legero, M. Merimaa, C. Lisdat, and U. Sterr, *Opt. Lett.* **40**, 2112 (2015).
- [8] D. G. Matei, T. Legero, S. Häfner, C. Grebing, R. Weyrich, W. Zhang, L. Sonderhouse, J. M. Robinson, J. Ye, F. Riehle, and U. Sterr, *Phys. Rev. Lett.* **118**, 263202 (2017).
- [9] K. Numata, A. Kemery, and J. Camp, *Phys. Rev. Lett.* **93**, 250602 (2004).
- [10] G. D. Cole, W. Zhang, M. J. Martin, J. Ye, and M. Aspelmeyer, *Nat. Phot.* **7**, 644 (2013).
- [11] T. Kessler, T. Legero, and U. Sterr, *J. Opt. Soc. Am. B* **29**, 178 (2012).
- [12] S. J. M. Kuppens, M. P. van Exter, and J. P. Woerdman, *Phys. Rev. Lett.* **72**, 3815 (1994).
- [13] J. Chen, *Chi. Sci. Bull.* **54**, 348 (2009).
- [14] D. Meiser, J. Ye, D. R. Carlson, and M. J. Holland, *Phys. Rev. Lett.* **102**, 163601 (2009).
- [15] G. A. Kazakov and T. Schumm, *Phys. Rev. A* **87**, 013821 (2013).
- [16] T. Maier, S. Kraemer, L. Ostermann, and H. A. Ritsch, *Opt. Express* **22**, 13269 (2014).
- [17] M. J. Martin, D. Meiser, J. W. Thomsen, J. Ye, and M. J. Holland, *Phys. Rev. A* **84**, 063813 (2011).
- [18] S. A. Schäffer, B. T. R. Christensen, S. M. Rathmann, M. H. Appel, M. R. Henriksen, and J. W. Thomsen, *J. Phys.: Conf. Ser.* **810**, 012002 (2017).
- [19] J. G. Bohnet, Z. Chen, J. M. Weiner, D. Meiser, M. J. Holland, and J. K. Thompson, *Nature (London)* **484**, 78 (2012).
- [20] W. Zhuang and J. Chen, *Opt. Lett.* **39**, 6339 (2014).
- [21] D. Pan, Z. Xu, X. Xue, W. Zhuang, and J. Chen, in *IEEE International Conference on Frequency Control Symposium (FCS), Taipei, Taiwan, 2014* (IEEE, Piscataway, NJ, 2014).
- [22] M. A. Norcia and J. K. Thompson, *Phys. Rev. X* **6**, 011025 (2016).
- [23] M. A. Norcia, M. N. Winchester, J. R. K. Cline, and J. K. Thompson, *Sci. Adv.* **2**, e1601231 (2016).
- [24] J. Ye, L. S. Ma, and J. L. Hall, *J. Opt. Soc. Am. B* **15**, 6 (1998).
- [25] L. S. Ma, J. Ye, P. Dubé, and J. L. Hall, *J. Opt. Soc. Am. B* **16**, 2255 (1999).

- [26] O. Axner, W. Ma, and A. Foltynowicz, *J. Opt. Soc. Am. B* **25**, 1166 (2008).
- [27] P. G. Westergaard, B. T. R. Christensen, D. Tieri, R. Martin, J. Cooper, M. J. Holland, J. Ye, and J. W. Thomsen, *Phys. Rev. Lett.* **114**, 093002 (2015).
- [28] B. T. R. Christensen, M. R. Henriksen, S. A. Schäffer, P. G. Westergaard, D. Tieri, J. Ye, M. J. Holland, and J. W. Thomsen, *Phys. Rev. A* **92**, 053820 (2015).
- [29] D. A. Tieri, J. Cooper, B. T. R. Christensen, J. W. Thomsen, and M. J. Holland, *Phys. Rev. A* **92**, 013817 (2015).
- [30] I. D. Leroux, N. Scharnhorst, S. Hannig, J. Kramer, L. Pelzer, M. Stepanova, and P. O. Schmidt, *Metrologia* **54**, 307 (2017).
- [31] F. Riehle, *Frequency Standards: Basics and Applications* (Wiley-VCH, Weinheim, 2004).
- [32] B. T. R. Christensen, Ph.D. thesis, University of Copenhagen, Niels Bohr Institute, 2016.

Towards passive and active laser stabilization using cavity-enhanced atomic interaction

S A Schäffer, B T R Christensen, S M Rathmann, M H Appel, M R Henriksen and J W Thomsen

The Niels Bohr Institute, University of Copenhagen, Blegdamsvej 17, DK-2100, Denmark

E-mail: schaffer@nbi.dk

Abstract. Ultra stable frequency references such as the ones used in optical atomic clocks and for quantum metrology may be obtained by stabilizing a laser to an optical cavity that is stable over time. State-of-the-art frequency references are constructed in this way, but their stabilities are currently limited by thermally induced length fluctuations in the reference cavity. Several alternative approaches using the potential for frequency discriminating of highly forbidden narrow atomic transitions have been proposed in, e.g., [1] and [2]. In this proceeding we will present some of the ongoing experimental efforts derived from these proposals, to use cavity-enhanced interaction with atomic ^{88}Sr samples as a frequency reference for laser stabilization. Such systems can be realized using both passive and active approaches where either the atomic phase response is used as an error signal, or the narrow atomic transition itself is used as a source for a spectrally pure laser. Both approaches shows the promise of being able to compete with the current state of the art in stable lasers and have similar limitations on their ultimately achievable linewidths [1, 2].

1. Introduction

Quantum metrology and ultra-stable optical atomic clocks rely on the frequency stability of reference lasers [3, 4, 5]. These lasers have been demonstrated with linewidths down to tens of mHz [6], relying heavily on stabilization to ultra-stable reference cavities [7] whose fractional frequency stability is currently limited by the Brownian motion in the mirror substrates [8]. The possibility of using cavity-enhanced non-linear spectroscopy on narrow transition lines has been studied extensively over the years. In the context of laser stabilization recent experimental studies in [9, 10] have demonstrated the potential for a stability comparable to the state of the art. It has also been proposed to use the direct emission of radiation from atoms with narrow transition linewidths [2, 11]. Such radiation emitted directly from a narrow transition requires unrealistically large atomic samples due to the small decay rate, which renders it impractical for reference purposes. However, when operated as a laser in the bad cavity regime, not only can the emission rate be significantly increased, the laser linewidth can also experience a further spectral narrowing compared to the natural linewidth [2, 12, 13]. These effects arise if one considers the case of superradiant or superfluorescent emission of light. In this case the photon emission flux can be considerably increased by collective atomic decay, while simultaneously achieving a spectral narrowing of the emitted light inversely proportional to the single atom cooperativity [12, 13]. Pioneering advances have already been made in connection with proof-of-principle quasi-continuous superfluorescent systems [12, 14] using atoms loaded into an optical lattice at very low temperatures, as well as high temperature gas active laser systems [13, 15].

In this proceeding we will present recent experimental advances in both the passive and active approaches using ^{88}Sr . The passive approach follows [10] but uses an optimized system with an increased



cavity finesse. For improved noise characteristics of the measured signals we employ the heterodyne detection technique, NICE-OHMS [16]. Here the atom-cavity system acts as a passive frequency reference in the bad cavity regime, and we show recent results concerning the maximally obtainable phase-response.

Additionally, we report the observation of superfluorescent-like behaviour of an ensemble of thermal strontium atoms freely moving at temperatures of about 5 mK. The atoms have a strong collective coupling to a single cavity mode, significantly enhancing their collective cooperativity, and allowing them to emit a burst of photons into the cavity mode. In this approach the atoms act as the active part of the laser allowing enhanced emission intensity on a narrow atomic transition. This system may also be important for entanglement studies of atomic ensembles [17, 18] as it can move easily between interesting regimes.

Before delving into the specifics of the passive and active approach respectively we will characterize the experimental system under investigation, which is common to the two cases.

2. Cavity enhancement

Since both the passive and the active systems we are investigating here can operate on essentially the same cavity-enhanced system, this section is dedicated to the description of such a system and the physical parameters of it. In figure 1 a sketch of the atom-cavity system can be seen. It consists of an ensemble of ^{88}Sr atoms that are laser-cooled and trapped in a Magneto-Optical Trap (MOT) inside an optical cavity. The atomic transition of interest to us is the narrow $(5s^2)^1\text{S}_0 - (5s5p)^3\text{P}_1$ dipole transition at 689 nm. This transition is dipole-forbidden and has a natural linewidth of $\Gamma/2\pi = 7.5$ kHz making the requirements on the probing laser relatively relaxed, while simultaneously providing very promising results for the final laser stability. The cavity decay rate is given by $\kappa/2\pi = 539$ kHz and the free spectral range is $\Omega/2\pi = 781$ MHz resulting in a cavity finesse of $\mathcal{F} = 1450$. The coupling between the atom and the cavity field is characterized by the coupling parameter $g/2\pi = 815$ Hz. Here $g = d/\hbar \sqrt{\hbar\omega/2\epsilon_0 V_{\text{eff}}}$, where d is the transition dipole moment, ω is the transition frequency, ϵ_0 is the vacuum permittivity, and V_{eff} is the effective mode-volume of the cavity field.

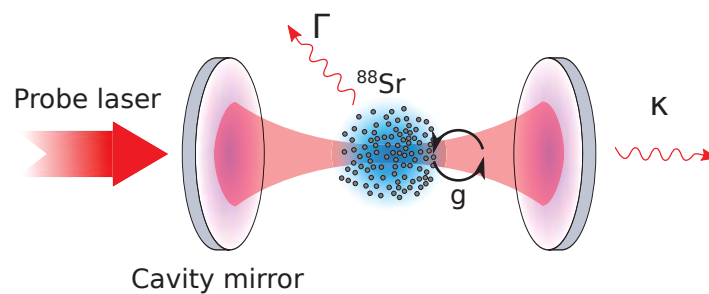


Figure 1. ^{88}Sr atoms are cooled and trapped inside a large-waist optical cavity. The atoms couple to the intra-cavity field with the coupling strength g . Cavity losses are given by the rate κ and the natural decay rate of the $(5s^2)^1\text{S}_0 - (5s5p)^3\text{P}_1$ atomic transition is given by Γ . During experiments the cooling light is switched off while cavity is kept in resonance with the probe light.

We wish to operate the system in the bad cavity regime, where the cavity linewidth κ is much larger than the natural linewidth of the atoms Γ . This ensures that the transition linewidth becomes decisive in terms of frequency discriminating properties and suppresses any line-pulling effects that may arise due to fluctuations in the cavity mirror positions. This bad-cavity limit is thus instrumental in obtaining the narrow laser linewidths we are targeting. The dynamics of the atom-cavity coupling in the system can be quantified by the single atom cooperativity $C_0 = 4g^2/\kappa\Gamma$ representing the cavity-field mediated interaction of an atom with itself, or the coherence buildup in the system relative to the coherence

decay. This quantity can also be expressed by geometrical considerations as $C_0 = \frac{6}{\pi^3} \mathcal{F} \lambda^2 / w_0^2$ where λ is the cavity field wavelength on resonance with the atomic transition, and w_0 is the waist radius of the cavity mode intensity. Since we are considering large atomic samples the system dynamics may be represented by the collective cooperativity $C_N = C_0 N$ where the total number of atoms in the cavity mode is typically $N = 2 \cdot 10^7$. In the following experiments we investigate a regime where we have strong collective coupling $C_N \Gamma \gg \Gamma_{\text{decoherence}}$, but weak single-atom coupling $C_0 \Gamma \ll \Gamma_{\text{decoherence}}$. By fulfilling these requirements we can simultaneously achieve large collective effects, and good suppression of cavity noise effects. Ideally then, we would want a high number of atoms N and a low cavity finesse \mathcal{F} .

Here the system behaviour is recorded by observing the field leaking out of the mirrors, with either a seeding field incident on the cavity, or by using a probe laser to record the absorption and phase response. The cavity length is controlled in order to ensure resonance conditions with the seed or probing laser at all times.

3. Passive approach

In a first approach to laser stabilization we will discuss passive stabilization which centers on the idea of having an external laser stabilized to a narrow frequency discriminator. This frequency discriminator should be able to provide a signal with high signal-to-noise ratio while simultaneously being very sensitive to any frequency-deviations. Here we follow [10] in using direct spectroscopy on the $(5s^2)^1S_0 - (5s5p)^3P_1$ transition in ^{88}Sr . The cavity enhances the effective interaction length with the atomic sample, by order of the finesse \mathcal{F} , while simultaneously increasing the saturation parameter by about a factor of 500. This places us deep in the saturated regime whose behaviour close to resonance was described in [10]. By sending in a probing laser and using the NICE-OHMS technique [16] we can record the phase-response of the system with good signal-to-noise ratio, see figure 2. We modulate the probing light in order to induce sidebands on the carrier frequency. These sidebands are used as reference in the heterodyne beating as they are far detuned from atomic resonance and do not interact with the atoms. They are separated by one free spectral range (FSR) of the cavity ensuring that they are transmitted through the cavity together with the carrier signal. A photodiode (PD) records the beat-signal, which is then demodulated using a mixer, thus producing the phase measurement. The antisymmetric phase-response acts as an error signal close to resonance where it has a linear dependence on the frequency detuning of the probing laser. In our case the probing laser is prestabilized to a linewidth of $\Gamma_{\text{probe}}/2\pi = 800$ Hz on the $100 \mu\text{s}$ timescale of a single measurements. By feeding the error signal obtained back to the laser it can thus be stabilized to the atom-cavity system. By ensuring that we are deep in the bad-cavity regime, the system resonance is primarily dictated by the atomic resonance, and all fluctuations on the cavity resonances are strongly suppressed.

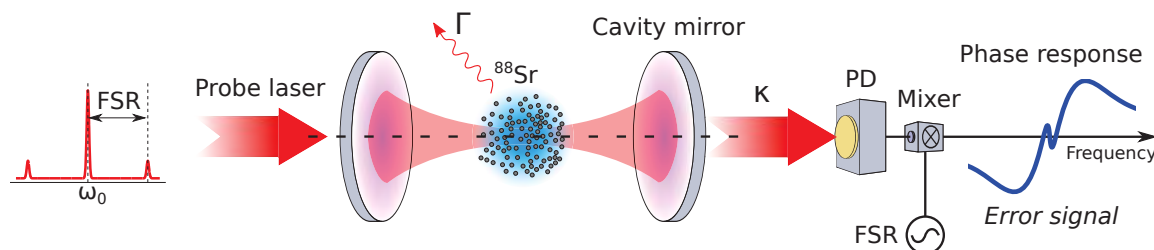


Figure 2. Sketch of a passive system where atoms inside the optical cavity are probed with an external laser having sidebands at $\pm\text{FSR}$. The frequency sidebands are used for the NICE-OHMS technique, and the beat-signal recorded on a photodiode (PD) is then demodulated. The phase-response is recorded, producing an error signal that can be used to act back on the probing laser, correcting the probe laser frequency.

The atoms are trapped using a MOT with an anti-Helmholtz coil configuration and six beams of $I = 1.5 \text{ mW/cm}^2$ blue light, red-detuned by about 40 MHz from the strong $(5s^2)^1S_0 - (5s5p)^3P_1$ transition in strontium-88. We then map out the phase response of the system by first turning on the trap for up to 800 ms in order to accumulate atoms, which will then have a temperature of typically $T = 5 \text{ mK}$. The atoms are then released by shutting off the trapping light, and a single measurement at a given probe detuning is recorded over 100 μs . Reiterating this procedure while varying the probe laser detuning then produces traces such as the ones shown in figure 3. A theoretical model from [10] using our experimental parameters is also plotted. The signal-to-noise ratio is currently limited by the shot-to-shot variations in the atom number N , as well as the stability of the cavity field intensity.

For low atom numbers we observe structures similar to what was shown in [10] where a higher atom number and a cavity with much lower finesse $\mathcal{F}_{\text{low}} = 85$ was used. As the number of atoms is increased to a similar level as used in [10], the phase shift induced by the atom-cavity system is effectively much larger due to the higher finesse, $\mathcal{F} = 1450$, of the cavity in the current system. This causes the total phase to increase beyond $\pi/2$ which is seen in the measurements as a mirroring around some maximal value. In figure 3 this can be seen for $N = 1 \cdot 10^7$ (shown in pink) at about $\pm 500 \text{ kHz}$, where two new peaks seem to have appeared. These features do not affect the slope at the center of the resonance feature which is decisive in order to provide a good error signal for laser feedback. This inversion for an absolute phase shift of π does, however, put a maximum bound on the amplitude of the error signal. As we require a significant output signal in order for a lock to not be limited by the photon shot noise on the detectors, simply increasing the finesse of these systems will thus not be an adequate solution.

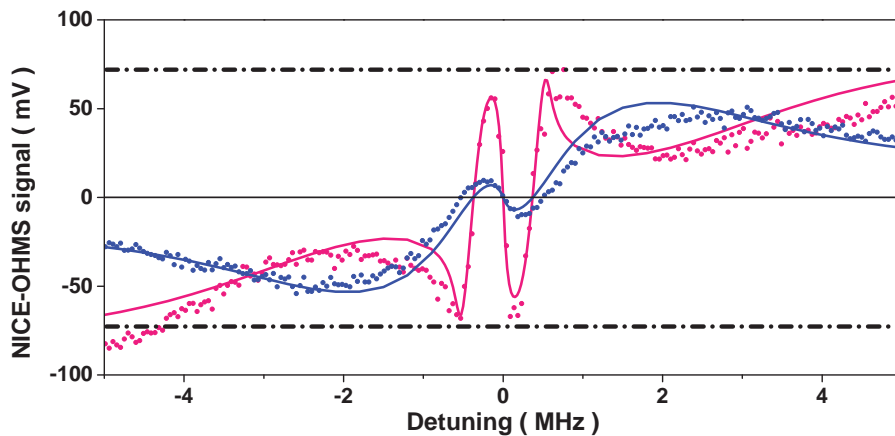


Figure 3. NICE-OHMS response of the passive system representing the phase for $N = 2 \cdot 10^6$ (blue) and $N = 1 \cdot 10^7$ (pink). Data is represented by dots whereas the full lines represents the theoretical model. For $N = 1 \cdot 10^7$ the phase shift becomes greater than $\pm\pi/2$ (corresponding to the black dot-dashed lines) at about $\pm 500 \text{ kHz}$ resulting in a mirroring of the signal at about $\pm 70 \text{ mV}$. Both signals were recorded for $T = 7 \text{ mK}$.

The shot noise limited linewidth of a laser perfectly locked to such a signal can be found following [1] and has been projected to be below 10 mHz [19] which is comparable with the state of the art in passive laser stabilization on empty optical cavities [6].

4. Active approach

Alternatively to a passively stabilized laser based on, e.g., a solid-state laser diode, the active approach seeks to use the narrow atomic transition directly as a lasing transition [2, 12, 14]. As an alternative to

having effectively stationary atoms in an optical lattice at μK temperatures, we consider here a simpler system with freely moving atoms at three orders of magnitude higher temperatures. The ultimate goal is to realize a so-called optical maser where collective effects can cause an ensemble of optical dipoles to synchronize and emit light of high spectral purity [20, 11] into the cavity mode. In a first generation of experiments pursuing these phenomena in our setup the atoms are pumped by an external source, say by applying a pi-pulse, and can coherently emit light into the cavity mode. This can happen spontaneously in a process known as superfluorescence, or by stimulation from a weak seed field inside the cavity mode. Although the introduction of a weak driving field is of less importance for the optical maser it has interesting applications for quantum optics schemes targeting entanglement of atomic ensembles. It turns out superradiance or superfluorescence is not sufficient to guarantee entanglement, but the introduction of a weak seed field may generate entanglement of the atomic ensemble [17, 18].

The condition for collective effects to be important is that the collectively enhanced emission rate is much larger than any decoherences of the system $C_N\Gamma \gg \Gamma_{\text{decoherence}}$. In the system investigated here the atoms are at a temperature of $T = 5 \text{ mK}$ resulting in the Doppler broadening of $\Gamma_{\text{Doppler}}/2\pi = 1 \text{ MHz}$ as the most important decoherence in the system. With the parameters given above we obtain a collective cooperativity of $C_N = 1 \cdot 10^4$ thus fulfilling the condition for strong collective coupling in the system, $C_N\Gamma/2\pi = 75 \text{ MHz}$. As a preliminary approach we have resonant seed-light in the cavity mode ensuring that the cavity and atomic resonances overlap. We inject a resonant pi-pulse of light at an angle of 45° with respect to the cavity axis, see figure 4. The pulse causes ground-state atoms to be excited, and collectively emit a burst of light into the cavity mode stimulated by the seed light with a delay τ_D .

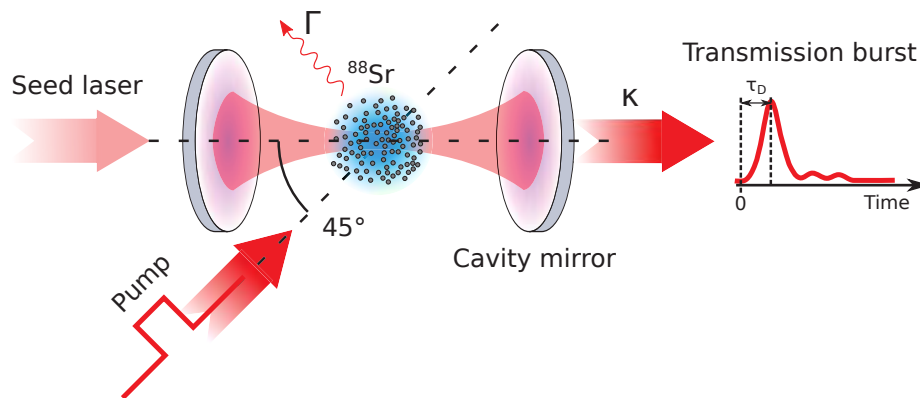


Figure 4. Sketch of an active system where ground state atoms are initially pumped into an excited state, and can subsequently be collectively stimulated to emit a burst of photons into the cavity mode after a time τ_D . The burst is observed on a photodetector through the field leaking out of the cavity.

The superfluorescent-like behaviour of the system with a seed-field in the cavity mode can be seen in figure 5 for a pump pulse of $\tau_\pi = 280 \text{ ns}$. The data was averaged over 128 data series, and retains its characteristic shape. The time τ_π corresponds to a 3π -pulse, and was chosen due to technical limitations. The delay of about $\tau_D = 1.5 \mu\text{s}$ is not limited by cavity leakage rate but attests the collective process that causes this emission of light. The decay rate of the burst can be seen to initially be far greater than the natural decay rate of the atomic transition, $1/\Gamma = 22 \mu\text{s}$, and after the initial burst small oscillations in the field intensity, partially washed out by the averaging, can be observed. Both features are characteristic for collective effects taking place, and reveals some level of coherence. Notice that the oscillations following the primary burst sit on top of two slopes. The first one is clearly visible from 2 to 4 μs and is expected to be caused by the averaging process where shot-to-shot variations in the atom number and seed power wash out some of the oscillatory behaviour. The second one is that caused by some atoms spontaneously decaying with the natural decay rate, a characteristic time of $\tau = 1/\Gamma = 22 \mu\text{s}$, and thus not participating

in the cooperative emission of light. This is attested by the fact that the final power in figure 5 is a few nW higher at $10 \mu\text{s}$ than the initial seed at $-1 \mu\text{s}$.

We have developed a theoretical description of the system allowing us to simulate the expected behaviour of the cavity transmission. This model relies on a Jaynes-Cummings approach with a classical pump-field and incorporates a constant thermal velocity distribution of the atoms. A simulation of the cavity transmitted field for typical parameters can be seen in figure 6, where a non-zero seed field is present in the cavity initially. The initial burst is seen to have similar behaviour and delay τ_D to the measured burst. It is followed by a series of oscillations that are much more pronounced than what we see experimentally. We expect that the great difference in these oscillations is caused by the spatial profile of our pump field which is narrower compared the spatial extend of the atomic cloud. This results in different Rabi frequencies for atoms at different positions and the effective population inversion obtained by the pump pulse is thus smaller in the experiment than what the simulation assumes.

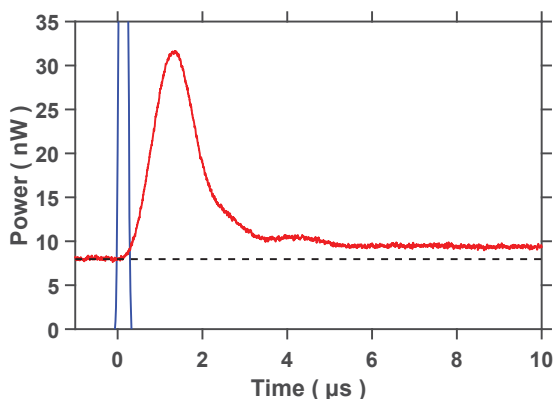


Figure 5. Recorded data of a light leaking out of the cavity (red) after a burst of light has been emitted by the atoms into the cavity mode. The initial pump-pulse (blue) is also shown. The initial decay rate of the flash is much faster than the natural decay rate Γ of the atomic transition. Though the signal is averaged over 128 data series, ringing effects are still visible. The non-zero start value is due to the seed field (dashed line) present in the cavity.

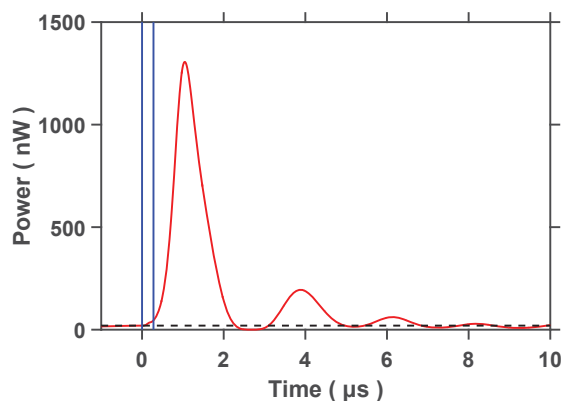


Figure 6. Simulation of a superfluorescent-like burst (red) following a 3π -pulse (blue). The initial decay of the pulse is much faster than the natural decay rate of the transition and is followed by coherent ringing characteristic for superfluorescence. Here no spatial effects of the system are included, resulting in a significant overestimation of the burst intensity. Notice that the initial value of the transmission curve is non-zero due to the seed field (dashed line).

The larger power predicted by the simulation is primarily caused by spatial dependences of the atoms and pump pulse in the system. When spatial distributions are included much better agreement between the predicted and experimentally observed power is expected. The detailed modelling of this will be the subject of future publications. The dynamical behaviour is quite similar and bodes well for a superfluorescent system with thermal atoms. By optimizing the spatial configurations of the setup, thus increased the number of participating atoms, and by better controlling some of the decoherence effects, we expect an improvement of the burst intensity by at least an order of magnitude may be obtained.

5. Conclusion

We have described our approach to and preliminary results from two of the novel methods that are currently receiving broad interest in the laser stabilization and quantum metrology communities. While these approaches rely on technically and experimentally very different approaches they have a great deal

in common when one considers the physical systems. Here we have presented the physical systems in a way that underline these similarities.

The passive approach boasts impressive predictions that should be comparable to and beyond the state of the art in laser stabilization technology. In the active approach, the emission line-narrowing effect expected by the single atom cooperativity can provide a laser with a linewidth much narrower than the natural linewidth of the lasing transition making superfluorescence in the bad cavity regime an interesting alternative approach towards an ultra narrow continuous laser source. The narrowing of the linewidth in the superfluorescent light means that such a device could significantly increase the stability and accuracy of reference lasers used in, say, optical atomic clocks.

Both techniques require a continuous system such as a beamline of ultra cold atoms in order to take full advantage of the potential for narrow laser linewidths. We are currently constructing such a beamline system in order to demonstrate both a continuous active laser as well as a passive continuously locked laser.

Acknowledgments

The authors wish to thank Jun Ye, Jingbiao Chen, James K. Thompson, and Matthew A. Norcia for valuable discussions. The research was funded by ESA Contract No. 4000108303/13/NL/PA-NPI272-2012 and the Brødrene Hartmann Foundation.

References

- [1] Martin M J, Meiser D, Thomsen J W, Ye J and Holland M J 2011 *Phys. Rev. A* **84** 063813
- [2] Meiser D, Ye J, Carlson D and Holland M J 2009 *Phys. Rev. Lett.* **102** 163601
- [3] Bloom B J, Nicholson T L, Williams J R, Campbell S L, Bishof M, Zhang X, Zhang W, Bromley S L and Ye J 2014 *Science* **506** 71
- [4] Le Targat R et al. 2013 *Nat. Comm.* **4** 2109
- [5] Ushijima I, Takamoto M, Das M, Okhubo T and Katori H 2015 *Nat. Phot.* **9** 185
- [6] Bishof M, Zhang X, Martin M J and Ye J 2013 *Phys. Rev. Lett.* **111** 093604
- [7] Kessler T, Hagemann C, Grebing C, Legero T, Sterr U, Riehle F, Martin M J, Chen L and Ye J 2012 *Nat. Phot.* **6** 687
- [8] Cole G D, Zhang W, Martin M J, Ye J and Aspelmeyer M 2013 *Nat. Phot.* **7** 644
- [9] Westergaard P G, Christensen B T R, Tieri D, Cooper J, Holland M J, Ye J and Thomsen J W 2015 *Phys. Rev. Lett.* **114** 093002.
- [10] Christensen B T R, Henriksen M R, Schäffer S A, Westergaard P G, Tieri D, Ye J, Holland M J and Thomsen J W 2015 *Phys. Rev. A* **92** 053820
- [11] Chen J 2009 *Chi. Sci. Bull.* **54** 348
- [12] Bohnet J G, Chen Z, Weiner J M, Meiser D, Holland M J and Thompson J K 2012 *Nature* **484** 78
- [13] Zhuang W and Chen J 2014 *Opt. Lett.* **39** 21
- [14] Norcia M A and Thompson J K 2016 *Phys. Rev. X* **6** 011025
- [15] Pan D, Xu Z, Xue X, Zhuang W and Chen J 2014 *2014 IEEE International Frequency Control Symposium (FCS)* **15** 1-4
- [16] Ye J, Ma L and Hall J 1998 *JOSA B* **15** 6-15
- [17] Wolfe E and Yelin S F 2014 *Phys. Rev. Lett.* **112** 140402
- [18] Wolfe E and Yelin S F 2014 *arXiv:1405.5288v2*
- [19] Tieri D, Cooper J, Christensen B T R, Thomsen J W, Holland M J 2015 *Phys. Rev. A* **92** 013817
- [20] Gross M and Haroche S 1982 *Phys. Rep.* **93** 5 301-396

Lasing on a narrow transition in a cold thermal strontium ensemble

Stefan A. Schäffer, Mikkel Tang, Martin R. Henriksen, Asbjørn

A. Jørgensen, Bjarke T. R. Christensen, and Jan W. Thomsen

Niels Bohr Institute, University of Copenhagen, Blegdamsvej 17, 2100 Copenhagen, Denmark

Highly stable laser sources based on narrow atomic transitions provide a promising platform for direct generation of stable and accurate optical frequencies. Here we investigate a simple system operating in the high-temperature regime of cold atoms. The interaction between a thermal ensemble of ^{88}Sr at mK temperatures and a medium-finesse cavity produces strong collective coupling and facilitates high atomic coherence which causes lasing on the dipole forbidden $^1\text{S}_0 \leftrightarrow ^3\text{P}_1$ transition. We experimentally and theoretically characterize the lasing threshold and evolution of such a system, and investigate decoherence effects in an unconfined ensemble. We model the system using a Tavis-Cummings model, and characterize velocity-dependent dynamics of the atoms as well as the dependency on the cavity-detuning.

I. INTRODUCTION

Active optical clocks have been suggested as an excellent way to improve the short-time performance of optical clocks by removing the requirement for an ultra stable interrogation laser [1–3]. Current state-of-the-art neutral-atom optical lattice clocks with exceedingly high accuracy are typically limited in precision by the interrogation lasers and not by the atomic quantum projection noise limit. The high Q-value of the atomic transitions ($Q > 10^{17}$) exceeds that of the corresponding reference laser stability for the duration of the interrogation cycle [4–8]. State-of-the-art reference lasers now perform below the level of 10^{-16} fractional frequency stability at 1 s [9–11]. This recent advance in performance is enabled by using crystalline mirror coatings and spacers as well as employing cryogenic techniques. Nevertheless these lasers continue to be limited by the thermal noise induced in the reference cavity mirrors [12, 13]. By using an active optical clock, the narrow spectral features of the atoms themselves produce the reference light needed, via direct generation of lasing in an optical cavity. Operation in the bad-cavity limit, where the cavity field decays much faster than the bare atomic transition, allows high suppression of the cavity noise in these lasers. It has been predicted that such systems could reach Q-factors in excess of the transition Q-factor due to narrowing caused by collective effects [3, 14]. It was recently shown experimentally that an active optical atomic clock can perform at the 10^{-16} fractional frequency stability level between 1 – 100 s, and with a fractional frequency accuracy of 4×10^{-15} by using a cyclically operated optical lattice with ^{87}Sr atoms [15]. Other systems with atoms at room temperature have shown continuous lasing with performance at the 10^{-12} level of fractional frequency stability [16].

These results demonstrate the potential of active atomic clocks, and motivates the present attempt to improve the understanding of atom dynamics in such a system. We concentrate on a cold atomic gas consisting of bosonic ^{88}Sr cooled to a temperature of $T \approx 5$ mK, and permitted to expand freely as a thermal gas while lasing.

Superradiant lasing in such a system would substantially reduce the technological challenges of maintaining truly continuous operation compared to the case of atoms confined in an optical lattice trap [17, 18].

We experimentally demonstrate pulsed lasing on a narrow transition in ^{88}Sr and describe the characteristic dynamics of our system. Using a Tavis-Cummings model we simulate the full system consisting of up to 8×10^7 individual atoms and give a qualitative explanation of the dynamics. Rich velocity- and position-dependent dynamics of the atoms are included in the description and become an important factor for understanding the lasing behavior. The model allows us to quantify these behaviors and set requirements on ensemble size and temperature to realize strongly driven or weakly driven superradiance respectively. Such requirements are useful for the future development of truly continuous lasing on ultra-narrow clock transitions in strontium, or other atomic species.

In section II we describe the physical characteristics of our system and the experimental routine. Section III describes our theoretical model for the cold-atom based laser, and the proposed lasing dynamics. In Section IV the lasing characteristics are presented and comparisons between experiment and simulations are made.

II. EXPERIMENTAL SYSTEM

The system consists of an ensemble of cold ^{88}Sr atoms cooled and trapped in a 3D Magneto-Optical Trap (MOT) from a Zeeman-slowed atomic beam, using the $^1\text{S}_0 \leftrightarrow ^1\text{P}_1$ transition. The atomic cloud partially overlaps with the mode of an optical cavity, and can be state manipulated by an off-axis pumping laser, see Fig. 1. The cavity can be tuned on resonance with the $^1\text{S}_0 \leftrightarrow ^3\text{P}_1$ intercombination line, and has a linewidth of $\kappa = 2\pi \cdot 620$ kHz. Our mirror configuration ensures a large cavity waist radius of $w_0 = 450$ μm , which ensures a reasonably high intra-cavity atom number, N_{cav} of order 2×10^7 . N_{cav} is estimated from fluorescence measurements and lasing pulses, giving $N_{cav} = \eta_{cav} N$ of the full

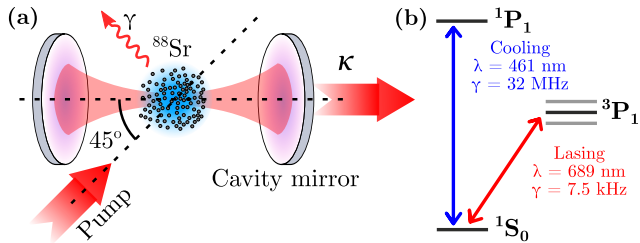


FIG. 1. (a) Schematic of the experimental system showing a thermal ensemble of strontium atoms partially overlapping with the cavity mode. Pumping prepares the atoms in the excited state, and allows subsequent emission of a coherent pulse into the cavity mode. Light couples out of both ends of the cavity with the cavity decay rate κ , and is detected at one end only. (b) Level scheme for ^{88}Sr showing the cooling and lasing transitions. Wavelength (λ) and natural transition decay rates (γ) are indicated.

MOT atom number N , where $\eta_{cav} = 0.2$. Throughout this paper the atom number within the cavity N_{cav} is an effective number since all atoms have different velocities and positions, resulting in a coupling g^j for the j 'th atom to the cavity mode. While this is included in the theoretical simulations, we permit ourselves to assume a constant effective coupling, g_{eff} , and effective atom number when discussing regimes and general scaling behavior.

The large cavity waist ensures a negligible decoherence induced from transit time broadening of $\Gamma_{tt} = 2\pi \cdot 2.2$ kHz. While the $^1\text{S}_0 \leftrightarrow ^3\text{P}_1$ transition used for operation has a linewidth of $\gamma = 2\pi \cdot 7.5$ kHz, the ensemble temperature T causes a Doppler broadening of the order of $\Gamma_D = 2$ MHz. The bare atoms are thus deep in the bad-cavity regime, $\gamma \ll \kappa$, whereas the total inhomogeneously broadened ensemble is just below the bad-cavity threshold. Here, the cavity field decay rate and total atomic decoherence rate is of similar size $\kappa \sim \Gamma_{dec}$, and ensemble preparation can heavily affect the lasing process and the attainable suppression of cavity noise. We characterize the system by its collective cooperativity $C_N = C_0 N_{cav}$, and the single-atom cooperativity is given by $C_0 = \frac{(2g_{eff})^2}{\kappa\gamma}$. This leads us to the definition of a collective coupling rate $\Omega_N = 2\sqrt{N_{cav}}g_{eff}$. While the spectral linewidth of the emitted light is controlled by C_0 [3, 19], the coherence build-up, and thus lasing power, is determined by C_N . Increasing the coupling rate g_{eff} , and thus the single-atom cooperativity, will then improve interaction at the expense of the ultimately attainable lasing linewidth.

After preparing the MOT, the cooling light is switched off, and an off-axis pumping beam is used to excite the atoms to the $^3\text{P}_1$ state. By pumping the atoms on resonance for 170 ns a peak excitation of approximately 85% is obtained for the atoms within the cavity mode. Inhomogeneous Doppler detuning caused by the thermal distribution of the atoms, and the large spatial distribution of the full atomic ensemble with respect to the

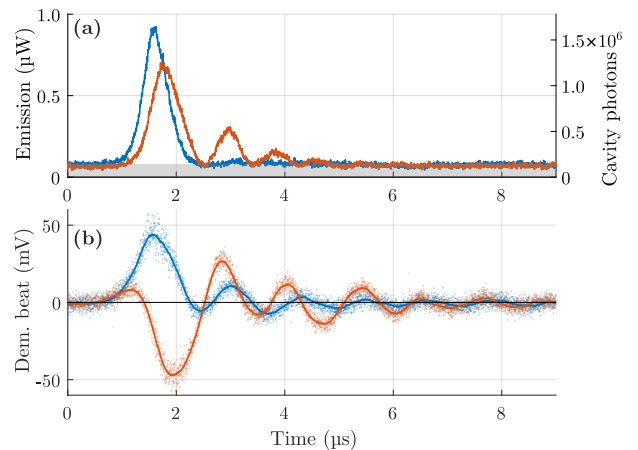


FIG. 2. Experimental data showing the time evolution of the lasing pulse after pumping for cavity-atom detuning $\Delta_{ce} = 0$ kHz (blue) and $\Delta_{ce} = 900$ kHz (orange) respectively. The pumping pulse ends at time $t = 0$ μs . (a) A background power level of 75 nW in shaded gray indicates the constant non-interacting reference laser field. (b) Beat signal between reference field and laser pulses. The dots are data whose running mean is shown with full lines.

pumping field result in varying Rabi frequencies for different atoms. The collective atomic Bloch vector will thus contain some level of atomic coherence from the imperfect pump pulse. Due to the excitation angle of 45° the pump phase periodicity along the cavity axis suppresses any forced coherence between the atoms and cavity field. Additionally, the spatial coherence of the fast atoms will wash out as they propagate inhomogeneously along the cavity axis. In order to remove any remaining phase-coherence we apply light at 461 nm detuned about $\Delta\nu = -41$ MHz from the $^1\text{S}_0 \leftrightarrow ^1\text{P}_1$ for 500 ns after pumping. This results in an average of 1.3 scattering events per atom, and ensures atoms are either in the excited or ground state. We see no quantifiable change in the lasing behavior by doing this.

Once excited, the atoms will build up coherence mediated through the cavity field and emit a coherent pulse of light into the cavity mode. Light leaking through one of the cavity mirrors is then detected on a photodiode. We couple a reference field, s , into a cavity mode tuned far off resonance, $\Delta_{sc} = 780$ MHz, with the $^1\text{S}_0 \leftrightarrow ^3\text{P}_1$ transition, allowing us to lock the cavity length on resonance with the atoms.

Fig. 2 shows an example of a lasing pulse and the associated beat signal when the cavity is on resonance (blue) and detuned $\Delta_{ce} = 900$ kHz (orange) from the atomic resonance respectively. The pumping pulse ends at $t = 0$ s and after some delay, τ (on the order of few μs), a lasing pulse is emitted into the cavity mode. The lasing pulses are followed by a number of ringings. This is a fingerprint of the coherent evolution of the cavity-atom system, where light emitted into the cavity mode

is reabsorbed by the atoms, and is then re-emitted into the cavity mode. The lasing pulse shown in Fig. 2 (a) is detected superimposed on a 75 nW background. This background is a reference field used for locking the length of the cavity, and provides the opportunity for a heterodyne beat with the lasing pulse. At zero cavity-atom detuning ($\Delta_{ce} = 0$) the ringings are barely visible due to reference field intensity noise. When detecting the beat signal, however, the signal scales linearly rather than quadratically with the lasing E-field E_{las} , and here multiple ringings are visible in both the resonant and off-resonant cases.

The beat signal is down-sampled and given by $S_{beat} \propto |E_{las}| \sin \phi$. The envelope thus gives us a less noisy information on the amplitude of the lasing pulse. $\sin \phi$ allows us to retrieve the phase information. In Fig. 2 (b) we see the phase during the initial lasing pulse differ between the two datasets. This is a result of the randomized phase of the atomic coherence for each experimental realization. A rapid-fire pulse laser is thus limited by the lack of memory between subsequent lasing pulses.

III. SEMI-CLASSICAL MODEL

In order to gain an improved understanding of the dynamics involved in our system, we simulate the behavior with a Monte-Carlo approach. We model the system using a Tavis-Cummings hamiltonian for an N-atom system. The description includes a classical pumping field at frequency ω_p . In the Schrödinger picture the full expression becomes:

$$H = \hbar\omega_c a^\dagger a + \sum_{j=1}^N \hbar\omega_e \sigma_{ee}^j \quad (1)$$

$$+ \sum_{j=1}^N g_c^j (\sigma_{ge}^j + \sigma_{eg}^j) (a + a^\dagger)$$

$$+ \sum_{j=1}^N \hbar \frac{\chi_p^j}{2} (\sigma_{ge}^j + \sigma_{eg}^j) \left(e^{i\vec{k}_p \cdot \vec{r}_j - i\omega_p t} + e^{-i\vec{k}_p \cdot \vec{r}_j + i\omega_p t} \right).$$

Here ω_c is the angular frequency of the cavity mode, a is the corresponding lowering operator. The involved electronic energy states $|g\rangle$ and $|e\rangle$ correspond to the ground and excited atomic states, with a transition frequency of ω_e , as seen in Fig. 1 (b). The interaction between cavity field and the j 'th atom is governed by the coupling factor g_c^j and the pump beam has a semi-classical interaction term with Rabi frequency χ_p^j . The position of the atom is given by \vec{r}_j , and \vec{k}_p is the pump beam wavevector.

By entering an interaction picture, and using the rotating wave approximation, the time evolution of the system operators can be obtained. Here we make the semi-classical approximation of factorizing the expectation values for operator products, which results in linear scaling of the number of differential equations with

the number of atoms. This approximation results in the neglect of all quantum noise in the system, and by consequence any emerging entanglement [20–22]. We motivate this assumption by the very large number of atoms in the system, whose individual behaviors are taken into account with separate coupling factors g_c^j . The quantum noise is then expected to be negligible compared to the single-operator mean values. The operator mean values are described by three distinct forms of evolution:

$$\begin{aligned} \langle \dot{\sigma}_{ge}^j \rangle &= - \left(i\Delta_{ep} + \frac{\Gamma}{2} \right) \langle \sigma_{ge}^j \rangle \quad (2) \\ &+ i \left(g_c^j \langle a \rangle + \frac{\chi_p^j}{2} e^{-i\vec{k}_p \cdot \vec{r}_j} \right) (\langle \sigma_{ee}^j \rangle - \langle \sigma_{gg}^j \rangle) \\ \langle \dot{\sigma}_{ee}^j \rangle &= -\Gamma \langle \sigma_{ee}^j \rangle + i \left(g_c^j \langle a^\dagger \rangle + \frac{\chi_p^j}{2} e^{i\vec{k}_p \cdot \vec{r}_j} \right) \langle \sigma_{ge}^j \rangle \\ &- i \left(g_c^j \langle a \rangle + \frac{\chi_p^j}{2} e^{-i\vec{k}_p \cdot \vec{r}_j} \right) \langle \sigma_{eg}^j \rangle. \\ \langle \dot{a} \rangle &= - \left(i\Delta_{cp} + \frac{\kappa}{2} \right) \langle a \rangle - \sum_{j=1}^N i g_c^j \langle \sigma_{ge}^j \rangle. \end{aligned}$$

Here $\Delta_{nm} = \omega_n - \omega_m$ is the detuning of the n 'th field with respect to the m 'th field. Because of the semi-classical approximation the hermitian conjugate of these operators are simply described by the complex conjugate of their mean values, while $\langle \sigma_{ee}^j \rangle + \langle \sigma_{gg}^j \rangle = 1$. This leaves us with a total of $1 + 2N$ coupled differential equations where N is on the order of 10^7 .

The Monte-Carlo simulation assumes the atoms are initially in the ground state, and subsequently pumped into the excited state and left to evolve with time. Atomic positions and velocities are sampled randomly from a 3D Gaussian and a thermal Maxwell-Boltzmann distribution respectively. The positions are distributed with standard deviations of 0.8 mm, and the velocities according to a temperature of $T = 5$ mK, both found from experimental assessment of our system. Atomic motion is treated classically and without collisions. The atoms interact only via the cavity field, and any spontaneous emission into the cavity mode is neglected. The lasing process is initiated by an initial nonzero total coherence $\sum_{j=1}^N \sigma_{ge}^j$, resulting from the pumping pulse. This replaces the role of quantum noise in the system, and without it the system would couple only to the reservoir.

Our simulations indicate that the lasing occurs in three characteristic regimes determined by the ratios of the atomic decay rate γ , the cavity decay rate κ and the collective atomic coupling factor Ω_N , see Fig. 3. We consider only $\Omega_N > \gamma$ since for $\Omega_N < \gamma$ the spontaneous atomic decay to the reservoir will dominate. In the bad cavity regime where $\gamma < \kappa$ a low coupling strength will allow the output power to scale quadratically with atom number, whereas high coupling strength will result in a linear power scaling and multiple Rabi oscillations in the

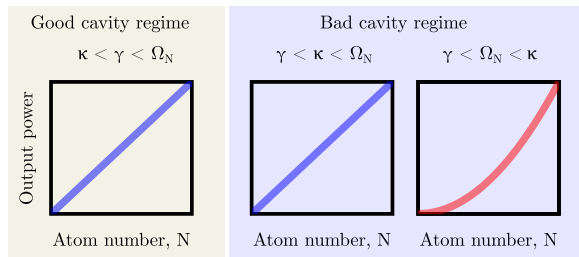


FIG. 3. Three distinct lasing regimes. In our system we operate on the intersection of all three and seem to realize both N and N^2 atom number scaling behaviors.

atomic population during a single lasing pulse. Broadening effects can lead to higher effective decoherence rates Γ_{dec} which must be considered.

IV. SYSTEM CHARACTERIZATION

We characterize the lasing properties and pulse dynamics of the system by varying cavity-atom detuning and atom number. We compare the measurements with simulated experiments to verify the understanding in the numerical model. This will then allow us to draw out some behaviors from the model that are inaccessible experimentally.

A. Lasing Threshold

By varying the total number of atoms in the trap, we find the lasing threshold of the system. This gives an atom number dependency of the pulse power and the associated delay, see Fig. 4 (a). We plot the peak power of the emitted lasing pulse as a function of the atom number N in the full atomic cloud for 795 experimental runs. Each point is about 40 binned experimental runs, with the standard deviation indicated. For low atom numbers (white region), $N \leq 3 \times 10^7$, excited atoms decay with their natural lifetime, $\tau = 22 \mu\text{s}$. In an intermediate regime of $3 \times 10^7 < N < 5 \times 10^7$ (red region) the peak power appears to scale quadratically with the atom number, as the onset of lasing occurs. This is what we would expect according to the parameter regimes illustrated in Fig. 3. Finally, for higher atom numbers (blue region), $N > 5 \times 10^7$, the peak power becomes linearly dependent on the atom number, as the collective coupling Ω_N becomes much larger than κ . We show a red and blue curve fitted to their corresponding regions with an N^2 - and N -scaling respectively. The green points show the results from simulation, and appear to agree well with experiment. The curves are fitted to the raw data, within the respective regions before any binning, and the lasing threshold is determined from the quadratic fit. While the lasing process does not initiate for low atom numbers due to the requirement that $C_N \gamma \gg \Gamma_{dec}$, for high

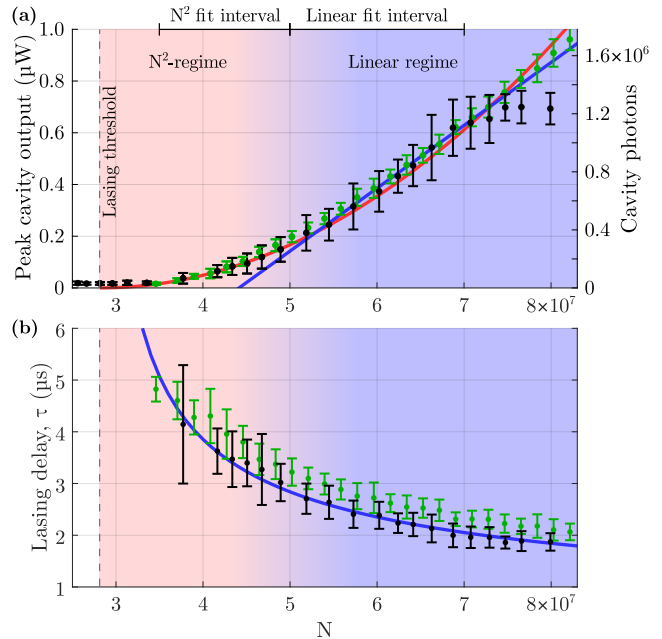


FIG. 4. Primary pulse behavior. (a) Atom number dependency of peak cavity output power at a single mirror. Black points indicate data, whereas green points indicate simulation results. Threshold (N_{th}) is determined by fitting the quadratic curve (red), and the linear curve (blue) is fitted only to $N = 5$ to 7×10^7 . (b) Delays between pumping and lasing pulses. The delay is defined as the time interval between the end of the pumping pulse, and the peak intensity of the subsequently emitted laser pulse. The blue curve is fit using $a/\sqrt{N - N_{th}}$.

N the cavity field builds up sufficiently that the slowest atoms become strongly driven. At high atom numbers ($N > 7 \times 10^7$) the cavity output seems to saturate as the assumption of linear scaling of the cavity atom number (N_{cav}) with respect to the MOT atom number (N) breaks down, and these points are not included in the linear fit. The nonzero value of the data below threshold is caused by random noise.

In Fig. 4 (b) we plot the delay between the end of the pumping pulse and the associated peak in laser pulse emission. The delay has high uncertainties in the red region where we expect an $1/N$ scaling [23]. For high N we expect a $1/\sqrt{N}$ trend [25] (blue), and we choose to fit this to the entire dataset. When going to low atom numbers background noise becomes increasingly important until no emission peak is visible, and the effective delay goes to infinity. Once again we show the simulation with green dots. Notice that there is a clear tendency towards longer delays in the simulation. We believe this to be caused by the fact that the model does not include spontaneous emission into the cavity mode.

As the number of atoms decreases, so does the collective cooperativity, and thus the ensemble coherence build-up. The time it takes for the ensemble to phase-synchronize increases, leading to the increased delay time

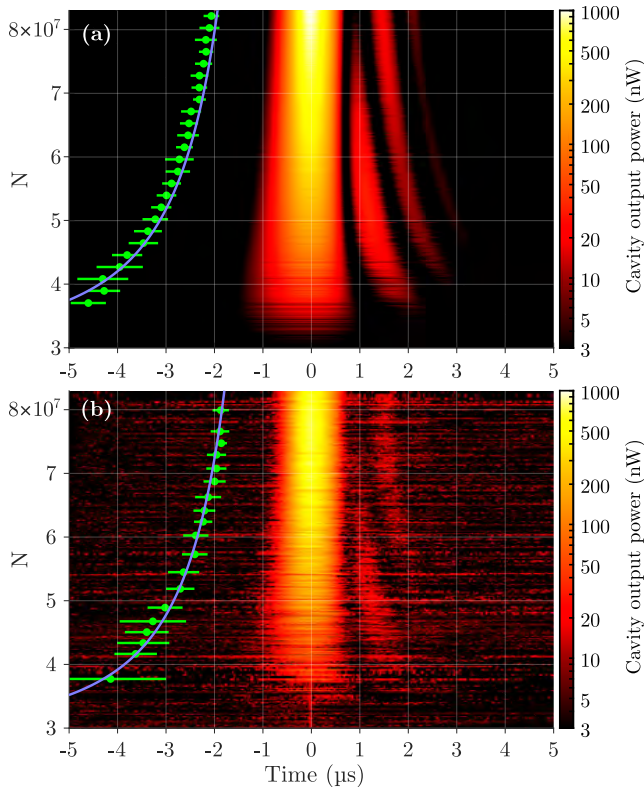


FIG. 5. Atom number (N) dependency. **(a)** Simulation results. When the cavity mode is at atom resonance, the characteristic ringing frequency of the lasing pulses, varies weakly with the atom number. The pulse delays τ are shown with a $a/\sqrt{N - N_{th}}$ -fit (blue). **(b)** Experimental results. The simulations are nicely replicated by experiment, with the first ringing disappearing in noise at around $N = 7 \times 10^7$.

and associated decrease in peak intensity. The total number of photons emitted during a pulse is not constant, but scales with the collective cooperativity C_N , just as the peak output power in Fig. 4.

B. Pulse evolution

We map out the time evolution as a function of atom number and cavity-atom detuning respectively. To ease interpretation we align all datasets to the peak intensity at $t = 0$ s in figures 5 and 6. The delay in the system can be seen as the distance between this maximal value at time zero and the green dots indicating the end of the pumping pulse.

1. Atom number variation

In Fig. 5 (a) we simulate the behavior of the lasing pulse when the atom number is changed. We set the cavity-atom detuning to zero ($\Delta_{ce} = 0$) and vary the

atom number in the MOT while keeping the density profile constant. The green points indicate the end of the pumping pulse, and are binned in order to ease interpretation. The ringing frequency decreases as the atom number is reduced, and at low atom numbers only a single lasing pulse is visible.

On Fig. 5 (b) experimental results are shown. We vary again the atom number, allowing comparison to the simulations. A clear primary peak can be seen for atom numbers $N > 3 \times 10^7$, and a subsequent ringing in the light emission is observed. The reference light used for cavity locking shows up as a noisy background in the experimental data, and a constant offset corresponding to the mean value of the background signal has been subtracted in both figures 5 (b) and 6 (b). The data was recorded in sets of 50 with a randomly varying $N^{set-point}$. This means that slowly varying experimental conditions show up as slices of skewed data, but avoids unintended biasing of the results.

The ringing behavior is well explained by following the evolution of the atomic inversion. For high atom numbers the collective coupling in the system becomes strong enough that the photons emitted into the cavity mode are not lost before significant reabsorption takes place. This leads to an ensemble that is more than 50% excited by the end of the primary lasing pulse, and subsequent laser emission (ringing) will thus follow. In this regime where the collective coupling rate is much larger than the cavity decay rate $\Omega_N > \kappa$ the system output is expected to behave as the central plot of Fig. 3. At low atom numbers we get $\Omega_N < \kappa$ and light emitted by the atoms is lost from the cavity mode too fast to be reabsorbed by the atoms. As a result the primary lasing pulse creates a significant reduction in the ensemble excitation so that no further collective decay occurs, and the atoms subsequently decay only through spontaneous emission. In this regime the output power is expected to scale as N^2 , illustrated by the rightmost graph of Fig. 3. This is the behavior expected from an ideal superradiant system [23–25].

2. Cavity detuning

With a constant atom number of $N = 7.5 \times 10^7$, we now vary the cavity-atom detuning Δ_{ce} in Fig. 6. Here a broad range of cavity-atom detunings, up to about $\Delta_{ce} = \pm 2$ MHz is seen to facilitate lasing. At zero detuning the primary lasing feature is maximal and subsequent ringings are suppressed. The lasing pulse delay is seen to scale as Δ_{ce}^2 , and is thus linearly insensitive to fluctuations close to $\Delta_{ce} = 0$.

For non-zero detuning the oscillatory behavior of the lasing intensity is seen to increase in frequency, scaling with the generalized Rabi frequency of the coupled atom-cavity system $\Omega'_N = \sqrt{4N_{cav}g^2 + \Delta_{ce}^2}$ [26, 27]. A noticeable effect is the apparent suppression of ringings for any detunings $\Delta_{ce} \leq 200$ kHz.

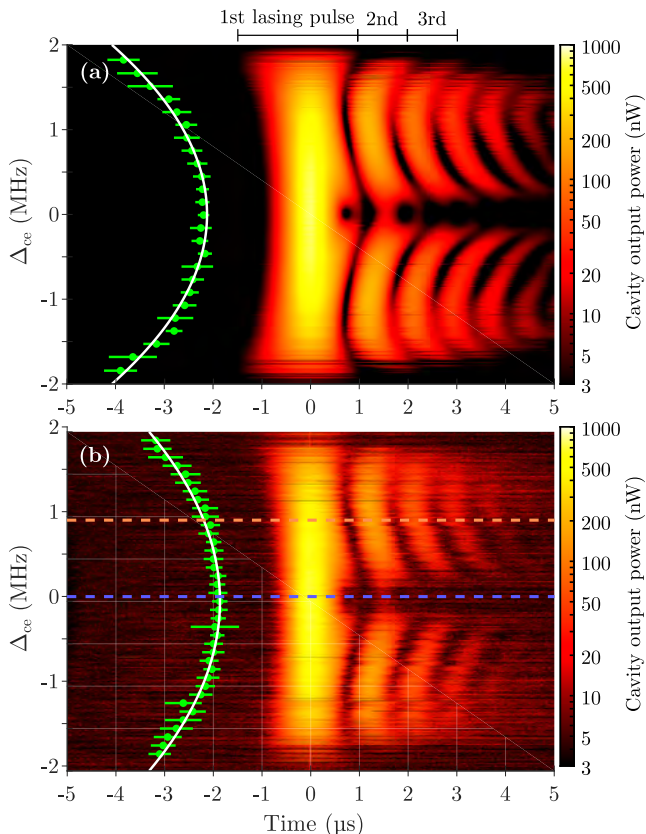


FIG. 6. Cavity-atom detuning dependency of the lasing pulse. The oscillatory behavior is strongly suppressed at resonance, but appears clearly once the cavity is detuned. Here at least four subsequent ringings are visible. The ringing frequency scales with the detuning frequency and appears symmetric around zero detuning. The white line is a Δ_{ce}^2 -fit to the pulse delays τ . The atom number is $N = 7.5 \times 10^7$. (a) Simulation results. The temperature was set to $T = 5$ mK. (b) Experimental results. The dashed blue and orange lines indicate the cuts shown in Fig. 2 (a).

The cavity-atom detuning range for which a significant lasing pulse is produced can be quite broad compared to the natural transition linewidth γ . The effective coupling between the atomic ensemble and the cavity field scales with the overlap of the cavity resonance and the atomic ensemble linewidth. The inhomogeneous broadening of this atomic linewidth caused by build-up of optical power in the cavity thus increases this range significantly. The pulse can be initiated by only a few photons in the cavity field. As the intensity in the cavity mode builds up, power broadening acts to increase the effective mode overlap between the field and individual atoms. This increases the effective gain in the system, both at finite and zero detuning, allowing more atoms to participate and more energy to be extracted than would have otherwise been the case. For the case of a much colder atomic ensemble ($\sim \mu\text{K}$) the Doppler broadening of the atomic transition is no longer significant, but

further simulations indicate that the width of the cavity-atom detuning region that supports lasing remains wide.

3. Velocity-dependent dynamics

During the lasing process, the Rabi frequency of each atom will vary in time due to the changing cavity field intensity, while the atomic motion along the cavity mode leads to velocity-dependent dynamics. A typical thermal atom may move a distance of a few wavelengths during the lasing process in this temperature regime. Our simulation shows how atoms affect the lasing process differently, depending on their velocities along the cavity axis, see Fig. 7. With an angle of 45° between the cavity axis and the pump pulse beam, the slow atoms along the cavity axis are preferentially excited during pumping. These atoms initiate the lasing process, while faster atoms may suppress it by absorbing light. Different velocity classes dominate emission or absorption of the cavity photons at different times during the initial pulse and subsequent ringings. The theoretical description of the velocity-dependent behavior shown in Fig. 7 provides a qualitative understanding of the effect of having thermal atoms in the system. As atoms are cooled further, their behavior becomes increasingly homogeneous, and the asynchronous behavior of hot atoms no longer destroys the ensemble coherence.

Fig. 7 (a) illustrates the velocity dynamics for the case of a resonant cavity, $\Delta_{ce} = 0$. For a range of different velocity groups, this shows the rate of change of the atomic ground state population due to interactions with the cavity field. Significantly more ringings after the primary pulse are visible here than in the emitted power on Fig. 5. Most of these ringings see an approximately equal amount of emission and absorption, causing the energy to remain in the atomic excitations rather than being lost from decay of the cavity mode. They can, however, be seen in the phase response of the system as illustrated in Fig. 2 (b). Eventually loss from spontaneous emission into the reservoir becomes an important decay channel. Concentrating on the slowest atoms, we see emission during the full length of the primary lasing pulse. For the subsequent pulses these atoms alternate between absorbing or emitting light. If we could isolate the light from the slowest atoms, we would thus only see every second oscillation in the output power. For atoms with larger velocities, there will sometimes be both emission and absorption during any single pulse, and we even see the tendency of some velocity groups to consistently emit ($v = 0.5$ m/s) or absorb ($v = 0.65$ m/s) throughout the full process (red dashed lines on Fig. 7). This indicates that even for the case of a resonant cavity the velocity groups contributing most to the emitted light during the pulse ringings are not the resonant ones. In the case of a detuned cavity mode, Fig. 7 (b), the initial behavior is very similar. The atoms whose Doppler detuning brings them on resonance with the detuned cavity, emit

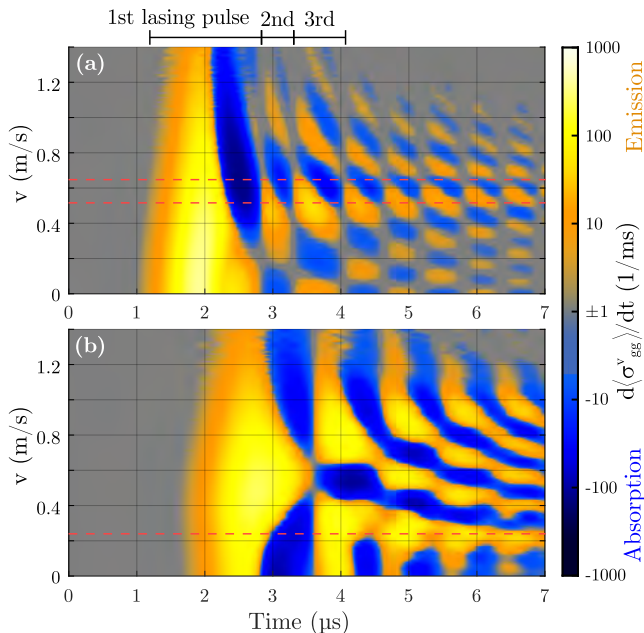


FIG. 7. Velocity-dependent atomic absorption and emission during the lasing process for the case of a resonant and detuned cavity respectively. The atoms are pumped by an excitation pulse ending at time zero. Yellow colors represent emission into the cavity mode while blue represents absorption. Red dashed lines indicate velocity groups that behave consistently throughout the ringings. (a) Resonant cavity. Ringings after the primary pulse can be seen as vertical lines where $d \langle \sigma_{gg}^v \rangle / dt = 0$. The atom number used here is $N = 7.5 \times 10^7$. (b) The cavity field is detuned by $\Delta_{ce} = 1$ MHz, and the peak emission contribution during the primary pulse comes from atoms with a speed of $v = 0.6$ m/s along the cavity axis.

throughout the primary lasing pulse, whereas others will begin to absorb. Once again some atoms ($v = 0.25$ m/s) appear to emit light throughout the pulse ringings. The periods of zero emission or absorption between ringings (gray) are no longer visible, as some light is always emitted and absorbed by the atoms. The minima in the emitted power is thus no longer caused by zero emission, but rather by the cancellation between different velocity classes. This behavior corresponds well to the results of Fig. 6 where ringings are much more pronounced in the case of large cavity-atom detuning. Future studies of the spectral properties of superradiant light in cold-atom systems, could elucidate the dependency of emitted light frequency on the finite temperature of the atoms.

V. CONCLUSION

In this paper we have investigated the behavior of an ensemble of cold atoms excited on a narrow transition and coupled to the mode of an optical resonator. The enhanced interaction provided by the cavity facilitates

synchronization of the atomic dipoles, and results in the emission of a lasing pulse into the cavity mode. This realizes the fundamental operating principle for an active optical clock, where superradiant emission of laser light can be used as a narrow-linewidth and highly stable oscillator.

We mapped out the emitted laser power as a function of atom number in order to identify the threshold of about $N_{cav}^{threshold} = 6 \times 10^6$ atoms inside the cavity mode. Two different scalings of laser output power in the bad cavity regime are identified, and though our system is at the limit of the bad cavity regime, both regimes are realized by varying the atom number.

In an attempt to quantify the decoherence effects resulting from finite atomic temperature, a Tavis-Cummings model was developed. By using detailed parameters of the pumping sequence, atomic spatial distribution and orientation, the model is seen to reproduce the experimental results to a high degree. The emitted energy from the atoms is seen to exhibit temporal Rabi oscillations as it undulates between atomic and cavity excitation. This behavior is elucidated via the numerical simulation by investigating the change in atomic excitation as a function of atomic speed throughout the lasing pulse sequence. We see that different velocity groups behave anti-symmetrically, with respect to each other. Surprisingly the velocity group mainly contributing to emission rapidly changes from resonant atoms to atoms that are more detuned with respect to the cavity. This is caused by a faster initial loss of excitation for resonant atoms. A similar effect is seen in the case of a detuned cavity. Here the atomic behavior is much more uniform across different atomic speeds, as the relation between atom number and cavity coupling becomes more homogeneous.

This system relies on rapid-fire pulses of lasing from independent ensembles of atoms, which limits the pulse-to-pulse phase coherence. The phase coherence remains intact between pulses if we could ensure atoms are always present in the cavity as a memory, e.g., in a continuous system. The prospect of a continuously lasing atom-cavity system based on unconfined cold atoms is intriguing because of the severe reduction in engineering requirements compared to a system based on, e.g., sequential loading of atoms into an optical lattice [18]. The velocity-dependent dynamics are important in order to understand what kind of equilibrium one can expect in such a system. An investigation of the spectral characteristics of stationary atomic systems have been shown in [14, 15], and are promising for the transition we have used here. Investigation of the spectral properties in an unconfined ensemble will be presented in future work.

ACKNOWLEDGMENTS

SAS and MT contributed equally to the scientific work. The authors would like to thank J. H. Müller, A. S.

Sørensen, J. Ye, J. K. Thompson, and M. Norcia for helpful discussions. This project has received funding from the European Union’s Horizon 2020 research and innovation programme under grant agreement No 820404 (iqClock project), the USOQS project (17FUN03) under the EMPIR initiative, and the Q-Clocks project under the European Commission’s QuantERA initiative. JWT and BTRC were additionally supported by a research grant 17558 from Villum fonden.

observations) by $P = \hbar\omega_c n \kappa / 2$.

Appendix A: Simulation parameters

Simulations of the system are based on numerical integration of Eqs. 2 [28]. The system is initiated with all atoms in the ground state and no coherence. The atoms are randomly distributed, assuming a Gaussian density profile in each dimension, and randomly generated thermal velocities for a temperature of $T = 5$ mK. These velocities are assumed constant due to negligible collision rates. The pumping is simulated by turning on the Rabi frequency χ_p^j , which is calculated for each atom based on their coupling to the running-wave pump pulse and its intensity. The spatial intensity distribution is estimated based on measurements of the pump beam with a CCD camera and an optical power meter. After spatial smoothing to even out noise, the data from the CCD camera is used directly in the simulations, and correspond approximately to a slightly non-Gaussian elliptic profile with waists of $w_0^g = 2.7$ mm and $w_0^m = 1.5$ mm. The minor axis of the ellipse is rotated by 35° with respect to the magnetic symmetry axis, and the intensity used is $P_{pump} = 98.4$ mW. The simulated time evolution of the pumping pulse ignores the ramp-up and ramp-down of the AOM, and assumes a square pulse for 160 ns. Furthermore, the MOT coils impose a quantization axis for the $\Delta m = 0$ transition. The pump pulse is polarized along the MOT coil axis, and as a result, atoms near the center of the MOT field are driven less strongly by the pump pulse. In the model, this is accounted for by introducing an effective intensity driving the transition, given by $I \cdot 4y^2 / (x^2 + 4y^2 + z^2)$, where y is the MOT coil axis. In the simulations the MOT cloud center is offset by 2 mm with respect to $y = 0$ based on measurements of the energy splittings of the magnetic states. The pumping leaves the ensemble inhomogeneously excited, with the excitation being highest for atoms slightly away from the beam axis and for the slowest atoms along the beam axis. On average 85 % of atoms are excited within the cavity waist at the end of the pump pulse. Atomic spontaneous decay at a rate γ and leak of cavity photons through the mirrors at a rate κ are accounted for by Liouvillian terms. Throughout the simulation each atom interacts with the cavity mode with different coupling rates g_c^j depending on their positions relative to the Gaussian cavity mode waist ($w = 0.45$ mm) and the standing wave structure. We calculate the cavity output power from one mirror (comparable to our experimental

-
- [1] J. Chen, "Active optical Clock", *Chi. Sci. Bull.* **54** 348 (2009)
- [2] J. Chen and X. Chen, "Optical Lattice Laser", *Proceedings of the 2005 IEEE International Frequency Control Symposium and Exposition*, 608-610 (2005)
- [3] D. Meiser, J. Ye, D. R. Carlson, and M. J. Holland, "Prospects for a Millihertz-Linewidth Laser", *Phys. Rev. Lett.* **102**, 163601 (2009)
- [4] E. Oelker et al., "Optical clock intercomparison with 6×10^{-19} precision in one hour", *arXiv* 1902.02741 (2019)
- [5] W. F. McGrew et al., "Atomic clock performance enabling geodesy below the centimetre level", *Nature*, **564**, 8790 (2018)
- [6] T. L. Nicholson et al., "Systematic evaluation of an atomic clock at 2 1018 total uncertainty", *Nat. Comm.* **6**, 6896 (2015)
- [7] I. Ushijima, M. Takamoto, M. Das, T. Ohkubo, and H. Katori, "Cryogenic optical lattice clocks", *Nat. Phot.* **9**, 185-189 (2015)
- [8] N. Huntemann, C. Sanner, B. Lipphardt, C. Tamm, E. Peik, "Single-ion atomic clock with 3×10^{18} systematic uncertainty", *Phys. Rev. Lett.*, **116**, 063001 (2016)
- [9] D. G. Matei et al., "1.5 μm Lasers with Sub-10 mHz Linewidth", *Phys. Rev. Lett.*, **118**, 263202 (2017)
- [10] W. Zhang et al., "A silicon cavity in a 4 K closed-cycle cryostat with 1×10^{16} instability", *Phys. Rev. Lett.*, **119**, 243601 (2017)
- [11] J. Robinson, E. Oelker, W. R. Milner, W. Zhang, T. Legero, D. G. Matei, F. Riehle, U. Sterr, and J. Ye, "Crystalline optical cavity at 4 K with thermal noise limited instability and ultralow drift", *arXiv*:1812.03842v1 (2018)
- [12] K. Numata, A. Kemery, and J. Camp, "Thermal-Noise Limit in the Frequency Stabilization of Lasers with Rigid Cavities", *Phys. Rev. Lett.*, **93**, 250602 (2004)
- [13] G. D. Cole, W. hang, M. J. Martin, J. Ye and M. Aspelmeyer, "Tenfold reduction of Brownian noise in high-reflectivity optical coatings", *Nat. Phot.*, **7**, 644-650 (2013)
- [14] K. Debnath, Y. Zhang and K. Mølmer, "Lasing in the superradiant crossover regime" *Phys. Rev. A* **98**, 063837 (2018)
- [15] M. A. Norcia, J. R. K. Cline, J. A. Muniz, J. M. Robinson, R. B. Hutson, A. Goban, G. E. Marti, J. Ye, and J. K. Thompson, "Frequency Measurements of Superradiance from the Strontium Clock Transition" *Phys. Rev. X* **8** 021036 (2018)
- [16] D. Pan, T. Shi, and J. Chen, "A highly integrated single-mode 1064 nm laser with 8.5 kHz linewidth for dual-wavelength active optical clock", *IEEE Transactions on Ultrasonics, Ferroelectrics, and Frequency Control*, **65**, 10 1958-1964 (2018)
- [17] M. A. Norcia and J. K. Thompson, "Cold-Strontium Laser in the Superradiant Crossover Regime", *Phys. Rev. X* **6** 011025 (2016)
- [18] G. A. Kazakov and T. Schumm, "Active optical frequency standard using sequential coupling of atomic ensembles" *Phys. Rev. A*, **87**, 013821 (2013)
- [19] S. J. M. Kuppens, M. P. van Exter, and J. P. Woerdman, "Quantum-Limited Linewidth of a Bad-Cavity Laser" *Phys. Rev. Lett.* **72**, 3815 (1994)
- [20] A. Gonzalez-Tudela and D. Porras, "Mesoscopic Entanglement Induced by Spontaneous Emission in Solid-State Quantum Optics" *Phys. Rev. Lett* **110**, 080502 (2013)
- [21] E. Wolfe and S. F. Yelin, "Spin Squeezing by means of Driven Superradiance" *arXiv*:1405.5288v2, (2014)
- [22] D. Barberena, R. J. Lewis-Swan, J. K. Thompson and A. M. Rey, "Driven-Dissipative Quantum Dynamics in Ultra Long-lived Dipoles in an Optical Cavity" *arXiv*:1812.02291v1, (2018)
- [23] M. Gross and S. Haroche, "Superradiance: an essay on the theory of collective spontaneous emission" *Phys. Rep.*, **93**, 5, 301-396 (1982)
- [24] R. H. Dicke, *Phys. Rev.*, "Coherence in spontaneous radiation processes", **93**, 1, pp. 99-110 (1954)
- [25] A. Kumarakrishnan and X. L. Han, "Superfluorescence from optically trapped calcium atoms", *Phys. Rev. A*, **58**, 5, 4153 (1998)
- [26] J. Bochmann, M. Mücke, G. Langfahl-Klabes, C. Erbel, B. Weber, H. P. Specht, D. L. Moehring, and G. Rempe, "Fast Excitation and Photon Emission of a Single-Atom-Cavity System", *Phys. Rev. Lett.* **101**, 223601 (2008)
- [27] R. J. Brecha, L. A. Orozco, M. G. Raizen, M. Xiao, and H. J. Kimble, "Observation of oscillatory energy exchange in a coupled-atom cavity system", *J. Opt. Soc. Am. B*, **12**, 12, 2329 (1995)
- [28] M. Tang, "Modeling lasing in a thermal strontium ensemble", *Thesis, Niels Bohr Institute, University of Copenhagen*, (2018)

ACKNOWLEDGMENTS

The work presented here has been performed over the course of 4 years at the Niels Bohr Institute in Copenhagen, Denmark while teaching courses and during a stay as guest researcher at NIST in Boulder, USA. I have thoroughly enjoyed my time discovering the world of cold atoms and their interactions with light, and am looking forward to continuing my adventures in that world.

My primary supervisor, *Jan W. Thomsen*, is a true experimentalist, and as such the past four years have not just been a research period, but have largely been about learning a trade. There are so many things necessary for an experimental setup to function properly that have not been mentioned in this thesis. JWT has introduced me to everything I know in the lab, ranging from his great vacuum systems know-how, through feedback loops, how to act fast when things go wrong, mechanical design and construction, as well as the thorough analysis of experimental data. I have spent many hours assembling and changing vacuum systems with him – sometimes with a pounding heart. I also had the privilege of enjoying a great many long-winded physics discussions with him. He has been an excellent mentor, and has introduced me to most of the atomic physics community that I am now a part of. Thank you to *Betina Dam Sørensen* for mediating the continuous requests for available meeting times for the last two years since JWT became the head of institute in summer 2017.

My colleagues in the Quantum Metrology group have also been an important part of my time there. I did my masters thesis in the group with the company of *Bjarke Takashi Røjle Christensen* as a PhD student at the time, and with *Martin Romme Henriksen* as a fellow masters student. BTRC acted as a second mentor in the beginning, and his positive attitude toward the group and excitement for the physics we saw, has been an important part of the daily life. A laboratory without MRH is hard to imagine, and his excellent skills in RF electronics has taught me a great deal. I have discussed just about all of my experimental investigations with him, and we have collaborated on a great deal of projects. I will be looking forward to getting back in the laboratory with him. *Asbjørn Arvad Jørgensen* was a bachelor student in the group, and has since then rejoined the group as a PhD student, where he has had to take on a very large supervision responsibility when both I and MRH were abroad. His programming skills have pulled the laboratory infrastructure from the pre-internet age towards an internet of things, and facilitated a number of excellent improvements. Whenever I feel like discussing the true meaning of a laser linewidth he is an easy victim for the wonders of the Allan deviation.

Through my responsibilities as a teaching assistant I have had the pleasure of

teaching the courses Optics and Atomic physics to bachelor students at the Niels Bohr Institute, and here I want to thank the institute for this opportunity, and JWT as well as *Jörg Helge Müller* for the great collaboration in this respect.

These courses were also my first encounter with *Mikkel Tang*, who later joined the laboratory as a masters student under my supervision. MT and I have collaborated intensely on the superradiant laser, and MT worked on the model and simulations of the system during his masters thesis and are currently perfecting the models as presented here and elsewhere while doing his PhD in the group. MT is also an essential part of the collaboration we are starting up within the iqClock consortium.

A number of technicians at the Niels Bohr Institute have been instrumental in helping us realize the experiments. The electronics department and mechanical workshop are always welcoming places that try to take a genuine interest in what the best solutions to your needs are. Here I want to mention in particular *Axel Boisen* from the electronics workshop for his help with any- and everything even remotely related to electronics. Borrowing equipment, advice on measurement strategies, construction of devices, purchasing and long stories from exotic countries are always possible. I want to thank *Michael Heide Berndt* who has been essential in the beginning where mechanical design and construction was a large part of the working process. Finally *Thomas Hedegaard* has been a great help in the last year when considering optimal ways to reduce acoustic noise in the lab and experimental systems.

In order to have a change of scientific environment UCPH encourages us to do research abroad with other research groups. I spent 5 months in the laboratory of *Andrew D. Ludlow* at NIST, Boulder in order to gain experience with a state-of-the-art atomic clock. ADL acted as my supervisor during the time at NIST, and made it the excellent experience it was. I am very grateful for being invited to join in the research done at NIST, and would not have been without the experience. I want to thank my NIST colleagues for making my stay both socially and scientifically more than worthwhile. In particular I want to thank *William F. McGrew* and *Xiaogang Zhang* who I spent most of my time in the lab with, and *Kyle Beloy* for being a secondary mentor there. I also want to thank *Robbie J. Fasano* and *Daniele Nicolodi*. It was in large part because of my great colleagues that the trip with my wife and daughter was such a success.

Finally I want to thank my wife *Turi Kirstine Schäffer* for allowing me to dedicate a lot of my time to PhD studies. She has always politely listened to my rants on more or less interesting things from the lab and my head. She is an amazing mother to my two daughters who have both arrived during my PhD. Without her support and leniency, finishing the thesis in reasonable time would not have been possible.

LIST OF FIGURES

1.1	Cs clock concept [7]	2
1.2	Clock frequency perturbations	4
1.3	Modified Allan deviation from the record cavity stabilization [83]	5
1.4	Allan deviation from Yb optical lattice clock [70]	6
2.1	Strontium energy levels	12
2.2	Susceptibility	15
3.1	Types of ECDL used	25
3.2	Overview of the cooling laser path.	27
3.3	Atomic temperature vs MOT detuning	28
3.4	Repumping laser path	29
3.5	Probe laser distribution path	30
3.6	Pumping laser path	31
3.7	Physics cavity	32
3.8	Clock laser setup	34
3.9	Clock laser spectrum	35
3.10	Inside the acoustic enclosure of the reference laser	36
3.11	Reference laser setup	37
3.12	Reference laser spectrum	38
3.13	Clock and reference laser comparison	38
4.1	Spectral profiles	41
4.2	Saturated absorption	42
4.3	Ideal dispersion features	42
4.4	Schematic of the NICE-OHMS detection setup	44
4.5	NICE-OHMS scheme	45
4.6	Cavity dispersion	48
4.7	Cavity-limited dispersion signal	50
4.8	Phase slope and projected Linewidth of a NICE-OHMS Lock	51
4.9	Limitations on the dynamical locking range	53
4.10	Dispersion signal sensitivity to cavity conditions	54
4.11	Dispersion signal with cooling light on	55
4.12	Analysis of NICE-OHMS error signal	57
4.13	In-loop NICE-OHMS Allan deviation	58
5.1	Laser schematic	61

5.2	Good and bad-cavity regimes	62
5.3	Incoherent pumping scheme	63
5.4	Phase relation of pumping and cavity fields	65
5.5	Operating cycle	65
5.6	Rabi flopping in the excitation and the amplitude dependency of lasing pulses	66
5.7	Power scaling regimes	69
5.8	Typical pulse behavior for resonant and detuned cavity	70
5.9	Lasing threshold and delay for pulsed emission	72
5.10	Experimental and simulated pulse evolution vs atom number	73
5.11	Experimental and simulated pulse evolution vs atom-cavity detuning	74
5.13	Lasing without and with decoherence induced by MOT beams.	76
5.14	Concept of seeded laser and typical behavior of emitted field	78
5.15	Heat map of seeded pulse vs. input power	79
5.16	Amplification in a seeded pulse	79
5.17	Heat map of seeded laser pulses and their phase evolution	80
5.18	Lasing pulse with beat signal	81
5.19	Spectral evolution of a single lasing pulse	82
5.20	Spectral line pulling in laser pulses	83
5.21	laser pulse frequency counting method	84
5.22	Overlapping Allan deviation of laser pulse frequency stability	85
6.1	Level structure of Yb	88
6.2	Two Yb clocks at NIST [70]	89
6.3	Multi-color laser locking to a single Fabry-Perot cavity	91
6.4	ESB locking scheme with PDH	92
6.5	Injection locking of a Ti:Sapphire Lattice laser	92
6.6	BBR enclosure and window heating [4]	94
6.7	DC stark shift measurements [4]	96
6.8	Yb clock performance [70]	98
6.9	Yb frequency measurements [71]	101
6.10	Yb - Sr - Al+ comparison stability [60]	102
A.1	Capillary tube holder for Sr-2 oven	108
A.2	Model of 2D MOT section in Sr-2	109
A.3	2D MOT B-field measurement	110
A.4	Technical drawing of interference filter ECDL design	112
A.5	Mounted Sr-2 interrogation cavity	113
A.6	Technical drawing of cavity spacer in Sr-II	114
A.7	Technical drawing – Transfer/interrogation cavity spacer	116
A.8	Transfer cavity mount	117
A.9	Technical drawing – Support rings	117
B.1	Laboratory vibration level	120
B.2	Laboratory vibration level	121

LIST OF TABLES

3.1 Laser systems in Sr I	26
A.1 MOT current	110

BIBLIOGRAPHY

- [1] L. Allen and G. Peters, “Superradiance, coherence brightening and amplified spontaneous emission”, *Physics Letters A*, vol. 31, no. 3, pp. 95–96, Feb. 1970.
- [2] N. Ashby, T. E. Parker, and B. R. Patla, “A null test of general relativity based on a long-term comparison of atomic transition frequencies”, *Nature Physics*, vol. 14, no. 8, pp. 822–826, Aug. 2018.
- [3] K. Beloy, N. Hinkley, N. B. Phillips, J. A. Sherman, M. Schioppo, J. Lehman, A. Feldman, L. M. Hanssen, C. W. Oates, and a. D. Ludlow, “Atomic Clock with 1×10^{-18} Room-Temperature Blackbody Stark Uncertainty”, *Physical Review Letters*, vol. 113, no. 26, p. 260 801, Dec. 2014.
- [4] K. Beloy, X. Zhang, W. F. McGrew, N. Hinkley, T. H. Yoon, D. Nicolodi, R. J. Fasano, S. A. Schäffer, R. C. Brown, and A. D. Ludlow, “Faraday-Shielded dc Stark-Shift-Free Optical Lattice Clock”, *Physical Review Letters*, vol. 120, no. 18, p. 183 201, May 2018.
- [5] BIPM, “The International System of Units (SI)”, Tech. Rep., 2006.
- [6] M. Bishof, X. Zhang, M. J. Martin, and J. Ye, “Optical Spectrum Analyzer with Quantum-Limited Noise Floor”, *Physical Review Letters*, vol. 111, no. 9, p. 093 604, Aug. 2013.
- [7] S. Bize, “The unit of time: Present and future directions”, *Comptes Rendus Physique*, 2019.
- [8] B. J. Bloom, T. L. Nicholson, J. R. Williams, S. L. Campbell, M. Bishof, X. Zhang, W. Zhang, S. L. Bromley, and J. Ye, “An optical lattice clock with accuracy and stability at the 10-18 level.”, *Nature*, vol. 506, no. 7486, pp. 71–5, Feb. 2014.
- [9] J. Bochmann, M. Mücke, G. Langfahl-Klabes, C. Erbel, B. Weber, H. P. Specht, D. L. Moehring, and G. Rempe, “Fast excitation and photon emission of a Single-Atom-Cavity system”, *Physical Review Letters*, vol. 101, no. 22, pp. 1–4, 2008. arXiv: [0806.2600](https://arxiv.org/abs/0806.2600).
- [10] J. G. Bohnet, Z. Chen, J. M. Weiner, D. Meiser, M. J. Holland, and J. K. Thompson, “A steady-state superradiant laser with less than one intracavity photon”, *Nature*, vol. 484, no. 7392, pp. 78–81, Apr. 2012.
- [12] T. Bothwell, D. Kedar, E. Oelker, J. M. Robinson, S. L. Bromley, W. L. Tew, J. Ye, and C. J. Kennedy, “JILA SrI Optical Lattice Clock With Uncertainty of 2.0×10^{-18} ”, pp. 1–24, 2019. arXiv: [1906.06004](https://arxiv.org/abs/1906.06004).

- [13] R. J. Brecha, L. A. Orozco, M. G. Raizen, M. Xiao, and H. J. Kimble, "Observation of oscillatory energy exchange in a coupled-atom-cavity system", *Journal of the Optical Society of America B*, vol. 12, no. 12, p. 2329, 1995.
- [14] S. M. Brewer, J.-S. Chen, A. M. Hankin, *et al.*, "Measurements of $^{27}\text{Al}^+$ and $^{25}\text{Mg}^+$ magnetic constants for improved ion clock accuracy", no. Dc, Mar. 2019. arXiv: [1903.04661](https://arxiv.org/abs/1903.04661).
- [15] R. C. Brown, N. B. Phillips, K. Beloy, *et al.*, "Hyperpolarizability and Operational Magic Wavelength in an Optical Lattice Clock", *Physical Review Letters*, 2017. arXiv: [1708.08829](https://arxiv.org/abs/1708.08829).
- [16] S. L. Campbell, R. B. Hutson, G. E. Marti, *et al.*, "A Fermi-degenerate three-dimensional optical lattice clock", *Science*, vol. 358, no. 6359, pp. 90–94, Oct. 2017. arXiv: [1702.01210](https://arxiv.org/abs/1702.01210).
- [17] J. Chen, "Active optical clock", *Chinese Science Bulletin*, vol. 54, no. 3, pp. 348–352, 2009.
- [18] B. B. T. R. Christensen, M. R. Henriksen, S. S. A. Schäffer, *et al.*, "Nonlinear Spectroscopy of Sr Atoms in an Optical Cavity for Laser Stabilization", *Physical Review A*, vol. 92, no. 5, p. 053 820, Nov. 2015.
- [19] B. T. R. Christensen, S. A. Schäffer, M. R. Henriksen, P. G. Westergaard, J. Ye, and J. W. Thomsen, "Laser Stabilization on Velocity Dependent Nonlinear Dispersion of Sr Atoms in an Optical Cavity", in *IEEE proceedings of IFCS-EFTF*, IEEE, 2015.
- [20] B. T. R. Christensen, "Laser Stabilization With Laser Cooled Strontium", PhD thesis.
- [21] G. D. Cole, W. Zhang, M. J. Martin, J. Ye, and M. Aspelmeyer, "Tenfold reduction of Brownian noise in high-reflectivity optical coatings", *Nature Photonics*, vol. 7, no. 8, pp. 644–650, Jul. 2013.
- [22] M. Corporation, "Data Sheet: MHM 2010 Maser", 2010.
- [23] W. Demtröder, *Laser Spectroscopy vol 1 - Basic Principles*, Fourth Edi. Springer.
- [24] H. Denker, L. Timmen, C. Voigt, S. Weyers, E. Peik, H. S. Margolis, P. Delva, P. Wolf, and G. Petit, "Geodetic methods to determine the relativistic redshift at the level of 10^{-18} in the context of international timescales : a review and practical results", *Journal of Geodesy*, vol. 92, no. 5, pp. 487–516, 2018.
- [25] R. H. Dicke, "Coherence in spontaneous radiation processes", *Physical Review*, vol. 93, no. 1, pp. 99–110, Jan. 1954.
- [26] R. H. Dicke and R. H., "The Coherence Brightened Laser", *Quantum Electronics; proceedings of the third international congress. Edited by P. Grivet and N. Bloembergen. Published by Dunod Éditeur, Paris, and Columbia University Press, New York, 1964, p.35*, p. 35, 1964.
- [27] T. H. Dinh, A. Dunning, V. A. Dzuba, and V. V. Flambaum, "Sensitivity of hyperfine structure to nuclear radius and quark mass variation", *Physical Review A - Atomic, Molecular, and Optical Physics*, vol. 79, no. 5, pp. 1–4, May 2009.

- [28] V. A. Dzuba and V. V. Flambaum, "Limits on gravitational Einstein equivalence principle violation from monitoring atomic clock frequencies during a year", *Physical Review D*, vol. 95, no. 1, pp. 1–6, Jan. 2017. arXiv: [1608.06050](#).
- [29] L. Essen and J. L. Parry, "Anatomic standard of frequency and time interval", *Nature*, vol. 176, pp. 280–282, 1955.
- [30] European Space Agency (ESA), *How the Galileo Atomic clocks work*, 2012.
- [31] S. Falke, N. Lemke, C. Grebing, *et al.*, "A strontium lattice clock with 3×10^{-17} inaccuracy and its frequency", *New Journal of Physics*, vol. 16, p. 18, 2014.
- [32] V. V. Flambaum and V. A. Dzuba, "Search for variation of the fundamental constants in atomic, molecular, and nuclear spectra", *Canadian Journal of Physics*, vol. 87, no. 1, pp. 25–33, Jan. 2009.
- [33] V. V. Flambaum and A. F. Tedesco, "Dependence of nuclear magnetic moments on quark masses and limits on temporal variation of fundamental constants from atomic clock experiments", *Physical Review C - Nuclear Physics*, vol. 73, no. 5, p. 055 501, May 2006.
- [34] C. J. Foot, *Atomic Physics*. Oxford: Oxford University Press, 2005, vol. 11.
- [35] M. Fujieda, S. H. Yang, T. Gotoh, *et al.*, "Advanced Satellite-Based Frequency Transfer at the 10^{-16} Level", *IEEE Transactions on Ultrasonics, Ferroelectrics, and Frequency Control*, vol. 65, no. 6, pp. 973–978, 2018.
- [38] C. Grebing, A. Al-Masoudi, S. Dörscher, S. Häfner, V. Gerginov, S. Weyers, B. Lipphardt, F. Riehle, U. Sterr, and C. Lisdat, "Realization of a timescale with an accurate optical lattice clock", *Optica*, vol. 3, no. 6, p. 563, Jun. 2016. arXiv: [1511.03888](#).
- [39] M. Gross and S. Haroche, "Superradiance: An essay on the theory of collective spontaneous emission", *Physics Reports*, vol. 93, no. 5, pp. 301–396, Dec. 1982.
- [40] J. Grotti, S. Koller, S. Vogt, *et al.*, "Geodesy and metrology with a transportable optical clock", *Nature Physics*, vol. 14, no. 5, p. 1705.04089, May 2017. arXiv: [1705.04089](#).
- [41] H. Hachisu and T. Ido, "Intermittent optical frequency measurements to reduce the dead time uncertainty of frequency link", *Japanese Journal of Applied Physics*, vol. 54, no. 11, 2015.
- [42] A. M. Hankin, E. R. Clements, Y. Huang, S. M. Brewer, J. .-.S. Chen, C. W. Chou, D. B. Hume, and D. R. Leibbrandt, "Systematic uncertainty due to background-gas collisions in trapped-ion optical clocks", no. 5, pp. 1–5, Feb. 2019. arXiv: [1902.08701](#).
- [44] M. R. Henriksen, "Cavity Enhanced Spectroscopy on Ultra Cold Atoms", PhD thesis, University of Copenhagen, M.Sc. Thesis, 2014.
- [45] M. R. Henriksen, S. A. Schäffer, B. T. R. Christensen, P. G. Westergaard, D. Tieri, J. Cooper, M. Holland, J. Ye, and J. W. Thomsen, *Observing Collective Effects of Sr in an Optical Cavity*, 2013.

- [46] N. Hinkley, "An atomic clock for 10–18 timekeeping", PhD thesis, University of Colorado, Boulder, 2016.
- [47] N. Hinkley, J. A. Sherman, N. B. Phillips, M. Schioppo, N. D. Lemke, K. Beloy, M. Pizzocaro, C. W. Oates, and A. D. Ludlow, "An Atomic Clock with 10–18 Instability", *Science*, 2013. arXiv: [1305.5869](#).
- [48] S. Häfner, S. Falke, C. Grebing, S. Vogt, T. Legero, M. Merimaa, C. Lisdat, and U. Sterr, " 8×10^{-17} fractional laser frequency instability with a long room-temperature cavity", *Optics Letters*, vol. 40, no. 9, p. 2112, May 2015.
- [49] E. M. Kessler, P. Kómár, M. Bishof, L. Jiang, A. S. Sørensen, J. Ye, and M. D. Lukin, "Heisenberg-Limited Atom Clocks Based on Entangled Qubits", *Physical Review Letters*, vol. 112, no. 19, p. 190 403, May 2014.
- [50] T. Kessler, C. Hagemann, C. Grebing, T. Legero, U. Sterr, F. Riehle, M. J. Martin, L. Chen, and J. Ye, "A sub-40-mHz-linewidth laser based on a silicon single-crystal optical cavity", *Nature Photonics*, vol. 6, no. 10, pp. 687–692, Sep. 2012.
- [51] H. Kim, M. S. Heo, W. K. Lee, C. Y. Park, H. G. Hong, S. W. Hwang, and D. H. Yu, "Improved absolute frequency measurement of the ^{171}Yb optical lattice clock at KRISS relative to the Si second", *Japanese Journal of Applied Physics*, vol. 56, no. 5, pp. 12–16, 2017.
- [52] T. Kohno, M. Yasuda, K. Hosaka, H. Inaba, Y. Nakajima, and F. L. Hong, "One-dimensional optical lattice clock with a fermionic ^{171}Yb isotope", *Applied Physics Express*, vol. 2, no. 7, 2009.
- [53] S. Kolkowitz, I. Pikovski, N. Langellier, M. D. D. D. Lukin, R. L. L. L. Walsworth, and J. Ye, "Gravitational wave detection with optical lattice atomic clocks", *Physical Review D*, vol. 94, no. 12, pp. 1–15, Dec. 2016.
- [54] S. B. Koller, J. Grotti, S. Vogt, A. Al-Masoudi, S. Dörscher, S. Häfner, U. Sterr, and C. Lisdat, "Transportable Optical Lattice Clock with 7×10^{-17} i Uncertainty", *Physical Review Letters*, vol. 118, no. 7, p. 073 601, Feb. 2017.
- [55] P. Kómár, T. Topcu, E. M. Kessler, A. Derevianko, V. Vuletić, J. Ye, and M. D. Lukin, "Quantum Network of Atom Clocks: A Possible Implementation with Neutral Atoms", *Physical Review Letters*, vol. 117, no. 6, p. 060 506, Aug. 2016.
- [56] A. Kumarakrishnan and X. Han, "Superfluorescence from optically trapped calcium atoms", *Physical Review A*, vol. 58, no. 5, pp. 4153–4162, 1998.
- [57] T. Laske, H. Winter, and A. Hemmerich, "Superradiant laser with metastable calcium atoms", vol. 1, pp. 1–5, Mar. 2019. arXiv: [1903.10196](#).
- [58] N. D. Lemke, "An Optical Lattice Clock with Spin 1/2 Atoms", PhD thesis, University of Colorado, 2012.
- [59] N. D. Lemke, A. D. Ludlow, Z. W. Barber, T. M. Fortier, S. A. Diddams, Y. Jiang, S. R. Jefferts, T. P. Heavner, T. E. Parker, and C. W. Oates, "Spin-1/2 optical lattice clock", *Physical Review Letters*, vol. 103, no. 6, pp. 10–13, 2009.

- [60] H. Leopardi, K. Beloy, M. I. Bodine, *et al.*, “Measuring Optical Frequency Ratios with Uncertainties Below 10^{-17} via the Boulder Atomic Clock Network”, in *Conference on Lasers and Electro-Optics*, Washington, D.C.: OSA, May 2019.
- [61] H. Leopardi, J. Davila-Rodriguez, J. Sherman, F. Quinlan, S. Diddams, and T. Fortier, “Absolute frequency comb comparisons and the measurement of optical atomic clock transitions”, in *Conference on Lasers and Electro-Optics*, Washington, D.C.: OSA, 2018, SM1L.4.
- [62] Y. G. Lin, Q. Wang, Y. Li, F. Meng, B. K. Lin, E. J. Zang, Z. Sun, F. Fang, T. C. Li, and Z. J. Fang, “First Evaluation and Frequency Measurement of the Strontium Optical Lattice Clock at NIM”, *Chinese Physics Letters*, vol. 32, no. 9, 2015.
- [63] J. Lodewyck, S. Bilicki, E. Bookjans, *et al.*, “Optical to microwave clock frequency ratios with a nearly continuous strontium optical lattice clock”, *Metrologia*, vol. 53, no. 4, pp. 1123–1130, 2016. arXiv: [1605.03878](#).
- [64] J. Lodewyck, M. Zawada, L. Lorini, M. Gurov, and P. Lemonde, “Observation and cancellation of a perturbing dc stark shift in strontium optical lattice clocks”, *IEEE Transactions on Ultrasonics, Ferroelectrics, and Frequency Control*, vol. 59, no. 3, pp. 411–415, 2012.
- [65] A. D. Ludlow, M. M. Boyd, J. Ye, E. Peik, and P. O. Schmidt, “Optical atomic clocks”, *Reviews of Modern Physics*, vol. 87, no. 2, pp. 637–701, Jun. 2015.
- [67] M. J. Martin, D. Meiser, J. W. Thomsen, J. Ye, and M. J. Holland, “Extreme non-linear response of ultra-narrow optical transitions in cavity QED for laser stabilization”, *Physical Review A*, vol. 84, no. 1, p. 5, May 2011. arXiv: [1105.2373](#).
- [68] D. G. Matei, T. Legero, C. Grebing, *et al.*, “1.5 μm Lasers with Sub-10 mHz Linewidth”, *Physical Review Letters*, vol. 118, p. 263 202, 2017. arXiv: [1702.04669v2](#).
- [69] F. P. Mattar, H. M. Gibbs, S. L. McCall, and M. S. Feld, “Transverse Effects in Superfluorescence”, *Physical Review Letters*, vol. 46, no. 17, pp. 1123–1126, 1981.
- [70] W. F. McGrew, X. Zhang, R. J. Fasano, *et al.*, “Atomic clock performance beyond the geodetic limit”, *Nature*, vol. 564, pp. 1–32, 2018. arXiv: [1807.11282](#).
- [71] W. F. McGrew, X. Zhang, H. Leopardi, *et al.*, “Towards the optical second: verifying optical clocks at the SI limit”, *Optica*, vol. 6, no. 4, p. 448, Apr. 2019. arXiv: [1811.05885](#).
- [72] T. E. Mehlstäubler, G. Grosche, C. Lisdat, P. O. Schmidt, H. Denker, O. Piet, and H. Denker, “Atomic Clocks for Geodesy”, *Reports on Progress in Physics*, vol. 81, no. 6, p. 064 401, Jun. 2010. arXiv: [1803.01585](#).
- [73] D. Meiser, J. Ye, D. Carlson, and M. Holland, “Prospects for a Millihertz-Linewidth Laser”, *Physical Review Letters*, vol. 102, no. 16, p. 163 601, Apr. 2009.

- [74] H. J. Metcalf and P. van der Straten, *Laser Cooling and Trapping 1*. Springer, 1999, pp. 1–18.
- [75] P. Meystre and M. Sargent, *Elements of Quantum Optics*. 2007.
- [76] P. W. Milonni and J. H. Eberly, *Laser Physics*. Hoboken, NJ, USA: John Wiley & Sons, Inc., Mar. 2010, p. 830.
- [77] V. Natarajan, *Modern atomic physics*. CRC Press, 2015.
- [78] N. Nemitz, T. Ohkubo, M. Takamoto, I. Ushijima, M. Das, N. Ohmae, and H. Katori, “Frequency ratio of Yb and Sr clocks with 5×10^{-17} uncertainty at 150 seconds averaging time”, *Nature Photonics*, 2016. arXiv: [1601.04582](#).
- [79] T. L. Nicholson, S. L. Campbell, R. B. Hutson, *et al.*, “Systematic evaluation of an atomic clock at 2×10^{-18} total uncertainty”, *Nature Communications*, vol. 6, 2015. arXiv: [1412.8261](#).
- [80] M. A. Norcia, J. R. K. Cline, J. A. Muniz, J. M. Robinson, R. B. Hutson, A. Goban, G. E. Marti, J. Ye, and J. K. Thompson, “Frequency Measurements of Superradiance from the Strontium Clock Transition”, *Physical Review X*, vol. 8, no. 2, p. 021 036, May 2018. arXiv: [1711.10407](#).
- [81] M. A. Norcia and J. K. Thompson, “Cold-Strontium Laser in the Superradiant Crossover Regime”, *Physical Review X*, vol. 6, no. 1, p. 011 025, Mar. 2016. arXiv: [1510.06733](#).
- [82] K. Numata, A. Kemery, and J. Camp, “Thermal-noise limit in the frequency stabilization of lasers with rigid cavities”, *Physical Review Letters*, vol. 93, no. 25, pp. 1–4, 2004.
- [83] E. Oelker, R. B. Hutson, C. J. Kennedy, *et al.*, “Optical clock intercomparison with 6×10^{-19} precision in one hour”, Feb. 2019. arXiv: [1902.02741](#).
- [84] D. Pan, T. Shi, and J. Chen, “Dual-Wavelength Good–Bad-Cavity Laser System for Cavity-Stabilized Active Optical Clock”, *IEEE Transactions on Ultrasonics, Ferroelectrics, and Frequency Control*, vol. 65, no. 10, pp. 1958–1964, Oct. 2018.
- [85] C. Y. Park, D. H. Yu, W. K. Lee, *et al.*, “Absolute frequency measurement of $1S_0(F = 1/2)$ - $3P_0(F = 1/2)$ transition of ^{171}Yb atoms in a one-dimensional optical lattice at KRISS”, *Metrologia*, vol. 50, no. 2, pp. 119–128, 2013.
- [86] S. Peil, S. Crane, J. L. Hanssen, T. B. Swanson, and C. R. Ekstrom, “Tests of local position invariance using continuously running atomic clocks”, *Physical Review A - Atomic, Molecular, and Optical Physics*, vol. 87, no. 1, pp. 4–7, Jan. 2013.
- [87] M. Pizzocaro, P. Thoumany, B. Rauf, F. Bregolin, G. Milani, C. Clivati, G. A. Costanzo, F. Levi, and D. Calonico, “Absolute frequency measurement of the $1S_0 - 3P_0$ transition of ^{171}Yb ”, *Metrologia*, vol. 54, no. 1, pp. 102–112, 2017.

- [88] S. G. Porsev and A. Derevianko, "Multipolar theory of blackbody radiation shift of atomic energy levels and its implications for optical lattice clocks", *Physical Review A - Atomic, Molecular, and Optical Physics*, vol. 74, no. 2, pp. 4–7, 2006.
- [89] I. Reichenbach and I. H. Deutsch, "Sideband cooling while preserving coherences in the nuclear spin state in Group-II-like atoms", *Physical Review Letters*, vol. 99, no. 12, pp. 1–4, 2007.
- [90] F. Riehle, *Frequency Standards - Basics and Applications*. Braunschweig: Wiley, 2004.
- [91] W. J. Riley, *Handbook of Frequency Stability Analysis*. NIST, 2008.
- [92] J. M. Robinson, E. Oelker, W. R. Milner, W. Zhang, T. Legero, D. G. Matei, F. Riehle, U. Sterr, and J. Ye, "Crystalline optical cavity at 4 K with thermal-noise-limited instability and ultralow drift", *Optica*, vol. 6, no. 2, p. 240, Feb. 2019. arXiv: [1812.03842](#).
- [93] T. Rosenband, D. B. Hume, P. O. Schmidt, *et al.*, "Frequency Ratio of Al⁺ and Hg⁺ Single-Ion Optical Clocks; Metrology at the 17th Decimal Place", *Science*, vol. 319, no. 5871, pp. 1808–1812, Mar. 2008.
- [94] M. S. Safronova, S. G. Porsev, C. Sanner, and J. Ye, "Two Clock Transitions in Neutral Yb for the Highest Sensitivity to Variations of the Fine-Structure Constant", *Physical Review Letters*, vol. 120, no. 17, p. 173 001, Apr. 2018. arXiv: [1801.06239](#).
- [96] M. Schioppo, R. C. Brown, W. F. McGrew, *et al.*, "Ultrastable optical clock with two cold-atom ensembles", *Nature Photonics*, vol. 11, no. 1, pp. 48–52, Jan. 2017. arXiv: [1607.06867](#).
- [97] S. A. Schäffer, "Studies of Collective Effects in Atomic Strontium", PhD thesis, University of Copenhagen, 2015, p. 125.
- [98] S. A. Schäffer, B. T. R. Christensen, S. M. Rathmann, M. H. Appel, M. R. Henriksen, and J. W. Thomsen, "Towards passive and active laser stabilization using cavity-enhanced atomic interaction", *Journal of Physics: Conference Series*, vol. 810, no. 1, p. 012 002, Feb. 2017.
- [99] S. A. Schäffer, B. T. R. Christensen, M. R. Henriksen, and J. W. Thomsen, "Dynamics of bad-cavity-enhanced interaction with cold Sr atoms for laser stabilization", *Physical Review A*, vol. 96, no. 1, p. 013 847, Jul. 2017. arXiv: [1704.08245](#).
- [100] S. A. Schäffer, M. Tang, M. R. Henriksen, A. A. Jørgensen, B. T. R. Christensen, and J. W. Thomsen, "Lasing on a narrow transition in a cold thermal strontium ensemble", *Submitted to Physical review A*, 2019. arXiv: [1903.12593](#).
- [101] S. A. Schäffer, M. Tang, and J. W. Thomsen, "Cold-atom based optical amplifier", 2019.
- [102] N. Skribanowitz, I. P. Herman, J. C. MacGillivray, and M. S. Feld, "Observation of dicke superradiance in optically pumped HF gas", *Physical Review Letters*, vol. 30, no. 8, pp. 309–312, 1973.

- [103] L. L. Smith, "A Transportable Strontium Optical Lattice Clock Towards Space", PhD thesis, The University of Birmingham, 2016.
- [104] D. Swierad, S. Häfner, S. Vogt, *et al.*, "Ultra-stable clock laser system development towards space applications", *Scientific Reports*, vol. 6, no. September, pp. 1–8, 2016.
- [105] M. Takamoto, I. Ushijima, M. Das, *et al.*, "Frequency ratios of Sr, Yb, and Hg based optical lattice clocks and their applications", *Comptes Rendus Physique*, vol. 16, no. 5, pp. 1–10, 2015. arXiv: [1505.03207](#).
- [106] T. Tanabe, D. Akamatsu, T. Kobayashi, *et al.*, "Improved Frequency Measurement of the $1S_0$ - $3P_0$ Clock Transition in ^{87}Sr Using a Cs Fountain Clock as a Transfer Oscillator", *Journal of the Physical Society of Japan*, vol. 84, no. 11, pp. 1–2, 2015.
- [107] M. Tang, S. A. Schäffer, and J. W. Thomsen, "Spectral properties of lasing on a narrow transition in a cold Sr ensemble", 2019.
- [108] M. Tang, "Modeling Lasing in a Thermal Strontium Ensemble", PhD thesis, University of Copenhagen, 2018, p. 91.
- [109] M. Tang and S. A. Schäffer, "Det aktive atomur – en laser i sin reneste form", *Kvant - Tidsskrift for Fysik og Astronomi*, vol. 4, 2018.
- [110] H. Tanji-Suzuki, I. D. I. Leroux, M. H. Schleier-Smith, M. Cetina, A. T. Grier, J. Simon, V. Vuletic, and V. Vuletić, *Interaction between Atomic Ensembles and Optical Resonators. Classical Description*, November 2011. Apr. 2011, vol. 60, pp. 201–237. arXiv: [1104.3594](#).
- [111] J. I. Thorpe, K. Numata, and J. Livas, "Laser frequency stabilization and control through offset sideband locking to optical cavities.", *Optics express*, vol. 16, no. 20, pp. 15980–90, 2008.
- [112] D. A. Tieri, J. Cooper, B. T. R. Christensen, J. W. Thomsen, and M. J. Holland, "Laser stabilization using saturated absorption in a cavity QED system", *Accepted for publication in Physical Review A*, pp. 1–8, 2015. arXiv: [1506.08210](#).
- [113] I. Ushijima, M. Takamoto, M. Das, T. Ohkubo, and H. Katori, "Cryogenic optical lattice clocks", *Nature Photonics*, vol. 9, no. 3, pp. 185–189, 2015.
- [114] G. Vallet, E. Bookjans, U. Eismann, S. Bilicki, R. L. Targat, and J. Lodewyck, "A noise-immune cavity-assisted non-destructive detection for an optical lattice clock in the quantum regime", *New Journal of Physics*, vol. 19, no. 8, p. 083002, Aug. 2017. arXiv: [1703.04609](#).
- [115] S. Vogt, S. Häfner, J. Grotti, S. B. Koller, A. Al-Masoudi, U. Sterr, and C. Lisdat, "A transportable optical lattice clock", *Journal of Physics: Conference Series*, vol. 723, no. 1, 2016.
- [116] V. Vuletic, "An almost lightless laser", *Nature*, vol. 484, no. 7392, pp. 44–6, 2012.
- [117] F. Walls and D. Howe, "A Passive Hydrogen Maser Frequency Standard", in *32nd Annual Symposium on Frequency Control. IEEE*, 1978, pp. 492–498.

- [118] P. Wcisło, P. Ablewski, K. Beloy, *et al.*, “First observation with global network of optical atomic clocks aimed for a dark matter detection”, pp. 1–9, Jun. 2018. arXiv: [1806.04762](#).
- [119] P. G. Westergaard, “Horloge à réseau optique au Strontium : en quête de la performance ultime”, PhD thesis, SYRTE, 2010.
- [120] P. G. Westergaard, B. T. R. Christensen, D. Tieri, *et al.*, “Observation of Motion-Dependent Nonlinear Dispersion with Narrow-Linewidth Atoms in an Optical Cavity”, *Physical Review Letters*, vol. 114, no. 9, p. 7, Mar. 2015. arXiv: [1408.3983](#).
- [121] S. Weyers, V. Gerginov, M. Kazda, J. Rahm, B. Lipphardt, G. Dobrev, and K. Gibble, “Advances in the accuracy, stability, and reliability of the PTB primary fountain clocks”, *Metrologia*, vol. 55, no. 6, pp. 789–805, Dec. 2018. arXiv: [1809.03362](#).
- [122] Z. C. Xu, D. Pan, W. Zhuang, J. Chen, and C. Science, “Dual-Wavelength Bad Cavity Laser as Potential Active Optical Frequency Standard”, *Chinese Physics Letters*, vol. 32, no. 9, pp. 2–6, 2015.
- [123] J. Yao, J. A. Sherman, T. Fortier, *et al.*, “Optical-Clock-Based Time Scale”, *Submitted to Nature Photonics*, 2019.
- [124] J. Yao, J. Sherman, T. Fortier, *et al.*, “Progress on optical-clock-based time scale at NIST: Simulations and preliminary real-data analysis”, *Navigation*, vol. 65, no. 4, pp. 601–608, Dec. 2018.
- [125] M. Yasuda, H. Inaba, T. Kohno, *et al.*, “Improved absolute frequency measurement of the 171Yb optical lattice clock towards a candidate for the re-definition of the second”, *Applied Physics Express*, vol. 5, no. 10, 2012.
- [126] J. Ye, L.-S. Ma, and J. L. Hall, “Ultrasensitive detections in atomic and molecular physics : demonstration in molecular overtone spectroscopy”, *Journal of the Optical Society of America B*, vol. 15, no. 1, pp. 6–15, 1998.
- [127] W. Zhang, J. M. Robinson, L. Sonderhouse, *et al.*, “Ultrastable Silicon Cavity in a Continuously Operating Closed-Cycle Cryostat at 4 K”, *Physical Review Letters*, vol. 119, no. 24, p. 243 601, Dec. 2017. arXiv: [1708.05161](#).